

Sheffield Hallam University

Fatigue mechanisms in FV520B, a turbine blade steel.

CLARK, Anita

Available from the Sheffield Hallam University Research Archive (SHURA) at:

<http://shura.shu.ac.uk/3127/>

A Sheffield Hallam University thesis

This thesis is protected by copyright which belongs to the author.

The content must not be changed in any way or sold commercially in any format or medium without the formal permission of the author.

When referring to this work, full bibliographic details including the author, title, awarding institution and date of the thesis must be given.

Please visit <http://shura.shu.ac.uk/3127/> and <http://shura.shu.ac.uk/information.html> for further details about copyright and re-use permissions.

CITY CAMPUS, POND STREET,
SHEFFIELD, S1 1WB.

TELEPEN

100364210 1



REFERENCE

Fines are charged at 50p per hour

17 JUL 2002 5pm

23 FEB 2005

9pm

21 NOV 2005 4.04 pm

20 MAR 2006 9pm

23 JUN 2006 5pm

27 JUN 2006

- 5 OCT 2007 (6pm)

ProQuest Number: 10694351

All rights reserved

INFORMATION TO ALL USERS

The quality of this reproduction is dependent upon the quality of the copy submitted.

In the unlikely event that the author did not send a complete manuscript and there are missing pages, these will be noted. Also, if material had to be removed, a note will indicate the deletion.



ProQuest 10694351

Published by ProQuest LLC (2017). Copyright of the Dissertation is held by the Author.

All rights reserved.

This work is protected against unauthorized copying under Title 17, United States Code
Microform Edition © ProQuest LLC.

ProQuest LLC.
789 East Eisenhower Parkway
P.O. Box 1346
Ann Arbor, MI 48106 – 1346

FATIGUE MECHANISMS IN FV520B, A TURBINE BLADE STEEL

Anita Clark

A Thesis submitted in partial fulfillment of the requirements of
Sheffield Hallam University for the degree of Doctor of Philosophy.

April 1999



LEVEL 1

PREFACE

This thesis is submitted in partial fulfillment of the requirements of Sheffield Hallam University for the degree of Doctor of Philosophy. It contains an account of research carried out between November 1993 and April 1999 in the Materials Research Institute, Sheffield Hallam University, under the supervision of Professor JD. Atkinson and Dr EA. Wilson. Except where acknowledgment and reference is appropriately made, this work is, to the best of my knowledge, original and has been carried out independently. No part of this thesis has been, or is currently being, submitted for any degree or diploma at this, or any other University.

Anita Clark
April 1999

ACKNOWLEDGMENTS

I acknowledge the support and encouragement which I have received from Professor John Atkinson and Dr Eric Wilson during the course of this research project. I also acknowledge the Materials Research Institute and the School of Engineering at Sheffield Hallam University for the provision of the laboratory facilities.

I would like to thank all the technical staff in the Materials Research Institute and School of Engineering for their help and assistance during the course of the experimental work. Special thanks are extended to Mr Paul Slingsby, Mrs Cheryl Shaw, Mr Keith Wright, Mr Peter Haythorne, Mr Dick Mitchell and Mr John Ross-Smith; the latter for his expertise in preparing the test specimens. Finally, my thanks go to Mr Richard Frost for his work on the illustrations in this thesis.

I would also like to thank Mr John Truman and Dr Upul Fernando for their helpful discussions during the course of this research programme. I am also indebted to Alan Sayles and British Steel Technical for their provision of the MMC Quenching Dilatometer at Swinden Laboratory.

Thanks are also extended to both my family and my dear friend Claudia for their unfailing support. A special thanks is extended to my friends Christine, Richard, Dave, and Paul; all have unknowingly inspired me to complete this thesis.

ABSTRACT

An investigation has been undertaken to examine the effect of microstructure on the mechanical properties of FV520B, a precipitation hardenable martensitic stainless steel. This high performance grade of stainless steel was heat treated to three commercially available material specifications, namely the peak hardened, standard and softened overaged conditions. These three precipitation hardened conditions were found to exhibit a range of tensile properties. In order to determine the role of the microstructure, a full materials characterisation programme was performed.

The investigative techniques used to characterize the microstructures, were Transmission Electron Microscopy (TEM); Analytical Scanning Electron Microscopy (ASEM); optical microscopy; dilatometry and X-Ray Diffraction (XRD). The microstructural phases and features identified were measured and quantified wherever possible.

The effect of the material microstructure and environment on the fatigue properties of FV520B have been investigated. Fatigue tests were performed under uniaxial loading conditions at a stress ratio R ($\sigma_{\min}/\sigma_{\max}$) of -1. The tests were undertaken using highly polished specimens to determine the fatigue strength of the three precipitation hardened conditions. The test conditions employed were air and a corrosive 3.5% sodium chloride environment, at pH2 and ambient temperature. The role of the microstructure and the effectiveness of the tensile strengthening mechanisms on the fatigue and corrosion fatigue strength have been discussed. Using SEM, the fatigue crack nucleation mechanisms prevalent within the three microstructures in air and the chloride environment have also been identified. For the peak hardened material, non-metallic inclusions dominated the fatigue crack nucleation process in air and chloride environments. For the softened overaged condition, multiple site nucleation due to slip band cracking was the prevalent mechanism especially at higher nominal stress amplitudes. The tolerance of this high strength material to small defects at higher stress levels and the actual size of the critical microstructural defects initiating failure have also been highlighted.

The microstructure has been shown to strongly influence the processes of fatigue crack nucleation, Stages I and II crack propagation and the concept of the microstructure acting as barriers and providing resistance to crack growth have been discussed. The effectiveness and the size of these microstructural barriers to crack growth have been considered. This discussion has led to the proposal of a model that facilitates flow stress and fatigue lifetime predictions as a function of the quantity of a key microstructural phase. The key microstructural phase, namely reverted austenite affected both the tensile and fatigue properties of FV520B as a function of the heat treatment. The standard overaged material was found to exhibit the greatest resistance to fatigue crack propagation.

STATEMENT OF POSTGRADUATE STUDY

During the period in which the research work was carried out, two papers have been published and a conference attended. In addition to this a number of courses and seminars were attended. Details are given below:

- Publication of a paper entitled "Further Observations of Early Fatigue Crack Development" published in *Fatigue Fract. Engng. Mater. Struct* (1996), Vol. 19, No. 5, pp. 623-627.
- Publication of a paper entitled "Effect of Microstructure and Environment on the Fatigue Strength of a 14%Cr Stainless Turbine Blade Steel", presented at "Recent Advances in Corrosion Fatigue", 16-17 April 1997, Sheffield, UK.
- Attendance at a course on "Fracture Mechanics", 21-23 March and 18-20 April 1994, at Sheffield University, Sheffield, UK.
- Attendance at "Junior Euromat '94", organised by Deutsche Gesellschaft für Materialkunde e.V. (DGM), sponsored by The Federation of European Materials Societies (FEMS), 28 August-2 September in Lausanne, Switzerland.
- Attendance at several informal research seminars at Sheffield Hallam University.
- Attendance at a series of lectures based on "Fatigue and Fracture", "Crystallography" and "Electron Microscopy and X-Ray Techniques", at Sheffield Hallam University.

CONTENTS

	Page
PREFACE	i
ACKNOWLEDGMENTS	ii
ABSTRACT	iii
STATEMENT OF POSTGRADUATE STUDY	iv
CONTENTS	v
CHAPTER 1 INTRODUCTION	1
CHAPTER 2 LITERATURE REVIEW	6
2.1 Introduction	6
2.1.1 Low Pressure (LP) Steam Turbine Blade Materials	6
2.1.2 FV520B - A Turbine Blade Steel.	10
2.2 Dependence of Flow Strength on the Microstructure	12
2.2.1 Introduction	12
2.2.2 Tensile Strengthening Mechanisms	14
2.2.3 Tensile Strengthening Mechanisms in Lath Martensite	14
2.2.4 Quantifying the Flow Strength	15
2.3 Metal Fatigue	19
2.3.1 Introduction	19
2.3.1.1 Formation of PSBs & Fatigue Crack Nucleation	21
2.3.1.2 Microstructural Aspects of Early Crack Growth	25
2.3.1.3 Fatigue Crack Propagation	26
2.3.2 Short Fatigue Crack Behaviour	27
2.3.2.1 Introduction	27
2.3.2.2 Microstructural Barriers	29
2.3.2.3 Environmental Effects	31
2.3.3 Non-Metallic Inclusions	32
2.3.3.1 Introduction	32
2.3.3.2 Inclusions and Fatigue Crack Nucleation in Air	34
2.3.3.3 Prediction of the Fatigue Limit	36
2.4 Pitting Corrosion	39
2.5 Corrosion Fatigue	43

2.5.1 Introduction	43
2.5.2 Earlier Work on Corrosion Fatigue	45
2.5.3 Corrosion Fatigue Crack Nucleation Models	46
2.5.4 Corrosion Fatigue Crack Initiation at Corrosion Pits	46
2.5.5 Factors Affecting Corrosion Fatigue	47
2.5.5.1 Metallurgical Factors	47
2.5.5.2 Environmental Factors	48
2.5.6 Further Comments	48
2.5.7 Anodic Dissolution and Hydrogen Embrittlement	49
2.6 Stress Corrosion Cracking in Martensitic Stainless Steels	50
CHAPTER 3 EXPERIMENTAL PROCEDURE	52
3.1 Introduction	52
3.2 Materials Characterisation	52
3.2.1 Heat Treatment	52
3.2.2 Optical Microscopy	53
3.2.3 Transmission Electron Microscopy	53
3.2.3.1 Thin Foil Preparation	53
3.2.4 Point Count of Delta Ferrite	54
3.2.5 Grain Size Determination	56
3.2.6 X-Ray Diffraction	57
3.2.6.1 Sample Preparation	57
3.2.6.2 Peak Indexing	58
3.2.6.3 Quantitative Analysis of Reverted Austenite	59
3.2.6.4 Evaluation of the Theoretical Intensity	61
3.2.7 Precipitation Hardening Curve	64
3.2.8 Dilatometry Work	64
3.2.9 Non-Metallic Inclusion Study	65
3.3 Scanning Electron Microscopy	65
3.3.1 Sample Preparation	65
3.3.2 Modes of Operation	66
3.4 Fatigue Crack Nucleation and Short Fatigue Crack Monitoring	67
3.5 Mechanical Testing	68
3.5.1 Vickers Hardness Measurements	68

3.5.2 Tensile Testing	68
3.5.3 Fatigue Testing	69
3.5.3.1 Fatigue Specimen Design	72
3.5.4 Corrosion Fatigue Testing	73
CHAPTER 4 EXPERIMENTAL RESULTS	75
4.1 Introduction	75
4.2 Materials Characterisation	75
4.2.1 Chemical Analysis	75
4.2.2 Microstructures	77
4.2.2.1 Homogenisation	77
4.2.2.2 Hardening or Solution Treatment	78
4.2.2.3 Artificial Precipitation Hardening Treatment	78
4.2.3 Transmission Electron Microscopy	83
4.2.4 Point Count of Delta Ferrite	84
4.2.5 Grain Size Determination	84
4.2.6 X-Ray Diffraction (XRD)	84
4.2.7 Precipitation Hardening Curve	87
4.2.8 Dilatometry Results	87
4.2.9 Non-Metallic Inclusion Study	88
4.2.10 The Modified Schaeffler Diagram	103
4.3 Scanning Electron Microscopy (SEM)	103
4.3.1 Corrosion Fatigue Initiation Sites	103
4.4 Mechanical Testing Results	107
4.4.1 Vickers Hardness Measurements	107
4.4.2 Tensile Testing	107
4.4.3 Endurance Testing	107
CHAPTER 5 DISCUSSION	108
5.1 Introduction	108
5.2 Influence of the Microstructure on the Flow Stress	109
5.2.1 Prediction of the Flow Stress of FV520B	109
5.2.2 Tensile Properties of FV520B	117
5.3 Influence of Microstructure and Environment on Fatigue Crack Nucleation	122

5.3.1 Peak Hardened Material	122
5.3.2 Softened Overaged Material	126
5.3.3 Standard Overaged Material	130
5.3.4 The Effect of Test Frequency	132
5.3.5 Typical Crack Nucleation Sites in Chloride Environment	135
5.3.6 Further Comments on Crack Nucleation	143
5.4 Influence of Microstructure and Environment on Fatigue Strength	143
5.4.1 The Fatigue Strength in Air	143
5.4.2 The Fatigue Strength in a Chloride Environment	146
5.4.3 Short Fatigue Cracks in FV520B	149
5.4.4 The Stress Fatigue Life Relationship	154
5.5 Fatigue Lifetime Prediction Model for FV520B	156
5.5.1 Fracture Processes in FV520B	156
5.5.2 Proposed Lifetime Prediction Model	159
5.6 Stress Corrosion Cracking in FV520B	169
5.7 Concluding Remarks	169
 CHAPTER 6 CONCLUSIONS	 173
 CHAPTER 7 FURTHER WORK	 176
 REFERENCES	
 APPENDICES	
Appendix I - Data Tables	
Appendix II - FV520B Manufacturer's Data Handbook	
Appendix III - Chemical Analysis of Maraging Steels	
Appendix IV - Published Work	

CHAPTER 1

INTRODUCTION

The lifetime of a turbine is expected to lie between 30 to 40 years. During that time, the loading and environmental conditions which the low pressure (LP) turbine blades experience, can be severe. The blades which are often rotating at 50 Hertz are subjected to high stresses from the centrifugal loads generated during operating conditions. Superimposed on these high static stresses are high frequency load cycles which result from vibratory or rotary bending stresses [1]. The amplitude of these service stresses are known to be variable, but their magnitude however, is largely unknown. Figure 1.1 illustrates the low pressure (LP) rotor and last stage LP blades. The length of the last stage blades in Figure 1.1 is approximately 1m.

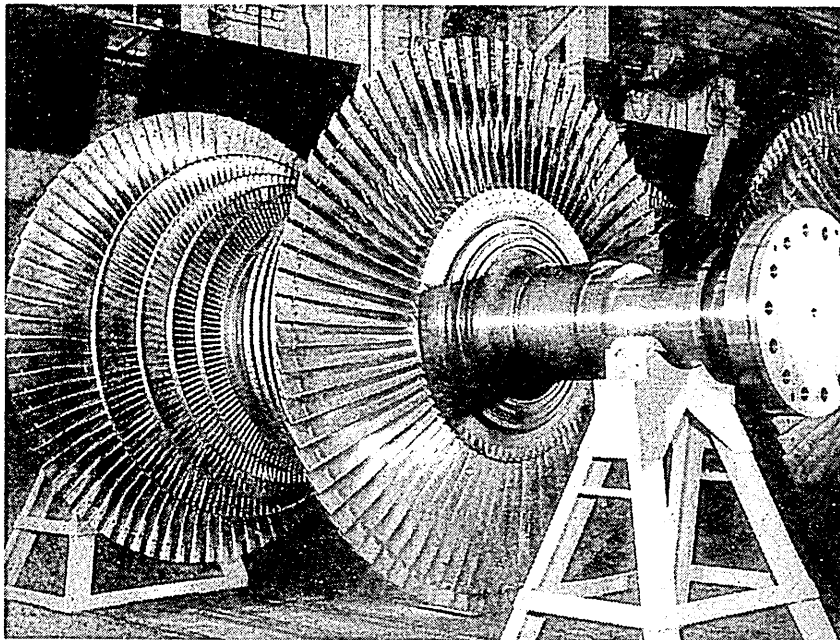


Figure 1.1 A Low Pressure (LP) Rotor and Last Stage Blades.

In the last rows of the low pressure (LP) turbine, a condensate is likely to form just in front of what is commonly known as the Wilson-line (moisture line). In this region, impurities which have low solubility, can be readily deposited on the LP blades whilst the small amount of condensate present will concentrate them [2]. The major

impurities found at the Wilson-line are chloride, sulphide, silicate and phosphate anions [3]. It is chloride [4-7] and sulphide anions that are particularly aggressive towards martensitic stainless steels which otherwise possess good pitting corrosion resistance. It is this combined effect of pitting corrosion and cyclic service loads which can result in the premature failure of LP blades by corrosion fatigue.

FV520B is widely used as LP blading material in the UK's coal-fired power stations. It possesses a combination of properties such as high tensile and fatigue strength, in addition to good pitting corrosion resistance. These exceptional mechanical properties render FV520B befitting for use as an LP turbine blading material; where resistance towards fluctuating stresses in condensing steam is of utmost importance. Over recent years, FV520B has replaced the slightly lower alloyed FV566 due to its superior mechanical properties, pitting corrosion resistance and resistance to stress corrosion cracking (SCC). However, corrosion fatigue failures of blading material manufactured from FV520B still occur. Figure 1.2 illustrates the shape of a low pressure turbine blade. The blade is approximately 1 m in length.

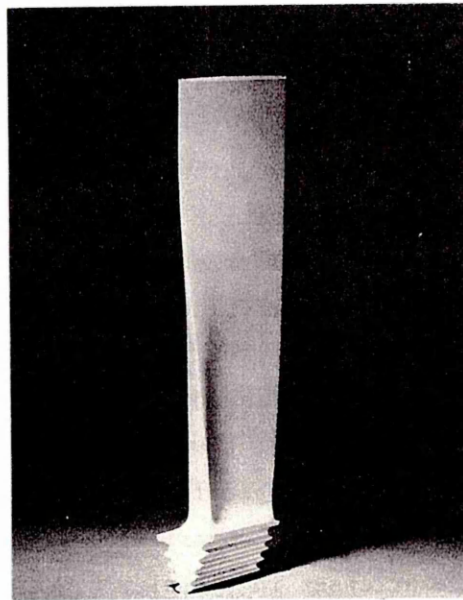


Figure 1.2. A Low Pressure Turbine Blade.

Although FV520B is extensively used within both the power generating and aerospace industries, only a limited amount of materials property data has been published to date [8-14]. Moreover, whilst the available literature for FV520B

concentrates on structure and mechanical property relationships [15] [16], there appears to be a definite gap in understanding the effects of material microstructure on environmentally assisted cracking mechanisms. One researcher [17] has assisted our understanding when investigating the propensity of FV520B to stress corrosion cracking (SCC) as a function of microstructure. From that study, it was concluded that FV520B, treated to give the superior tensile properties, namely the peak hardened condition, was found least resistant to SCC in an aggressive caustic solution. Whilst our understanding of SCC mechanisms in FV520B is reasonably clear, a few questions relating the microstructure to the fatigue strength, remain unanswered. Kitagawa [18] has attempted to bridge this gap by relating the material microstructure, tensile properties and the fatigue strength of a wide range of engineering steels, although he excluded stainless steels.

It has therefore been the primary objective of this research programme to understand the effect of microstructure on the tensile and fatigue strength of FV520B. The influence of a corrosive environment has also been considered. These objectives have been met by studying three commercially available microstructures of FV520B which cover a range of tensile strength levels. The heat treated conditions of FV520B under investigation were the peak hardened, standard and softened overaged conditions. Aspects concerning the physical metallurgy of these three materials, in addition to fatigue loading in both the air and a chloride environment led to an in-depth understanding of the fatigue crack nucleation mechanisms. Additionally, theories on short crack and material interactions and their significance at high stress amplitudes have been recognised and studied. The importance of predicting the fatigue lifetime of a rotating body under fluctuating stresses is also understood to be important and has led to the development of a prediction model.

During the course of this study, in excess of 50 high cycle fatigue tests have been performed under uniaxial loading. The tests were conducted under load control conditions at a stress ratio ($\sigma_{\min}/\sigma_{\max}$) of -1. Uniaxial, i.e. push-pull testing, was the most appropriate loading mode for the simulation of the in-service loading conditions experienced by the LP turbine blades. The blades are known to experience tensile stresses due to the fluctuating centrifugal forces and in addition to this, cyclic bending stresses will also subject the blades to tensile and compressive forces. Although the service loading condition is such as to produce a stress ratio greater than zero, a

stress ratio of -1 was used, hence the effect of mean stress was not studied in this investigation. The hour-glass specimen design facilitated the taking of plastic replicas whilst their highly polished surface allowed the effect of the microstructure during fatigue crack nucleation and propagation to be examined. It is understood that in the near future, a leading power generating company will be utilising highly polished turbine blades, in an effort to minimise the number of blade failures.

From this investigation, the following conclusions were made. Firstly, the non-metallic inclusions were found to render the peak hardened material sensitive to notch-like features. The inclusion population which was constant for the three microstructures, proved to be the dominant microstructural feature acting as sites for fatigue crack nucleation for the peak hardened condition in air. It is thought that these inclusions were also primary sites for corrosive attack in the chloride environment, which ultimately led to crack nucleation. Therefore, from these observations it can be concluded that steel cleanliness is of primary importance when considering the peak hardened material for any engineering application. In contrast, for the case of the two overaged microstructures, the inclusions were not solely responsible for crack nucleation in either the air or the chloride environment. However, a relatively low strength phase, namely reverted austenite which these two conditions contain in significant amounts, is thought to be responsible for the multiple fatigue crack nucleation observed. It is understood that, although the presence of this softer phase was partly responsible for reducing the tensile strength of the standard and softened overaged conditions, it had the overall benefit of reducing the notch-sensitivity aspects of the material. The size of the fatigue crack in Stage I in the three microstructures was found to be small and comparable to the size of the key microstructural features, i.e. 6 to 25 μm . However, it is thought that a significant portion of the fatigue lifetime was spent in Stage I crack propagation.

In the air environment, the tests were conducted at stress amplitudes that ranged from 816 to 427 MNm^{-2} , i.e. maximum stress ranges of 1632 to 854 MNm^{-2} which gave corresponding fatigue lifetimes of 67,000 and 1×10^8 cycles respectively. In the chloride environment, these lifetimes were reduced to a range of from 25,450 to 281,770 cycles when tested over a stress amplitude that ranged from 700 to 520 MNm^{-2} respectively. In air, the peak hardened material exhibited superior fatigue strength over the standard and overaged conditions and therefore the fatigue strength

could be approximately related to the tensile strength. However, under the chloride environment, the fatigue strengths for the three microstructures based on 1×10^6 cycles to failure were found to be similar and therefore no dependency between the tensile properties and fatigue strength in a chloride environment was found.

Two empirical models have been proposed for predicting the flow stress and the fatigue lifetime of FV520B under tensile and cyclic loading respectively. These facilitate predictions of FV520B's behaviour as a function of the quantity of the weaker phase, ie reverted austenite.

The results from this investigation would suggest that the standard overaged condition, which is FV520B that is heat treated to its intermediate strength level, may be more suitable as all LP blading material than the high strength peak hardened condition. This conclusion was derived from the mechanical testing results where an improvement in the fracture resistance property was apparent. Good fracture resistance is essential for high strength materials utilised at high stresses and would be a primary consideration when selecting a microstructure of FV520B for LP turbine blading.

CHAPTER 2

LITERATURE REVIEW

2.1 Introduction

The aim of this chapter is to present a concise review on the tensile, fatigue, pitting corrosion and corrosion fatigue behaviour of metals. The effect of the metallurgical and environmental conditions on each of these factors are discussed. Stress corrosion cracking and hydrogen assisted fracture mechanisms which are also known to affect martensitic microstructures in a chloride environment are also mentioned. A number of quantitative models which have been developed to predict the tensile and fatigue strength of metals, in addition to the fatigue crack threshold conditions, are reviewed where appropriate.

The literature in this particular field is acknowledged as being extensive. Therefore, a bias towards high strength steels and in particular 12-14% Cr martensitic stainless steels, has been maintained throughout this review.

2.1.1 Low Pressure (LP) Steam Turbine Blade Materials

Steam turbine blade reliability is determined by the inter-relationship of three key areas as depicted in Figure 2.1. Measures taken to reduce corrosion fatigue failures has involved action in all three areas [19].

Extensive work [1] has been carried out to identify the most suitable LP turbine blading material, in terms of its resistance to high cycle fatigue and pitting corrosion resistance [20]. To meet these materials performance criteria, LP turbine blade materials have traditionally been highly alloyed stainless steels based on the 12% chromium grades.

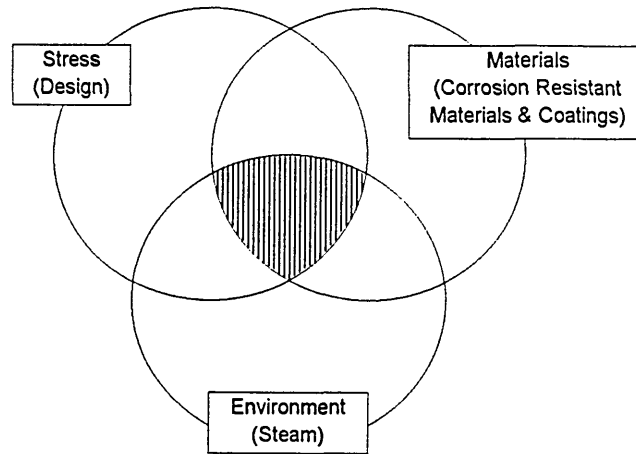


Figure 2.1 Factors to be Considered for Steam Turbine Reliability.

The modified Schaeffler diagram [119], is a tool used for determining the resultant microstructures of highly alloyed steels. This diagram allows the contribution of individual alloying elements to be assessed, in terms of their chromium and nickel equivalents. The diagram predicts the resultant microstructure on the basis of an alloying element's propensity towards forming ferrite or stabilising austenite.

Since the quantity of chromium dictates the materials corrosion resistance (and molybdenum in the case of pitting corrosion resistance), it has been suggested that the chromium equivalent can be used as a guide to assess the corrosion resistance of potential blade materials [19]. The modified Schaeffler diagram shows that current ferrous turbine blade materials could potentially belong to the following classes of stainless steels:

- (i) martensitic stainless
- (ii) precipitation hardenable martensitic stainless
- (iii) austenitic stainless
- (iv) duplex stainless
- or (v) ferritic stainless steels

Figure 2.2 highlights the microstructures of current LP turbine blading steels according to their respective chromium and nickel equivalents.

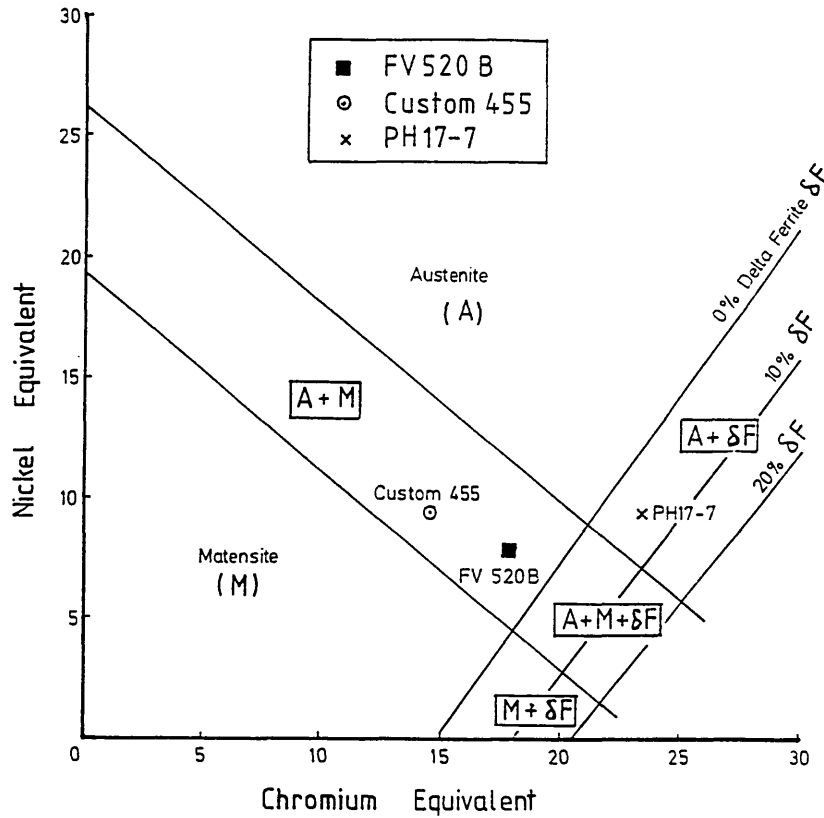


Figure 2.2 The Modified Schaeffler Diagram [119].

The chromium, and nickel equivalents of FV520B used in this study have been evaluated as 17.04 and 7.74 respectively. The full results are presented in Section 4.2.10.

In general, the precipitation hardenable grades of martensitic stainless steel provide an excellent combination of strength, toughness and corrosion resistance [19]. When compared to a standard 13%Cr grade, the pitting corrosion resistance of a 14%Cr precipitation hardenable stainless steel in a chloride environment was found to be the superior [6]. This was primarily due to the higher chromium and molybdenum content. The elemental compositions of three different LP turbine blade materials, namely X5CrNiMoCuNb145, X20Cr13 and FV520B are presented in Table 2.1.

Material Specification	Element (bal Fe)										
	C	Si	Mn	Cr	Ni	Mo	Cu	Nb	P	S	
FV520B	0.07 max	0.7 max	1.00 max	13.2- 14.7	5.0- 6.0	1.2- 2.0	1.2- 2.0	0.20 - 0.70	0.040 max	0.040 max	
x20Cr13	0.19	0.38	0.40	12.8	-	-	-	-	0.016	0.017	
x5CrNiMoCuNb145	0.06	0.27	0.79	13.84	5.46	1.79	1.70	0.36	0.012	0.004	

Table 2.1 The Material Specifications of FV520B and Various Ferrous Turbine Blading Materials.

Elemental Notation carbon (C), silicon (Si), manganese (Mn), chromium (Cr), nickel (Ni), molybdenum (Mo), copper (Cu), niobium (Nb), phosphorous (P), sulphur (S), iron (Fe).

The pitting corrosion and hence the corrosion fatigue resistance of titanium alloys are known to be superior to martensitic stainless steels [131]. This has resulted in some turbines being refitted with titanium alloy blades. However, the inherent expense of titanium alloys has resulted in the continued use of the martensitic stainless steel grades.

2.1.2 FV520B - A Turbine Blade Steel.

FV520B is a low carbon, precipitation hardening martensitic stainless steel. It possesses a combination of properties such as high strength, excellent corrosion resistance, good high temperature oxidation resistance and toughness [8]. These properties render FV520B a suitable blading material for use in the low pressure (LP) section of the steam turbine. FV520B principally contains 14% chromium, which imparts the stainless property by forming a stable, transparent passive surface film. The incorporation of 5-6% nickel increases the corrosion resistance (to strong acids) by strengthening the passive film. Additions of 1-2% molybdenum improves the pitting resistance of the surface especially against corrosive attack by chlorides. The addition of 1-2% copper increases the tensile and fatigue strength, whilst slightly improving the corrosion resistance.

To obtain the required mechanical properties, FV520B must undergo a three stage heat treatment schedule. These three stages are homogenisation, solution treatment and a final precipitation hardening heat treatment. Three stage heat treatments can prove time consuming, (financially) costly and in a production situation are not always desired. This initiated a study [14] whereby the physical properties of FV520B were investigated with a view to developing an alternative two stage treatment. This study involved replacing the first two stages with a combined homogenisation and solution treatment stage which would then be followed by the precipitation hardening treatment.

FV520B has been likened to a maraging steel by a worker [16], possibly due to the similarities in microstructure and carbon content and due to the dependence of precipitation hardening providing a significant portion of the tensile strength. In this study [16], the effect of heat treatment on the microstructure and properties was

investigated. Several other workers [14-16] have also attempted to characterise the microstructure of FV520B.

The isothermal precipitation hardening curve (at 450°C) for FV520B in the peak hardened condition is shown in Figure 4.5. It is generally accepted that on increasing the materials hardness, the tensile strength of the material will also increase. The first precipitation hardening reaction, which is of the greatest importance from a commercial point of view, was thought to be the precipitation of elemental copper [21]. Others [22] [23] have made tentative suggestions that Ni_3Mo and Fe_2Mo precipitates may also form, although it is not known whether these precipitates form in FV520B. This current investigation and a previous study [16] has not endeavoured to characterise these precipitates in terms of their chemical composition, morphology, size and interparticular spacing. The reasoning behind this is that precipitation hardening at 450°C is known to produce fine sub-microscopic particles, which are inherently difficult to resolve in the electron microscope [24]. The technique of field-ion microscopy (field-ion microscope-atom probe) however, has been shown capable of resolving such fine precipitates [25]. In an iron-1.4^{at}% copper alloy, the average diameter of the particles resolved using this technique was 2.4 nm. On implementing a precipitation hardening treatment which overaged the microstructure, the size of the particles increased which allowed them to be resolved under the transmission electron microscope [24] [26].

Maraging steels are known to experience a reversion of the lath microstructure to austenite during the precipitation hardening treatment. This reverted phase is commonly known as reverted austenite. Reverted austenite is produced on heating close to or above the temperature at which austenite starts to transform, i.e. the A_{c1} temperature. The quantities of reverted austenite in certain maraging steels has been so pronounced, that a number of workers [27-29] have made detailed studies investigating the factors which promote the reversion reaction. The reversion is due to a diffusion controlled mechanism that is primarily driven by temperature; particularly at temperatures between 500-700°C. In general, the higher the precipitation hardening temperature or the longer the treatment time at lower temperatures, the greater the percentage volume of reverted austenite is produced [29]. For example, in one particular investigation, no reverted austenite was detected on precipitation hardening at 430°C for a period of 64 hours [27]. In contrast, 30% was detected after

3 hours at 675°C [28]. These studies [26] [27] have not questioned the impact or influence of such high volumes of reverted austenite on the mechanical properties of these maraging steels.

The characteristics of several maraging steels found to comprise reverted austenite has been tabulated in Table 2.2. The chemical analyses of these steels are presented in Table E1, in Appendix III.

2.2 Dependence of Flow Strength on the Microstructure

2.2.1 Introduction

The flow stress can be defined as the strength level at which either the onset of plastic deformation or fracture occurs; otherwise known as the yield stress and the ultimate tensile stress respectively. Some researchers may even use the flow stress to define a strength level between these two values. The flow stress is dependent on the microstructure and its effectiveness in impeding the movement of dislocations. For example, in the case of grain boundary strengthening, the grain boundaries provide an effective obstacle to the motion of dislocations. As yielding within a single grain occurs, the dislocations pile-up at the grain boundaries since they are unable to progress due to differences in crystallographic orientation in the adjacent grains. Yielding within the adjacent grains will only occur if additional dislocations are generated and this requires an increase in the applied stress. The process of localised yielding is repeated throughout the microstructure as the microstructural barriers are overcome and deformation on a macroscale is evident.

Reverted austenite is known to improve certain tensile properties, namely the ductility of maraging steels due to the occurrence of strain induced transformations [29] [31]. The onset of plastic deformation would provide the driving force required for the strain induced transformation of the reverted austenite to martensite. The initial quantity of reverted austenite and the test temperature under which the material was deformed was found to dictate the level of ductility achieved. The reverted austenite has found to be metastable under the application of an impact stress [31].

Ref.	Precipitation Hardening Treatment	Type of Reverted Austenite	Location of Reverted Austenite	Percentage Volume	Width of Reverted Austenite (nm)	Comments
[27]	430°C for 64 hours	-	-	none observed		-
[27]	500°C for 8 hours	lath-like	prior austenite boundaries, martensite lath boundaries	-	5.3	austenite rich in nickel, diffusion controlled transformation
[27]	570°C for <4 hours	lath-like	prior austenite boundaries martensite lath boundaries	-	> 5.3	-
[27]	570°C for 4 hours	lath-like	prior austenite boundaries, martensite lath boundaries	-	> 5.3	austenite rich in nickel, diffusion controlled transformation
[27]	640°C	plate-like	within martensite laths	-	> 5.3	shear dominated phase transformation
[27]	640°C	lath-like	prior austenite boundaries, martensite lath boundaries	-		
[27]	640°C	plate-like	within martensite laths	-		
[28]	675°C for 3 hours cold rolled + 490°C for 3 hours	plate-like	within martensite laths	30	100	
[29]	580°C for 3 hours	-	-	33	-	-
[29]	620°C for 3 hours	-	-	45	-	-
[29]	660°C for 3 hours	-	-	63	-	-

Table 2.2 Microstructural Features of Several Maraging Steels, After Various Workers.

2.2.2 Tensile Strengthening Mechanisms

The Hall-Petch equation, equation (2.1) defines the relationship between the yield stress and the grain size for pure iron and carbon steels [32] [33].

$$\sigma_y = \sigma_0 + k_y d^{-\frac{1}{2}} \quad (2.1)$$

where σ_y is the yield stress. The value of σ_0 is the friction stress equivalent to the yield stress of a constrained single crystal. The constant k_y is the dislocation locking factor which is related to the ease of yielding from one grain to another. The grain size is represented by d .

According to equation (2.1) refining the grain size is one of the most effective methods employed to increase the yield stress of many low alloy and carbon steels. A common heat treatment practice used for refining the grain size is normalising. During normalising, the grain size is refined, resulting in an increase in the number of potential interactions between grain boundaries and dislocations. The deformation bands which are often evident on a steel sample surface subject to tensile loading are commonly known as Lüders bands [39].

2.2.3 Tensile Strengthening Mechanisms in Lath Martensite

Pure iron can be used as a classic example of a material with a simple microstructure. However, commercially, pure iron is of little use as a construction material simply due to its poor mechanical properties, such as low tensile strength. By adding a combination of alloying elements to iron, its mechanical properties are significantly improved rendering the steel of greater commercial importance.

Low alloy steels are such an important class of materials which may form by alloying iron and implementing a particular heat treatment. Often these steels are heat treated to the quenched and tempered condition and hence the resultant microstructure would be tempered lath martensite.

The microstructural features present in a tempered lath martensite microstructure are the prior austenite grain boundaries; lath packets; the individual laths themselves; a high density of dislocations; carbon in interstitial solid solution or as carbide precipitates and elements in substitutional solid solution [113] [132]. It follows that the Hall-Petch equation in its present form, as is given by equation (2.1), does not adequately describe the strengthening mechanism for quantifying the yield stress for a tempered lath martensite microstructure.

When considering more highly alloyed steels, for example a precipitation hardenable martensitic stainless steel such as FV520B, the microstructure becomes even more complex. Therefore more complicated empirical expression is required to define and reflect the additional strengthening mechanisms operating in the FV520B microstructure. It is thought that in this case additional strength would be provided from the precipitation hardening in addition to the strengthening mechanisms previously described for low alloy steels.

2.2.4 Quantifying the Flow Strength

Quantifying the flow stress in terms of the contributions from the individual strengthening mechanisms described earlier allows the mechanical properties of a steel to be designed for a specific engineering application.

In the case of low carbon iron, the following relationship defines the flow stress [122].

$$\sigma = G\alpha_1 b \rho^{\frac{1}{2}} + G\alpha_2 b \frac{1}{\lambda} + \frac{\alpha_3 f}{b a_0^3} \quad (2.2)$$

The first term $G\alpha_1 b \rho^{\frac{1}{2}}$ represents strengthening due to strain hardening whilst the second term $G\alpha_2 b \frac{1}{\lambda}$ describes the strengthening effects from precipitates of spacing

λ . The third term, i.e. $\frac{\alpha_3 f}{b a_0^3}$ defines strengthening by interstitial solid solution

hardening due to carbon and nitrogen, and has been defined according to the Snoek effect [122].

The parameters f and b represent the atomic fraction of the interstitial elements and the Burgers vector respectively; whilst a_0 is the lattice parameter of the solvent, i.e. iron. The parameter ρ is the dislocation density and λ is the interparticular spacing for solute atoms. The value of the shear modulus G ; the Burgers vector b and the constants α_1 , α_2 , and α_3 for low carbon iron [122] are given in Table 2.3.

Table 2.3 The Constants used for Evaluating the Flow Stress of Iron [122].

Constant	Value
G	82.5 GN/m ²
b	0.248 nm
α_1	0.3-0.4
α_2	0.3-0.4
α_3	38x10 ⁻²⁰

Equation (2.2) has been used to define the flow stress of a medium carbon steel (0.3%C). However, the modification of equation (2.2) has been required to account for the additional strengthening effect in martensite which results from greater additions of carbon. It has been found that the increase in flow stress is partly due to carbon in interstitial solid solution which has been related to the carbon concentration.

According to the earlier studies of Winchell and Cohen [125], the flow stress in lath martensite steels, was thought to be proportional to the cube root of the carbon content, as given in equation (2.3).

ie.

$$\Delta\sigma = \alpha_4 C^{\frac{1}{3}} \quad (2.3)$$

where $\Delta\sigma$ is the increase in flow stress and C is the concentration of carbon.

The third term $\frac{\alpha_3 f}{ba_0^3}$ in equation (2.2) for low carbon iron was replaced by the $C^{1/3}$ relationship to define strengthening by interstitial carbon in martensite. Therefore equation (2.2) becomes:

$$\sigma = G\alpha_1 b \rho^{\frac{1}{2}} + G\alpha_2 b \frac{1}{\lambda_{\text{carbide}}} + \alpha_4 C^{\frac{1}{3}} \quad (2.4)$$

In contrast to equation (2.3), Fleischer [123] proposed that the flow stress could be related to the square root of the carbon concentration, i.e. $C^{1/2}$ which is given in equation (2.3). Fleischer's model facilitates the prediction of the flow stress for a dislocation bending around an interstitial solute atom.

i.e.

$$\Delta\sigma = \alpha_4 C^{\frac{1}{2}} \quad (2.5)$$

$\Delta\sigma$ is the increase in the flow stress due to carbon in interstitial solid solution and α_4 is a constant. (Note: the value of α_4 in equation (2.3) is different to the value of α_4 in equation (2.5)). For the present study only the equation (2.3) has been used.

Equation (2.4) was further extended in order to account for the addition of 1.5% copper to the 0.3% carbon steel. Therefore, for the case of the medium carbon low alloy steel (0.3%C-1.5%Cu), the increase in flow stress can be expressed by equation (2.6). This additional strength can be attributed to precipitation hardening due to copper.

i.e.

$$\Delta\sigma = G\alpha_5 b \frac{1}{\lambda_{\text{copper}}} \quad (2.6)$$

where α_5 is a constant and λ_{copper} is the interparticular spacing for copper precipitates.

Incorporation of equation (2.6) in equation (2.4) becomes (2.7) for the 0.3%C-1.5%Cu steel [24]:

$$\sigma = G\alpha_1 b \rho^{\frac{1}{2}} + G\alpha_2 b \frac{1}{\lambda_{\text{carbide}}} + \alpha_4 C^{\frac{1}{3}} + G\alpha_5 b \frac{1}{\lambda_{\text{copper}}} \quad (2.7)$$

The estimated values of the shear modulus (G); the Burgers vector (b) and the constants α_1 , α_2 , α_4 and α_5 used in equations (2.4) and (2.7) are presented in Table 2.4.

Table 2.4 The Constants used for Evaluating the Flow Stress of a 0.3%C and 0.3%C-1.5%Cu Steel [24].

Constant	Estimated Value
G	82.5 GN/m ²
b	0.248 nm
α_1	5.2×10^{-9}
α_2	5.2×10^{-9}
α_4	116
α_3	6.7×10^{-9}

The grain structure of lath martensite microstructure mentioned in this section are known to comprise prior austenite grain boundaries, the lath martensite packets and the individual laths themselves. All these grain boundaries act as barriers to dislocation movement and are thought to contribute to the flow strength of the material.

For a medium carbon steel such as AISI 4340, the 0.2% yield strength ($\sigma_{0.2}$) can be described by the relationship as in equation (2.8) [34]. This is an extension of the Hall-Petch equation, given in equation (2.1) to account for the effects of grain boundary strengthening due to the lath packets:

$$\sigma = \sigma_0 + 126 \times 10^{-2} \bar{w} + 4.21 \times 10^{-3} \frac{1}{\lambda_{\text{carbide}}} \quad (2.8)$$

where σ_0 is the Peierls stress. The value of \bar{w} is represented by $d^{-1/2}$ where d is the lath packet size. However, the use of this equation has limitations as it requires a value of σ_0 .

2.3 Metal Fatigue

2.3.1 Introduction

The relevance of alternating stresses to component failures well below the yield stress has been recognised for over 150 years. During this time, a substantial amount of literature has been published in an effort to improve our understanding and with a view to preventing what are known as metal fatigue failures. There are a number of individuals who as engineers or materials scientists have provided a significant contribution to our understanding of this phenomena. Within the scope of this literature review, an attempt has been made to recognise these workers and their outstanding efforts.

In the 1850's, August Wöhler [35] was one of the first engineers to systematically perform fatigue tests during a study of rail axle failures. Presenting his findings as endurance data or S-N curves, led to the discovery of what is commonly known as the fatigue or endurance limit. The fatigue limit in an inert atmosphere is considered to be the stress amplitude below which fatigue cracks may initiate and propagate until constrained by the microstructure [36].

The fatigue life in the high cycle regime is usually expressed by the power law relationship, as proposed by Basquin [38]:

$$\sigma_a = \sigma_f' (2N_f)^b = \frac{\Delta \epsilon_E E}{2} \quad (2.9)$$

where σ_a is the stress amplitude; $2N_f$ is the number of stress reversals to failure (1 reversal is $\frac{1}{2}$ cycle); σ_f' is the fatigue strength coefficient and b is the fatigue strength exponent (Basquin's exponent). $\frac{\Delta \epsilon_E E}{2}$ is the elastic strain range and E is Young's modulus.

An expression for the low cycle fatigue behaviour was developed by Coffin et al [133] and Manson et al [117] who recognised that plastic strains were responsible for

fatigue damage. They developed the following expression, to account for the considerable plastic deformation which occurs during high strain cyclic loading.

$$\frac{\Delta \epsilon_p}{2} = \epsilon_f' (2N_f)^c \quad (2.10)$$

where $\frac{\Delta \epsilon_p}{2}$ is the plastic strain range; ϵ_f' and c are the fatigue ductility coefficient and fatigue ductility exponent respectively.

The total strain range, i.e. $\frac{\Delta \epsilon_T}{2}$ can be represented by the summation of the elastic and the plastic components. Thus equations (2.9) and (2.10) become:

$$\frac{\Delta \epsilon_T}{2} = \frac{\Delta \epsilon_E}{2} + \frac{\Delta \epsilon_p}{2} = \frac{\sigma_f'}{E} (2N_f)^b + \epsilon_f' (2N_f)^c \quad (2.11)$$

The equations (2.9), (2.10) and (2.11) have been represented schematically in Figure 2.3.

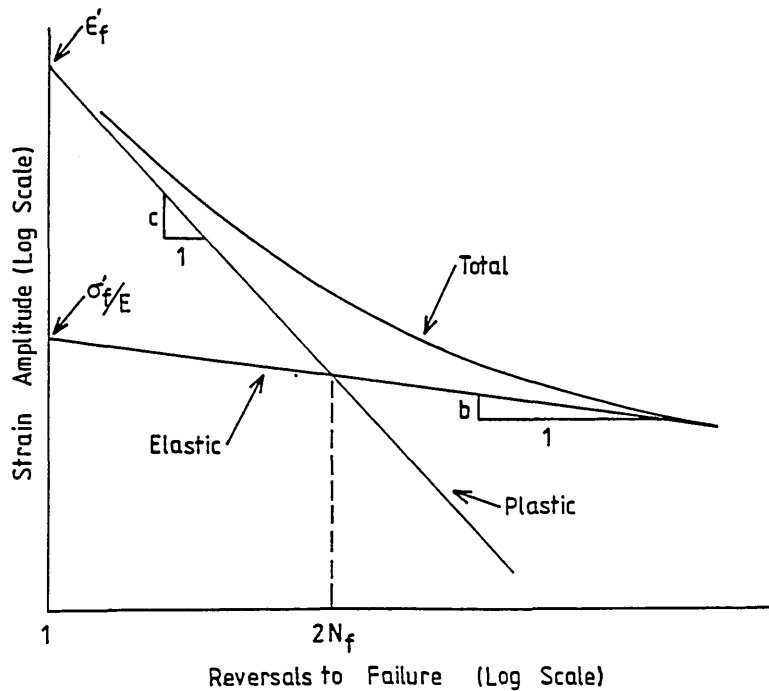


Figure 2.3. Plastic, Elastic and Total Strain Life Curves.

The parameters σ_f' , ϵ_f' , b and c are material properties and reflect a material's resistance to cyclic loading. As seen from Figure 2.3, at higher fatigue lives, the elastic strain amplitude is the dominant variable and the major part of the fatigue life, in this case, is spent in the nucleation or propagation of short fatigue cracks. Hence, the resistance of a material to crack nucleation or short crack propagation is reflected by the constants σ_f' and b . Typical values of b for a low carbon (SAE 1015) and a high carbon steel (SAE 1045) are -0.11 and -0.081 respectively [39]. At shorter fatigue lives, endurance is controlled by the plastic strain amplitude. Since the majority of the fatigue life in this case, is spent on propagating fatigue cracks, the materials resistance to crack propagation is described by the constants ϵ_f' and c . Coffin [133] showed that the value of the fatigue ductility exponent c is approximately constant for most metals, estimating its value to be -0.5. It has been shown that the empirical relationship developed by Coffin-Manson can be derived from the Paris equation [136] for crack propagation, as widely used in Linear Elastic Fracture Mechanics (LEFM).

2.3.1.1 Formation of PSBs & Fatigue Crack Nucleation

The fundamental mechanism for fatigue crack nucleation is believed to be understood. In plain or smooth specimens, in the absence of internal defects, fatigue cracks generally initiate at the free surface. The surface grains are not fully constrained by the bulk material, thus allowing slip to occur readily with less resistance. In general, the widely accepted view of the fatigue crack nucleation process is the result of the accumulation of irreversible slip under repeated or cyclic loading.

Ewing and Humphrey [127] were regarded as the first engineers to experimentally observe fatigue damage around the turn of the century. They discovered surface roughening, ie plastically deformed material at the surface which subsequently lead to the nucleation of fatigue cracks. Highly localised plastic (permanent) deformation occurs due to irreversible slip in a few grains where the slip direction is favourably orientated to the applied loading. These permanent changes may occur within the microstructure after only a few thousand load cycles and may led to the formation of slip bands. Thompson et al [42] revealed that the life of a copper alloy could be extended considerably by electropolishing and removing some of the surface

damage, i.e. slip bands. However, after further fatigue cycling, the slip bands reappeared in the same location and so the term persistent slip band (PSB) was realised. A taper sectioning technique enabled Wood [126] to identify what appeared to be a herringbone-type structure within a slip band. This would later be identified as the dislocation sub-structure.

Forsyth [43] discovered surface roughening in the form of thin ribbons of extruded metal. These were found to emanate from persistent slip bands in a partially precipitation hardened aluminium-4 wt% copper alloy. These extruded ribbons of metal measured approximately 0.1 μm and 10 μm in thickness and length respectively, see Figure 2.4. The formation of extrusions was thought to be an extension of the slip band formation process which required slip on intersecting planes (cross-slip) and some irreversibility of slip [130]. The reverse process to extrusion formation, namely intrusion formation has also been observed at the surface after fatigue loading [44] [46]. These crevices act as regions of stress concentration and are known to promote additional slip and fatigue crack nucleation [46]. Forsyth [47] (aluminium-4wt% copper alloy) and Cottrell and Hull [45] (in copper) proposed mechanisms for the formation of extrusions and intrusions pairs. These models predict that extrusions and intrusions will be inclined with respect to each other, with a large angle between them. Cottrell and Hull's model for cyclic slip from intersecting slip planes is schematically illustrated in Figure 2.5. However, extrusion and intrusion pairs have been observed parallel to each other and even along the same slip band [49].

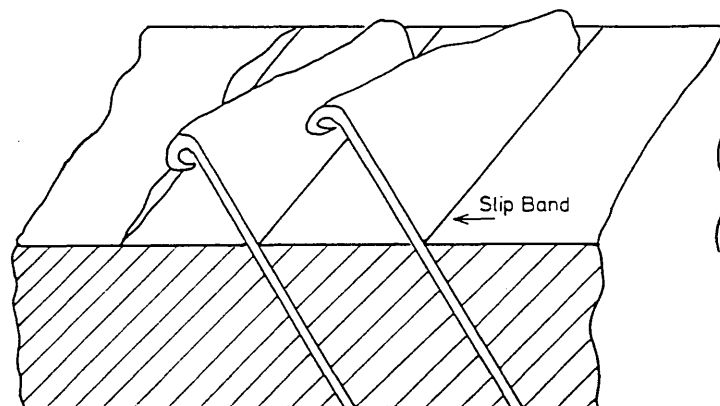


Figure 2.4 Slip Band Extrusions.

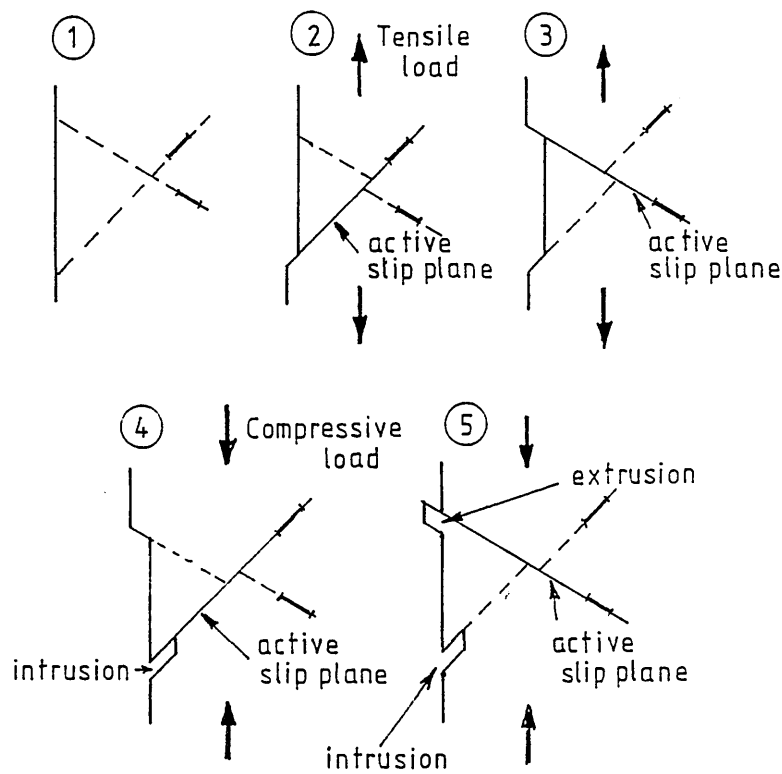
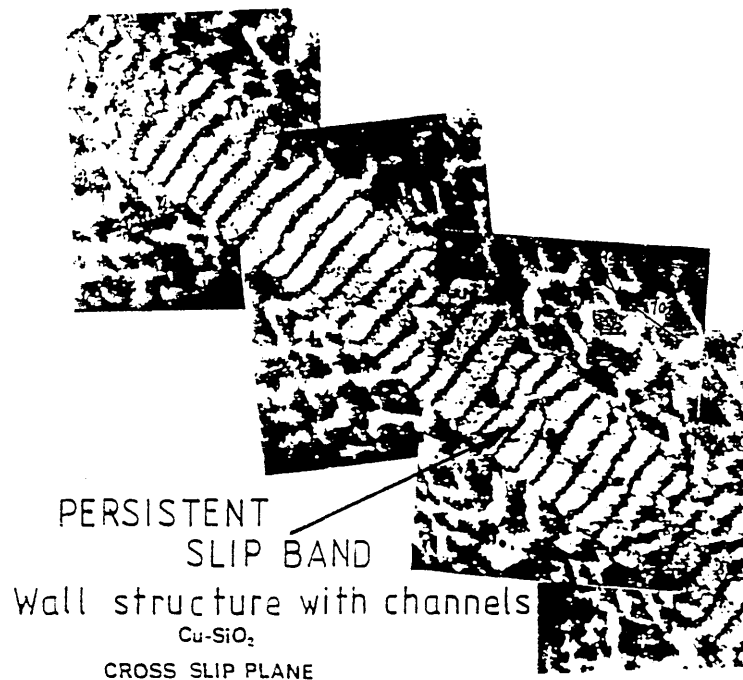


Figure 2.5 Cottrell and Hull's Model for Cyclic Slip from Intersecting Slip Planes [45].

The development of taper sectioning has facilitated high resolution studies of fatigue damaged microstructures and persistent slip bands in the Transmission Electron Microscopy (TEM). Persistent slip bands are known to form in both single crystals and within the soft phases of low strength polycrystalline metals. The observation of a threshold stress or strain required for the formation of PSB's implies the existence of a fatigue limit [48].

PSB's are regions of localised slip or permanent microstructural damage which results in the pile-up of dislocations and leads to the formation of complex dislocation structures. In a similar manner to the formation of Lüders bands at the yield point, the plastic strain becomes localised into PSB's. PSB's emerge at the free surface and generally appear in the form of a protrusion which may comprise several intrusions and extrusions. Due to the high dislocation density gradient between the PSB and the adjacent matrix, on loading, the strain may become highly localised at the PSB and matrix interface [52]. It has been reported [50] that the strain within the PSB may be in the order of ten times greater than the adjacent matrix thus constituting a likely site for fatigue crack nucleation.

In the absence of certain microstructural features such as grain boundaries and second phase particles or precipitates, the dislocations are free to move unimpeded over considerable distances. This results in the formation of complex ladder-like (wall and vein) dislocation structures, as shown in Figure 2.6. In a single crystal, the dislocations will move uninhibited over distances of the order of 10 μm to 100 μm . This compares to less than approximately 1 μm in some polycrystalline materials due to the presence of second phase particles which impede the movement of dislocations. The interactions between dislocations and particles in polycrystalline materials are therefore classed as short range, in comparison to those encountered in single crystals. Previous work has shown that the introduction of a fine dispersion of second phase particles such as SiO_2 , Al_2O_3 and BeO [49] into copper single crystals can prohibit the movement of dislocations through the material, by creating a barrier effect. This is a common mechanism employed for strengthening materials and is known as dispersion strengthening. It was established that on introducing second phase particles the resolved shear stress required to overcome the barrier effect is higher than that for the matrix material itself.



Figures 2.6 A Persistent Slip Band in a Copper Single Crystal [49].

2.3.1.2 Microstructural Aspects of Early Crack Growth

In recent years, research has intensified in an attempt to clarify the fatigue crack nucleation process for single crystal and polycrystalline materials in both qualitative and quantitative terms. The use of surface replication and acoustic microscopy has been key to the understanding of the fatigue crack nucleation process.

It is generally accepted that in polycrystalline metals fatigue cracks nucleate at persistent slip bands. However, the definition of the point at which a crack has initiated is somewhat arbitrary and often varies from one investigator to another. Generally, the crack length corresponding to "nucleation" may vary between a few microns and 1 mm and can depend on the resolution of the technique used to detect it. For example, the use of plastic replicas will facilitate the detection of shorter cracks when compared to those detected using an optical travelling microscope [41].

Mayr et al [51] emphasised the importance of stress amplitude, environmental conditions and test frequency in influencing where crack nucleation occurred. In their study of a plain carbon steel, they discovered that at low stress amplitudes, fatigue cracks initiated preferentially at the interface between persistent slip bands and the matrix. Another worker [52] has indicated that at low nominal stresses, microcracks have initiated at various points or locations within the microstructure of a low alloy steel. Those regions, as indicated by surface replication, were at the sites of persistent slip bands; along grain boundaries; from grain boundary carbides or at an inclusion/matrix interface.

Solberg [53] emphasised that most commercial alloys comprise complex, multi-phase microstructures and inevitably, under reversed cyclic loading conditions it is the weaker or softer microstructural phases which readily accommodates plastic strain. Compared to a single crystal material, a polycrystalline material will comprise many microstructural features such as grain boundaries and second phase particles and precipitates which will interact with dislocations and hence impede their movement.

A polycrystalline, multi-phase microstructure such as that observed in a coarse-grained weld heat affected zone (HAZ); contained the transformation products of bainite, martensite and acicular ferrite. Slip lines were first observed in the weaker

phases of bainite and acicular ferrite, in preference to the stronger, harder martensitic phase. The prior austenite grain boundaries had no influence on the nucleation of fatigue cracks. A number of other researchers [54-56] have observed slip band micro-cracking within grains of ferrite in low carbon steels. Ferrite is known to be the weaker constituent of the ferrite and pearlite microstructure.

Inclusions often play an important role in the air fatigue crack nucleation process in high strength steels. This is discussed in greater detail in Section 2.3.3.2.

2.3.1.3 Fatigue Crack Propagation

In ductile metals, once the fatigue cracks have initiated, they propagate in two distinct stages known as Stage I and Stage II crack growth [57], as shown in schematically in Figure 2.7.

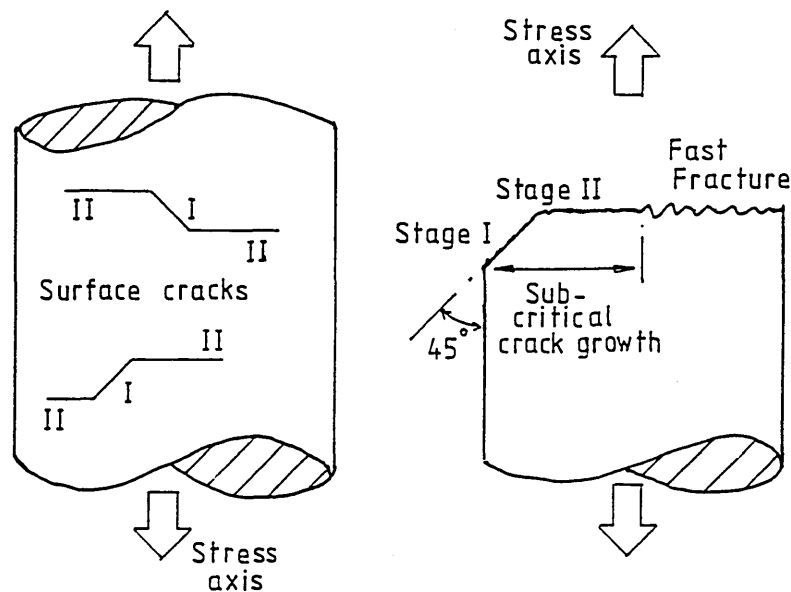


Figure 2.7. Schematic Representation of a Stage I, Stage I to II and Stage II Crack Path.

Stage I crack growth occurs by a shear dominant fracture process. Since the orientation of persistent slip bands of polycrystalline metals is determined by the direction of the maximum shear stress, stage I cracks grow on planes of maximum shear. Under push-pull loading, there are two equi-loaded planes of maximum shear where stage I cracks can grow, as depicted in Figure 2.7. In smooth specimens

subjected to low nominal stresses, Stage I crack growth may account for approximately 90% of the total life, in which the shear crack may only propagate within a few grains [40].

The transition between stage I and stage II crack propagation does not occur instantly, but is a gradual process which may occur over several grains.

Stage II crack growth occurs in a direction normal to the maximum tensile stress and in ductile metals is characterised by fatigue crack striations on the fracture surface. In Stage II, each striation forms after one load cycle due to the opening of the crack tip which allow the crack to advance. The stress intensity factor which characterises the stress field surrounding the crack tip governs the rate at which the Stage II crack advances.

2.3.2 Short Fatigue Crack Behaviour

2.3.2.1 Introduction

The problem of short fatigue cracks has received much attention over the last 20 years or so due to the existence of anomalies in crack growth rates at small defect sizes [128]. Short fatigue crack problems arise because of the break-down in the continuum similitude concept, rendering their behaviour difficult to predict. Predictions of short crack growth rates using Linear Elastic Fracture Mechanics (LEFM) leads to a dangerous overestimation of the fatigue life under the same driving force conditions [129]. In addition to this, short cracks are known to propagate at stress intensities below the long crack threshold. Long and short fatigue crack growth behaviour is schematically illustrated in Figure 2.8.

The study of short cracks has two primary objectives [58]:

1. Firstly, to determine the location at which cracks nucleate and identify any mechanical or microstructural features which may affect their propagation.
2. Secondly, to develop mathematical, physical and analytical models which enable short crack propagation rates to be predicted.

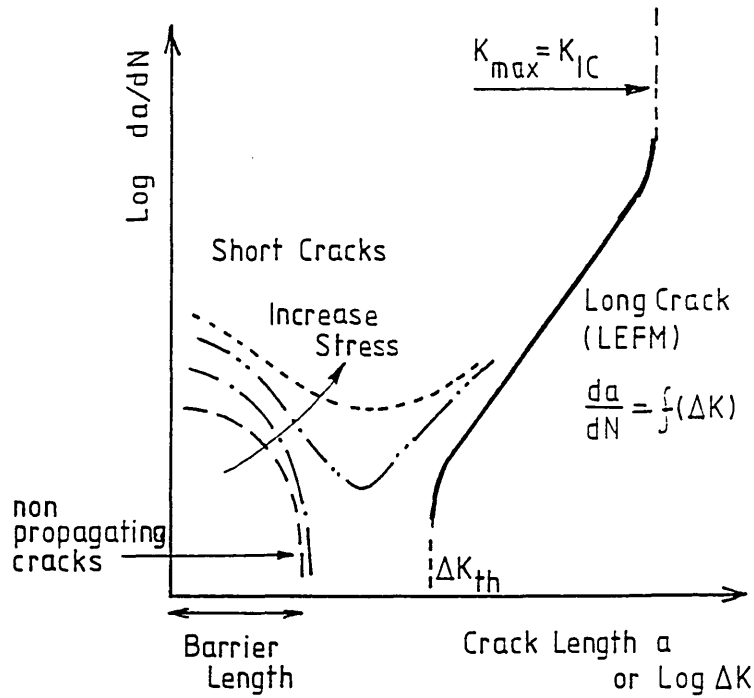


Figure 2.8 Crack Growth Behaviour of Long and Short Fatigue Cracks.

Hobson and Brown [59] have developed an empirical model which predicts the short crack growth rate in a medium carbon steel. The model accounts for fluctuations in the crack growth rate which arise due to the microstructure acting as barriers to propagation.

For a surface crack, until the first barrier is approached:

$$\frac{da}{dN} = k(d - a) \quad (2.12)$$

$\frac{da}{dN}$ represents the fatigue crack growth rate; k is a constant; whilst d is the distance between microstructural barriers (barrier size) and a is the crack length.

once the crack has propagated beyond the first barrier, ie $a > d$

$$\frac{da}{dN} = Ga - D \quad (2.13)$$

where G is the shear modulus and D represents the crack threshold rate.

Navarro-de los Rios [60] have also developed a model for predicting short crack growth behaviour. Their prediction model is based on a theory of continuously distributed dislocations for the crack tip opening displacement for short cracks.

$$\frac{da}{dN} = B(\Phi)^m \quad (2.14)$$

B is a material constant and Φ is plastic displacement at the crack tip. The exponent m represents the fatigue crack growth exponent.

2.3.2.2 Microstructural Barriers

The 'defect' sizes associated with short cracks are comparable with the microstructural features of the material, eg. the grain boundaries, inclusions and second phase particles. Furthermore, the interactions between short cracks and these microstructural features are thought to influence the fatigue crack growth rates. In addition to this, they affect the fatigue lives in the long-life regime [41].

Hicks et al [61] showed that there were significant differences between the growth behaviour of long and short cracks for a number of gas turbine materials. Moreover, it was found that the microstructure played a minimal role in influencing the growth rates of long cracks. In contrast, the microstructure greatly influenced short crack growth behaviour whereby the crack growth rates had a tendency to be dictated more by crystal structure than microstructure. For example, on increasing the grain size of a nickel alloy (fcc - face centred cubic), from 5 to 50 μm , the crack growth rate increased due to a decrease in the number of crack path deflections encountered. In a titanium alloy (cph - closely packed hexagonal), the occurrence of approximately 200 times as many high angle grain boundaries resulted in a decrease in the average growth rate by a factor of five.

An additional limitation of using LEFM when predicting the behaviour of short cracks occurs when the crack length is comparable to the degree of local plasticity at the crack tip. In a precipitation hardened aluminium alloy (7075-T6), Lankford [62] attributed disturbances in the short crack growth rate to localised microplasticity in certain preferentially orientated grains. He found that as the crack propagated, the

grain boundaries limited the degree of microplasticity and hence resulted in transient retardations and sometimes permanent arrest in crack growth. In other words, the grain boundaries acted as microstructural barriers to short crack propagation. Lankford also suggested that short cracks behaved in a similar manner to long cracks once the plastic zone ahead of the crack tip began to exceed the size of the maximum grain dimension.

The influence of the grain size and the barrier effect of grain boundaries on the short fatigue crack growth rate is illustrated in Figure 2.9. For a range of grain sizes, the minimum crack growth rate occurred at a crack length that approximates to the smallest grain diameter, as shown by Lankford. The corresponding crack growth rate minima has been found to be the 'deepest', due to difficulties in crack re-nucleation within the adjacent grain, i.e. due to microplasticity effects in traversing the adjacent grain boundary. The greater the mis-orientation between adjacent grains the greater the retardation in the growth rate.

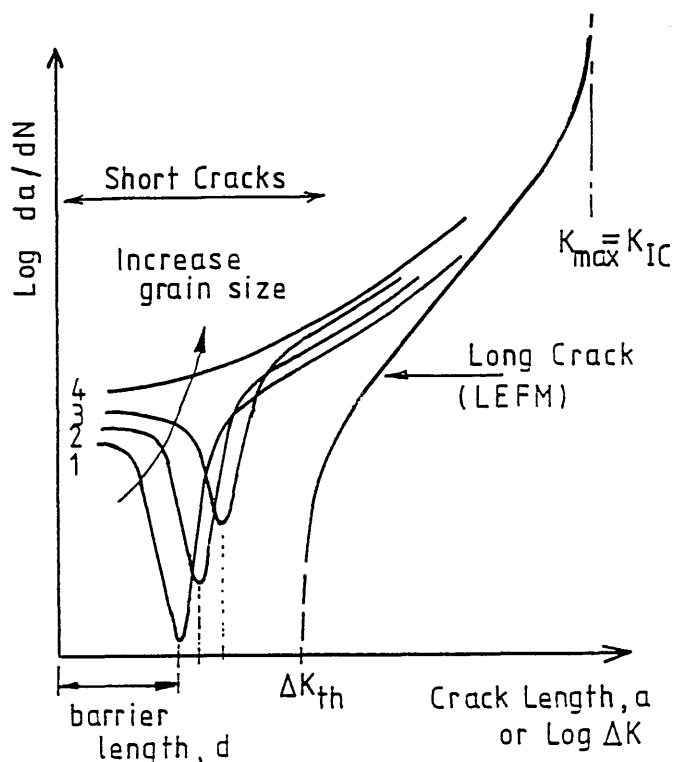


Figure 2.9 The Effect of Grain Size on the Short Crack Growth Rate.

A more recent investigation [31] suggested that the presence of 40% volume percentage reverted austenite within the microstructure of a high strength steel (material specification 03Kh11.N8M2F) provided a degree of resistance to the long crack growth behaviour. This emphasises the influence of microstructural barriers on both the short and long crack propagation regimes. However, the authors failed to investigate the possible barrier effects imposed by the reverted austenite on the short crack behaviour; which would be more pertinent for this material when subjected to high stresses.

Due to the fine nature of the microstructure features which comprise FV520B, it is anticipated that the critical barrier size would be approximately 1 μ m to 14 μ m. These coincide with the dimensions of the martensite laths and prior austenite grain boundaries respectively. It is recognised that these critical barrier sizes for this high strength material are significantly smaller than in those materials that have previously been studied. It has been suggested by a previous worker [58] that the short cracks in an ultra-high strength and carbon steels may be a few and a few hundred microns in length respectively. It follows that, the study of short fatigue crack growth rates in high strength compared to lower strength steels is inherently difficult due to the magnitude of the short crack sizes involved.

2.3.2.3 Environmental Effects

Physically small cracks are generally longer than the microstructural features and under inert conditions are amenable to being characterised using Linear Elastic Fracture Mechanics (LEFM). Under corrosive environmental conditions, however, their growth rates are accelerated considerably and predictions using LEFM are no longer valid, as shown in Figure 2.10. These cracks are then commonly known as chemically short cracks. According to Suresh [63], the environmental effects are dominant for chemically short cracks and this is due to a strong influence of the corrosion fatigue phenomena on crack dimensions. Another worker [64] has demonstrated that the growth rate for chemically short cracks in a corrosive chloride environment was significantly greater than that in an air environment. In the absence of any environmental effect, the growth rates would have been comparable to those of long cracks and predictions using LEFM would in this instance have been valid.

The Hobson-Brown and Navarro-de los Rios models were modified to incorporate a constant anodic dissolution term to account for the effects of the corrosion process on short crack growth [36]. This was found to disturb the crack growth retardation at a microstructural barrier and therefore the effects of the environment were found to be more significant as the microstructural barrier was approached.

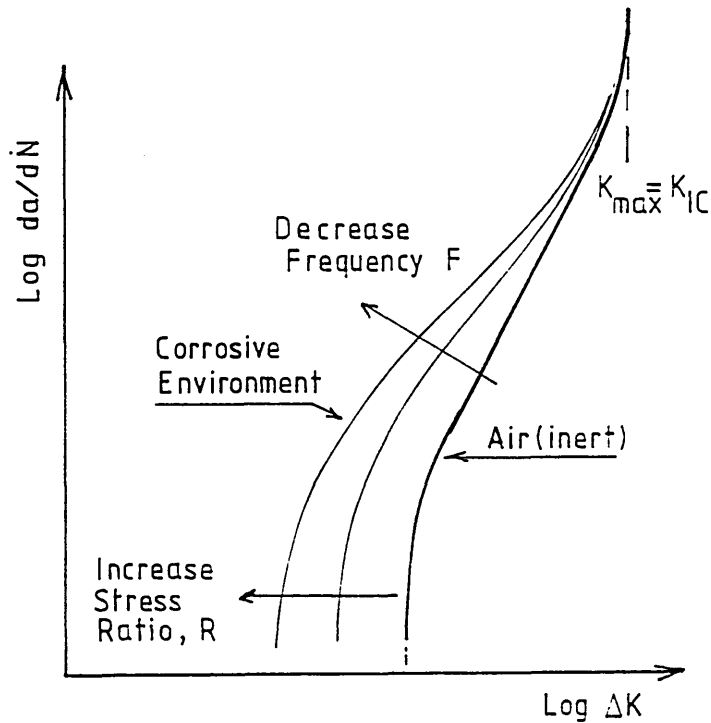


Figure 2.10. A Schematic Representation of the Effect of Environment and Loading on the Corrosion Fatigue Crack Growth Behaviour.

2.3.3 Non-Metallic Inclusions

2.3.3.1 Introduction

Non-metallic inclusions (hereafter referred to as inclusions) are an inherent feature of steel and their presence is unavoidable. They can be categorised according to their origin and therefore can either be exogenous or indigenous. Exogenous inclusions are usually oxides and as their name suggests they arise from a source external to the steelmaking process, i.e. the refractory lining. In general, exogenous inclusions tend to be large and sporadic in nature. Indigenous inclusions, however are

produced as a direct result of the steelmaking process. It is commonly known that inclusions are either oxide or sulphide type particles.

Inclusions can have a profound affect on the mechanical properties of certain grades of steel which sometimes can be beneficial. For example, deliberate additions of sulphur to a high sulphur free cutting such as BS970 Grade 220M07, will aid machinability. These steels are therefore are referred to as “free machining” or “free-cutting” steels. Often, however the presence of inclusions are detrimental to the mechanical properties, especially the fatigue strength of high strength steels.

There has been a significant reduction in the number of inclusions in steels over the last 35 years, as indicated in Table 2.5. This follows industry’s need or demand for “cleaner” steels, especially in safety critical applications such as the nuclear or aerospace industries. This has been achieved through advances in steelmaking technology and the implementation of certain steel refining techniques, such as vacuum induction melting (VIM) and vacuum arc remelting (VAR). The use of such refining techniques has resulted in a tighter control over levels of oxygen, sulphur and phosphorous in the melt. The effect of reduced oxygen and sulphur contents in the steel melt has led to significant improvements in certain mechanical properties.

Table 2.5 The Relative Reduction in Oxygen and Sulphur Levels in Steels Over a 20 Year Period [65].

Year	circa 1965	circa 1985
Oxygen Level (ppm)	20-50	5-50
Sulphur Level (ppm)	100-200	5-50

There are two qualities of steel available to industry, namely airmelt and remelt grades. Due to the method employed to refine the steel melt, remelt grade possesses a lower inclusion content and hence has superior mechanical properties compared to airmelt grade. The inclusion population in remelt grades are known to be fine in size and to be present in a highly distributed and fragmented form. Remelt grades of steel are often employed in safety critical applications such as the

aerospace and nuclear industries where excellent mechanical properties are essential.

2.3.3.2 Inclusions and Fatigue Crack Nucleation in Air

Inclusions play a major role in the fatigue crack nucleation process in air. Whether an inclusion will initiate a fatigue crack is highly statistical in nature and dependent on several interrelated factors. These are:

- (a) The chemical composition of the inclusion and whether it is an oxide or sulphide type inclusion.
- (b) The size and shape of the inclusion which is known to be dependent on the steelmaking or steel refining route.
- (c) The location of the inclusion with respect to the free surface, ie whether it is positioned at the surface, sub-surface or within the bulk material.
- (d) The orientation of the inclusion relative to the direction of loading.
- (e) The degree of coherency between the inclusion and the steel matrix. This is dependent on the deformability of the inclusion during thermomechanical processing and is affected by the chemical composition of the inclusion. These by which the inclusion deforms during processing is usually expressed in terms of a deformability index [80].
- (f) The loading conditions.
- (g) The tensile strength of the steel.

It is generally accepted that high strength steels have a low fracture toughness. In addition to this, the presence of defects will further impair the fatigue strength of high strength steels when utilised at high stresses, simply due to their intolerance to small surface imperfections. The presence of oxide type inclusions, especially alumina are particularly detrimental to the fatigue strength of steels and this has been highlighted

by a number of workers [67] [68]. In contrast, inclusions within low and medium strength steels have little influence on their fatigue behaviour because of their greater inherent ductility or improved fracture toughness [66].

Oxide inclusions generally have an angular morphology and under cyclic loading tend to generate stress concentrations, ie tensile stresses of the order of approximately 1.5-1.7 times the applied stress. The effect of stress concentrations and the incompatibility of strain between the steel matrix and inclusions results in the enhancement of slip at the matrix/inclusion interface. This is precursor to fatigue crack nucleation. In contrast, manganese sulphide inclusions are less susceptible to debonding due to both their greater coherency and strain compatibility with the steel matrix. Manganese sulphide inclusions seldom nucleate cracks during fatigue loading in air [69]. Unlike in an aqueous environment. The role of manganese sulphide inclusions in an aqueous environment is discussed further in Section 2.5.5.1.

Another physical model has been proposed for fatigue crack nucleation at inclusions in a high strength steel [68]. The model, as illustrated in Figure 2.11, highlights the gradual debonding process of the inclusion from the steel matrix. This mechanism eventually leads to a stress concentration which results in the formation of point surface defects or microvoids within the matrix a few micrometres from the inclusion. Under continued cyclic loading, these microvoids coalesce to form fatigue cracks. The role of slip in this mode of crack nucleation is not clearly understood.

The influence of the applied stress and hence the role of slip in the fatigue crack nucleation process adjacent to spheroidal alumina inclusions has been clearly established for the high strength En16 steel [67]. At a stress level immediately above the fatigue limit, ie in the high cycle regime, the localised stresses at the inclusion and steel matrix interface were insufficient for slip to occur and hence fatigue cracks to nucleate. In this instance, the inclusions remained undamaged and firmly bonded to the steel matrix. However, on increasing the nominal stress, slip readily occurred which ultimately led to the debonding of the inclusion and the nucleation of a fatigue crack.

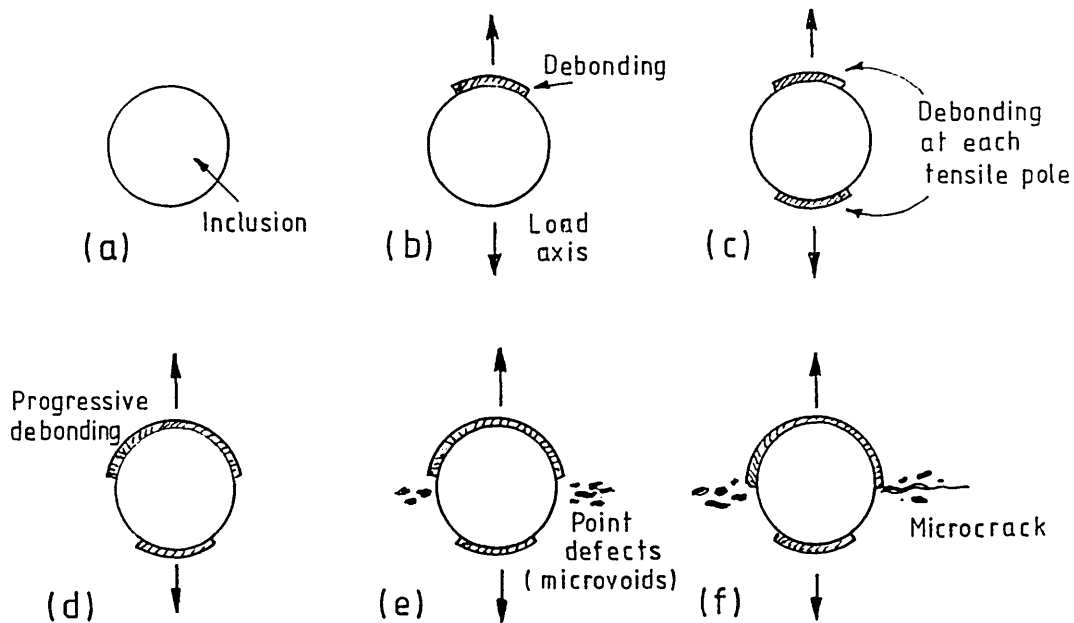


Figure 2.11 Model Depicting the Debonding and Fatigue Crack Nucleation at an Inclusion.

2.3.3.3 Prediction of the Fatigue Limit

It is understood that inclusions below a certain size do not effect the fatigue life of high strength steels [70]. This has led to several workers defining a critical inclusion size below which fatigue crack nucleation will not occur. However, in some of these investigations [69] [71] [72], the cracks initiating at inclusions have become non-propagating and as a result failure did not occur.

For a ball bearing steel, it has been shown that only oxide inclusions greater than $30\mu\text{m}$ affected the fatigue life. This compares with surface inclusions of $10\mu\text{m}$ in size initiating fatigue cracks in a high strength En24 steel [70]. For sub-surface inclusions, a larger critical size was observed, ie at a distance of $100\mu\text{m}$ from the free surface the critical size increased to $30\mu\text{m}$. This point highlights the importance of inclusion location relative to the free surface and has previously been discussed in Section 2.3.3.2. The inclusions responsible for initiating fatigue cracks in FV520B are significantly smaller than those observed in the En24 type steel.

A number of empirical relationships have been developed to predict the effects of defects such as inclusions and crack or notch-like defects on the fatigue strength of high strength steels.

One of the earliest empirical relationships defining the fatigue limit using a critical defect length was developed by Frost [74], equation (2.15). He studied the effects of two-dimensional surface defects in low to medium strength steels. The effects of inherent inclusions or defects were not exclusively studied; but rather simulated notches as structural discontinuities were used for this investigation. The empirical formula is based on considerably large notches. However, it is thought that this equation can be applied to defects such as inclusions or crack-like defects within the given size range of 100 μm to 20.9 mm:

$$\sigma_w^3 l = k \quad (2.15)$$

where σ_w represents the fatigue limit; l is the defect length and k is a materials constant.

The above model has been used to predict the effect of inclusions on the fatigue limit of a 13%Cr martensitic stainless steel turbine blade material [73]. The diameter of the inclusions initiating fatigue cracks in highly polished specimens of this material under air and steam environments, ranged from 10 to 30 μm [73]. The experimental data indicated that the fatigue limit was in good agreement with those predictions using Frost's model. This suggests that this model can be applied to prediction the effect of smaller inclusion on the fatigue limit.

Another model, as in equation (2.16), was proposed to account for small defects sizes [75], ie:

$$\sigma_w^4 l = k \quad (2.16)$$

where σ_w represents the fatigue limit; l is the defect length and k is a materials constant. The length (l) of the defects considered ranged between 30 μm to 1100 μm .

A disadvantage of equations (2.15) and (2.16) is that they are empirical and require the generation of fatigue data to evaluate the material constants, k. Additionally, the validity of these equations for an inclusion population less than 10µm in size has not been investigated. This places a limitation on their use especially since modern day steels comprise oxide-type inclusions which are generally smaller than 10µm in size.

Murakami et al [76] has investigated S45C and SAE 9254 steels. He has suggested that the behaviour of inclusions can be considered to be similar to that of small cracks if their respective projected areas are identical. He has proposed that the threshold stress intensity factor (ΔK_{th}) for an inclusion is dependent on its size, ie $\sqrt{\text{area}}$, as in equation (2.17).

$$\Delta K_{th} = 3.3 \times 10^{-3} (H_v + 120) (\sqrt{\text{area}})^{\frac{1}{3}} \quad (2.17)$$

where H_v represents the Vickers hardness of the material and $\sqrt{\text{area}}$ is the projected area of the inclusion. These symbols have the same definition for equations (2.18) and (2.19).

It should be noted that the threshold conditions given in equation (2.17) is not related to crack nucleation but rather to the non-propagation of a crack emanating from a defect or inclusion.

For surface inclusions, the fatigue limit (σ_w) was expressed by equation (2.18).

$$\sigma_w = \frac{143H_v + 120}{(\sqrt{\text{area}})^{\frac{1}{6}}} \quad (2.18)$$

For sub-surface three dimensional defects, Murakami et al [76] proposed equation (2.19):

$$\sigma_w = \frac{156H_v + 120}{(\sqrt{\text{area}})^{\frac{1}{6}}} \quad (2.19)$$

The expressions given in (2.18) and (2.19) are similar to equation (2.15), with the exception that Murakami's equation requires the projected area of the inclusion rather than the maximum defect length.

2.4 Pitting Corrosion

Pitting corrosion is a highly localised form of corrosive attack which occurs in both ferrous based and non-ferrous materials. It is a potentially hazardous form of corrosion since perforations can occur in thin sectioned components with only a relatively small amount of metal loss. The engineer may also be unaware of the extent of pitting since the metal loss may not be evident on the component surface. Additionally, for high strength steels such as 17-4PH which is known to have low fracture toughness, pits have acted as regions stress concentration. Under the application of a high impact load, fracture has been shown to occur with the possible assistance of hydrogen embrittlement [77].

Pitting occurs at sites which are relatively small compared to the overall exposed metal surface. These sites are usually particular to certain microstructural features which are anodic to the steel matrix. Examples of microstructural heterogeneities which are likely sites for pitting include slight compositional differences, i.e. a banded microstructure; inclusions [135]; grain boundaries and second phase particles such as carbide precipitates. Therefore, it is the composition and microstructure of a metal which affects or determines the corrosion behaviour and therefore the factors which affect the physical metallurgy must be considered [78]. It is acknowledged that differences in anion and oxygen concentrations may also influence the initiation of corrosion pits.

Stainless steel may be protected from pitting corrosion in an aqueous solution by its passive surface film which forms as the chromium content reaches 11% and above. Molybdenum additions will improve the pitting resistance whilst the addition of copper is thought to improve a stainless steel's general corrosion resistance. However, in an aqueous environment containing chloride ions, FV520B, in addition to other 12-14%Cr martensitic stainless steels, are known to suffer pitting corrosion. The two

mechanisms which are thought to cause pitting in a stainless steel exposed to chlorides are [79]:

- (a) The preferential dissolution of manganese sulphide inclusions in the presence of an aqueous solution [80] [65].
- (b) The disruption of the passive layer due to localised chemical deficiencies or internal stresses. This may occur at, for example, inclusions which may lead to the penetration of aggressive fluids around the inclusions and resulting in their preferential dissolution.

Resistance to pitting corrosion is therefore highly dependent on the stability of the protective oxide surface layer and the absence of surface manganese sulphide inclusions.

Pitting corrosion is a purely electrochemical process which results in the formation of a corrosion product from metal-environmental interactions. Corrosion is the result of one anodic (oxidation) and generally more than one cathodic (reduction) reactions which occur simultaneously [81]. The process of corrosion pit formation is illustrated schematically in Figure 2.12.

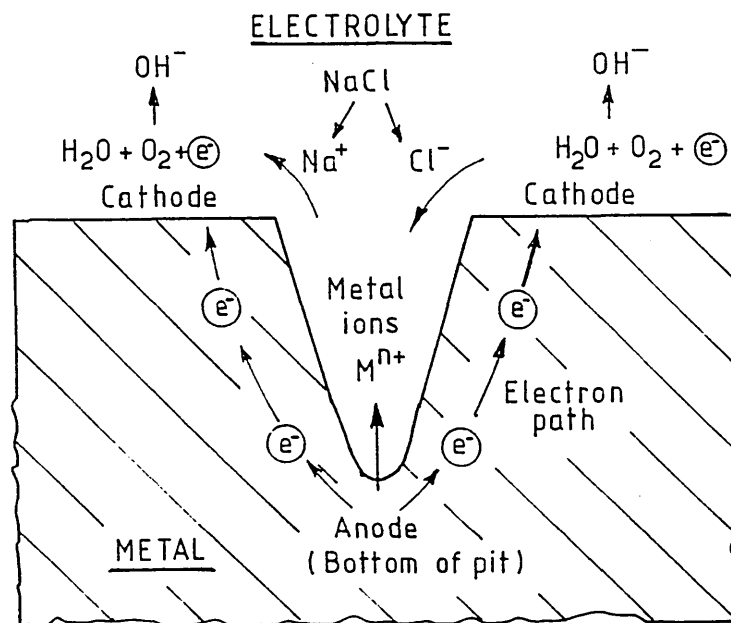


Figure 2.12. Schematic Representation of Corrosion Pit Formation [82].

In an aqueous environment, the metal species is dissolved according to the anodic reaction:



where M is the metal species; e^{-} and n represent the electrons and the valency of the ion respectively. For FV520B, the predominant metal species (M) is likely to be either iron (Fe) or chromium (Cr).

The electrons generated from the dissolution of metal (in equation (2.20)) are consumed during the complementary cathodic reaction, namely, during the reduction of the hydrogen ions (H^{+}). This particular cathodic reaction results in the evolution of hydrogen gas (H_2).

i.e.



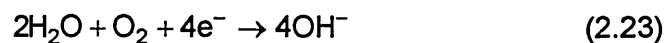
This reaction proceeds rapidly in acidic, aqueous environments, due to the presence of sodium ions which increases the conductivity of the electrolyte [78]. The sodium ions are generated from the dissociation of salt (NaCl).

i.e.



It is thought that this corrosion process would occur during the present corrosion fatigue studies of FV520B, owing to the low pH of the chloride environment used.

The remaining cathodic reaction occurs on the sample surface adjacent to the corrosion pit and involves the hydrolysis of water. This chemical reaction is largely driven by the presence of dissolved oxygen (O) within the electrolyte and is represented by the following chemical reaction:



The cathodic reactions presented in equations (2.21) and (2.23) will result in an excess of hydroxyl ions, ie (OH^{-}), which are free to migrate towards the anode, i.e. the

base of the pit. Similarly, the metal ions which are the by-product of the anodic reaction, will also migrate towards the cathode. As a result of this, the negatively and positively charged ions will be neutralised resulting in the deposition of the corrosion product.

The resultant chemical reaction thus becomes:



It is believed that the corrosion product in FV520B is likely to be Fe-Cr spinel or $Fe(OH)_2$ depending on the local Fe-Cr content.

As the reactions proceed, the metal surrounding the active pit is cathodically protected and so metal loss in these regions is minimal. If the ratio of the area of the anode to cathode is small then the corrosion rate will be accelerated.

Sulphide anions (S^-) which may also be present in the condensate in the LP turbine would also cause pitting corrosion in a similar manner to chloride anions (Cl^-).

In an aerated condensate environment, the depth of active pits in a 2NiCrMoV low alloy steel not subjected to a load has been shown to follow a parabolic growth law [83], as given by equation (2.25). This relationship indicates that pit growth is a time dependent process which is also governed by the environmental conditions.

$$d = At^n \quad (2.25)$$

where d and t represent pit depth and exposure time respectively. A is a constant which is dependent on the temperature and oxygen content of the condensate; n is the pit growth law exponent which has a value of approximately 0.3 to 0.7. It has been shown that the value of A and n is independent of the composition of the steel and the applied stress.

Equation (2.25) also reflects the pitting behaviour of a carbon steel [134] and an aluminium alloy [124]. However, the pit depth for aluminium alloy grade AlMn1,2 in an urban-marine atmosphere did not follow the relationship presented in equation (2.25).

For this particular case, the maximum pit depth was found to be of the order of 100 μm after an exposure of approximately 10 years. Increasing the exposure time beyond 10 years did not result in an increase in the pit depth. A schematic diagram representing the pitting behaviour of carbon steel [134] and an aluminium alloy [124] is presented in Figure 2.13.

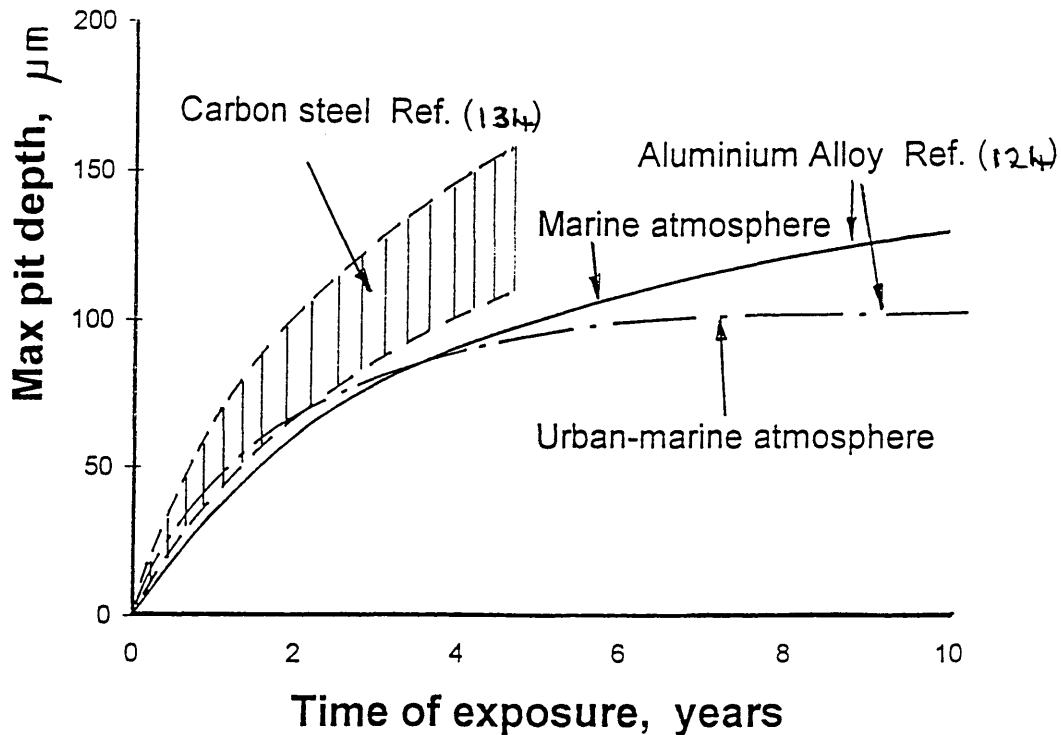


Figure 2.13. Schematic Diagram for the Pitting Behaviour of a Carbon Steel [134] and an Aluminium Alloy [124].

2.5 Corrosion Fatigue

2.5.1 Introduction

Corrosion fatigue occurs under the combined or synergistic action of cyclic stresses and a corrosive environment. The corrosive environment can either be aqueous or gaseous. However, this section will focus on the degradation of stainless steels under aqueous chloride environments which is of great commercial interest.

Corrosion fatigue failures can occur under a wide range of aqueous environments and specific anions are not required, unlike the case for stress corrosion cracking.

Corrosion fatigue causes a significant reduction in the fatigue strength, often with the disappearance of the fatigue limit. Figure 2.14 highlights this effect in a BS 251A58 low alloy steel after fatigue loading in a corrosive 0.6M NaCl (pH6) aqueous environment [88]. The results are presented as a stress amplitude-life curve (S-N curve). The severe effect of the environment on the fatigue strength is evident.

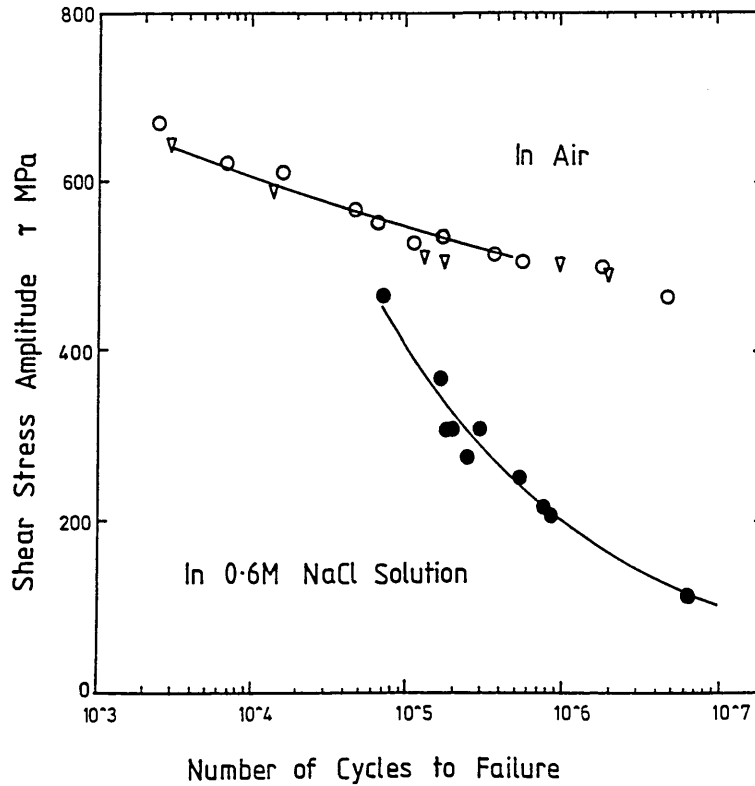


Figure 2.14 Endurance Data for BS 251 Grade A58 Steel in Air and Chloride Environments [88].

In general, the reduction in strength can be attributed to a fatigue crack initiating from the bottom of a corrosion pit. Pitting corrosion has been found to be a very prevalent mechanism for fatigue crack nucleation in most commercial alloys and it is this mechanism which is of primary concern in this study.

The reduction in fatigue strength is considerably greater than the effect of either fatigue loading or pitting corrosion acting independently [84]. It follows that, improving

the material's resistance to pitting corrosion will have a more beneficial affect against corrosion fatigue than by increasing the material's tensile strength alone [40]. Indeed, suppressing pit growth by controlling the aqueous environmental conditions and the oxygen content, will have a beneficial effect towards resistance to crack nucleation [85]. It has been suggested that the fatigue process enhances the corrosion rate and the corrosion processes enhance the fatigue crack growth rate [86] [87].

Corrosion fatigue strength is strongly dependent on the test frequency. The corrosion fatigue strength at a specific number of cycles will generally decrease as the frequency is decreased; as the time for material-environment interactions per stress cycle increases. This effect is most apparent at frequencies below 10 Hz. Increasing the cyclic frequency will reduce any environmental involvement, leaving the effects of mechanical damage to dominate the fracture process. In addition to this, at a constant test frequency, the effects of corrosion will dominate at low stresses as the time for corrosion increases. Similarly, the effects of mechanical damage will dominate at higher stresses.

Test frequencies of 20 kHz were employed to determine the high cycle corrosion fatigue strength of three LP turbine blades in a range of test environments [3]. The impetus for this particular study was to generate large amounts of fatigue strength data in a short testing period; thus facilitating the screening of a large number of potential turbine blade materials. The results indicated that the corrosion fatigue strengths from the high frequency tests were consistent with those conducted at considerably lower frequencies. This suggested that the ultrasonic frequency testing was a viable screening method. However, it must be noted that little information was imparted concerning the extent of the pitting corrosion. The absence of pitting due to the short exposure time to the environment may be the reason for the apparent 'high' corrosion fatigue strengths.

2.5.2 Earlier Work on Corrosion Fatigue

The earlier works were primarily concerned with the qualitative effects of corrosion and fatigue damage. Haigh [89] was first to publish an account of corrosion fatigue in 1917 during his study of fatigue in brasses. McAdam [90] followed with a more systematic approach to testing. He has been credited with inventing the term

corrosion-fatigue on realising the effects of the corrosion process on the fatigue properties of a range of metals and alloys. He also discovered the inter-relationship between the factors of stress, time and number of cycles on material damage. A series of comparative tests in air and a partial vacuum confirmed the corrosive effect of atmospheric air, that is air and water vapour, in reducing the fatigue life of copper [91].

More recent studies have been concerned with predicting lifetimes under the action of cyclic stresses and a corrosive environment. In a review of corrosion fatigue mechanisms, the necessity to develop quantitative models based on corrosion-deformation interactions and to move the emphasis away from empirically based lifetime prediction models has been highlighted [92].

2.5.3 Corrosion Fatigue Crack Nucleation Models

The models for the nucleation of fatigue cracks in a corrosive environment according to Suresh [63] are:

1. crack initiation at the roots of corrosion pits due to a stress concentration.
2. enhanced slip irreversibility due to the oxidation of the slip steps.
3. preferential attack at regions of localised plastic deformation e.g. persistent slip bands.
4. preferential chemical attack at the surface of a fatigued metal (slip steps or the crack tip) where the protective oxide film is ruptured.

2.5.4 Corrosion Fatigue Crack Initiation at Corrosion Pits

Quantitative analyses to evaluate the critical pit condition, using the concept of fracture mechanics, has led to fatigue life prediction equations. In a study of 12% chromium stainless steels, the critical pit condition was calculated by treating the pit as a short surface crack [93]. The pseudo-stress intensity factor for a critical pit was

then evaluated. The effects of mean stress, chloride concentration and corrosion current on the critical pit condition were also studied, for pitting acting as a precursor to fatigue crack nucleation.

2.5.5 Factors Affecting Corrosion Fatigue

2.5.5.1 Metallurgical Factors

Section 2.4 highlighted the significance of the surface with reference to a steel and its corrosion resistance. The importance of film repassivation kinetics at the surface during both stress corrosion cracking and corrosion fatigue failure mechanisms has been highlighted in stainless steels [94]. It has been suggested that in anodic dissolution controlled fracture processes, the renewal of the film and film stability are of extreme importance. The reasoning behind this is that the corrosion fatigue process can be enhanced either by anodic dissolution or hydrogen absorption during the time in which the film is broken [94]. The reduction in fatigue strength for a martensitic, a duplex and a tempered martensitic stainless steel was considered to be the result of the instability of the passive film in a chloride environment [95].

Carbides may also assist failure, especially if present in the highly stressed region ahead of the crack tip. Other microstructural features which affect corrosion fatigue crack growth rates are grain boundaries and interphase boundaries. Persistent slip bands and intense slip bands are very prone to preferential dissolution in the condition of generalised corrosion even if their internal dislocation microstructure is not affected.

As previously stated, the dissolution of sulphide type inclusions, namely manganese sulphide in aqueous environments has been known to initiate pits in low alloy and various grades of 12% chromium stainless steel [93] [20] [3] [65] [135]. Additionally, the sulphur content of pressure vessel steels has significantly affected the dissolution of sulphides enhancing pitting initiation and crack growth rates [86]. In contrast, oxide type inclusions seldom affect the corrosion fatigue strength, although rigid oxide inclusions have affected the strength of a tempered martensitic 13%Cr; a ferritic austenitic 22%Cr-5%Ni duplex and a soft martensitic 16%Cr-5%Ni stainless steel in a chloride environment [95].

It was shown that the corrosion fatigue strength of carbon and alloy steels in seawater is approximately independent of the tensile strength or the fatigue limit in air [18]. A similar trend has been reproduced in 13% Cr and precipitation hardenable type stainless steels. However, a slight dependency on the microstructure, namely the grain boundaries, was found to exist when comparing two plain carbon steels of differing grain sizes [118]. A criticism of this work is that it does not seem appropriate to make such comparisons using two differing steels whose compositional differences may affect the corrosion fatigue strength.

2.5.5.2 Environmental Factors

The oxygen concentration, pH and ion concentration of the aqueous solution can have a marked effect on the corrosion fatigue strength of a material [5]. Differential aeration i.e. a concentration gradient of oxygen will provide the driving force for the electrochemical reactions [86]. This can lead to an acceleration of the corrosion process and a reduction in the corrosion fatigue life.

Corrosion is a thermally activated process and therefore the mechanisms are influenced by temperature. An increase in temperature from 50°C to 150°C, in the presence of high oxygen resulted in a reduction in the corrosion fatigue strength of a structural steel BS1501-224 Grade 32B [86].

2.5.6 Further Comments

Corrosion fatigue cracks are usually transgranular, although intergranular cracking can occur in metals whose grain boundaries are attacked preferentially by the environment. The nucleation and the early stages of growth of corrosion fatigue cracks in a 12%Cr stainless steel occurred transgranularly when exposed to an air and a steam environment [115]. In the steam environment, these cracks were found to propagate intergranularly, on increasing the stress intensity to a limiting value. Further increases in the stress intensity lead to sporadic intergranular cracking. In this instance, the fracture mode was found to be dependent on the environment, namely the humidity level.

2.5.7 Anodic Dissolution and Hydrogen Embrittlement

For metal-aqueous environment systems subjected to cyclic loads, embrittlement can involve electrochemical reactions at freshly formed slip steps around the crack tip. This process can be described by two principal mechanisms of environmental damage, namely anodic dissolution and hydrogen embrittlement. Anodic dissolution is depicted in Figure 2.15.

With reference to Figure 2.15, the steps in which fracture by anodic dissolution occurs are:

- (a) The rupture of the protective oxide film at a slip step.
- (b) Metal dissolution of the exposed metal (slip step) surface.
- (c) The nucleation and re-growth of oxide on the bared surface i.e. passivation.
- (d) Further metal dissolution at the exposed metal (slip step) surface.

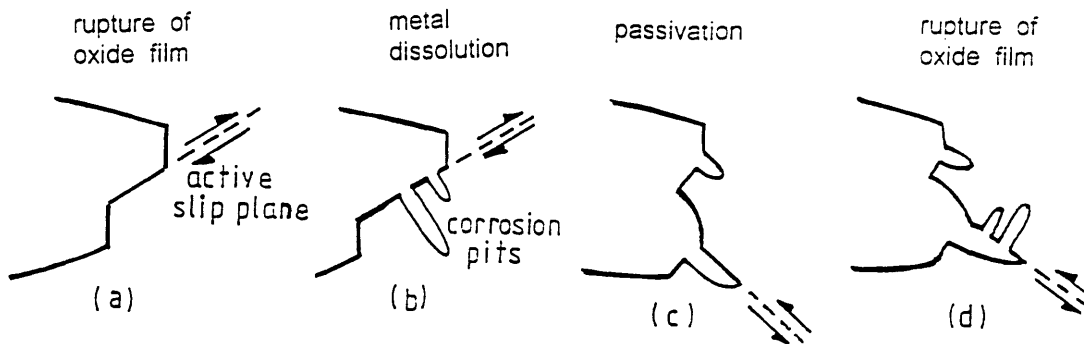


Figure 2.15. Anodic Dissolution in an Aqueous Environment.

2.6 Stress Corrosion Cracking in Martensitic Stainless Steels

Under the influence of a sustained tensile stress, martensitic stainless steels are susceptible to failure by stress corrosion cracking. Even in mildly corrosive environments, the supposedly corrosion resistant precipitation hardening grades such as FV520B and Custom 450 are sensitive to stress corrosion cracking. The material's tendency towards stress corrosion cracking are not only affected by environmental conditions, but also the elemental composition and the microstructure.

Additional fracture processes which may operate concurrently to stress corrosion cracking are active path corrosion and hydrogen embrittlement. These are illustrated in Figures 2.16a and 2.16b.

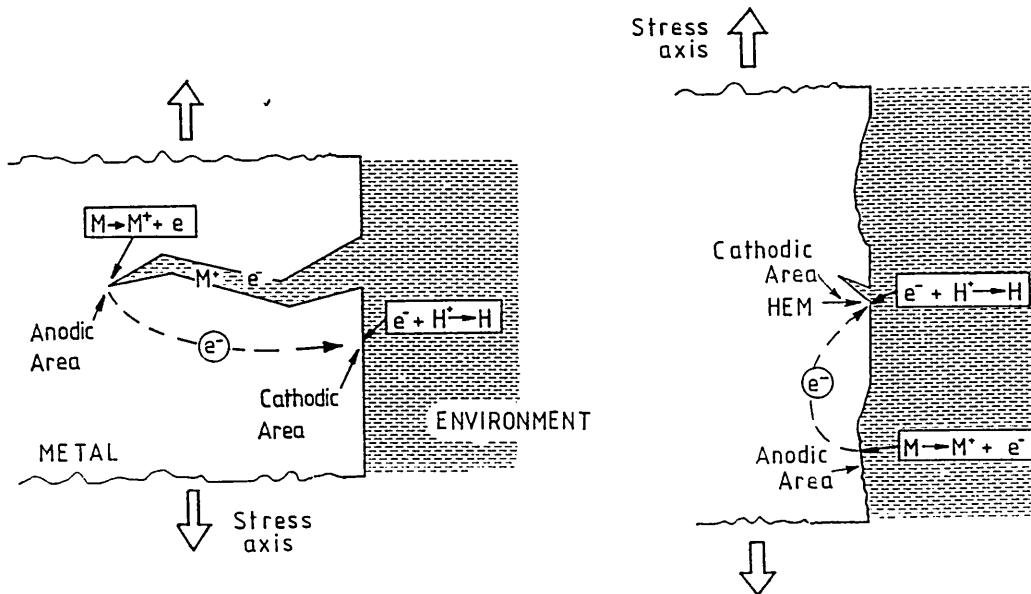


Figure 2.16 Schematic Representation of (a) Active Path Corrosion and (b) Hydrogen Embrittlement Cracking [96].

It is believed that stress corrosion cracking in high strength steels is assisted by the presence of hydrogen. Hydrogen is a by-product of the cathodic reaction and is evolved during the corrosion process see equation 2.21. To resist hydrogen induced cracking, a steel must have good corrosion resistance and toughness properties to tolerate the small amounts of hydrogen that may diffuse into the metal and lead to absorption at the crack tip. In addition to this, the critical value of the strain rate ($\dot{\epsilon}_{crit}$)

must also be exceeded. These are the governing factors which determine whether stress corrosion cracking will occur. Further evidence [97] suggests that the temper condition of a turbine blading material, grade En56C at high temperatures such as 650°C reduced the likelihood of stress corrosion cracking. This was in agreement with the findings on testing Custom 450 which has a similar material specification. The resistance of Custom 450 to stress corrosion cracking improved on increasing the ageing temperature to 510°C and above [13]. This was attributed to what was thought to be an increase in material toughness since the general corrosion and pitting corrosion characteristics did not undergo any significant changes.

It has also been suggested that stress corrosion cracking may also involve active path corrosion [98] in a chloride environment. Active path corrosion occurs rapidly along a very narrow crack front along zones depleted in chromium content which leads to fissures at the surface. For active path corrosion to be a viable mechanism, it must be demonstrated that under the application of a stress or strain ($\dot{\epsilon}$) the rate of corrosion will be accelerated. A particular surface feature has been identified as being a characteristic feature of active path corrosion, otherwise known as atolls. Atolls are annular stains which represent corrosion cells localised to specific types of carbides within the microstructure [99]. Therefore, it follows that the occurrence of stress corrosion cracking with active path corrosion is dependent on the type of carbide present in the microstructure and hence the tempering temperature employed.

It has also been proposed by one worker [12] that a material's propensity towards hydrogen embrittlement is dependent on its temper condition. Whilst certain temper conditions are associated with hydrogen embrittlement, i.e. a 450°C temper; other temper conditions i.e. a 620°C temper, may give rise to the chromium depletion phenomena in the region of the prior austenite grain boundaries. This would lead to active path stress corrosion cracking as previously described in this section.

CHAPTER 3

EXPERIMENTAL PROCEDURE

3.1 Introduction

The Experimental Procedure gives a detailed account of the experimental techniques employed during the course of this research programme.

3.2 Materials Characterisation

The grade of FV520B used during this study was manufactured by vacuum induction melting and refined by vacuum arc remelting. The material was supplied as rolled bar-stock of diameter 120 mm. The bars were reduced by hot forging to plate with dimensions of approximately 5 m x 100 mm x 40 mm.

3.2.1 Heat Treatment

Material blanks (with dimensions 20 mm x 20 mm x 130 mm) were sectioned from the longitudinal direction of the plate in preparation for heat treating in a Carbolite™ CFS 1200 furnace. Prior to heat treating, each blank was coated in a proprietary refractory known as Berkatekt™. Berkatekt™ reduced the likelihood of oxidation and decarburisation during the homogenisation treatment.

A K-type thermocouple was attached to the sample to monitor the temperature during heat treatment. The correct temperature was then maintained by adjusting the temperature controlling unit on the furnace. FV520B was heat treated according to the schedules presented in Table 3.1.

Table 3.1 The Three Stage Heat Treatment Schedules for FV520B.

Heat Treated Condition	Homogenisation	Solution Treatment	Precipitation Hardening Treatment
Peak Hardened	1 hour @ 1050°C air cooled	2 hours @ 850°C air cooled	4 hours @ 450°C air cooled
Standard Overaged	1 hour @ 1050°C air cooled	2 hours @ 750°C air cooled	2 hours @ 550°C air cooled
Softened Overaged	1 hour @ 1050°C air cooled	2 hours @ 750°C air cooled	2 hours @ 620°C air cooled

These schedules, in addition to the resulting mechanical properties are available in the manufacturers technical data handbook for FV520B. This handbook has been reproduced in Appendix II with the kind permission of Ken Thorpe at Special Melted Products, Sheffield.

Each heat treated blank was subsequently machined into either a fatigue or a tensile specimen, in preparation for mechanical testing.

3.2.2 Optical Microscopy

An Olympus Vanox optical microscope was used to examine the three microstructures of FV520B. The samples were prepared in the standard metallographic manner to a 1µm polish finish. This was followed by chemical etching using Vilella's reagent to reveal the tempered lath martensite microstructure. Vilella's reagent is commonly used for revealing the microstructure of martensitic and ferritic stainless steels [100].

3.2.3 Transmission Electron Microscopy

3.2.3.1 Thin Foil Preparation

Thin discs were removed from 3 mm diameter cylinders machined from the bulk material, in preparation for examination using the transmission electron microscope. The discs were carefully ground to a thickness of approximately 0.10 mm using 1200# silicon carbide grit paper. To produce an electron transparent region, the thin foils were perforated by electropolishing using a Tenupol-3 twin jet polishing unit. The

electropolishing solution used was 5% perchloric acid in high purity Analar grade methanol. This was maintained at a temperature of -30°C to -28°C. After electropolishing, the perforated thin foils were then washed in Analar grade methanol followed by propan-2-ol to remove any traces of the electropolishing solution. The electropolishing conditions were found to vary slightly between the three microstructures as highlighted in Table 3.2. However, the thin foils for each microstructure were reproducible using the conditions indicated.

Table 3.2 The Conditions for Electropolishing Thin Foils of FV520B.

Heat Treated Condition	Voltage (V)	Amps (A)	Solution Flow Setting	Sensitivity	Temp (°C)	Time (secs)
Peak Hardened	20	1.5	2	10	-28	125
Standard Overaged	20	1.5	2	10	-30	35
Softened Overaged	35	3.0	3	8	-30	30

A Philips CM20 transmission electron microscope (TEM) was used to examine the martensite lath sub-structure in the three heat treated conditions of FV520B. The operative accelerating voltage of the TEM microscope was 200 kV.

3.2.4 Point Count of Delta Ferrite

The volume fraction of delta ferrite (sometimes known as residual or free ferrite) was determined using the point counting method. This was carried out in accordance with BS 7590:1992 [101]. Point counting is a method of determining the volume fraction of a three dimensional microstructural constituent from a two dimensional planar section.

The three samples selected for examination were considered representative of the bulk material. Transverse, planar sections were prepared in the standard metallographic manner to a 1µm polish and etched to reveal only the constituent of interest. The etchant comprised a solution of 10 ml hydrochloric acid in 90 ml anhydrous ethyl alcohol. The samples were examined using a photomicroscope and

the point grid was superimposed upon the microscope viewing screen. The magnification was selected on the basis that the features of interest were approximately one-half of the spacing between grid points. The assumption that the delta ferrite phase was randomly distributed throughout the two dimensional section was made. Due to the heavily banded or anisotropic nature that is inherent in most hot and cold worked microstructures, numerous areas were randomly examined to maintain statistical viability.

The percentage of points within the feature of interest for each field can be determined from the following equation:

$$P_{P(i)} = \frac{P_i}{P_T} \times 100 \quad (3.1)$$

$P_{P(i)}$ is the proportion of grid points in the constituent of interest on the i th field expressed as a percentage of the total number of points on the grid. P_i and P_T represent the point count on the i th field and total number of points on the grid respectively.

The mean value of $P_{P(i)}$, ie \bar{P}_p can be evaluated from the following expression:

$$\bar{P}_p = \frac{1}{n} \sum_1^n P_{P(i)} \quad (3.2)$$

where n is the number of fields examined.

The standard deviation (s) can be written:

$$s = \left\{ \frac{1}{n-1} \sum_1^n (P_{P(i)} - \bar{P}_p)^2 \right\}^{\frac{1}{2}} \quad (3.3)$$

The 95% confidence interval (CI) may be calculated using:

$$CI = \pm \frac{2s}{\sqrt{n}} \quad (3.4)$$

The volume fraction (V_V) of delta ferrite is:

$$V_V = \bar{P}_P \pm CI \quad (3.5)$$

Relative error, in percentage terms is:

$$\text{Relative Error} = \frac{CI}{\bar{P}_P} \times 100 \quad (3.6)$$

3.2.5 Grain Size Determination

The average prior austenite grain size was determined using the mean linear intercept method (MLI) in accordance with BS 4490:1989 Section 3 [102] [103]. In order to reveal the prior austenite grains, the three microstructures were etched using a chromic and phosphoric electrolytic etch which was then followed by a Villela's swab etch. The samples were examined on a photomicroscope at a magnification of x160. The MLI was measured by traversing the etched sample over a total length (L) and the number of grain boundaries (N) which were intercepted linearly was counted. The mean number of intercepts (\bar{N}) was determined to evaluate the mean number of intercepts over the total distance, i.e. \bar{N}_L .

$$\bar{N}_L = \frac{\bar{N}}{L} \quad (3.7)$$

The grain size \bar{d} was expressed as the mean value of the intersected segment whilst assuming the prior austenite grains were equiaxed, that is:

$$\bar{d} = \frac{1}{\bar{N}_L} \quad (3.8)$$

3.2.6 X-Ray Diffraction

Previous workers [14-16] have used the technique of X-Ray Diffraction (XRD) to detect and determine the volume fraction of austenite within FV520B. The quantities of austenite determined by these studies were found to be significant and varied according to the precipitation hardening temperatures employed. In general, the process of precipitation hardening will temper any martensite and transform any austenite retained within the microstructure; and by increasing this 'tempering' temperature, significant quantities of austenite can be transformed. In the case of FV520B [14-16] and a maraging steel [29], since the quantity of austenite increased in accordance with an increase in the precipitation hardening temperature, the austenite was commonly known as reverted or reformed austenite.

Since it was known that reverted austenite would be present within FV520B, it was considered necessary to determine the actual quantities present, as a function of the precipitation hardening temperature. The technique of X-Ray Diffraction (XRD) was therefore used to determine the amount of reverted austenite in this particular material batch of FV520B.

3.2.6.1 Sample Preparation

Samples of the three microstructures were prepared for quantitative analysis using XRD. The samples were prepared to a 600# grit finish prior to electropolishing using a proprietary perchloric acid based electrolyte at a current density of 2 A/cm². This produced a planar, highly polished, stress free surface for subsequent XRD analysis.

The X-ray diffraction system comprised a Philips PW 1830 power generator that was coupled to a Philips PW 1820 vertical goniometer. This system was fitted to a Philips PW 1710 diffractometer controlling unit that facilitated the measurement of the diffracted X-rays. The system was driven and the data processed by Philips PC-APD diffraction software. The current and voltage settings used were 45 mA and 35 kV respectively. Copper K α radiation, monochromated by a graphite single crystal was used.

The background intensity at the Bragg angles either side of the diffracted peaks was measured for a period of 200 seconds (400 seconds in total). The background intensity was subtracted from the maximum intensity reading to obtain the peak intensity reading. X-ray intensities diffracting through Bragg angles of 47-101° were recorded. During the analysis, the sample was rotated about the diffracting plane at a constant velocity of 1 revolution per minute to reduce anomalous intensity readings that may have arisen from preferred orientations within a microstructure.

3.2.6.2 Peak Indexing

The spectra from the XRD analysis of the peak hardened, standard and softened overaged conditions are presented in Figures 4.4a, 4.4b and 4.4c respectively. These spectra show the variation in X-ray intensity as a function of the Bragg angle (2θ). The intensity maximas which are clearly indicated, represent diffraction of the incident X-ray beam by a crystallographic plane.

When a primary X-ray beam is incident on a crystalline material, diffraction is known to occur from a particular crystallographic plane, at a Bragg angle (2θ) which is characteristic of that microstructural phase. Therefore, prior to undertaking the quantitative phase analysis for reverted austenite, it was necessary to determine the diffracting (hkl) planes and hence crystal structure or microstructural phase responsible for diffraction.

For a cubic crystal, diffraction occurs when the values of θ , satisfy equation (3.11) which combines Bragg's Law, equation (3.9):

$$n\lambda = 2d\sin\theta \quad (3.9)$$

where n is an integer and λ is the wavelength of copper $K\alpha$ radiation (1.504 Å). The parameter d represents the interplanar spacing whilst 2θ is the Bragg angle.

The expression for the interplanar spacing is equation (3.10):

$$d = \frac{a}{\sqrt{h^2 + k^2 + l^2}} \quad (3.10)$$

i.e.
$$(h^2 + k^2 + l^2) = \left(\frac{\sin^2 \theta}{\frac{\lambda^2}{4a^2}} \right) \quad (3.11)$$

As previously, 2θ is the Bragg angle, λ is wavelength of copper $K\alpha$ radiation (1.504 Å) and a is the lattice parameter for iron as austenite or ferrite. These lattice parameters are presented in Table 3.3.

Table 3.3 Lattice Parameters for Iron.

Crystal Structure	Lattice Parameter (a) (nm)
α -Fe (bcc)	0.28665
γ -Fe (fcc)	0.36469

In order to index the diffraction peaks, a series of integers for (hkl) must be found to satisfy equation (3.11), for a known Bragg angle. The possible sets of integers for both body-centred and face-centred cubic structures are given in Ref. [105].

3.2.6.3 Quantitative Analysis of Reverted Austenite

The intensity of a diffracted peak from a particular phase will be dependent on the concentration of that phase within the mixture of phases [105]. On this basis, quantitative phase analysis can be undertaken using the technique of X-Ray Diffraction (XRD).

Several methods have been developed for quantitative phase analysis, but for the present study, the direct comparison method was used. For this particular method, it was assumed that only the two phases were present within the microstructure, i.e. austenite and martensite. Therefore, in determining the concentration of austenite, the intensities of the diffracting peaks from austenite were compared with those from martensite.

The direct comparison method is described in Ref. [105]. According to Reference [105], the relative intensity as derived experimentally is given by:

$$I = \frac{K_2 R}{2\mu} \quad (3.12)$$

where K_2 is a constant which is independent of the diffracting material and μ is the linear absorption coefficient.

R , the theoretical intensity which is dependent on the diffracting (hkl) plane, angle and material is given by [105]:

$$R = \left(\frac{1}{V^2} \right) \left[|F|^2 m_f \left(\frac{1 + \cos^2 2\alpha \cdot \cos^2 2\theta}{\sin^2 \theta \cos \theta} \right) \right] (e^{-2m}) \quad (3.13)$$

where

Structure Factor	-	$ F ^2$
Lorentz-Polarisation	-	$\frac{1 + \cos^2 2\alpha \cdot \cos^2 2\theta}{\sin^2 \theta \cdot \cos \theta}$
Multiplicity Factor	-	(m_f)
Temperature Factor	-	(e^{-2m})

The volume of the unit cell (V) is related to the lattice parameter (a) according to equation (3.14):

$$V = a^3 \quad (3.14)$$

For a particular diffracting peak from the martensite (α') phase alone, the expression for the diffracting intensity can be rewritten as $I_{\alpha'}$.

$$I_{\alpha'} = \frac{K_2 R_{\alpha'} C_{\alpha'}}{2\mu} \quad (3.15)$$

Similarly, the expression for the intensity of a diffracting austenite phase (γ) can be represented by I_{γ} :

and
$$I_{\gamma} = \frac{K_2 R_{\gamma} C_{\gamma}}{2\mu} \quad (3.16)$$

where C_{γ} and $C_{\alpha'}$ represent the volume fraction of austenite and martensite respectively.

Comparing equations (3.15) and (3.16) gives:

ie.
$$\frac{C_{\gamma}}{C_{\alpha'}} = \frac{R_{\alpha'} I_{\gamma}}{R_{\gamma} I_{\alpha'}} \quad (3.17)$$

substituting the known values of R and I, for austenite and martensite, the ratio of $C_{\gamma}/C_{\alpha'}$ can be evaluated.

For a dual phase microstructure:

$$C_{\gamma} + C_{\alpha'} = 1 \quad (3.18)$$

and so the volume percentage austenite (% γ) can be determined by:

$$\% \gamma = \frac{1}{1 + \left(\frac{C_{\alpha'}}{C_{\gamma}} \right)} \times 100 \quad (3.19)$$

3.2.6.4 Evaluation of the Theoretical Intensity

As given equation (3.13), the value of theoretical intensity R is dependent on the structure factor, Lorentz-polarisation, the multiplicity factor and the temperature factor.

The Structure Factor | F |²

The structure factor is calculated from the summation of the waves scattered by the individual atoms which represent the effect of scattering due to the atomic

arrangement. As given in Ref. [105], the structure factor $|F|^2$ can be expressed in the form:

$$|F|^2 = 16f_0^2 \quad \text{for fcc, i.e. austenite} \quad (3.20)$$

$$|F|^2 = 4f_0^2 \quad \text{for bcc, i.e. martensite} \quad (3.21)$$

where f_0 is the (corrected) atomic scattering factor which was determined from Ref. [106] for each element within FV520B.

Since the radiation used was close to the absorption edges of the elements present in FV520B, the atomic scattering factors for each element were corrected for the effects of absorption. The following correction was used:

$$\text{Corrected } f_c = f_0 + \Delta f' \quad (3.22)$$

where $\Delta f'$ is the scattering correction factor for each element, when using copper $K\alpha$ radiation [106].

The average value of the atomic scattering factor for FV520B was subsequently determined using the following expression using the summation for each element:

$$f_0 \text{ average} = \sum (\text{atomic fraction} \cdot f_0) \quad (3.23)$$

The structure factor was then calculated using equations (3.20) and (3.21).

The Lorentz-Polarisation Factor

The Lorentz-Polarisation factor considers polarisation of the diffracted beam.

In the presence of a graphite single crystal monochromator, the Lorentz-Polarisation factor is:

$$\text{Lorentz - Polarisation factor} = \frac{1 + \cos^2 2\alpha \cdot \cos^2 2\theta}{\sin^2 \theta \cdot \cos \theta} \quad (3.24)$$

where the factor $\cos^2 2\alpha$ accounts for the monochromated X-rays. The value of α for copper ($K\alpha$) radiation is 13.15° .

The Multiplicity Factors (m_r)

The multiplicity factors are used to account for the proportion of the planes of the same type and interplanar spacing, which may produce reflections. For example, crystals may be orientated such that diffraction occurs from the (100) plane; in contrast, other crystals may produce reflections from the (010) or (001) planes. In the case of the (100) plane, the multiplicity factor would be 6, which indicates that reflections could occur from any of the following planes, i.e. (100), (010), (001), $(\bar{1}00)$, $(0\bar{1}0)$, $(00\bar{1})$ planes.

The multiplicity factors for the diffracting planes in FV520B are presented in Table 3.4.

Table 3.4 The Multiplicity Factors [105].

Diffracting Plane (hkl)	(200)	(220)	(220)	(211)	(311)
m_r	6	8	12	24	24

The Temperature Factor (e^{-2m})

The structure factor considered atomic scattering affects whilst the atoms were in their 'resting' position. However, temperature effects which lead to an increase in thermal vibration can be accounted for by the temperature factor. The general effect of an increase in thermal vibration is a diffusion of the diffraction peaks, i.e. the peaks broaden over a greater range of 2θ and a reduction in their respective intensity is also apparent.

The temperature factor is evaluated by the expression:

$$e^{-2m} = e^{\left(\frac{-B \sin^2 \theta}{\lambda^2}\right)} \quad (3.25)$$

However, the temperature factor can be determined from tables of $\frac{\sin\theta}{\lambda}$ versus B which are given in Ref. [107].

where B, the temperature factor is:

$$B = B_T + B_0 \quad (3.26)$$

The values of B_T and B_0 which represent the zero point energy and the Debye temperature factor parameters respectively, are given in Ref. [108].

3.2.7 Precipitation Hardening Curve

The purpose of this study was to ascertain the time at which this second precipitation hardening reaction occurs and either confirm or disprove the results from a previous investigation [16]. A solution treated sample was isothermally heat treated at a temperature of 450°C and removed at intervals to measure the Vickers hardness (Hv_{30}). Figure 4.5 shows the variation in hardness as a function of treatment time. The experimental data is presented in Table D4, Appendix I.

3.2.8 Dilatometry Work

The purpose of this work was to determine the phase transformation temperatures of FV520B during thermal heating and cooling cycles. The thermal transformation temperatures of particular interest were the A_{C1} and A_{C3} temperatures on heating, and M_s and M_f temperatures on cooling.

The dilatometry work was performed at British Steel Swinden Technology Centre using a Materials Measuring Corporation (MMC) Quenching Dilatometer. A cylindrical dilatometer sample, whose diameter and length measured 5 mm and 10 mm respectively was heated in a small induction coil. The tests were performed under a vacuum at a constant heating rate of 5°C min⁻¹, to a maximum temperature of 1050°C. The sample was held for a period of 1 minute at 1050°C before being cooled to ambient temperature using helium gas. The temperature was monitored using a platinum-platinum/10% rhodium thermocouple (S-type) which was attached to the

sample. Any change in sample dimensions during the heating and cooling cycles was detected via push rods connected to a sensitive linearly variable differential transducer (LVDT). Any change in sample dimensions represented a phase transformation [109] [110].

3.2.9 Non-Metallic Inclusion Study

Longitudinal sections, from the bulk material were removed and metallographically prepared to a 1 μ m polish finish. Care ensured that non-metallic inclusion “pull-out” during the polishing stage was minimised. An advanced Philips XL40 Analytical Scanning Electron Microscope and Energy Dispersive X-Ray (EDX) Analyser was employed to examine the as-polished samples and facilitate elemental analysis. The investigation was performed using the back-scattered electron (BSE) imaging mode which highlighted differences in atomic number. Those inclusions of higher atomic number yielded greater numbers of electrons and therefore appeared brighter under the SEM.

As a result of the steel’s cleanliness, and the anticipated size range, magnifications in the order of x2500 and x5000 were used to resolve the inclusions.

3.3 Scanning Electron Microscopy

The Philip’s XL40 Analytical Scanning Electron Microscope was routinely used to examine the general features of both the material microstructure, in addition to the fractured samples.

3.3.1 Sample Preparation

Prior to examination, the threaded section of the fatigue samples were removed, in order to maximise the available depth of field in the SEM. The fractured samples were then ultrasonically cleaned for a period of 1-2 minutes in alcohol to remove any dust or salt deposits. The clean specimens were then mounted on aluminium stubs using a conductive silver paint, ready for SEM examination. Any specimen that underwent general microstructural SEM examination was mounted in conductive bakelite.

3.3.2 Modes of Operation

When a primary beam of electrons is incident on a solid sample, a number of interactions occur and the result is the emission of excited electrons and other radiation from what is regarded as the interaction or excitation volume. The three types of interaction employed during scanning electron microscopy are: secondary electrons, back-scattered electrons and X-rays. The range and spatial resolution of the electrons from the interaction volume have been summarised schematically in Figure 3.1.

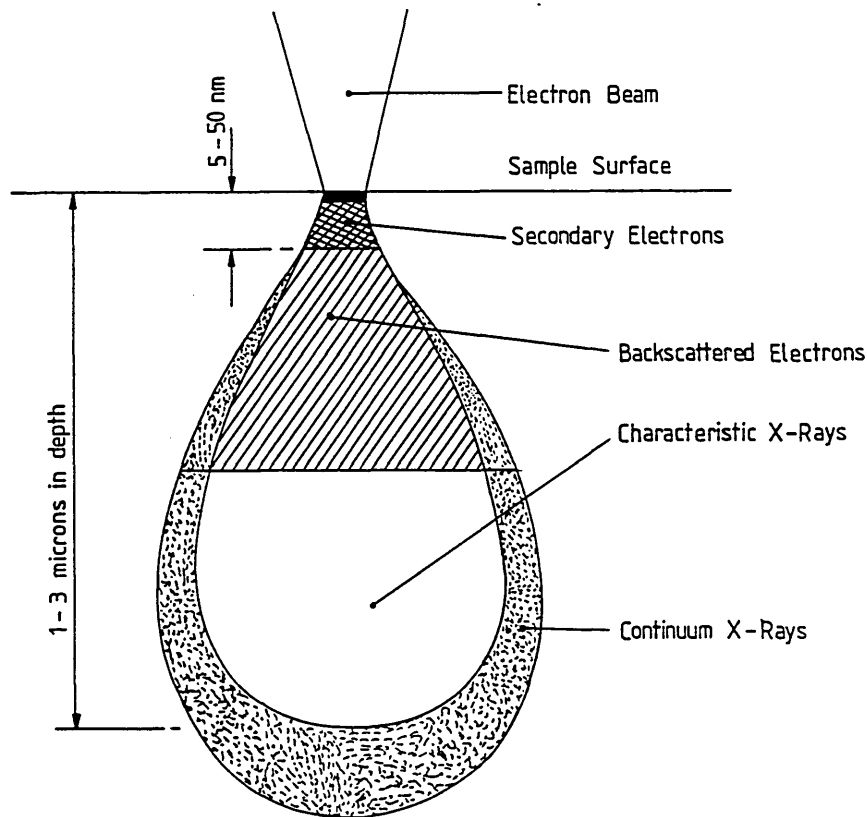


Figure 3.1. The Excitation Volume for the Scanning Electron Microscope (SEM).

The main advantages of using scanning electron microscopy (SEM) as an investigative tool are:

1. The depth of field available to the user, particularly when examining fracture surfaces which inherently possess a rough surface topography. For example the depth of field available at magnifications of $\times 10$ and $\times 10,000$ are 2 mm and $1\mu\text{m}$ respectively.

2. A large chamber which can accommodate large fractured components for bulk analysis.
3. A wide range of working magnifications from x15 up to x150,000 as a result of the high resolution capacity (approximately 5 nm).
4. Little sample preparation is often necessary.

The characteristics of the various interactions used for imaging and analysis under the SEM are summarised in Table 3.5 [111].

Table 3.5 The Interactions Used During Scanning Electron Microscopy.

Detected Signal	Information	Basic Effects	Resolution	Depth of Information
Secondary Electrons	surface topography, material contrast, crystal orientation contrast	SE yield depends strongly on surface tilt and weakly on atomic number and crystal orientation	5-20 nm	1-10 nm
Back Scattered Electrons	material composition, topography, crystal orientation	BE yield depends on atomic number, increasing for heavier elements	0.1-1 μm	0.1-1 μm depends on accelerating voltage
X-Rays	elemental distribution	emission of photons by electron bombardment	$\approx 1 \mu\text{m}$	1-10 μm

3.4 Fatigue Crack Nucleation and Short Fatigue Crack Monitoring

Replicas were taken during air and corrosion fatigue testing in an attempt to monitor the early stages of the fatigue process. The main advantage of using this technique was that the sample could remain in the test rig whilst the replicas were taken.

Since the technique for taking plastic replicas has been documented in detail elsewhere [58] [54] [120], only an outline of the technique was considered necessary. A 30 μm thick cellulose acetate medium was used for making the replicas of the sample surface. Prior to taking the replicas, care was required to ensure that all

equipment used, including the replicating medium and the specimen surface was free from debris to prevent artefacts being introduced onto the final replica. Entrapped air between the replica and the sample was also avoided otherwise features of interest may have been obliterated. Acetone was applied to the replica which was then offered to the sample surface. The capillary forces between the sample and the solvent resulted in the replica adhering to the surface. Once the acetone had completely evaporated, the plastic replica was mounted onto a glass slide in preparation for being examined using an optical microscope.

3.5 Mechanical Testing

3.5.1 Vickers Hardness Measurements

The Vickers hardness of the three microstructures of FV520B was measured using a 30 kg load. The results are presented in Table 4.6.

3.5.2 Tensile Testing

A 100 kN servohydraulic Mates testing machine was used to determine the tensile strength of FV520B. Figure 3.2 shows the geometry of the tensile specimen. All dimensions are in mm.

A displacement transducer was attached to the sample in order to monitor specimen extension during tensile loading. A graph of applied load versus specimen extension was plotted on a X-Y chart recorder which enabled the 0.2% proof stress and ultimate tensile stress for each heat treated condition to be determined. The tensile properties of FV520B are presented in Table 4.7.

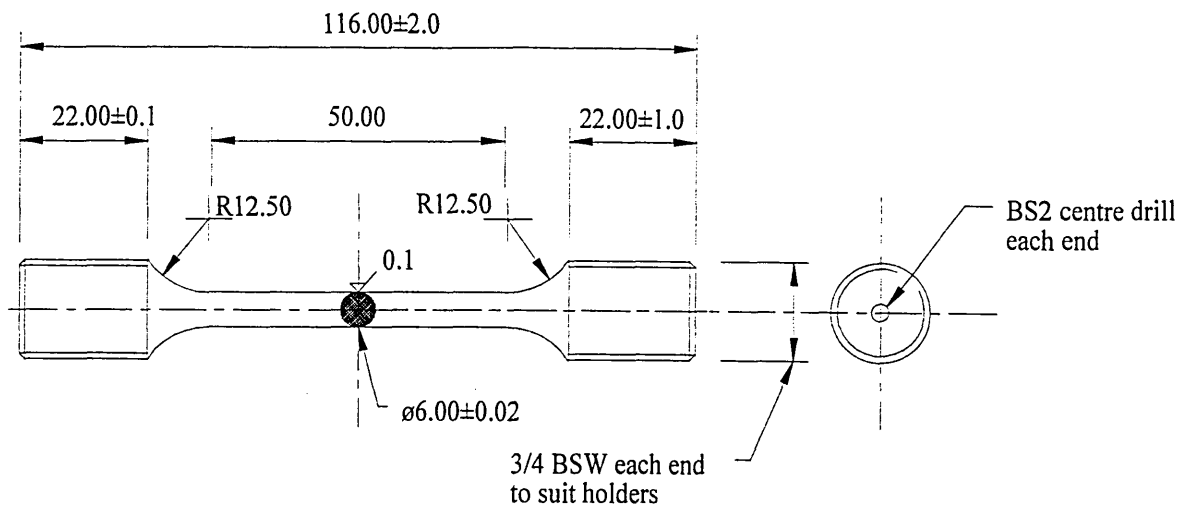


Figure 3.2 The Specimen Design for Tensile Testing.

3.5.3 Fatigue Testing

The stress amplitude-life (S-N) data was generated under constant load amplitude, fully reversed ($R = -1$), push-pull loading conditions. A 20 kN Amsler Vibrophore was employed for the air fatigue testing of the peak hardened and standard overaged conditions, Figure 3.3. A 20kN Mayes servo-hydraulic testing machine was used for the air fatigue testing of the softened overaged condition and the corrosion fatigue testing of all heat treated conditions, Figure 3.4. The air fatigue testing of the softened overaged condition was performed at a frequency of 4 Hz, except for two specimens, which were tested at 20 Hz and 196 Hz respectively.

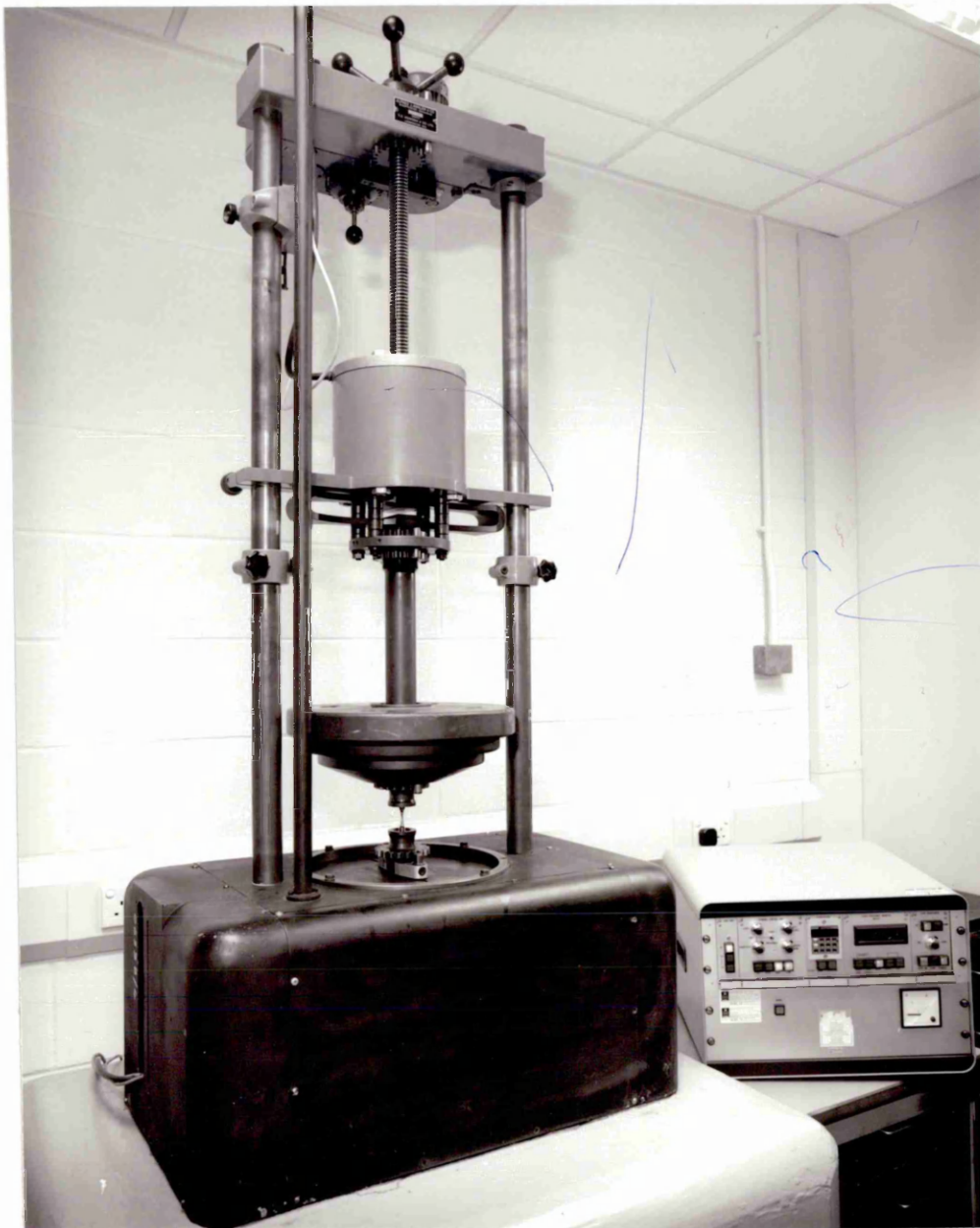


Figure 3.3 The Amsler Vibrophore.

The Amsler Vibrophore is an electromagnetic resonating fatigue testing machine which operates on the principle of a resonant 'spring-mass' system. The test frequency is highly dependent on the stiffness of the specimen, that is, the stiffer the specimen, the higher the operating frequency. The oscillating resonant frequency for FV520B was between 199-200 Hz. In order to reduce the test frequency, weights were added to the 'spring'. This imposed a restriction on the range of test frequencies available. The static (or mean) load was applied to the sample by displacing the leadscrew. The dynamic load, however was applied electromagnetically by setting an air gap between two electromagnetic "plates".

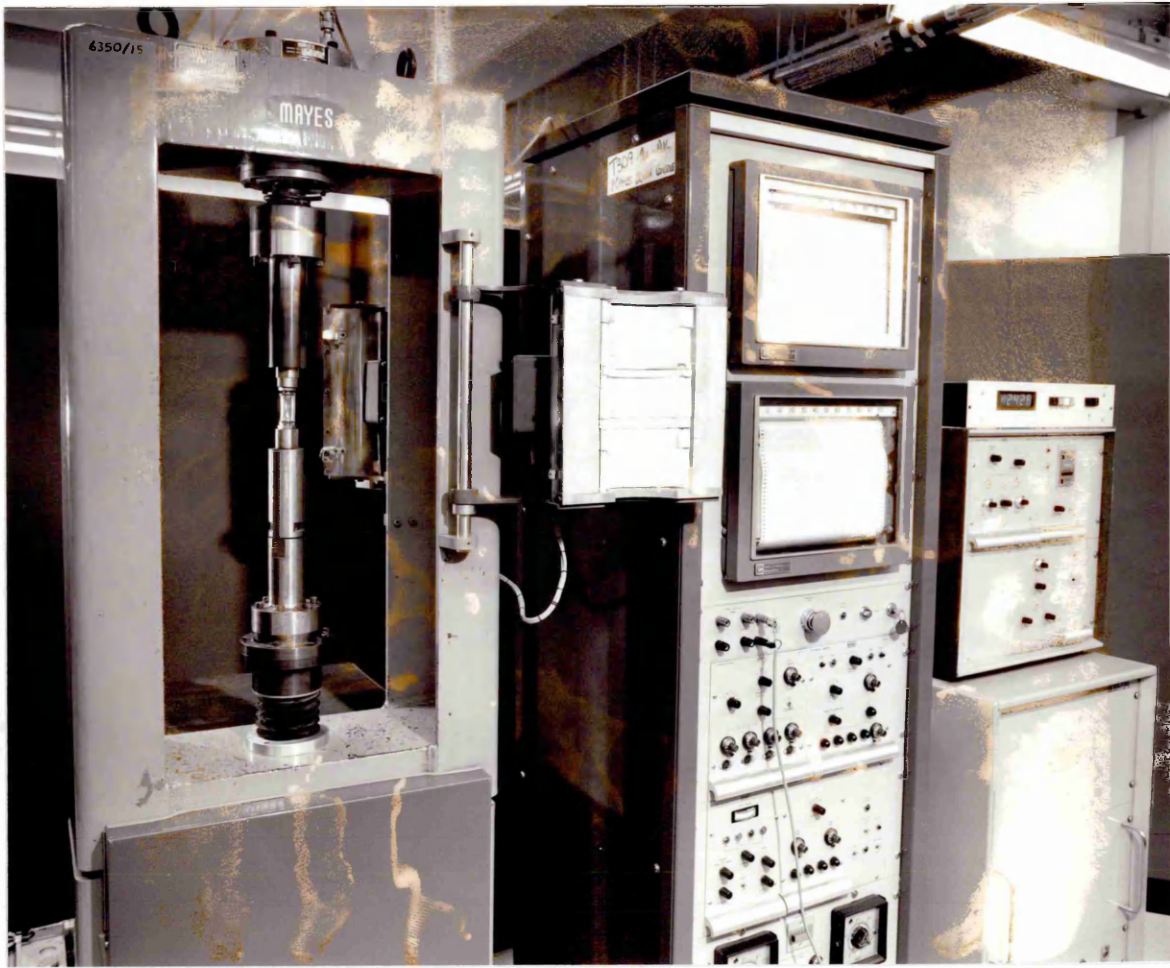


Figure 3.4 The Mayes Servo-Hydraulic Testing Machine.

3.5.3.1 Fatigue Specimen Design

The hour-glass fatigue specimen design was selected for the purpose of both air and corrosion fatigue testing. The specimen design is illustrated in Figure 3.5. All dimensions are in mm.

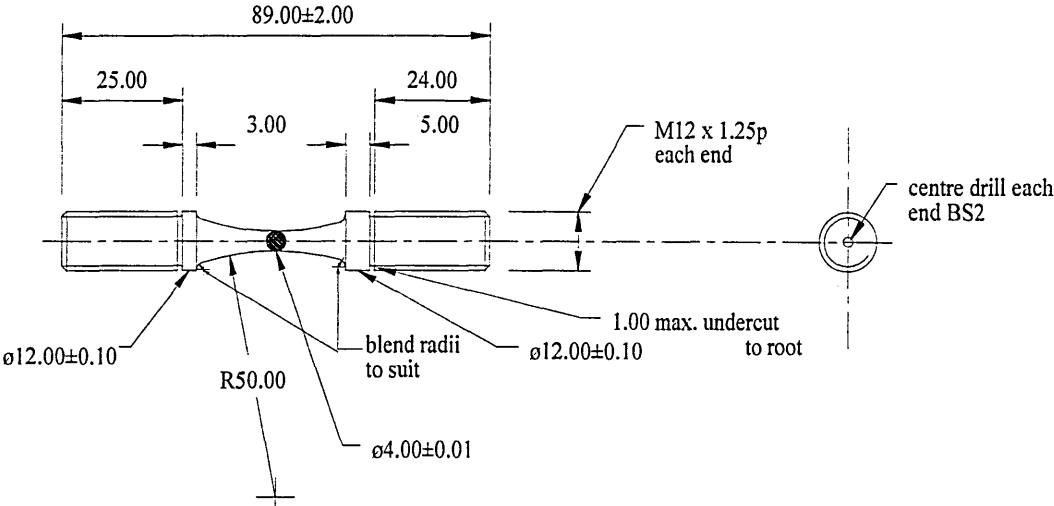


Figure 3.5 The Specimen Design for Fatigue Testing.

An optimum surface finish was achieved by using successively finer silicon carbide grit paper, until a 1200# grit finish was attained. The highly polished surface finish was accomplished by using a 6 followed by a 1 μ m polish. This mirror-like surface finish is shown in Figure 3.6.

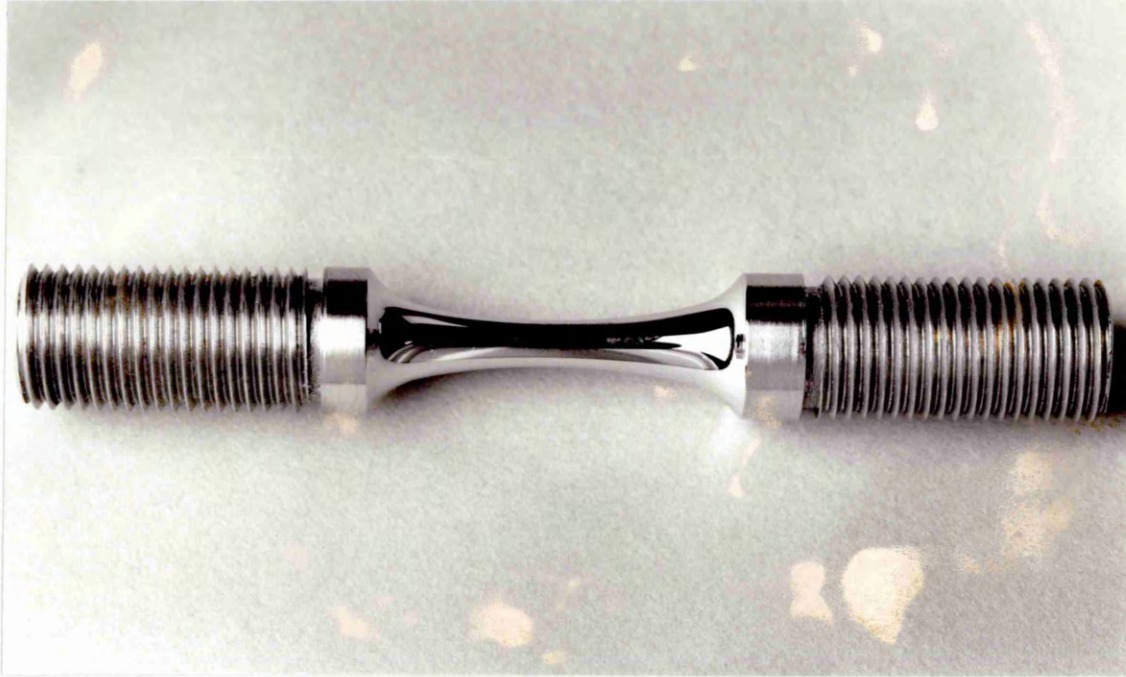


Figure 3.6 A Fatigue Test Specimen.

3.5.4 Corrosion Fatigue Testing

The corrosion fatigue test chamber comprised a plastic tube which when fitted to the sample provided the chamber that contained the aerated chloride solution. The solution was injected into the chamber using a hypodermic needle. During corrosion fatigue testing the samples corroded at their free corrosion potential. Table 3.6 highlights the air and the corrosion fatigue test programme.

Test	Environment	Test Frequency (Hz)	Temperature (°C)	Stress Ratio	Load Waveform	Test Rig
Air Fatigue	Laboratory air	199 to 200	Ambient	-1	Sinusoidal	Amsler Vibrophore
Air Fatigue	Laboratory air	4	Ambient	-1	Sinusoidal	Mayes
Corrosion Fatigue	3.5% NaCl pH2 aerated solution	0.5	Ambient	-1	Sinusoidal	Mayes

Table 3.6 The Test Conditions for Air and Corrosion Fatigue.

CHAPTER 4

EXPERIMENTAL RESULTS

4.1 Introduction

The results from the experimental work are presented in the following chapter.

4.2 Materials Characterisation

4.2.1 Chemical Analysis

A macrosection was removed from the plate for chemical analysis by optical emission spectrometry. Optical emission spectrometry facilitates quantitative chemical analysis by measuring the intensity of characteristic spectra which are emitted from the steel. The spectra (which appear as a series of 'lines') are generated by applying a high voltage which results in the emission of a spark or light energy. These 'lines', which are characteristic of the elemental constituents within the steel, are split according to their respective wavelengths using a diffraction grating. The elements are identified from the diffraction angle and the peak heights provide information on concentration of particular elements, following reference to standard samples.

The results from the chemical analysis are presented in Table 4.1. These results show that the chemical composition met the material specification requirements for FV520B, a precipitation hardenable stainless steel.

Sample Identification /Specification	Element (bal Fe)										
	C	Si	Mn	Cr	Ni	Mo	Cu	Nb	P	S	
FV520B	0.057	0.29	0.57	13.92	5.29	1.41	1.51	0.25	0.012	0.005	
Material Specification for FV520B	0.07 max	0.70 max	1.00 max	13.2-14.7	5.0-6.0	1.2-2.0	1.2-2.0	0.20-0.70	0.040 max	0.040 max	

Table 4.1 Chemical Analysis and Material Specification Requirements of FV520B.

4.2.2 Microstructures

A three stage heat treatment cycle was used to produce the microstructures with the required mechanical properties. The three stages comprised homogenisation, solution treatment and an artificial precipitation hardening treatment, as previously outlined in Table 3.1.

4.2.2.1 Homogenisation

Hot forging the as-rolled material produced a heavily deformed microstructure which is likely to possess anisotropic properties. In order to produce a homogenous microstructure with the required mechanical properties, the initial heat treatment stage must remove the effects of prior plastic deformation. In addition to this, the alloying elements must be absorbed into the austenitic solid solution, prior to subsequent heat treatment. During the homogenising stage, the material was held for a period at a temperature of 1050°C.

Commercially, FV520B would normally be homogenised at 1050°C for a period of only half an hour. However, microexamination of the microstructure after this treatment indicated that a heavily banded structure still remained. Therefore a trial was conducted to determine the optimum homogenisation period which would remove the effects of the prior deformation without compromising the fine grain size. Problems which arise from heat treating at such a high temperature include prior austenite grain coarsening (which determines the martensite lath packet size) and the formation of the stable delta ferrite phase. Additionally, the grain size has been known to affect the fatigue properties of a number of alloys [61]. Delta ferrite must be avoided since it detracts from both material toughness and strength and its high stability means that once formed, it cannot be taken back into solid solution at 1050°C [112].

Samples were heat treated at 1050°C for periods of 1, 2 and 4 hours. The sample homogenised for a period of 1 hour exhibited no appreciable grain growth although light microsegregation or banding remained. The 1 hour homogenisation heat treatment was therefore adopted for subsequent heat treatment of all fatigue and tensile specimen blanks.

4.2.2.2 Hardening or Solution Treatment

Heating to 750 or 850°C partially re-austenitised the steel, tempered any martensite within the microstructure and precipitated alloy carbides. The resultant microstructure on cooling to room temperature contained martensite, tempered martensite, alloy carbides and retained or reverted austenite.

4.2.2.3 Artificial Precipitation Hardening Treatment

The final step in the heat treating cycle was precipitation hardening. Precipitation hardening FV520B at 450°C produced a microstructure in it's peak hardened condition due to the precipitation of a fine dispersion of sub-microscopic copper particles [21].

FV520B is highly hardenable and requires no quenching medium other than air to produce a martensitic microstructure on cooling from above the A_{C1} . Table 4.3 highlights the phase transformation temperatures, as determined during the dilometric study.

Figures 4.1a-4.1c are the optical micrographs of the peak hardened, standard overaged and softened overaged microstructures respectively. Optical examination revealed that the microstructures comprised a slightly banded tempered lath microstructure with reverted austenite and alloy carbides. These microstructural features would be consistent with FV520B in the hardened and tempered condition.

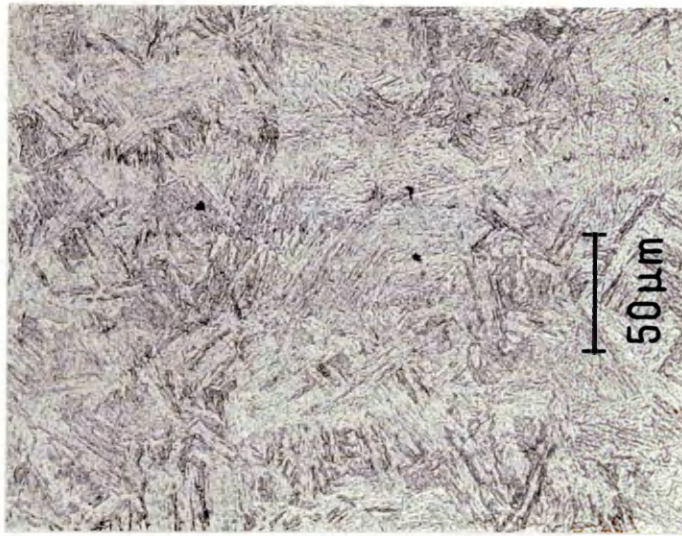


Figure 4.1a Optical Micrograph of the Peak Hardened Microstructure.



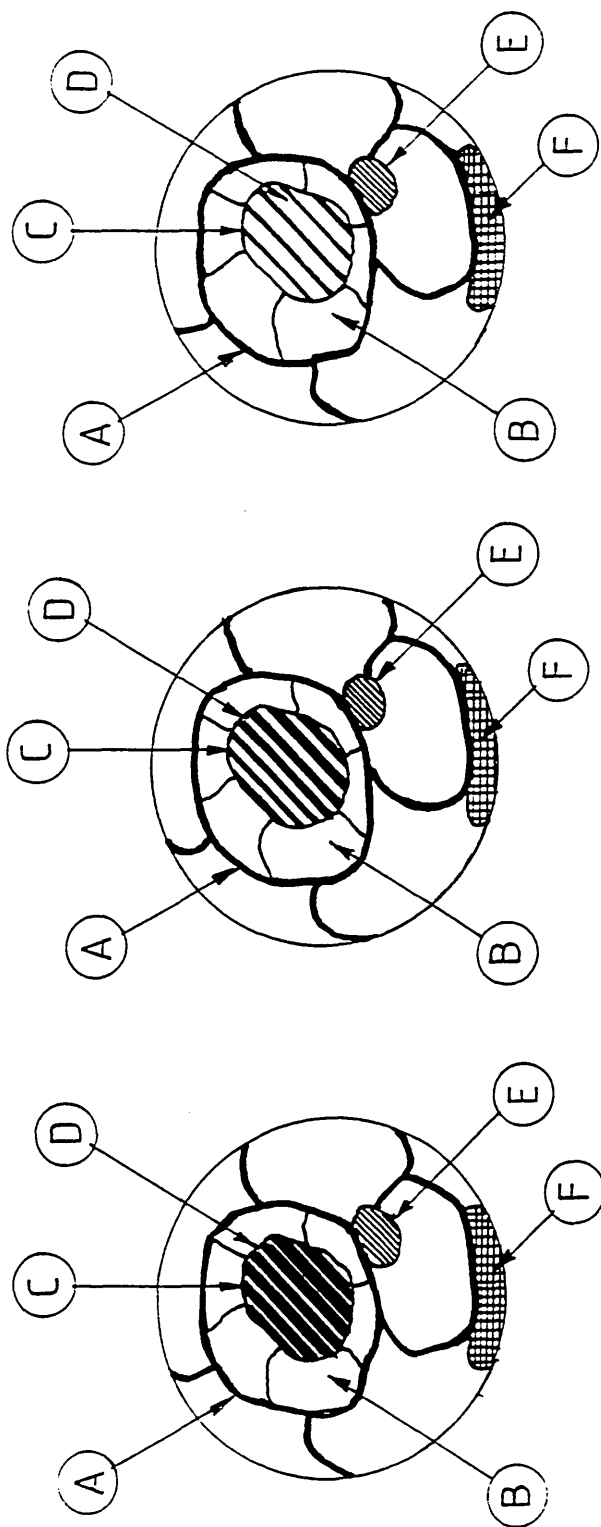
Figure 4.1b Optical Micrograph of the Standard Overaged Microstructure.



Figure 4.1c Optical Micrograph of the Softened Overaged Microstructure.

Figures 4.2a-4.2c depict the microstructural features of FV520B in schematic form. The primary difference between these three microstructures is the varying quantity of reverted austenite and the size of the individual austenite packets.

Table 4.2 shows the microstructural components and their respective quantities within the three microstructures studied.



(a) PEAK HARDENED (b) STANDARD OVERAGED (c) SOFTENED OVERAGED

Microstructural Feature	Approx. Size (μm)
A	14 (MLI)
B	4 - 14
C	1

Microstructural Feature	Approx. Size (μm)
D	--
E	4 - 10
F	variable

Figure 4.2. Schematic Representation of the Peak Hardened, Standard and Softened Overaged Microstructures.

Heat Treatment	Prior Austenite Grain Size (μm)	Reverted Austenite (Vol.%)	Delta Ferrite (Vol.%)	Lath Packet Size (μm)	Lath Width (μm)	Oxide Inclusion Size (μm)	Dislocation Density (cm^{-2}) [24]
Peak Hardened	14	3 ± 1.6	0.05 ± 0.005	4-14	1	<7	1.65×10^9
Standard Overaged	14	21 ± 8.7	0.05 ± 0.005	4-14	1	<7	2.70×10^9
Softened Overaged	14	43 ± 11.5	0.05 ± 0.005	4-14	1	<7	2.67×10^9

Table 4.2 Microstructural Features in FV520B.

4.2.3 Transmission Electron Microscopy

Figure 4.3a shows the lath structure of the peak hardened material whilst Figure 4.3b highlights the relatively tempered microstructure of the softened overaged condition.



Figure 4.3a Transmission Electron Micrograph of the Peak Hardened Microstructure. Magnification x11,500.

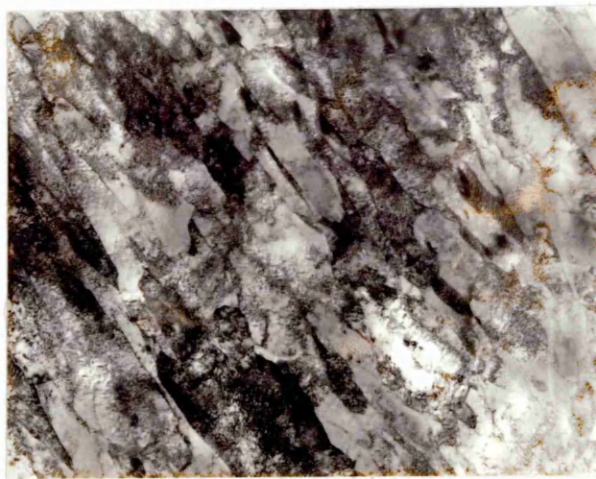


Figure 4.3b Transmission Electron Micrograph of the Softened Overaged Microstructure. Magnification x11,500.

4.2.4 Point Count of Delta Ferrite

The volume fraction of delta ferrite was 0.05 ± 0.005 .

According to the modified Schaeffler diagram in Figure 2.2, delta ferrite should not be present in FV520B. However, 0.050 by volume fraction was observed. Delta ferrite forms at temperatures in excess of approximately 1100°C and the presence of chromium and molybdenum would have promoted its formation. It is possible that the heavily banded microstructure which comprises microsegregation, i.e. areas enriched in chromium and molybdenum could have assisted the formation of delta ferrite. It is known that the material would have been hot forged at a temperature amenable to forming delta ferrite.

4.2.5 Grain Size Determination

The mean linear intercept of the prior austenite grains was 14µm, this is equivalent to ASTM grain size no. 9.

Measurements of the mean lath packet diameter were taken from representative scanning electron micrographs of FV520B. The mean lath packet size for the three microstructures was variable and measured between 4µm to 14µm.

The lath widths were measured using the procedure outlined in Section 3.2.5. The mean linear intercept of the martensite laths was 1µm.

4.2.6 X-Ray Diffraction (XRD)

The spectra from the XRD analyses are presented in Figures 4.4a, 4.4b and 4.4c for the peak hardened, standard and softened overaged conditions respectively. These spectra show the intensity of diffracting planes as a function of the Bragg angle (2θ). The results from the quantitative analyses of the reverted austenite phase are presented in Table 4.2, whilst the experimental data is presented in Tables D1-D3, Appendix I.

Peak indexing determined that diffraction occurred from the $(200)_\gamma$, $(220)_\gamma$, $(311)_\gamma$, $(200)_\alpha$, $(211)_\alpha$, $(220)_\alpha$ diffracting planes which produced strong reflections, as shown in Figures 4.4a, 4.4b and 4.4c.

The results from the phase analysis suggests that the quantity of austenite varied as a function of the precipitation hardened temperature employed. Indeed, as the precipitation hardening temperature became close to or in excess of the A_{C1} temperature, the quantity within the microstructure increased. Since the austenite content increased in accordance with the heat treatment temperature, the austenite can be categorised as reverted austenite [121].

The traces representing the analysis for the standard and softened overaged conditions, ie Figures 4.4b and 4.4c, show an additional diffraction peak at a Bragg angle of 98° . This additional peak which appeared more intense in the case of the softened compared to the standard overaged condition, represented diffraction from the $(222)_\gamma$ plane. The absence of this peak in Figure 4.4a suggested that diffraction from the $(222)_\gamma$ plane at 3% reverted austenite was weak and hence not resolvable in the peak hardened material.

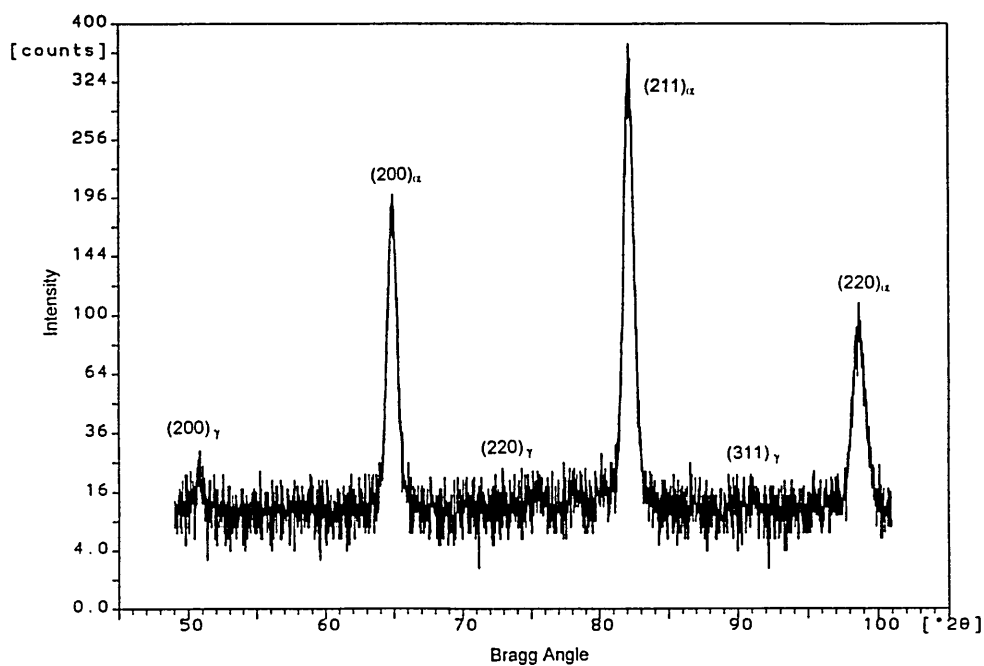


Figure 4.4a The X-Ray Diffraction Spectrum for the Peak Hardened Condition.

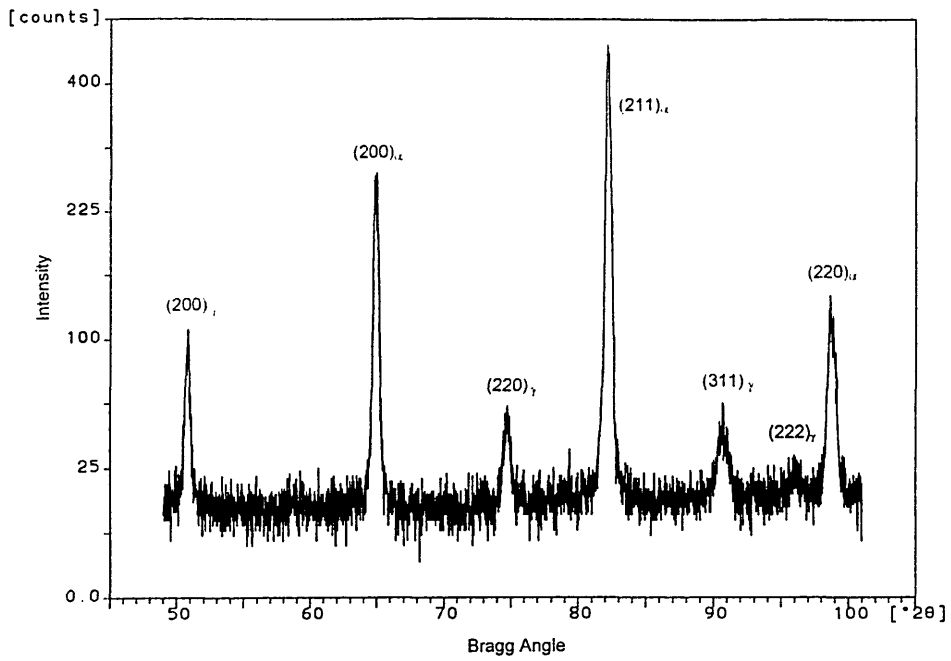


Figure 4.4b. The X-Ray Diffraction Spectrum for the Standard Overaged Condition.

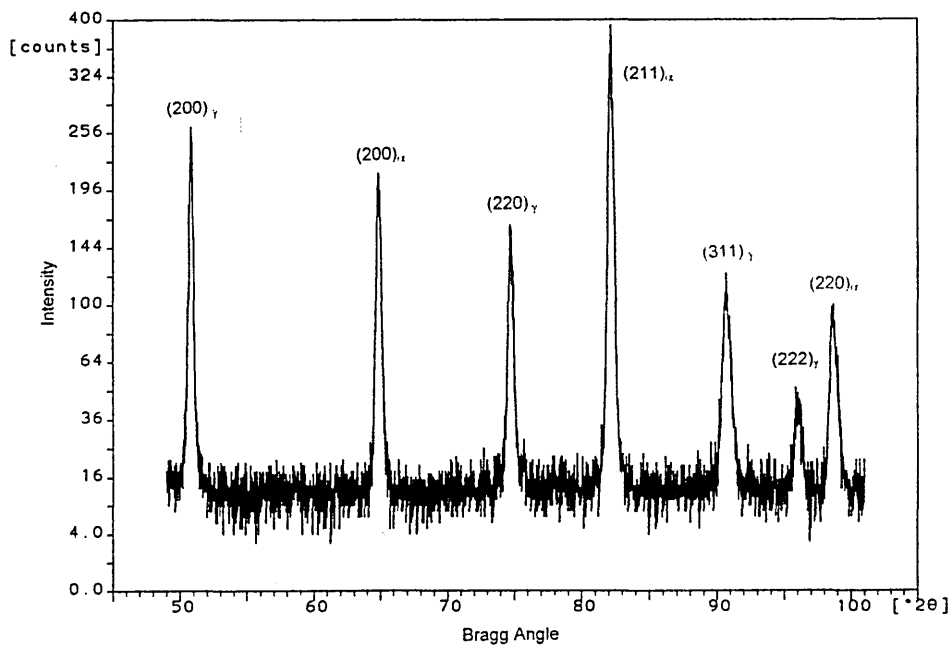


Figure 4.4c The X-Ray Diffraction Spectrum for the Softened Overaged Condition.

4.2.7 Precipitation Hardening Curve

Figure 4.5 shows the isothermal precipitation hardening curve for FV520B at 450°C. The first and second precipitation hardening peaks are evident after approximately 4 and 537 hours respectively. The 'dip' in the curve which is evident after approximately 15 hours represents overaging of the copper precipitates. The 4 hour hardening treatment is of greatest commercial interest and was therefore employed during the course of this study. The data from the isothermal precipitation hardening experiment is presented in Table D4, Appendix I.

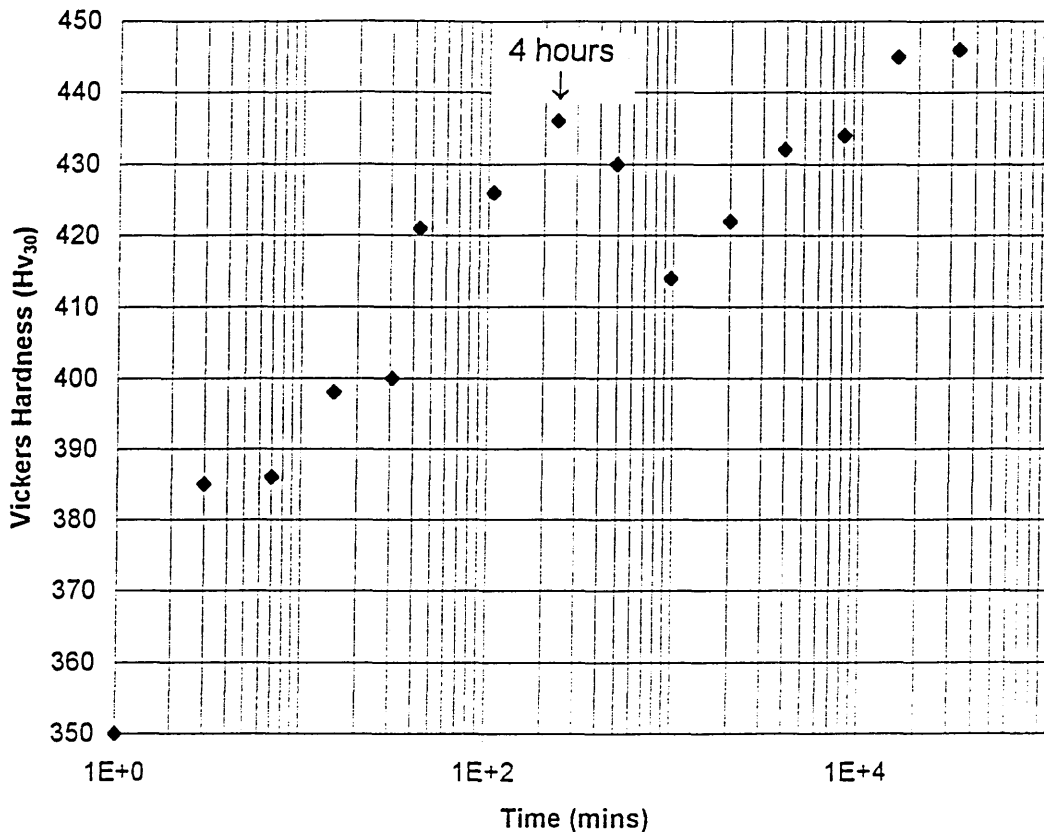


Figure 4.5 The Isothermal Precipitation Hardening Curve for FV520B.

4.2.8 Dilatometry Results

The transformation temperatures which were determined during the heating and cooling cycles of FV520B are presented in Table 4.3. The results indicate that on cooling from an austenitising temperature of 1050°C the martensite transformation start (M_s) and finish (M_f) temperatures were 130°C and 20°C respectively. The M_f

temperature was found to be slightly below room temperature. A fully martensitic microstructure may not be attained when the M_f is below room temperature. This can lead to the presence of a small quantity of untransformed product, ie retained austenite.

The austenite start (A_{c1}) and finish temperature (A_{c3}) were found to be 600°C and 780°C respectively. In maraging steels these can be equated to A_s and A_f respectively.

Table 4.3 The Thermal Phase Transformation Temperatures.

Phase Transformation	A_{c1}	A_{c3}	M_s	M_f
Temperature (°C)	600	780	130	20

4.2.9 Non-Metallic Inclusion Study

The advances achieved in steelmaking technology over the last 30 years has resulted in increasingly cleaner steels which are free from the foreign particles commonly known as inclusions. As a result of these cleaner steels with fewer and smaller particles, the methods employed to grade them in terms of their inclusion content have become more complex and more sophisticated techniques have been required. It has even been suggested [73] that current quality assessment techniques are insensitive to the factors which may influence fatigue life.

Two methods for characterising the inclusion population in vacuum arc remelt (VAR) grade of FV520B were considered. Firstly, the traditional method of assessing the inclusion content in a steel using the comparison method was considered. This method relies on a comparison between standard charts which grades the inclusions according to their frequency, size and type. Usually the study is performed at a magnification of X100. Steels manufactured by the vacuum arc remelt route such as the type used in this study are exceptionally clean in terms of the inclusion population. Those inclusions present are usually small in size, highly fragmented and widely distributed throughout the steel ingot. The result was that the comparison method

was considered unsuitable for this particular grade of steel containing 0.005% sulphur, since the inclusions were too small to be examined at the required magnification of X100. Employing a higher magnification of X500 would have required investigating a significantly greater number of fields to obtain a more representative view of the material.

The second method considered required generating X-ray distribution maps of the inclusions using the Scanning Electron Microscope (SEM), in conjunction with the Energy Dispersive X-Ray (EDX) analysis system. This method would yield information such as the number of inclusions in the steel, their distribution, the volume fraction and aspect ratios. The problem with this particular method was two fold. Firstly, the sulphur $K\alpha$ peak (likely to be present in the commonly found MnS inclusions) and the molybdenum $L\alpha$ and $L\beta$ peaks (from the steel matrix) would overlap rendering differentiating the two elements extremely difficult. Secondly, the size of inclusions under investigation and the spatial resolution of the system ($1\mu\text{m}^3$) may render those inclusions less than $5\mu\text{m}$ in size difficult to analyse. The resolution of EDX analysis was outlined in Section 3.3.2.

A more simple, but effective approach was adopted to characterise the non-metallic inclusion population in FV520B. The Philips XL40 Scanning Electron Microscope and Energy Dispersive X-Ray (EDX) Analyser in back-scattered electron mode was used to examine six representative longitudinal microsections taken from different regions of the steel plate. Simply, the type, morphology and the size range of the more commonly found inclusions were noted. The most frequently encountered inclusion was manganese sulphide (MnS) which was found as a stringer-type particle elongated in the direction of hot rolling. During the hot rolling process, the manganese sulphide particles are likely to be ductile and therefore highly deformable. Microexamination highlighted that this particular type was, in general, coherent with the steel matrix.

Inclusions with a globular morphology of the Ca-Si-S rich type which were coherent with the steel matrix were also observed. The characteristics of a representative selection of the inclusions observed are presented in Table 4.4. The minuteness of their size is emphasised. Other inclusions encountered were angular in morphology and were oxides of the SiO_2 and Al_2O_3 type. Oxide inclusions would not be ductile at the hot rolling temperature which explained why they appeared less coherent with the

steel matrix when compared to the sulphide inclusions. This was confirmed during microexamination as some of these particles appeared cracked. Some of the inclusions were observed not as individual, discrete particles, but in complex or agglomerated forms. Examples of some of these agglomerated particles are Al_2O_3 -MnS and MnS-CaS- Al_2O_3 and NbC-MnS types.

Figures 4.6 to 4.11 are representative scanning electron micrographs of the inclusions detected in FV520B. Their morphology and size are clearly shown and the accompanying EDX spectra highlights their chemical composition. It should be noted that the iron, chromium, nickel, molybdenum and copper detected by EDX analysis would originate from the steel matrix.

Figure Number	Type	Morphology	Longest Dimension (μm)	Shortest Dimension (μm)
Figure 4.6a and 4.6b Figure 4.11	SiO ₂	angular	4 4	4 1
Figure 4.7a, Figure 4.7b	CaS-Mn-O complex	globular	5	5
Figure 4.8a, Figure 4.8b	SiO ₂ -Al ₂ O ₃ complex	angular	6	5
Figure 4.9a, Figure 4.9b	Al ₂ O ₃ -MnS complex	stringer	62	8
Figure 4.10a, Figure 4.10b	MnS-NbC complex	stringer	16	4

Table 4.4 Summary of the Type, Morphology and Size Range of Typical Non-metallic Inclusions found in Remelt Grade of FV520B.

Figures 4.6a and 4.6b; 4.7a, 4.7b; 4.8a and 4.8b; 4.9a and 4.9b; 4.10a and 4.10b and 4.11 show Scanning Electron Micrographs of these Inclusions.

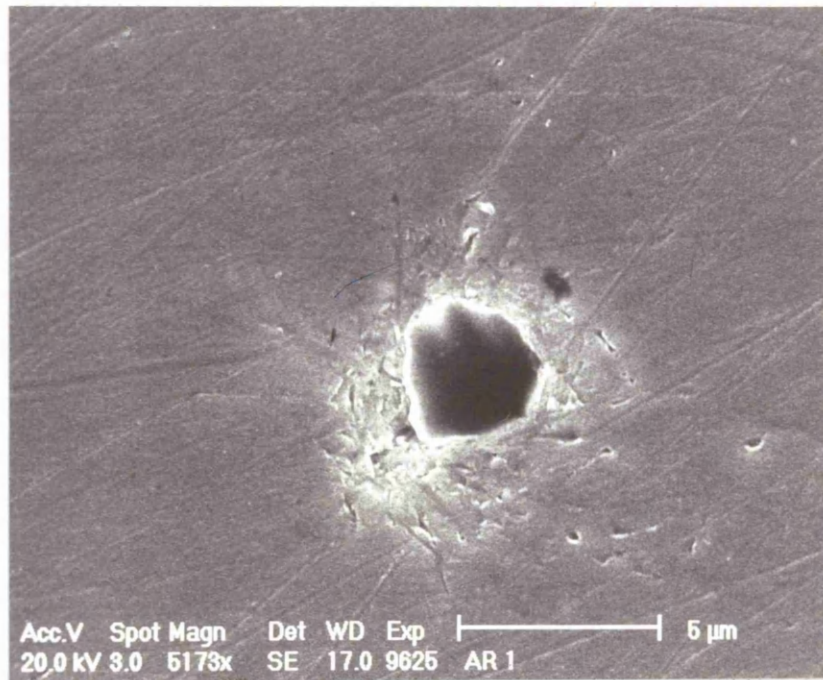


Figure 4.6a Scanning Electron Micrograph of a Representative Silica Inclusion as viewed in Secondary Electron Imaging Mode. Unetched Condition.

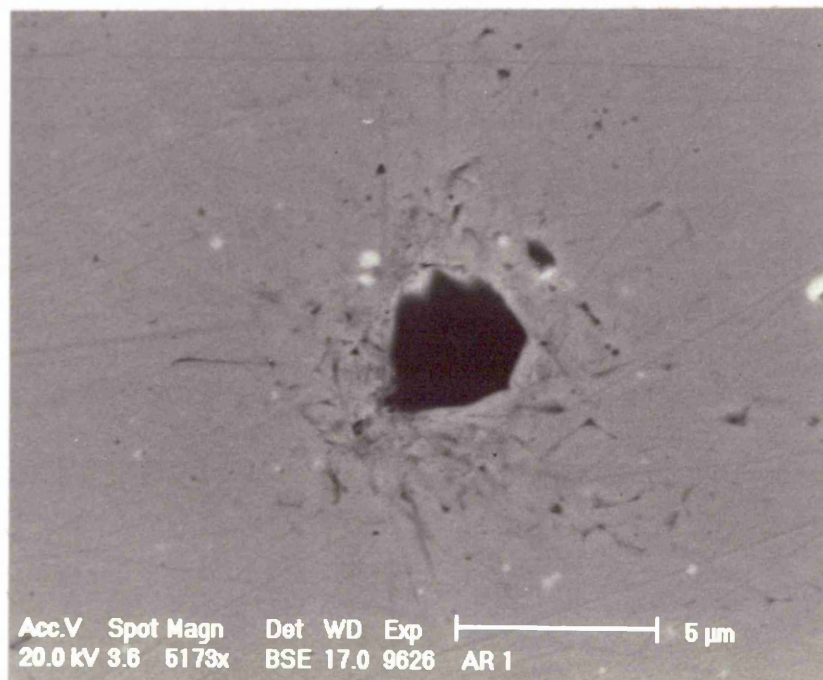


Figure 4.6b Scanning Electron Micrograph of the Silica Inclusion in Figure 4.6a as viewed in Backscattered Electron Imaging Mode. Unetched Condition.

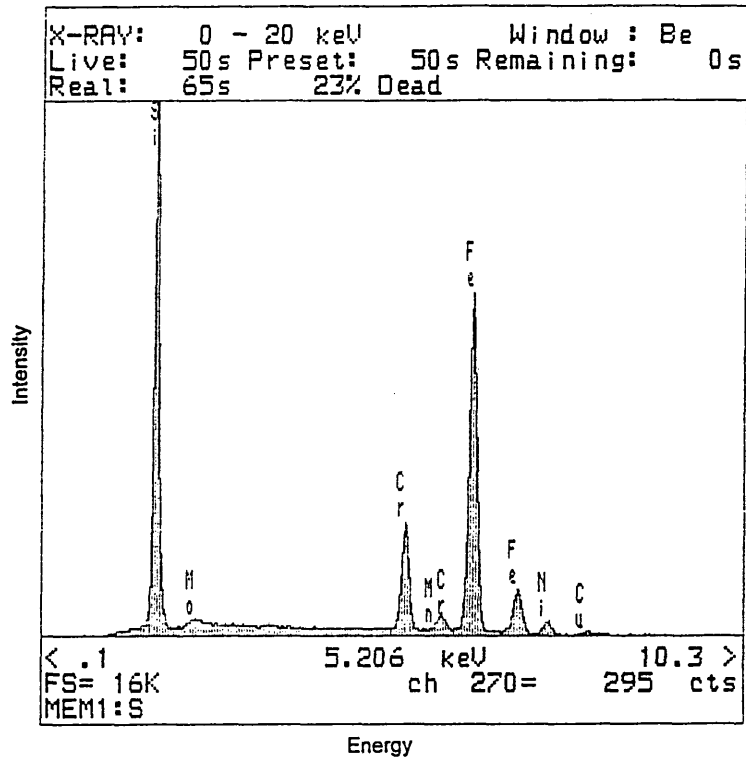


Figure 4.6c EDX Spectrum of the Inclusion in Figures 4.6a and b Highlighting the Strong Presence of Silicon.



Figure 4.7a Scanning Electron Micrograph of a Calcium Sulphide Inclusion, as viewed in Secondary Electron Imaging Mode. Unetched Condition.



Figure 4.7b Scanning Electron Micrograph of the Calcium Sulphide Inclusion in Figure 4.7a, as viewed in Backscattered Electron Imaging Mode. Unetched Condition.

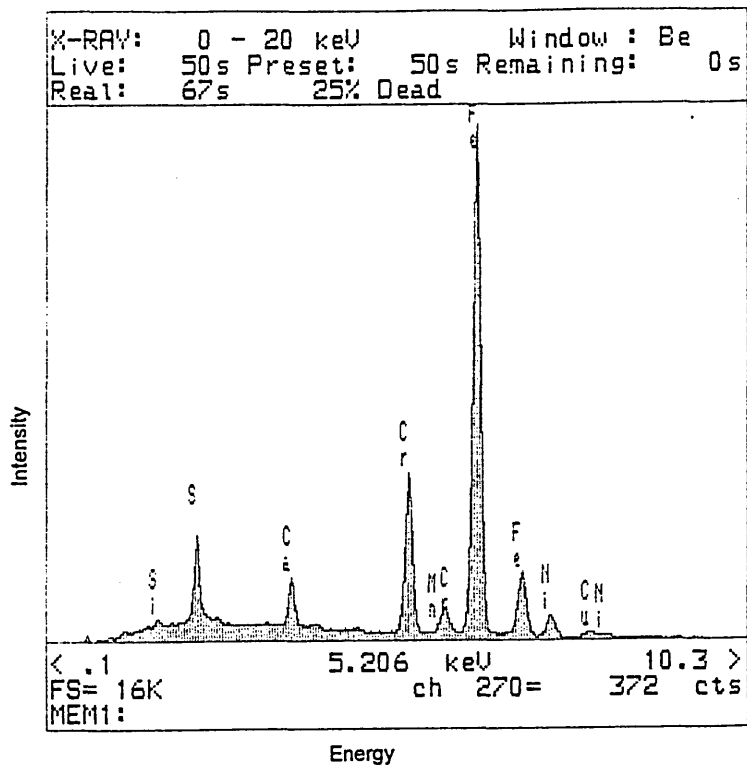


Figure 4.7c EDX Spectrum of the Inclusion in Figures 4.7a and b Highlighting the Presence of Calcium and Sulphur at the Centre of the Particle.

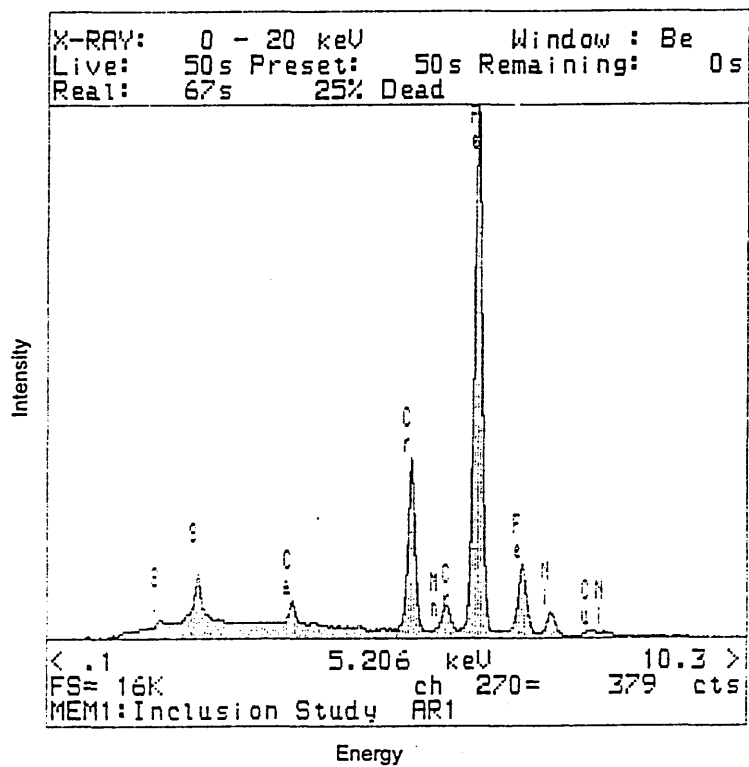


Figure 4.7d EDX Spectrum of the Inclusion in Figures 4.7a and b Highlighting the Presence of Calcium and Sulphur at the Edge of the Particle.

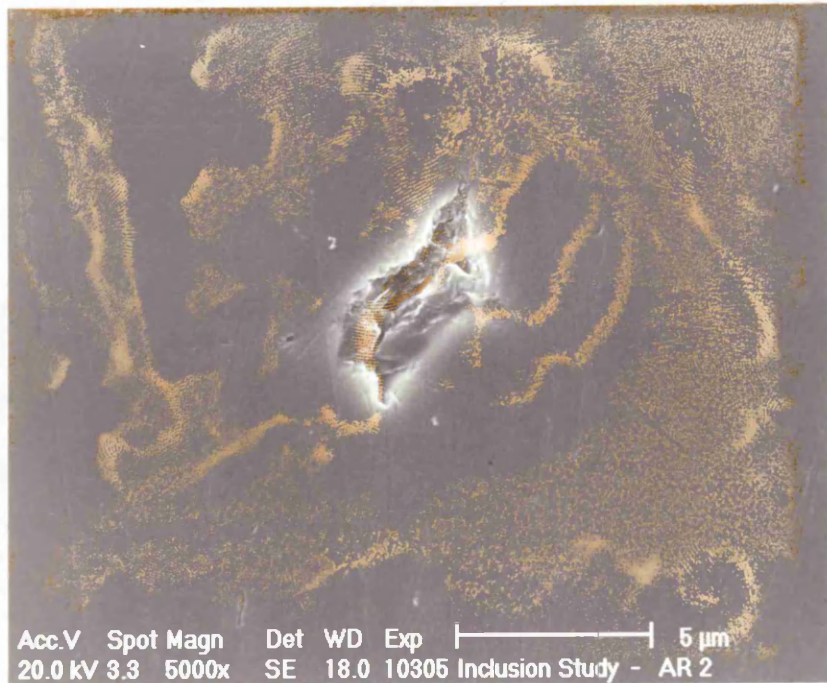


Figure 4.8a Scanning Electron Micrograph of a Silica-Alumina Inclusion, as viewed in Secondary Electron Imaging Mode. Unetched Condition.

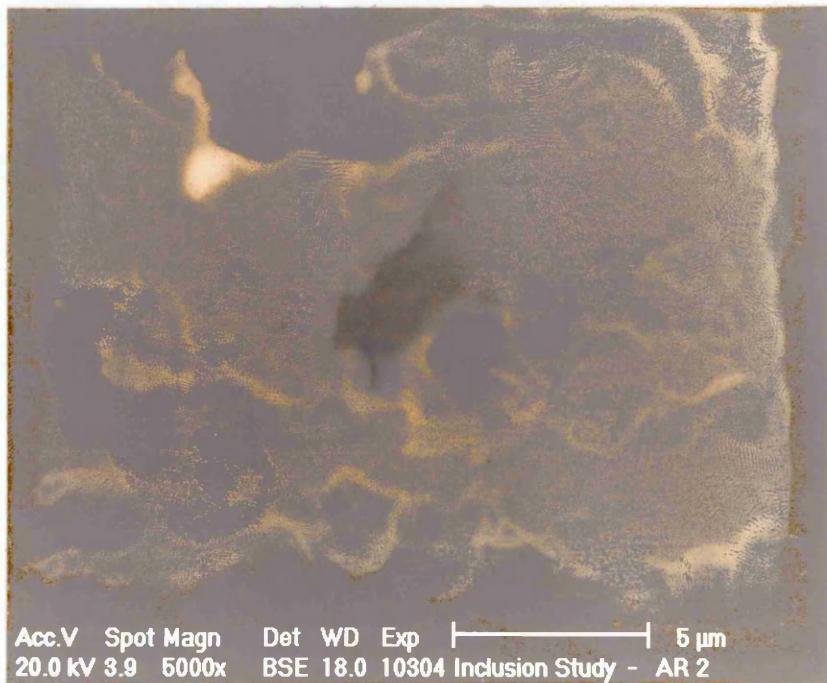


Figure 4.8b Scanning Electron Micrograph of the Silica-Alumina Inclusion in Figure 4.8a, as viewed in Backscattered Electron Mode. Unetched Condition.

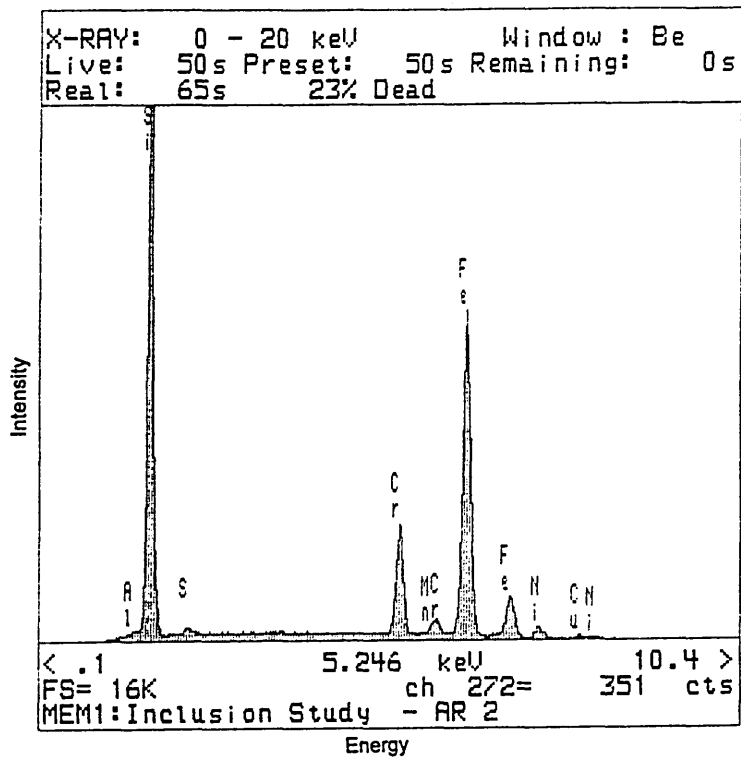


Figure 4.8c EDX Spectrum of the Inclusion in Figures 4.8a and b Highlighting the Presence of Silicon and Traces of Aluminium.

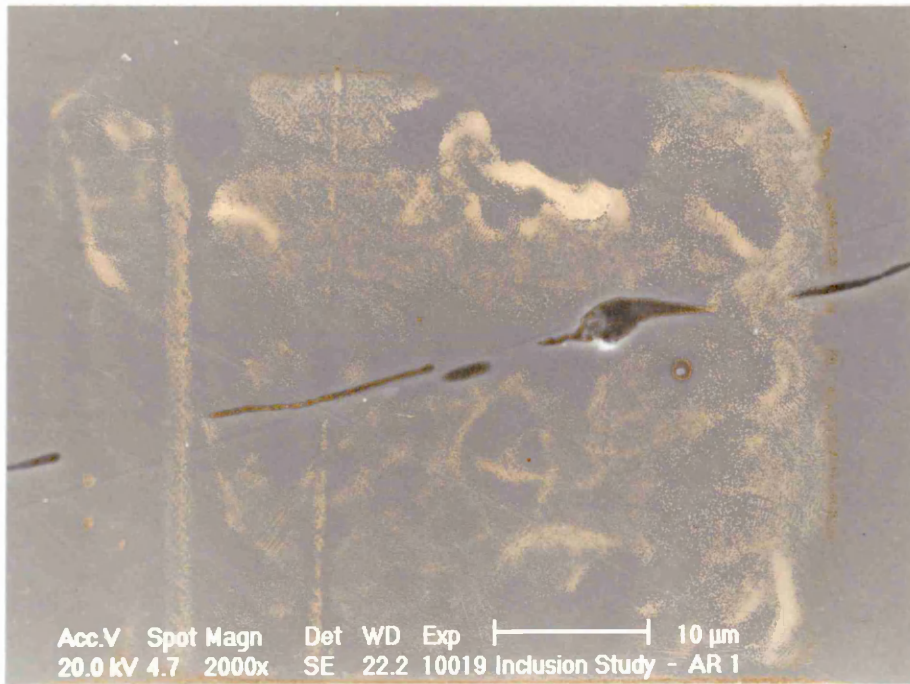


Figure 4.9a Scanning Electron Micrograph of a Manganese Sulphide-Calcium Sulphide-Alumina Inclusion, as viewed in Secondary Electron Imaging Mode. Unetched Condition.



Figure 4.9b Scanning Electron Micrograph of the Manganese Sulphide-Calcium Sulphide-Alumina Inclusion in Figure 4.9a, as viewed in Backscattered Electron Imaging Mode. Unetched Condition.

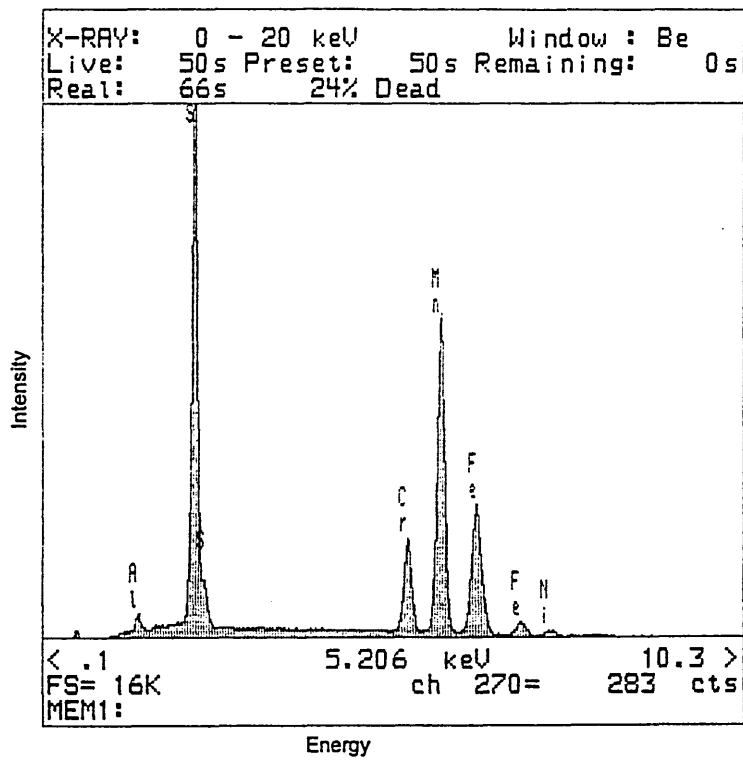


Figure 4.9c EDX Spectrum of the Inclusion in Figures 4.9a and b Highlighting the Presence of Manganese, Sulphur and Traces of Aluminium.

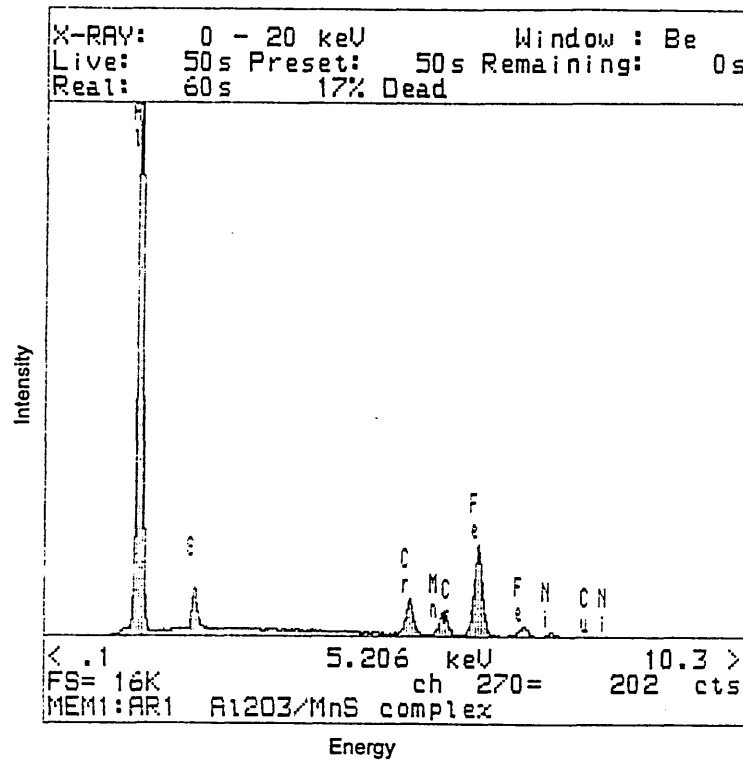


Figure 4.9d EDX Spectrum of the Inclusion in Figures 4.9a and b Highlighting the Strong Presence of Aluminium and Traces of Sulphur.

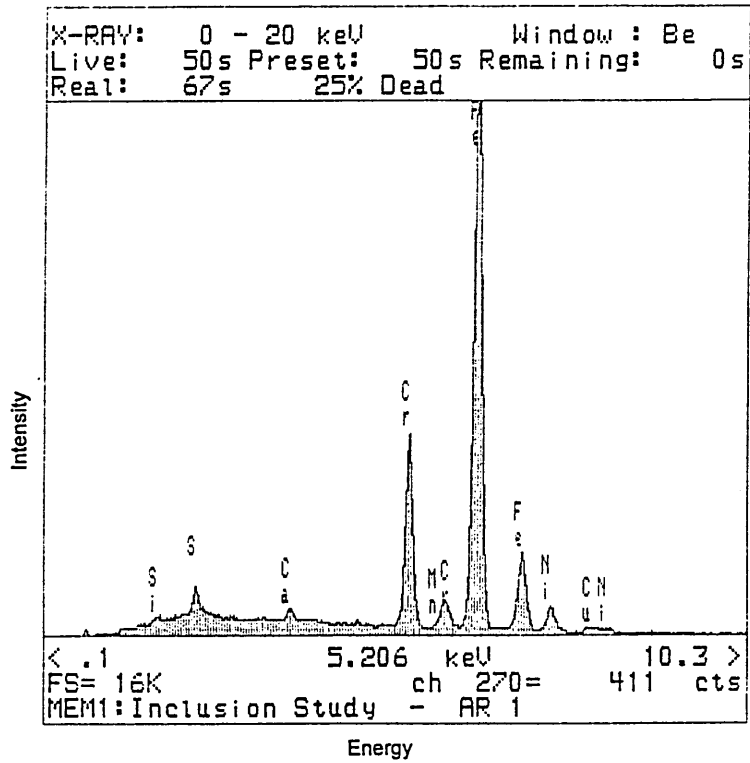


Figure 4.9e EDX Spectrum of the Inclusion in Figures 4.9a and b Highlighting the Presence of Calcium and Sulphur.

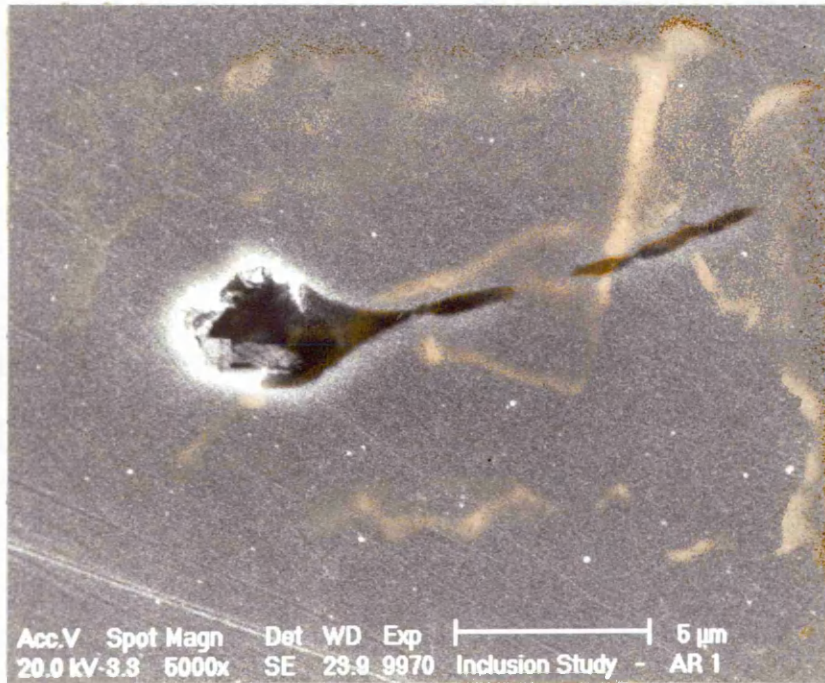


Figure 4.10a Scanning Electron Micrograph of a Manganese Sulphide-Niobium Carbide Inclusion, as viewed in the Secondary Electron Imaging Mode. Unetched Condition.

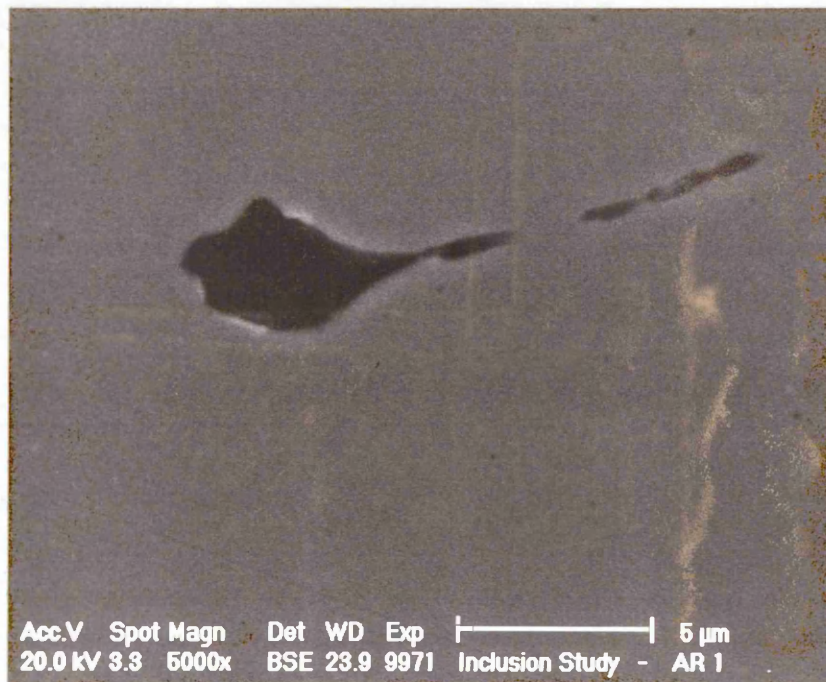


Figure 4.10b Scanning Electron Micrograph of the Manganese Sulphide-Niobium Carbide Inclusion in Figure 4.10a, as viewed in the Backscattered Electron Imaging Mode. Unetched Condition.



Figure 4.11 Scanning Electron Micrograph of an Oxide Inclusion. Unetched Condition.

4.2.10 The Modified Schaeffler Diagram

Figure 2.2 [119] showed the phases martensite (M), austenite (A) and delta ferrite (δ F) present in the steel; according to the composition of FV520B and its effect on the chromium and nickel equivalents. The chromium and nickel equivalents for FV520B were evaluated using equations (4.1) and (4.2).

$$\text{Chromium Equivalent} = \%Cr + (2x\%Si) + (1.5\%xMo) + (5x\%V) + (5.5x\%Al) + (17x\%Nb) + (1.5\%Ti) + (0.7x\%W) \quad (4.1)$$

$$\text{Nickel Equivalent} = \%Ni + 30(\%C + \%N) + (0.5x\%Mn) + (0.7x\%Co) + (0.3\%Cu) \quad (4.2)$$

The chromium and nickel equivalents for FV520B are:

Chromium Equivalent	17.04
Nickel Equivalent	7.74

These equivalents would indicate that martensite and austenite would form on austenitising and quenching FV520B, as shown in Figure 2.2.

4.3 Scanning Electron Microscopy (SEM)

4.3.1 Corrosion Fatigue Initiation Sites

The SEM and EDX analysis was used to examine and identify the microstructural features associated with the fatigue crack initiation sites of the corrosion fatigue specimens. The results are presented in Tables 4.5a-4.5c.

Sample	Fatigue Crack Initiation Sites	No. Fatigue Crack Initiation Sites	Bright Surface Finish	Stress Amplitude (MNm ⁻²)
CF FH 8	Particle	1	yes	550
CF FH 9	Silica inclusion	1	yes	570
CF FH 3	Unknown	4	yes	587
CF FH 6	Calcium rich inclusion	1	yes	600
CF FH 5	Corrosion pit	1	yes	625
CF FH 4	Corrosion pit	1	yes	650
CF FH 10	Corrosion pit	1	yes	700

Table 4.5a Initiation Details for the Corrosion Fatigue Samples in the Peak Hardened Condition.

Sample	Fatigue Crack Initiation Sites	No. Fatigue Crack Initiation Sites	Bright Surface Finish	Stress Amplitude (MNm ⁻²)
CF STD 18	Slip band cracking	2	yes	517
CF STD 21	Slip band cracking	1	yes	520
CF STD 20	Corrosion pit and slip band cracking	2	yes	540
CF STD 15	Silica inclusion	1	yes	560
CF STD 12	Corrosion pit and slip band cracking	2	yes	580
CF STD 17	Alumina inclusion with 2 adjacent corrosion pits	1	yes	600
CF STD 13	Corrosion pit and slip band cracking	4	yes	620
CF STD 14	Slip band cracking	4	yes	640

Table 4.5b Initiation Details for the Corrosion Fatigue Samples in the Standard Overaged Condition.

Sample	Fatigue Crack Initiation Sites	No. Fatigue Crack Initiation Sites	Bright Surface Finish	Stress Amplitude (MNm ⁻²)
CF S 20	Unknown	Unknown	yes	471
CF S 13	Slip band cracking	3	yes	475
CF S 18	Copper particle located in corrosion pit	1	yes	480
CF S 11	Corrosion pit and slip band cracking	2	yes	500
CF S 14	Corrosion pit, niobium rich particle and slip band cracking	20	yes	550
CF S 15	Slip band cracking	4	yes	575
CF S 12	Slip band cracking	20	yes	600

Table 4.5c Initiation Details for the Corrosion Fatigue Samples in the Softened Overaged Condition.

4.4 Mechanical Testing Results

4.4.1 Vickers Hardness Measurements

The results from the hardness measurements are presented in Table 4.6.

Table 4.6 Vickers Hardness Results (Hv₃₀).

Heat Treated Condition	Hv ₃₀
Peak Hardened	420 ± 2.0
Standard Overaged	340 ± 2.0
Softened Overaged	297 ± 1.7

4.4.2 Tensile Testing

The results from tensile testing are presented in Table 4.7. The values in brackets indicate the minimum specification requirements for FV520B.

Table 4.7 Mechanical Testing Results of FV520B.

Heat Treated Condition	UTS (MNm ⁻²)	0.2 Proof Stress (MNm ⁻²)	Elongation 5.65√Area (%)	Reduction in Area (%)
Peak Hardened	1313-1325 (1170-1310)	1127-1156 (1030)	3.8	52-63
Standard Overaged	975-1061 (925-1080)	957 (800)	4.6-5.3	57-74
Softened Overaged	955-960 (850-1000)	827.4 (540)	5.3-6.1	66-70

4.4.3 Endurance Testing

The results from the constant load amplitude endurance tests are presented as stress amplitude versus the number of load cycles to failure (S-N) curves. The S-N curve representing the air results is shown in Figure 5.16, whilst Figure 5.17 shows the endurance data from testing in the chloride environment. The raw data from the endurance testing is presented in Tables D5 - D11, Appendix I.

CHAPTER 5

DISCUSSION

5.1 Introduction

The aim of this chapter is to discuss the influence of the microstructure on the tensile and fatigue behaviour of FV520B, a high strength stainless steel. The material microstructure of FV520B and its effect on the 0.2% proof stress, fatigue strength and fatigue lifetimes have been considered. Empirical models which predict the 0.2% proof stress and fatigue lifetimes have been developed. These models account for the effects of the overaging process and the presence of a weaker microstructural phase, namely reverted austenite. The fatigue crack nucleation mechanisms and the microstructural features which dominate them in both the air and corrosive environment have also been discussed. In addition to this, the microstructural phases acting as potential barriers during the early stages of fatigue crack propagation have also been considered. The possibility of stress corrosion cracking in the chloride environment has also been mentioned.

For the purposes of this discussion, the tensile and fatigue properties of FV520B will be considered in separate sections. The tensile strength is a measure of the bulk property of the material which is derived from plastically deforming all the grains in the material. In contrast, metal fatigue occurs due to highly localised plastic deformation and is dependent on the slip characteristics within a few grains predominantly at the free surface. Since it occurs within a few grains which are preferentially orientated to the applied stress micro-yielding occurs in fatigue well below the macroscopic tensile yield stress observed under monotonic loading. It follows that, the fatigue resistance of a material is strongly controlled by the physical and mechanical properties of the grains at the free surface.

5.2 Influence of the Microstructure on the Flow Stress

5.2.1 Prediction of the Flow Stress of FV520B

It has been recognised for a considerable time that the tensile strength of a material is dependent on its microstructure. And according to Pickering [37], the material microstructure is reliant upon the elemental composition, mechanical processing route (i.e. cold or hot deformation) and the heat treatment schedule employed.

Section 2.2 highlighted a number of empirical formulae which quantified the contribution of the individual strengthening mechanisms in various materials, whilst subjected to tensile loading. For low alloy steels, the microstructural features known to affect the flow stress were summarised as the dislocation sub-structure; carbon in interstitial solid solution; the alloy carbide dispersion and the grain size [113]. For a highly alloyed steel, such as FV520B, the strengthening mechanisms known to increase the flow stress are the dislocation sub-structure; solid solution strengthening due to interstitial and substitutional solute atoms; precipitation hardening and grain boundary strengthening. It is known that an interdependence exists between some of the above parameters, for example, the dislocation density is understood to vary with the carbon content. However, in accordance with previous studies [24] [34], the effect of individual microstructural parameters in the relationship developed for FV520B will be expressed as separate entities.

An attempt has been made to express the flow stress of the three microstructures of FV520B, by expanding an existing empirical formula developed for a 0.3%C and a 0.3%C-1.5%Cu steel. The expression for the flow stress for the 0.3%C and the 0.3%C-1.5%Cu steel was presented in Section 2.2.4 and are given in equations (2.4) and (2.7).

$$\sigma = \alpha_1 G b \rho^{\frac{1}{2}} + \alpha_2 G b \frac{1}{\lambda_{\text{carbide}}} + \alpha_4 C^{\frac{1}{3}} \quad (2.4)$$

and

$$\sigma = \alpha_1 G b \rho^{\frac{1}{2}} + \alpha_2 G b \frac{1}{\lambda_{\text{carbide}}} + \alpha_4 C^{\frac{1}{3}} + \alpha_3 G b \frac{1}{\lambda_{\text{copper}}} \quad (2.7)$$

The values of the constants G , b , α_1 , α_2 , α_3 , and α_4 are given in Table 2.4, Section 2.2.4. The values of the terms representing the interparticle spacing for carbide/copper-rich precipitates λ ; the dislocation density ρ and carbon in interstitial solid solution C have been estimated for FV520B from the literature available [24]. These values, which vary in accordance to the heat treatment schedule, are presented in Table 5.1.

Table 5.1 Values of the Microstructural Features for FV520B Estimated from the Data Available from the Low Alloy Steel, after Cox.

Heat Treated Condition	Dislocation Density (ρ) (10^9 lines/cm)	Interstitial Carbon (C) (wt%)	Carbide Spacing (λ_{carbide}) (10^{-7} m)	Copper Precipitate Spacing (λ_{copper}) (10^{-8} m)
Peak Hardened	1.65	0.02	1.76	7.25
Standard Overaged	2.70	0.02	1.52	7.75
Softened Overaged	2.67	0.02	4.33	8.10

The experimental and predicted results for the flow stress of the two steels, namely 0.3%C and 0.3%C-1.5%Cu steels are presented in Figure 5.1. Cox found reasonable agreement in his predictions, as shown by the relative positions of the data points and the trend-line in Figure 5.1. The trend-line represents the ideally predicted results. Those data points located directly below this ideal trend-line indicate that Cox's empirical formulae has overestimated the actual proof strength. This overestimation is apparent for both the 0.3%C and the 0.3%C-1.5%Cu steel at proof strength levels in excess of 800 MNm^{-2} . The consequence of implementing this particular empirical formula and overestimating the strength levels would lead to the dangerous scenario of using steels whose strength levels would not meet the anticipated mechanical property requirements. At proof stresses below 400 MNm^{-2} , the empirical formulae

(equations 2.4 and 2.7) gave underestimation's of the actual proof strength level which potentially could lead to the under utilisation of the tensile properties.

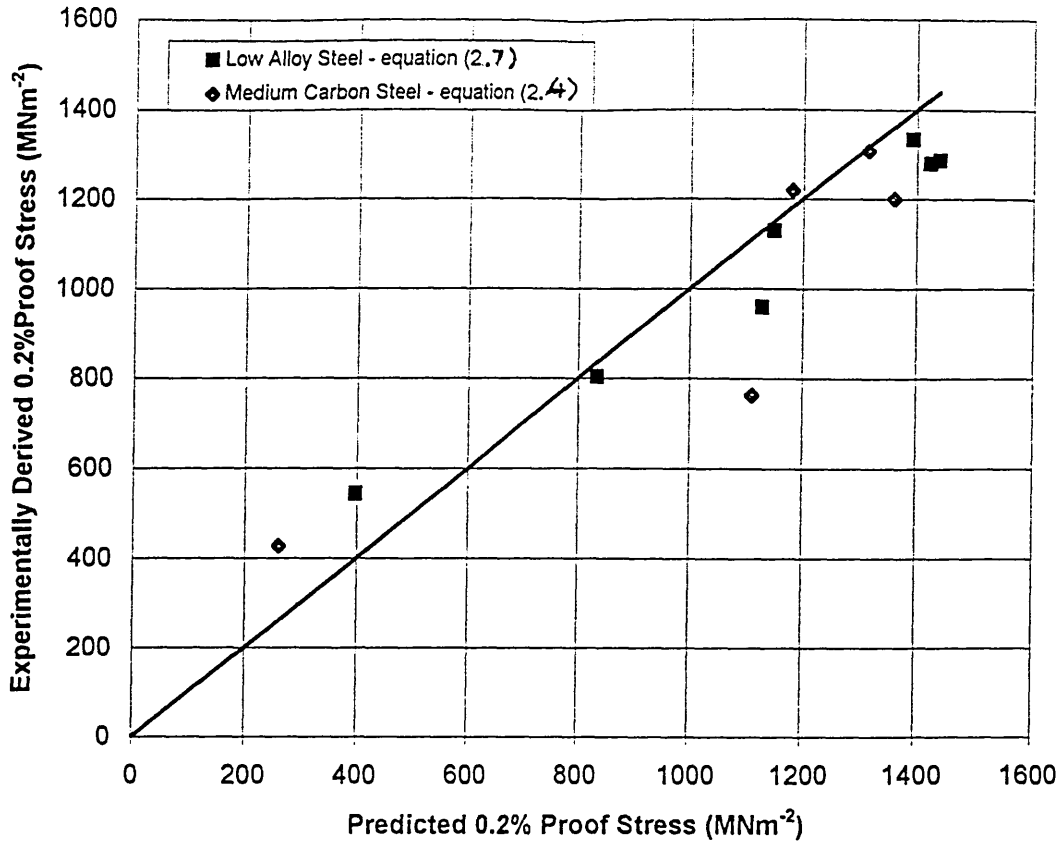


Figure 5.1 Experimental and Predicted Values of the 0.2% Proof Stress for a Low Alloy Steel, after Cox.

Equation (2.7) was used to predict the 0.2% proof strength for the three microstructures of FV520B. The purpose behind this was two-fold. Firstly, it would allow the proof stress to be predicted by inputting known microstructural parameters into the empirical formula, without performing time consuming and costly experiments. Secondly, the empirical formula would give scope for allowing the microstructure to be altered or designed to meet a specific 0.2% proof strength. The values for the microstructural features for FV520B were substituted into equation (2.7). These values are presented in Table 5.1.

Using equation (2.7), the predictions of the 0.2% proof stress for the peak hardened, standard and softened overaged conditions were 1127, 957 and 827 MNm⁻² respectively. These results are presented in Figure 5.2.

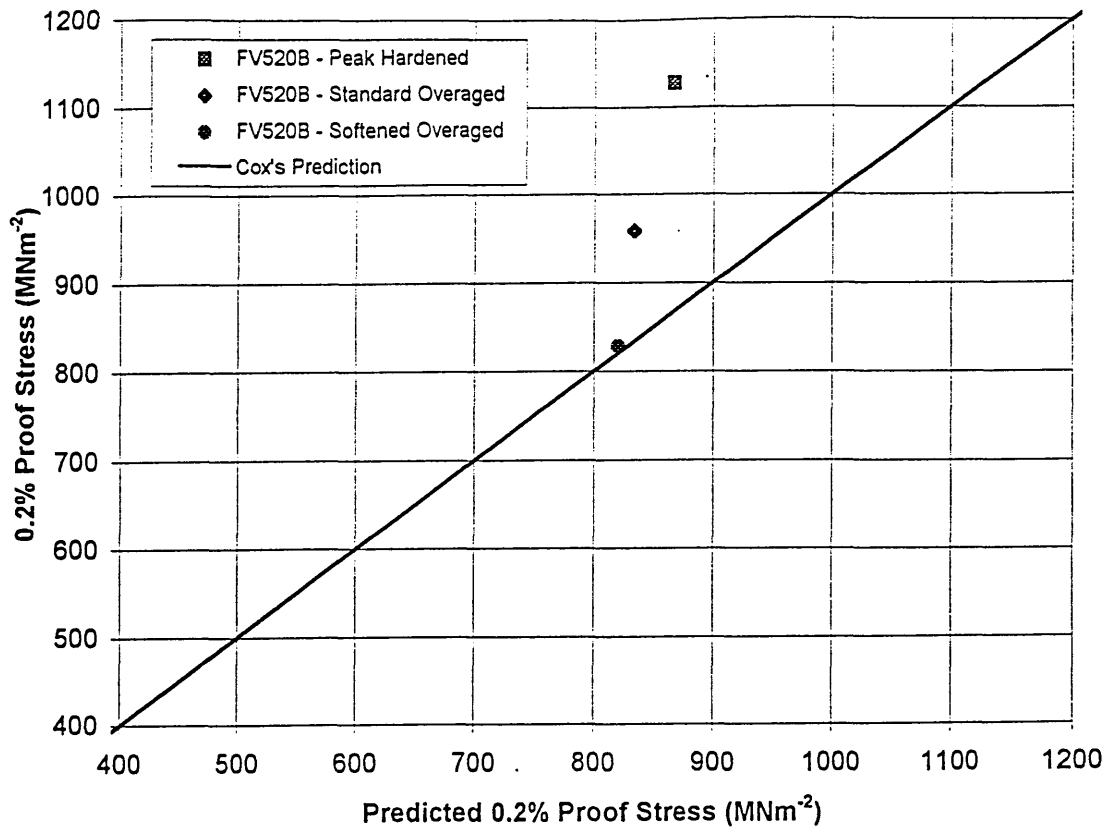


Figure 5.2 Comparisons Between Experimental and Predicted Values of the 0.2% Proof Stresses for FV520B.

In contrast to Cox's predictions, the predicted data for the peak hardened and the standard overaged material underestimated the proof stress. The factors by which they were underestimated was found to be more significant for the peak hardened than for the standard overaged material. The results also show that the predicted proof stress was in agreement with the experimental result for the softened overaged material.

The deviation from the ideally predicted values can be attributed to two factors. Firstly, it is acknowledged, that the contribution from the alloy carbides may have slightly overestimated the 0.2% proof stress, due to an error in the data used. (An

exact value for the carbide spacing was not available for the alloy carbides in FV520B.) Secondly, this overestimation does not conceal the fact that in addition to the effect of FV520B's enhanced alloying, additional strengthening mechanisms are operative. The second factor highlights a major flaw in the use of Cox's empirical formula, equation (2.7), for more highly alloyed steels such as FV520B; since all the strengthening mechanisms cannot be accounted for. It is thought that these additional strengthening factors must be considered and incorporated into a more complex expression to describe the 0.2% proof stress of FV520B.

FV520B contains considerably greater quantities of the alloying elements: chromium (Cr), nickel (Ni), molybdenum (Mo) and niobium (Nb). It is believed that these elements will increase the tensile properties of the steel with the implementation of the correct heat treatment schedule. Substitutional solid solution hardening by chromium, nickel and molybdenum solute atoms is the likely strengthening mechanism. Solid solution hardening plays an important role in increasing the flow stress of a material by increasing the resistance to the movement of dislocations through introducing localised strain fields within the lattice. The increase in strength due to the aforementioned elements in substitutional solid solution can be accounted for by the following expression, given by Fleischer:

$$\Delta\sigma = \alpha GbC^{\frac{1}{2}} \quad (5.1)$$

where $\Delta\sigma$ is the increase in flow strength whilst α and C are a constant and the concentration of the solute atoms respectively.

Moreover, since chromium, nickel and molybdenum are present in appreciable amounts, these elements will precipitate as alloy carbides which will serve to increase the 0.2% proof stress. The additional hardening caused by the presence of alloy carbides are accounted for in equations (2.4) and (2.7).

The various forms of alloy carbides precipitated in a hardened and tempered 12% Cr martensitic stainless steel tempered at different temperatures are presented in Table 5.2.

Table 5.2 The Alloy Carbides in a Hardened and Tempered 12% Cr Stainless Steel.

Heat Treated Condition	Carbide Type
Peak Hardened	M_2X (Mo stabilised)
Standard Overaged	M_7C_3 , $M_{23}C_6$
Softened Overaged	M_7C_3 , $M_{23}C_6$

where M and X represents chromium and carbon/nitrogen respectively.

The fine grain structure will also provide additional strength to FV520B. Niobium has been added to FV520B for the sole purpose of refining the prior austenite grain size. (It is likely that in refining the grain size, the flow stress would increase in accordance with the Hall-Petch relationship [32] [33], equation (2.1)). The manner in which niobium maintains a fine grain structure is by pinning the boundaries and hence impeding grain growth at the homogenisation temperature. In addition to this, niobium would also act as a carbon scavenger and consume any free carbon thus forming niobium carbide precipitates. The elimination of free carbon would prevent the formation of a precipitate which could potentially be detrimental to the mechanical properties of FV520B; a precipitate otherwise known as $M_{23}C_6$ i.e. $Cr_{23}C_6$. The presence of $Cr_{23}C_6$ precipitates at the prior austenite grain boundaries would render FV520B susceptible to stress corrosion cracking in a chloride environment.

It is thought that the niobium carbides in FV520B would be present as fine, submicroscopic precipitates which would be unresolvable in the Scanning Electron Microscope (SEM). However, some niobium carbides were resolved simply because of their coarse nature, as shown in Figures 4.10a and 4.10b. In addition to this, these coarse particles were not found located at the prior austenite grain boundaries as would be expected. The reasoning for such coarse niobium particles could be due to the temperature at which niobium carbide forms, in contrast with the treatment used for taking the alloying elements in solid solution. Niobium carbides generally form in the steel melt, i.e. at temperatures in excess of 1600°C. However, during the course of this study, the homogenising temperature used for FV520B was 1050°C. It therefore seems likely that the homogenisation temperature may have been too low to take the niobium into solid solution, providing the opportunity for niobium to precipitate

as fine grain boundary carbides. Although such coarse niobium carbides were observed, it is thought that the fine nature of the prior austenite grains can still be attributed to the presence and pinning effect of the fine, grain boundary niobium carbide precipitates.

The additions of niobium for grain refinement leads to further discussion on the subject of grain boundary strengthening. Cox, in addition to others e.g. [113], did not recognise (prior austenite) grain boundary strengthening as a viable strengthening mechanism. It is believed however, that for a martensitic structure, the prior austenite grain boundaries will not have a direct affect on the strength, but they are thought to influence the martensite packet (grain) size. Reducing the prior austenite grain size will probably restrict the size of the martensite lath packets; which according to the Hall-Petch equation, should result in significant improvements in the flow stress. The individual laths within the packets are also known to provide obstacles to dislocation movement and will have an effect on increasing the flow stress.

The increase in yield stress due to grain boundary strengthening, can be accounted for using the Hall-Petch relationship [32] [33]:

$$\Delta\sigma = k_y d^{-\frac{1}{2}} \quad (5.2)$$

where k_y is the dislocation locking factor and d is the lath packet size.

It is considered that the aforementioned strengthening mechanisms have adequately accounted for the increase in 0.2% proof stress of FV520B relative to the steels used by Cox. However, a reduction in the 0.2% proof stress between the peak hardened and the softened overaged microstructures was clearly evident which cannot be accounted for by the strengthening mechanisms considered so far. Since the reduction in strength due to the overaging of copper precipitates has already been accounted for, the other reason is probably due to the presence of reverted austenite. This was identified and quantified as a function of precipitation hardening temperature using the technique of X-Ray Diffraction (XRD). Reverted austenite is known to be of low strength relative to lath martensite. It follows that the greater the quantity of reverted austenite within the structure the greater the reduction in 0.2% proof stress.

The effect on the 0.2% proof stress as a function of the volume of reverted austenite for the three microstructures of FV520B is presented in Figure 5.3.

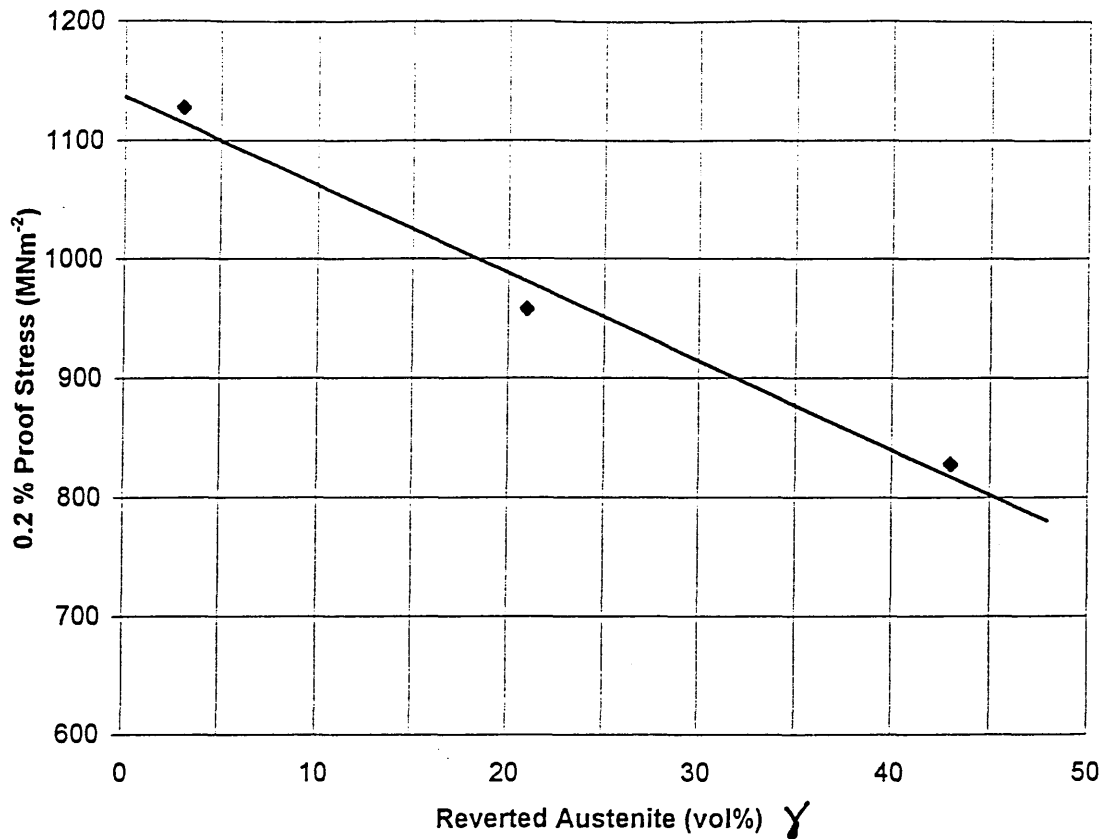


Figure 5.3 The Reduction in the 0.2% Proof Stresses of FV520B, as a Function of the Percentage Volume of Reverted Austenite.

From Figure 5.3, the effect of variable quantities of reverted austenite on the change in 0.2% proof stress can be expressed by the following term:

$$\Delta\sigma = (-) k\gamma \quad (5.3)$$

where k is considered to be a constant and γ represents the percentage volume of reverted austenite. The value of k has been evaluated as 7.5. The alloy carbide dispersion is also recognised as a possible factor which has reduced the 0.2% proof stress, although it has not been possible to quantify its contribution since the required data was not available.

The discussion so far has examined the individual strengthening mechanisms operating in this complex microstructure which has been greatly simplified. However, it has illustrated the role of the microstructure as a function of its elemental composition and heat treatment schedule on the 0.2% proof stress. The strengthening mechanisms which express the 0.2% proof stress of FV520B can therefore be summarised using the quantitative expression given in equation (5.4). The terms of the proposed model not evaluated could be derived, possibly from the literature and their values may be substituted into equation (5.4). These include the three terms for chromium, nickel, and molybdenum in substitutional solid solution and the contribution from the alloy carbide precipitates. Knowing these additional terms would allow the 0.2% proof stress for FV520B to be determined as a function of the overaging process and the presence of the weaker phase, i.e. reverted austenite.

$$\sigma = \alpha_1 G b \rho^{\frac{1}{2}} + \alpha_2 G b \frac{1}{\lambda_{\text{carbide}}} + \alpha_4 C^{\frac{1}{3}} + \alpha_3 G b \frac{1}{\lambda_{\text{copper}}} + [\alpha_5 G b C^{\frac{1}{2}}]_{\text{chromium}} + [\alpha_6 G b C^{\frac{1}{2}}]_{\text{molybdenum}} + [\alpha_7 G b C^{\frac{1}{2}}]_{\text{nickel}} + k_y d^{-\frac{1}{2}} - 7.5\gamma \quad (5.4)$$

5.2.2 Tensile Properties of FV520B

The mechanical properties of the peak hardened, standard and softened overaged materials are presented in Table 5.3. The compromise between the properties of tensile strength and ductility for the peak hardened and standard overaged conditions is evident.

Table 5.3 The Tensile Properties of FV520B.

Heat Treated Condition	UTS (MNm ⁻²)	0.2 Proof Stress (MNm ⁻²)	Elongation 5.65√Area (%)	Reduction in Area (%)
Peak Hardened	1313-1325 (1170-1310)	1127-1156 (1030)	3.8	52-63
Standard Overaged	975-1061 (925-1080)	957 (800)	4.6-5.3	57-74
Softened Overaged	955-960 (850-1000)	827.4 (540)	5.3-6.1	66-70

Examination of the fracture surfaces using a Scanning Electron Microscope (SEM) highlighted features typical of failure by ductile fracture. All fractures exhibited the classic “cup and cone” profile which indicated that fracture was caused by microvoid coalescence, followed by final fracture due to the shearing process. Additional features which suggested ductile fracture include gross plastic deformation i.e. a reduction in cross-section at the point of fracture, otherwise known as necking; 45° shear lips and a central region with a fibrous texture. Figures 5.4a and 5.4b show the tensile fractures from the peak hardened and standard overaged materials respectively. A comparison of Figures 5.4a and 5.4b show a notable difference in their respective reduction in the area.

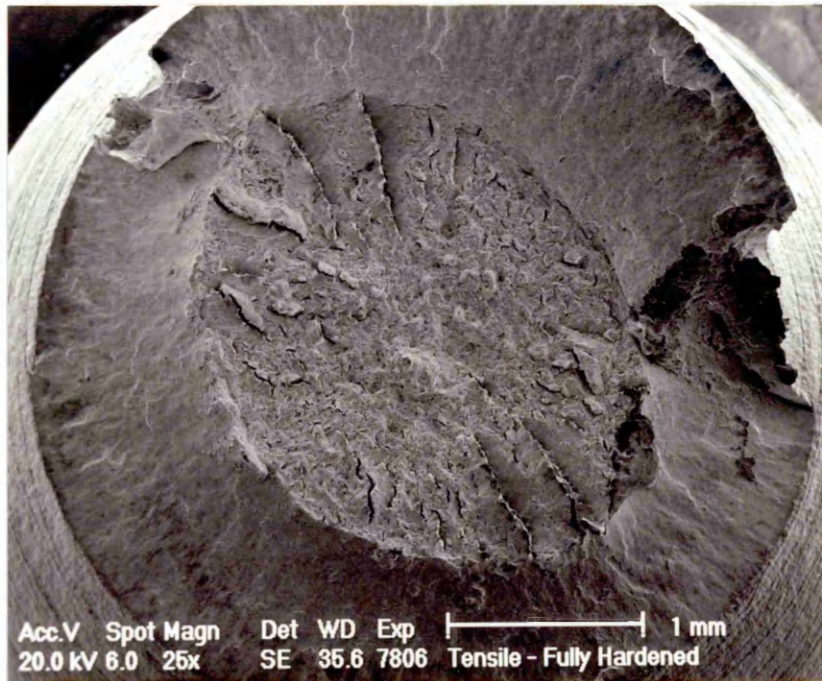


Figure 5.4a The Fractured Tensile Specimen from the Peak Hardened Material.

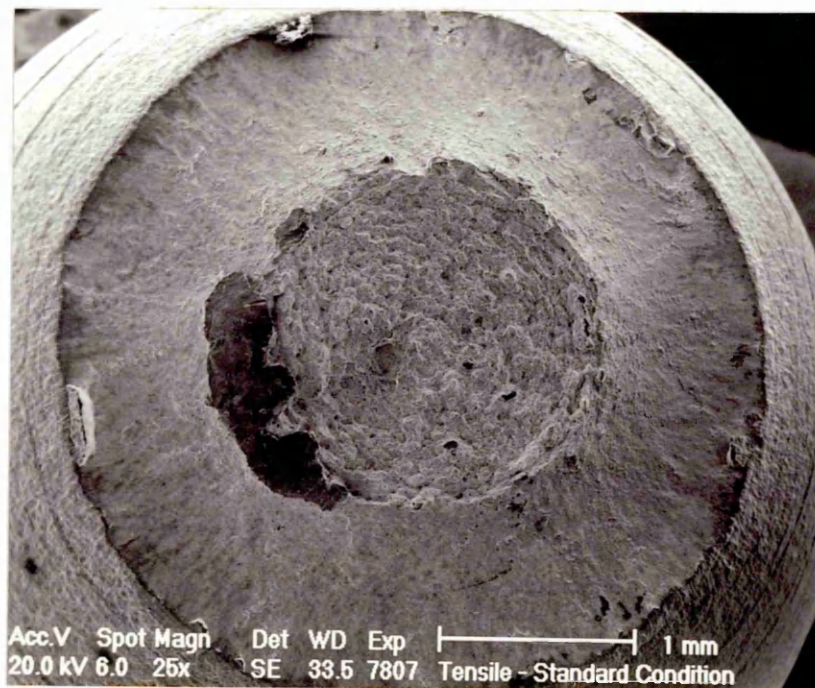


Figure 5.4b The Fractured Tensile Specimen from the Standard Overaged Material.

At a higher magnification, the finer fracture features associated with the failure mechanism were revealed. The fibrous region exhibited fine ductile dimples, as shown in Figure 5.4c for the peak hardened condition. These features are consistent with the initial stages of fracture by microvoid coalescence under a tensile load. In contrast, Figure 5.4d shows the elongated ductile dimpling on the 45° inclined surface of the standard overaged specimen, which form due to shearing.

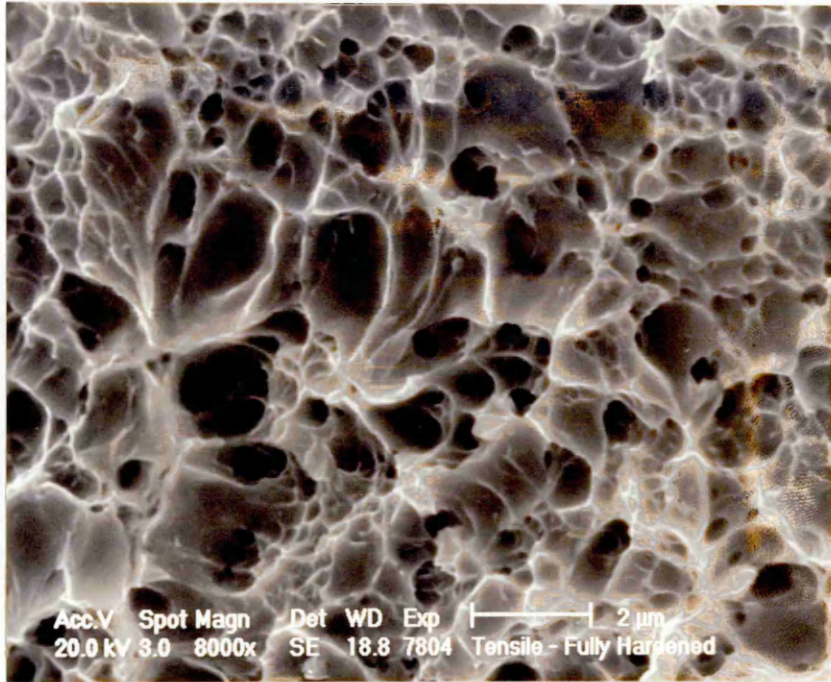


Figure 5.4c The Ductile Dimpling on the Fracture Surface of the Peak Hardened Specimen.

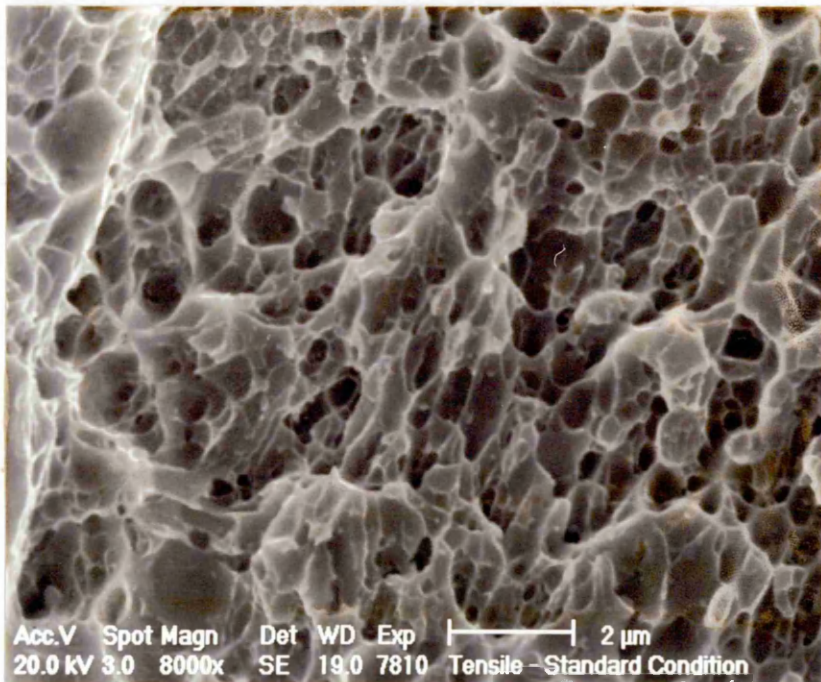


Figure 5.4d Elongated Ductile Dimpling on the Fracture Surface of the Standard Overaged Specimen.

5.3 Influence of Microstructure and Environment on Fatigue Crack Nucleation

The fatigue limit of FV520B in air was considered to be controlled by the nucleation of a stage I fatigue crack. In the presence of the corrosive chloride environment, either the formation of a stage I fatigue crack or a corrosion pit dominated the fracture process. The nucleation of a stage I fatigue crack or corrosion pit was found to be influenced by the material microstructure especially in the highest and lowest strength materials, i.e. peak hardened and softened overaged conditions respectively. For the standard overaged material which is heat treated to the intermediate strength level, fatigue cracks were found to nucleate by a combination of the mechanisms prevalent in peak hardened and softened overaged conditions.

5.3.1 Peak Hardened Material

The peak hardened material represents FV520B heat treated to its highest commercially available tensile strength level. In simple terms, the material, comprised a lath martensite microstructure with approximately 3% reverted austenite. The hardness was found to be 420H_v.

Fatigue crack nucleation of the peak hardened microstructure in both air and chloride environments was caused mainly by the formation of an individual stage I fatigue crack. The stage I fatigue crack subsequently propagated as a sub-critical stage II fatigue crack, eventually causing final fracture by ductile overload. Figure 5.5a highlights the fracture surface of a typical sample in the peak hardened condition. The markings which indicate the direction of crack propagation can be traced to a single point at the edge of the fracture surface, as indicated by the arrow. A closer view of this fatigue crack nucleation site is shown in Figure 5.5b. The evidence suggests that an individual stage I fatigue crack nucleated at the free surface of the sample and eventually propagated as a stage II tensile crack perpendicular to the applied stress axis.



Figure 5.5a The Fracture Surface of a Peak Hardened Specimen.
 [$\sigma_a=550\text{MNm}^{-2}$ in a 3.5% chloride (pH2), $R=-1$, $f=0.5\text{Hz}$ and $N_f=215,110$ cycles].

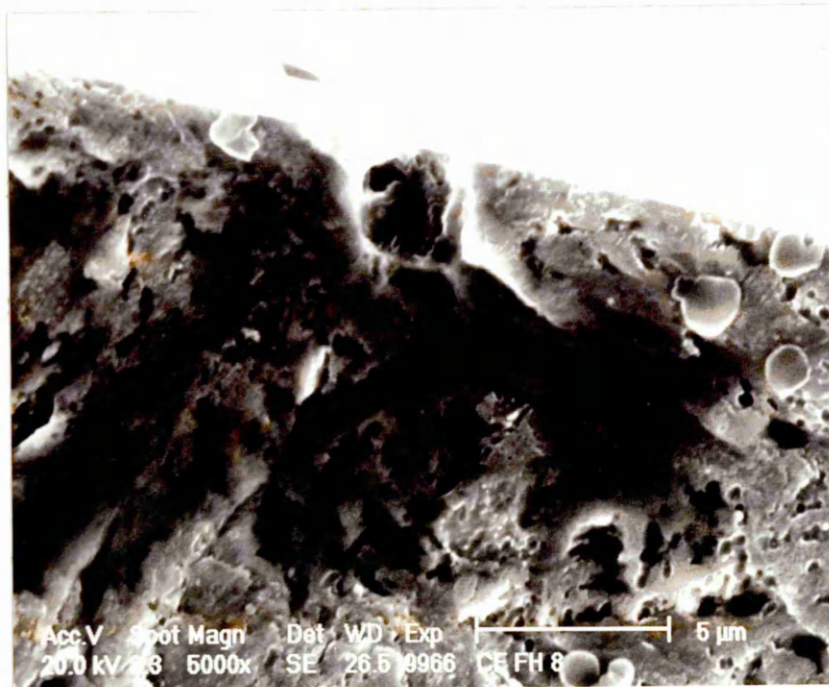


Figure 5.5b The Fatigue Crack Nucleation Site in the Peak Hardened Specimen.
 [$\sigma_a=550\text{MNm}^{-2}$ in a 3.5% chloride (pH2), $R=-1$, $f=0.5\text{Hz}$ and $N_f=215,110$ cycles].

The evidence of an individual stage I fatigue crack, as observed on the fracture surfaces, suggests that inclusions are likely to dominate the crack nucleation process for the peak hardened material in both the air and chloride environments. There is substantial evidence, as provided by the fractographic studies, which confirms that the inclusion population had a significant influence on the corrosion fatigue strength. However, although there is little direct evidence from the air results of this investigation, there is no evidence to suggest anything contrary to this theory. It follows that in both the air or the chloride environments, similar processes relating to the inclusion features will dictate fatigue crack nucleation. These features may include the inclusion type and hence physical properties; inclusion morphology and size; orientation with respect to the loading axis and location of the inclusion relative to the free surface. See Section 2.3.3.2.

It is thought that if the criteria for fatigue crack nucleation by inclusions were met, then the nucleation mechanism in air would probably be by slip band cracking at the interface between the inclusion and the steel matrix. The slip bands are likely to form as a result of the poor transmission of strain between a relatively elastic steel matrix and an inelastic (oxide) inclusion [65] [66]. For the case of oxide-type inclusions, the stresses at the interface are known to be higher than those for sulphide-type inclusions.

In the absence of a 'harmful' surface or sub-surface inclusion, fatigue crack nucleation in air may still occur by slip band cracking. Figure 5.6a shows a stage I fatigue crack in the peak hardened condition, as viewed from the specimen surface. This region is apparently devoid of an inclusion at the fatigue crack nucleation site. The direction of the 45° shear crack was probably dictated by the orientation of the martensite laths relative to the maximum shear plane. In the absence of any 'harmful' stress-raising inclusions, cyclic slip may originate in the relatively weaker, ductile reverted austenite located between the martensite laths. The literature suggests that in materials precipitation hardened at 450°C, lath-like reverted austenite is located between the martensite laths [27].

Figure 5.6b highlights the transition from the stage I shear crack to the stage II tensile crack for the failed specimen in Figure 5.6a. The transition point was approximately

20 μm from the specimen free surface. The length of the stage I crack is therefore slightly greater than mean linear intercept of a prior austenite grain (MLI = 14 μm).

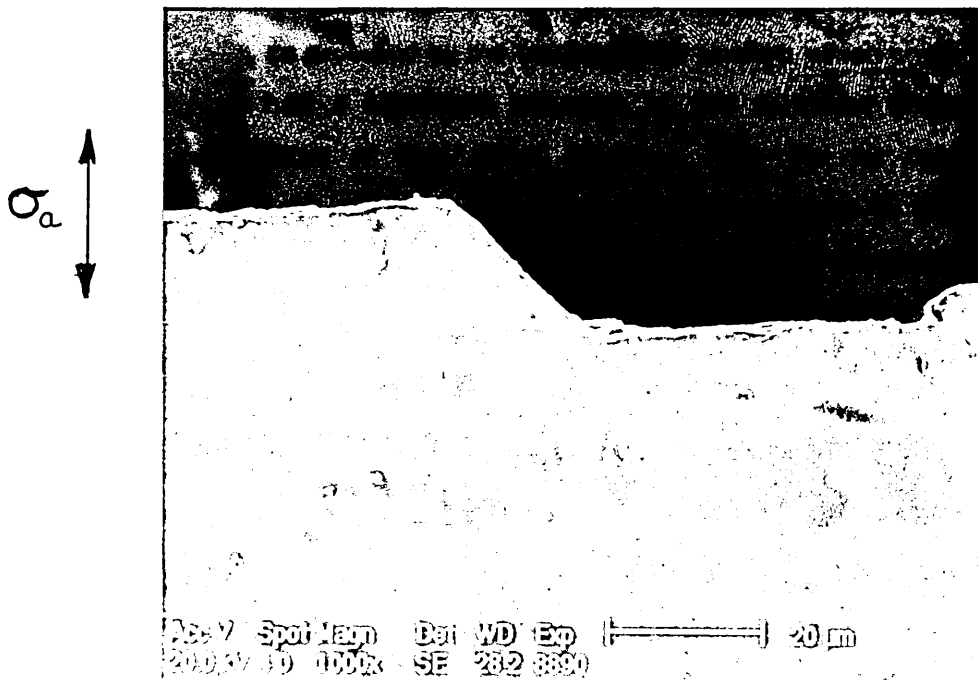


Figure 5.6a A Stage I Crack in the Peak Hardened Material.

[$\sigma_a=807.7\text{MNm}^{-2}$, in air at $R=-1$, frequency=196Hz and $N_f=76,100$ cycles].

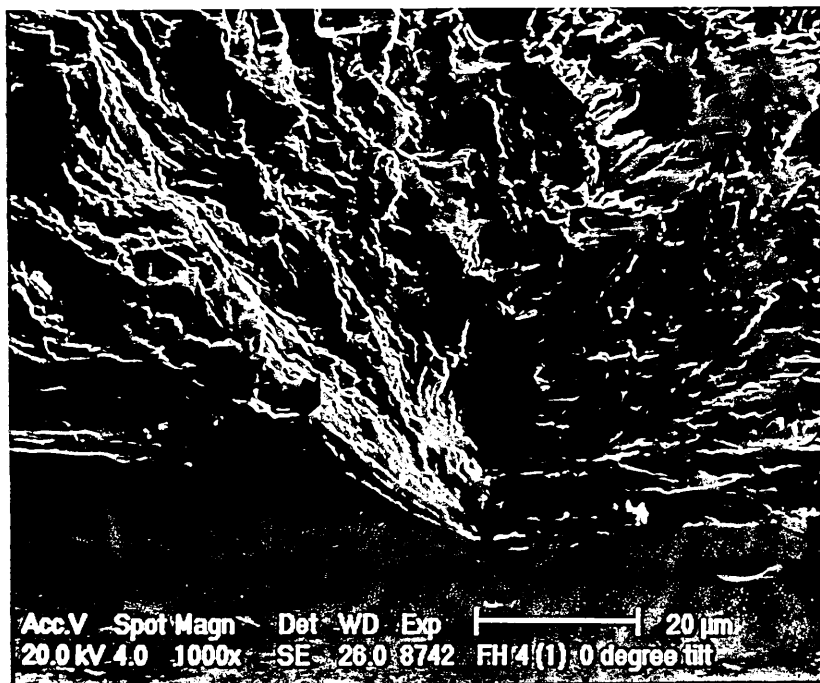


Figure 5.6b The Transition Point Between a Stage I to Stage II Crack is Indicated by the Arrows.

[$\sigma_a=807.7\text{MNm}^{-2}$ in air, $R=-1$, frequency=196Hz and $N_f=76,100$ cycles].

All three martensitic microstructures of FV520B studied in this investigation are considered to be high strength. High strength martensitic microstructures whose Vickers hardness are greater than approximately 350H_v, are usually considered susceptible to hydrogen embrittlement. Hydrogen embrittlement is caused by the presence of interstitial hydrogen atoms which diffuse into the material, introducing regions of highly localised strain within the lattice. Hydrogen atoms are capable of diffusing through martensitic microstructure to regions of high triaxial stress, for example, at prior austenite grain boundaries and crack tips. The diffusion of hydrogen causes a reduction in surface energy which in turn reduces the local fracture stress. After a period of time otherwise known as the incubation period, the local stresses are often relieved by the formation of micro-cracking which usually leads to an impairment of the tensile or fatigue strength. This effect is exacerbated by the presence of the internal stresses which are inherent within lath martensitic microstructures, especially those tempered at low temperatures. Hydrogen assisted fracture is thought to have influenced the crack nucleation process of the peak hardened condition in the acidified chloride environment (pH2).

5.3.2 Softened Overaged Material

The softened overaged material depicts the microstructure with the lowest tensile strength. This can be partly attributed to the presence of approximately 43% reverted austenite which also increased the ductility of the material.

Failure of the softened overaged microstructure in both air and chloride environments was nucleated by the formation of a number of individual stage I fatigue cracks. These cracks subsequently propagated as stage II fatigue cracks eventually joining together on almost parallel planes, as seen Figure 5.7a. The ratchet markings which are indicated by the arrows, represent the points on the fracture surface at which several fatigue cracks joined. As for the peak hardened material, final fracture also occurred by ductile overload when the remaining ligament could no longer sustain the applied load. The formation of multiple cracks, with the presence of a significant quantity of reverted austenite suggested that slip band cracking was probably the dominant crack nucleation mechanism. Some evidence for this argument is seen from Figures 5.7a and 5.7b. A previous investigation has highlighted that highly localised plastic deformation within (the weaker phase of) ferrite has led to the

nucleation of fatigue cracks in a high strength 12Cr-1Mo-V martensitic stainless steel [114].

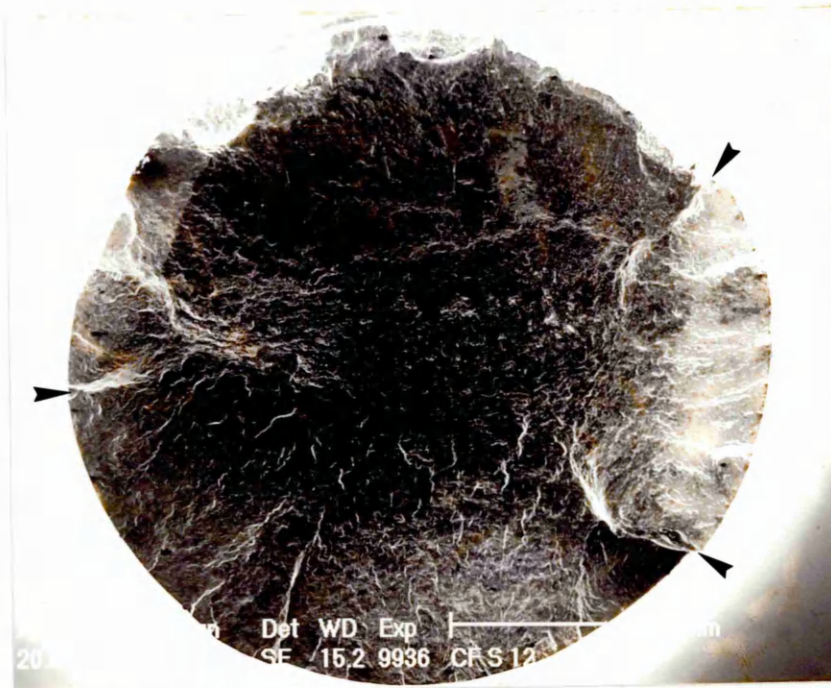


Figure 5.7a A Softened Overaged Specimen Exhibiting Multiple Fatigue Crack Nucleation.

[$\sigma_a=600\text{MNm}^{-2}$ in chloride, pH2, R=-1, frequency=0.5Hz and $N_f=43,470$ cycles].

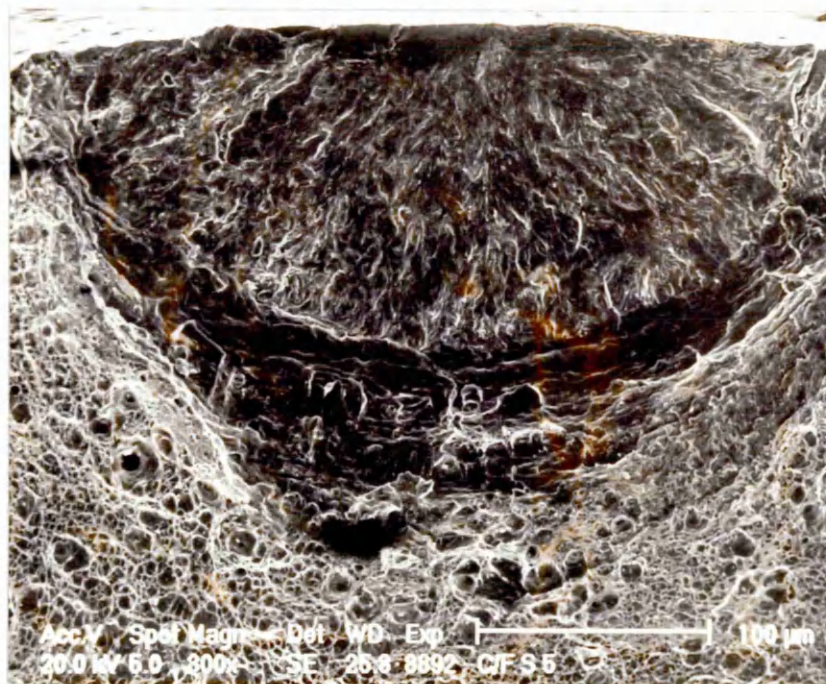


Figure 5.7b A Non-Propagating Crack in the Softened Overaged Material which Exhibited Multiple Fatigue Crack Nucleation.

[$\sigma_a=649.9\text{MNm}^{-2}$ in air environment, R=-1, frequency=5Hz and $N_f=79,500$ cycles].

In the softened overaged condition, slip band would be facilitated by the presence of the lower strength interlath, reverted austenite. It follows that, if the austenite in FV520B was preferentially orientated at approximately 45° to the applied stress, then the conditions for reversed cyclic slip and ultimately fatigue crack nucleation would be favoured. Figure 5.8a shows evidence of cyclic plastic strain which was approximately 45° to the stress axis in a softened overaged material. Figure 5.8b highlights a non-propagating crack in an adjacent region which is inclined approximately 45° to the stress axis. Previous workers [114] [115] have also observed 'marks' which were aligned along the martensite platelets of a 12% Cr martensitic stainless steel. These features were also orientated at 45° to the stress axis. From the evidence presented in Figures 5.8a and 5.8b, it is also feasible to suggest that the 'marks' of cyclic plastic strain may be persistent slip bands (PSB's), which are known to form in the softer phases of commercial alloys.



Figure 5.8a Plastic Strain in the Softened Overaged Material.
 [$\sigma_a=530\text{MNm}^{-2}$, in air, $R=-1$, frequency=5Hz and $N=109,690$ cycles. (not broken)].

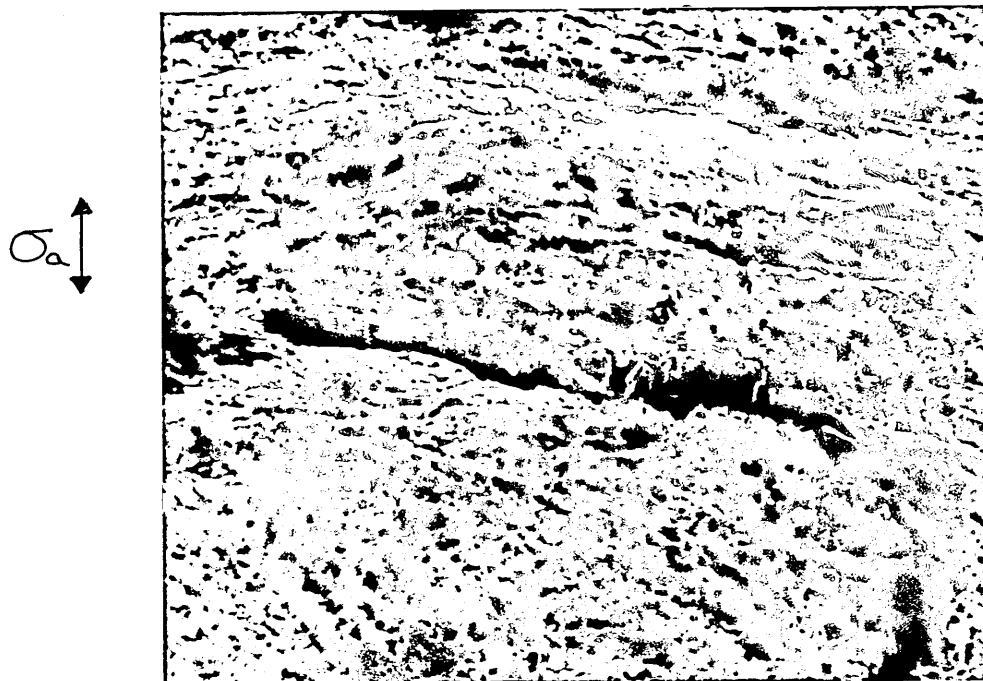


Figure 5.8b A Non-propagating Crack in a Region Containing Plastic Strain in the Softened Overaged Material. The crack is approximately $14\mu\text{m}$ in length.
 [$\sigma_a=530\text{MNm}^{-2}$, in air, $R=-1$, frequency=5Hz and $N=109,690$ cycles. (not broken)].

The relative reduction in the fatigue strength from air to the chloride environment suggests that the reverted austenite may have also been subjected to the effects of the aggressive environment. For example, as previously suggested, anodic dissolution of the slip bands which have ruptured the passive oxide film, may leave the underlying material exposed to further corrosive attack.

A hydrogen assisted fracture mechanism is believed to be unlikely in this material since the softer, tougher phase of reverted austenite would resist the embrittling effects of hydrogen due to the lower inherent microstructural stresses.

5.3.3 Standard Overaged Material

The standard overaged material represents a compromise in the tensile strength and ductile properties of the peak hardened and softened overaged conditions. This was partly achieved by the presence of approximately 21% reverted austenite within the microstructure.

The evidence suggests that the reduction in the fatigue strength in the standard overaged material which has a hardness of 340H_v, may be explained by a combination of the fatigue crack nucleation mechanisms prevalent in the peak hardened and softened overaged materials. This suggests that the fatigue crack nucleation mechanism may result from either a combination of the stress-raising influence of surface or sub-surface inclusions and corrosion pits or a hydrogen assisted slip band cracking mechanism. Figures 5.9 to 5.11 show fatigue crack nucleation due to a number of microstructural features. Figure 5.9 illustrates fatigue crack nucleation due to a sub-surface inclusion; whilst the stage I crack in Figure 5.10 suggests possible slip band cracking in the reverted austenite phase. Figure 5.11 depicts cracking due to the combined stress-raising effects of corrosion pits and a single alumina inclusion.

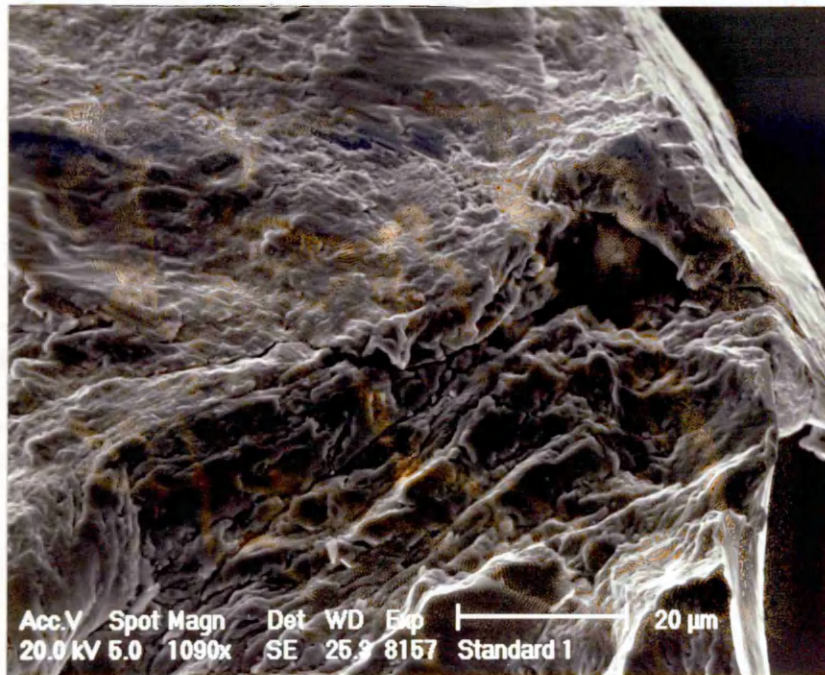


Figure 5.9 An Example of Fatigue Crack Nucleation by a Sub-surface Inclusion in the Standard Overaged Material.

[$\sigma_a=600\text{MNm}^{-2}$, in air, $R=-1$, frequency=125Hz and $N_f=13,400$ cycles].

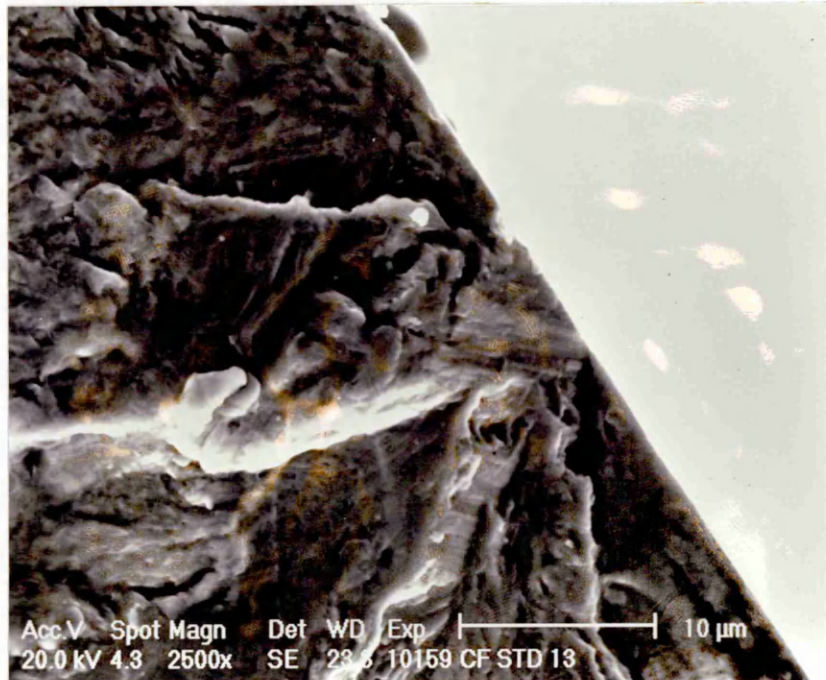


Figure 5.10 A Stage I Crack in the Standard Overaged Condition, Possibly due to Slip Band Cracking in the Weaker Reverted Austenite Phase.

[$\sigma_a=475\text{MNm}^{-2}$, in chloride, pH2, $R=-1$, frequency=0.5Hz and $N_f=204,230$ cycles].



Figure 5.11 Fatigue Crack Nucleation at Corrosion Pits Adjacent to an Alumina Inclusion in the Chloride Environment.

[$\sigma_a=600\text{MNm}^{-2}$, in chloride, pH2, R=-1, frequency=0.5Hz and $N_f=65,410$ cycles].

5.3.4 The Effect of Test Frequency

As previously mentioned in Section 2.5.1, significant reductions in the fatigue strength in corrosive environments are often encountered on reducing the test frequency. This is due to increased time for the initiation and propagation of a corrosion pit of a critical size, especially at low stress amplitudes.

It was anticipated that the corrosion fatigue strength of FV520B in the aggressive environment would be dramatically reduced on lowering the test frequency from 0.5Hz to 0.05Hz. Figures 5.12a and 5.12b, however, illustrate only a slight reduction in the fatigue strength of the peak hardened condition, after a longer exposure to the corrosive environment.

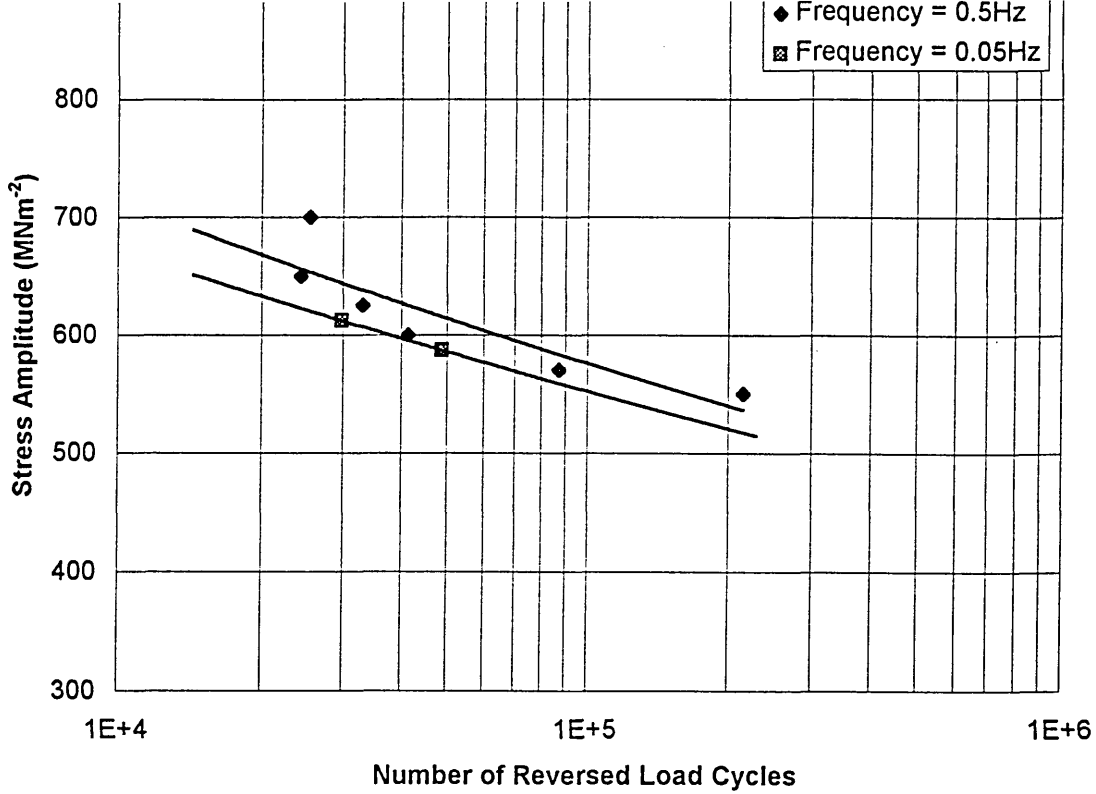


Figure 5.12a The Effect of Test Frequency on the Corrosion Fatigue Strength of the Peak Hardened Condition.

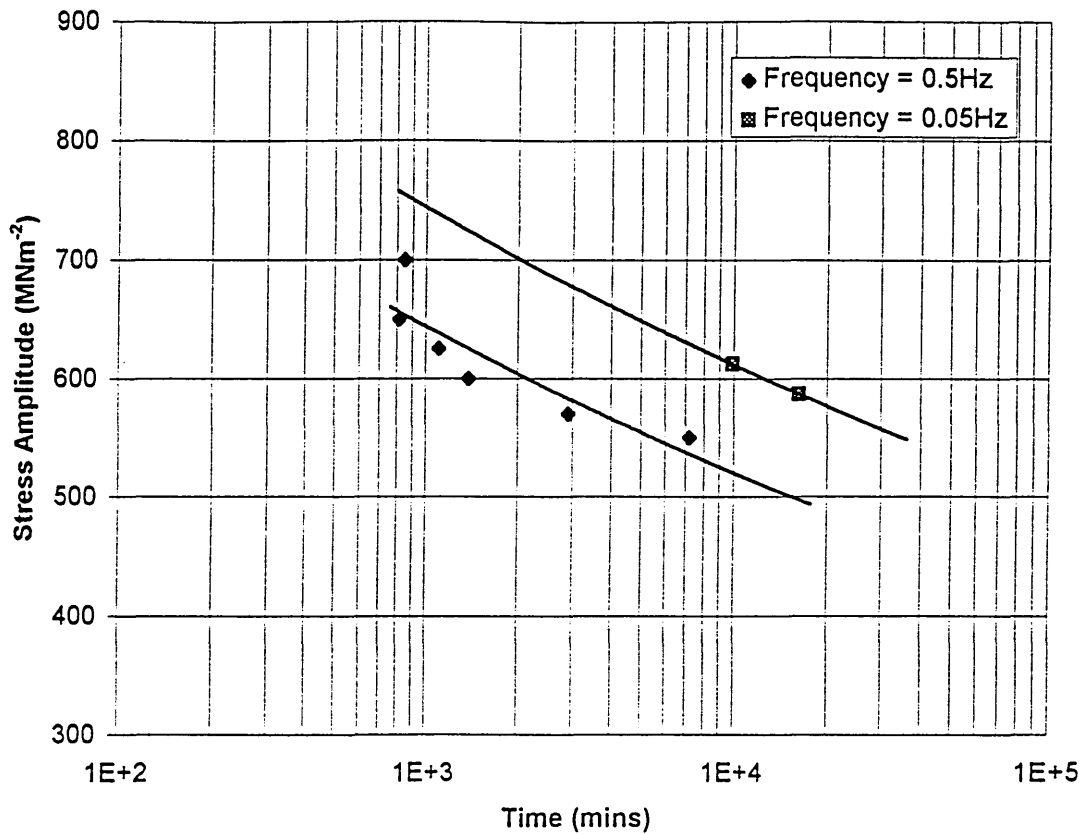


Figure 5.12b The Effect of Exposure Time on the Corrosion Fatigue Strength in the Peak Hardened Condition.

Corrosion pit growth is generally expressed in the form of a power law relationship, as in equation (2.25).

ie.
$$d = At^n \quad (2.25)$$

where d is the corrosion pit depth, t is exposure time and A and n are material constants. For a low alloy steel, the exponent was between 0.3 and 0.7 [83].

The trends in the endurance data from the present study suggests that pitting corrosion kinetics are less dependent on exposure time. Therefore, the power law equation presented in equation (2.25), may not be appropriate to explain the pitting behaviour of FV520B. The following equation is proposed to represent the pit growth behaviour of FV520B in the acidified chloride environment.

$$d = 7.8(1 - e^{-0.09 t}) \quad (5.5)$$

The pit growth behaviour for FV520B is presented in Figure 5.13 with equation (5.5). The observed behaviour was unexpected considering the aggressive nature of the environment, namely the presence of chloride anions; the acidic nature of the solution and the presence of oxygen which would provide the driving force behind the pitting kinetics. In addition to this, a by-product of the pitting reactions, ie the formation of hydrogen chloride would render the conditions at the base of the pit increasingly acidic, see Figure 2.12. The effect would be to reduce the corrosion fatigue strength further still.

The possible reasons for this apparent absence in the reduction in strength, could be due to non-active nature of the corrosion pits. The sites for corrosion and corrosion fatigue crack nucleation for the peak hardened condition will be discussed in Section 5.3.5.

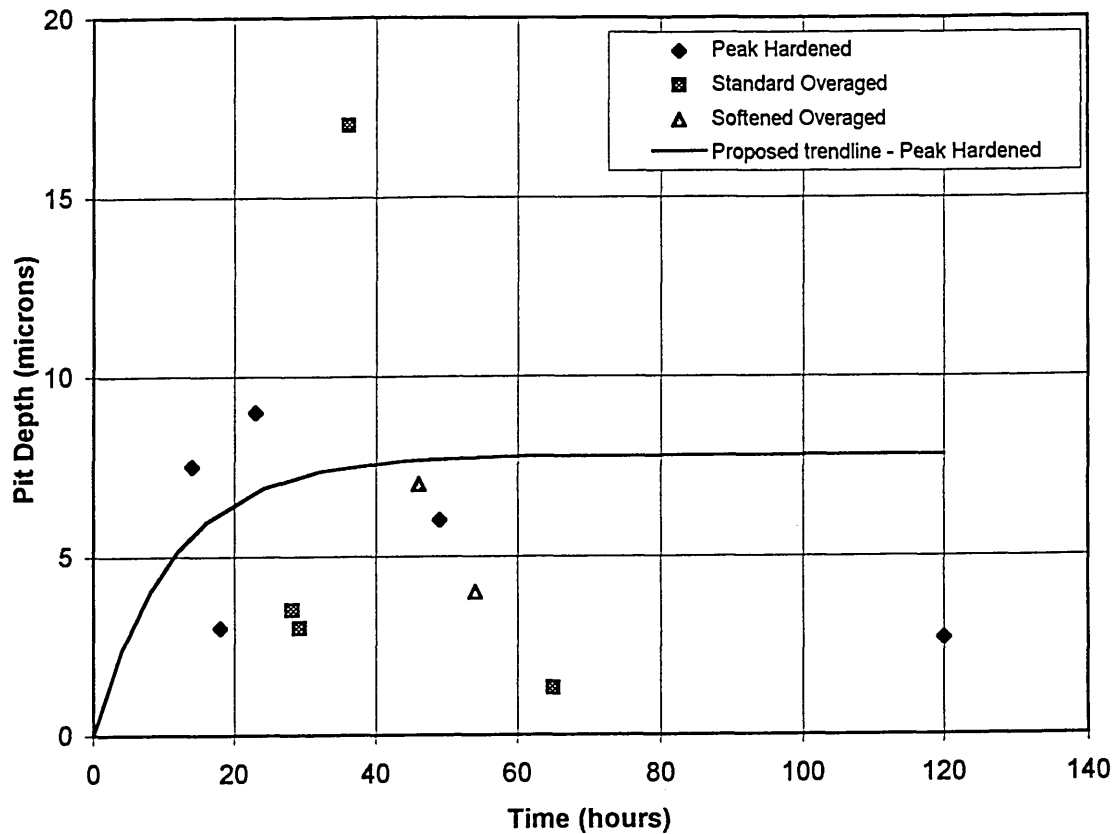


Figure 5.13 The Effect of Time on the Corrosion Pit Depth of FV520B in the Chloride Environment.

5.3.5 Typical Crack Nucleation Sites in Chloride Environment

The size and morphology of the critical corrosion pits in the peak hardened material appeared similar to the inclusion features. Comparisons between the critical pits in Figure 5.15a with the inclusions in Figures 4.6a, 4.6b, 4.7a, 4.7b, 4.8a, 4.8b, 4.10a and 4.10b suggest that the inclusions became active sites for corrosive attack under the chloride environment.

Previous workers [65] have indicated that in an aqueous environment, surface manganese sulphide inclusions are likely to dissolve, in preference to other inclusion types. A relatively high number of these manganese sulphide inclusions were detected in FV520B, such as those presented in Figures 4.9a, 4.9b, 4.10a and 4.10b. However, on examining the specimens post-fracture, there appeared to be no trace of

manganese sulphide in the corrosion pits. This would suggest that the sulphide inclusions had been dissolved during corrosion testing during or prior to slip band formation at the inclusion and steel matrix interface. In contrast, Figure 5.14 shows a silica inclusion (arrow) located adjacent to the corrosion pit. During the early stages of corrosion fatigue testing, it is probable that the slip bands at the inclusion-steel matrix interface damaged the passive oxide surface layer. Damage to the passive oxide layer would have rendered the underlying, unprotected metal exposed to the aggressive chloride solution, as outlined in Section 2.5.7. It is likely that this initial damage led to the steel matrix surrounding the silica inclusion being subjected to further corrosive attack and the formation of a corrosion pit. As a result of the poor coherency between the inclusion and the matrix, the inclusion would become detached, leaving a corrosion pit-type cavity in its wake. This is the preferred mechanism for oxide inclusions as opposed to the inclusion dissolution model which is befitting for manganese sulphide inclusions.

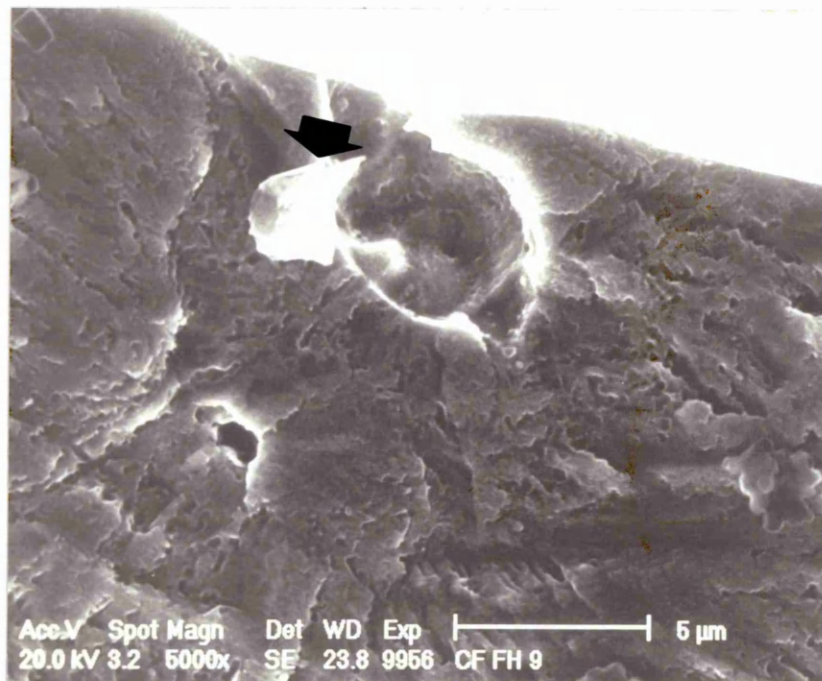


Figure 5.14 Pitting Corrosion at the Site of a Former Surface Silica Inclusion.
[$\sigma_a=550\text{MNm}^{-2}$ in chloride, pH2, R=-1, frequency=0.5Hz, and $N_f=87,370$ cycles].

Figures 5.15a, 5.15b and 5.15c show schematic representations of the typical metallurgical features at the corrosion fatigue crack nucleation sites for the peak hardened, standard overaged and softened overaged conditions respectively. These schematic diagrams are presented in conjunction with the endurance data for the chloride environment. The dimensions and morphology of the critical inclusions, corrosion pits at the nucleation sites, in addition to the stage I cracks which depict slip band cracking, are shown. In addition to this, a number of trends or patterns in behaviour emerge from the data presented which relates the applied stress amplitude; the number of fatigue cracks on the fracture surface and the crack nucleation mechanism.

Figure 5.15a shows the data for the peak hardened condition. As depicted, nucleation is by single fatigue crack nucleation due to either the presence of a critical corrosion pit or an inclusion. Note that the pit depths range from 7.5 to 30 μm compared with up to 280 μm in a low alloy steel in an aerated condensate environment [83]. Fatigue crack nucleation by the slip band cracking occurred infrequently in the peak hardened condition of FV520B.

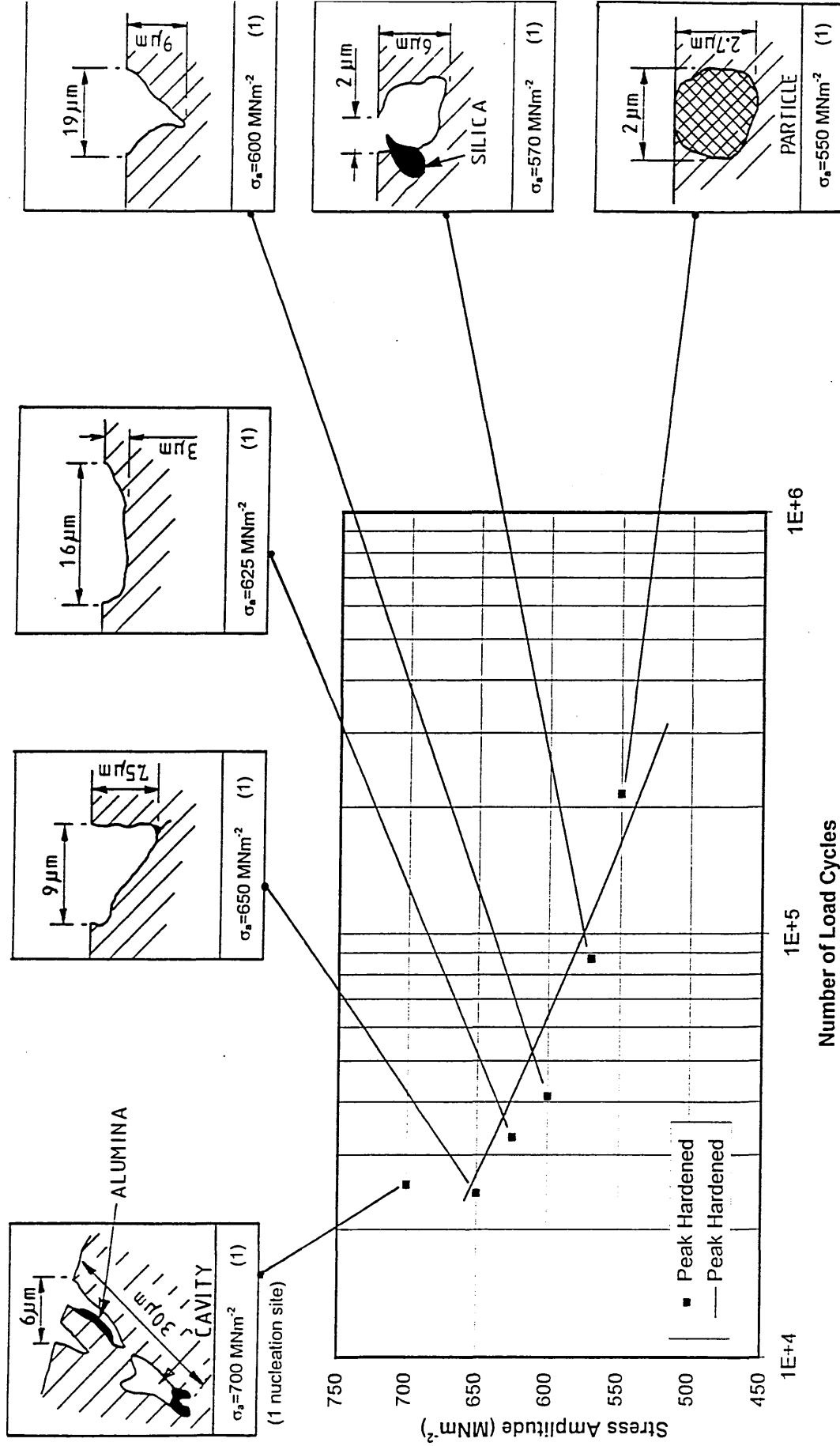


Figure 5.15a Corrosion Fatigue Crack Nucleation Sites and Endurance Data for the Peak Hardened Material.

Figure 5.15b shows the data for the standard overaged material. At low stress amplitudes, fracture was found to initiate by the formation of a single fatigue crack; whilst at higher stress amplitudes, multiple nucleation was observed. Additionally, the data suggests that slip band cracking at multiple sites was the predominant fatigue crack nucleation mechanism at higher applied stress amplitudes. This fracture mechanism is depicted diagrammatically by a stage I crack.

A previous worker [54] has also identified trends between the fatigue crack nucleation mechanism and the applied stress amplitude in a medium carbon low alloy steel also subjected to a chloride environment. In this study, multiple site slip band cracking was found to be the predominant fatigue crack nucleation mechanism at higher applied stress amplitudes.

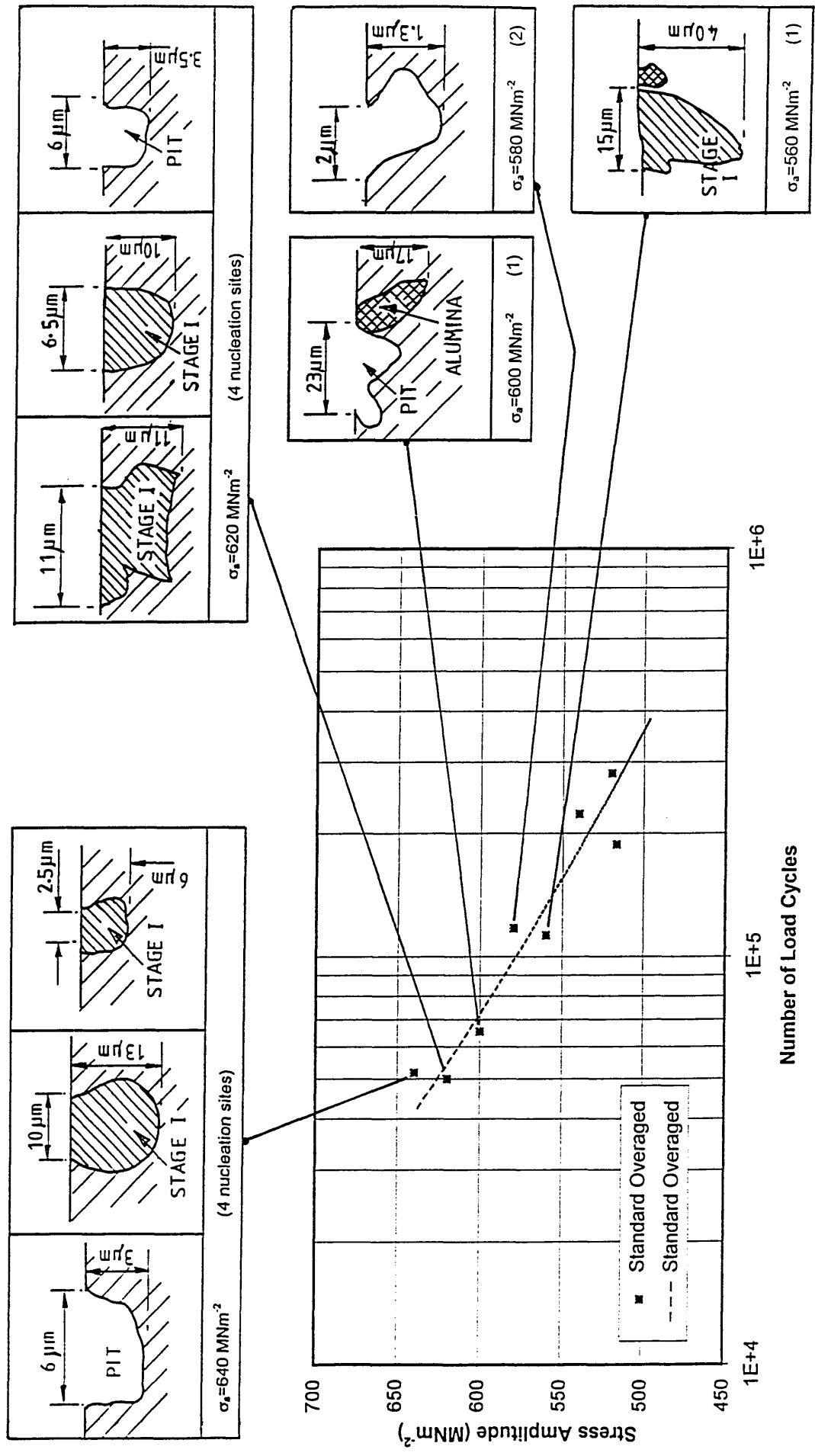


Figure 5.15b Corrosion Fatigue Crack Nucleation Sites and Endurance Data for the Standard Overaged Condition.

Figure 5.15c shows the data for the softened overaged material. At low applied stress amplitudes, fracture was the result of the formation of a single fatigue crack; whilst at higher stress amplitudes, multiple crack nucleation was evident. The occurrence of slip band cracking at the nucleation sites was consistent with specimens exhibiting multiple fatigue crack nucleation.

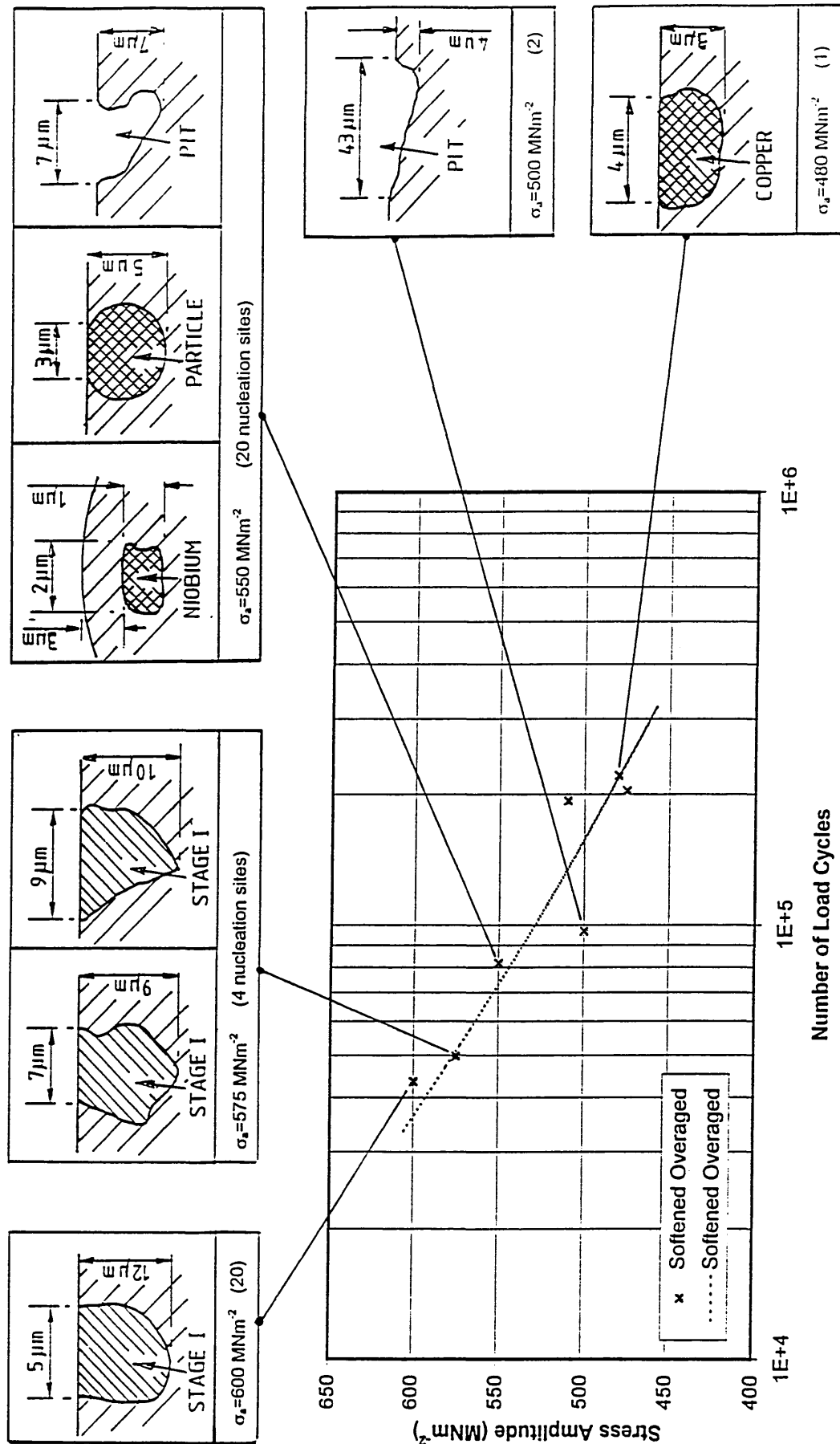


Figure 5.15c Corrosion Fatigue Crack Nucleation Sites and Endurance Data for the Softened Overaged Condition. 142

The schematic diagrams in Figures 5.15a to 5.15c which depict the early stages of the fatigue crack process, clearly show that the stage I cracks are longer than the critical corrosion pits which initiated fracture. It must be noted that, although no obvious stage I crack was observed propagating from the base of the corrosion pits, one may have been present, albeit extremely small in size.

5.3.6 Further Comments on Crack Nucleation

The nature of the crack path was found to be entirely transgranular for both air and corrosion fatigue samples. That is, FV520B did not exhibit any intergranular features under the chloride environment which would be suggestive of a brittle fracture mechanism. For a 13%Cr martensitic stainless steel in air [115], the fracture mode was also found to be transgranular. However, on introducing a steam environment the crack path reverted to an intergranular mode. This fracture mode was found to be highly dependent on the stress intensity factor range and on increasing to a certain value, the observed cracks were notably transgranular.

The fatigue specimens retained their highly polished, bright surface finish and exhibited no evidence of general corrosion, irrespective of the time exposed to the aggressive environmental test conditions. This is attributed to FV520B's excellent general corrosion resistance and the presence of chromium and molybdenum which improves pitting corrosion resistance. However, the three microstructures have been shown to be susceptible to limited pitting corrosion under the aggressive acid chloride conditions, as evident in Figures 5.15a to 5.15c.

5.4 Influence of Microstructure and Environment on Fatigue Strength

5.4.1 The Fatigue Strength in Air

In the absence of a corrosive environment, the fatigue limit of carbon and alloy steels has been correlated with the tensile strength and therefore the material microstructure [18].

The relative positions of the stress amplitude-life (S-N) curves for the three microstructures vaguely infers that the fatigue limit increases with an increase in the tensile strength. It also suggests that the complex strengthening mechanisms under tensile loading, were operating when the material was subjected to fluctuating loads. However, as previously mentioned, it is highly localised yielding within an individual grain at the free surface and not the bulk material effects which determines fatigue resistance. Figure 5.16 highlights the superior fatigue properties of the peak hardened condition compared to the standard and softened overaged conditions.

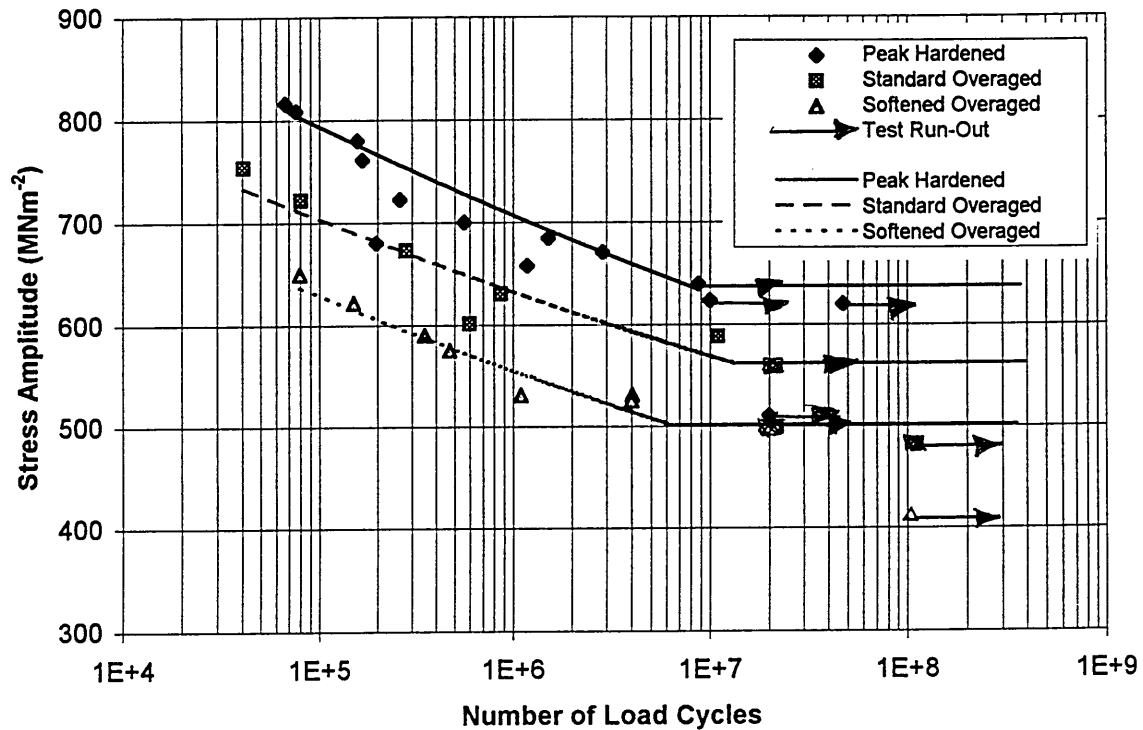


Figure 5.16 The Air Endurance Data for the Peak Hardened, Standard and Softened Overaged Conditions of FV520B.

Table 5.4 shows the fatigue limits for the three microstructures which are compared with their respective tensile strengths. The air fatigue limits clearly indicates that FV520B exhibits considerable high strength even under fatigue loading conditions. Note that, the fatigue limits of the three microstructures are of the order of the tensile

strength of a medium strength structural steel [54], which emphasises the excellent mechanical properties of FV520B.

Table 5.4 The Air Fatigue Limit, the Tensile Strength and Endurance Ratio of FV520B and BS 4360 Grade 50B.

Heat Treated Condition	Tensile Strength (MNm ⁻²)	Air Fatigue Limit (MNm ⁻²)	Air Endurance Ratio
Peak Hardened	1313-1325	640	0.48
Standard Overaged	1061-975	560	0.55
Softened Overaged	960-955	500	0.52
BS 4360 Grade 50B [116]	490-640	-	-

The endurance ratio is an indicator of the relative reduction between the fatigue limit and tensile strength. For most low strength engineering steels, the expected value of the endurance ratio is approximately 0.5; in general, this value will decrease on increasing the tensile strength. The endurance ratios for three microstructures of FV520B are given in Table 5.4. The value for the standard and softened material is approximately 0.55 and 0.52 respectively; a slightly lower value of 0.48 was obtained for the peak hardened condition.

The slight reduction in the endurance ratio of the peak hardened condition can be explained by considering the fracture toughness of the material; the crack nucleation mechanisms and the fracture processes involved.

The intolerance of high strength steels to small surface defects such as surface inclusions is characterised by fracture toughness, namely plane strain fracture toughness, which is considered to be a materials property. The fracture toughness data for the three conditions of FV520B are given in Table 5.5. Assuming the presence of an edge crack, (i.e. $K_{IC} = 1.12\sigma\sqrt{\pi a_{crit}}$), the critical defect size was estimated at the measured 0.2% proof strength and the fatigue limit of the three microstructures of FV520B. The critical defect sizes calculated are also presented in Table 5.5.

Table 5.5 Fracture Toughness Data for FV520B.

Heat Treated Condition	Fracture Toughness K_{Ic} ($MNm^{-3/2}$)	a_{crit} at $\sigma = 0.2\%$ Proof Stress (mm)	a_{crit} at $\sigma =$ Fatigue Strength (in air) (mm)
Peak Hardened	~80	1.3	4.0
Standard Overaged	100	2.8	8.0
Softened Overaged	100	3.7	10.0

The data would suggest that the standard and softened overaged conditions exhibited superior resistance to fracture in air. This corresponds with their superior ductility properties. The relatively low fracture toughness of the peak hardened material can be attributed to the relatively low ductility which was compromised in order to achieve its high tensile strength. The presence of tensile residual stresses in the peak hardened material may also have contributed towards the reduction in fracture toughness. The higher peak stress values in the case of the peak hardened material, combined with the low K_{Ic} , produced a much lower critical defect size. It has also been noted that the estimated critical defect size for the peak hardened material is of the order of 1.3 mm.

5.4.2 The Fatigue Strength in a Chloride Environment

The corrosion fatigue strength of carbon and alloy steels in seawater has been found to be independent of the tensile strength. In addition to this, the corrosion fatigue strengths of these steels were similar at longer fatigue lifetimes [18]. Similar trends have also been observed during the corrosion fatigue testing of a 13% Cr and a precipitation hardenable stainless steel.

The S-N curves presented in Figure 5.17 show the relative corrosion fatigue strengths of the three microstructures. The relative positions of the curves indicate that the corrosion fatigue strengths are similar. This suggests that the complex strengthening mechanisms which provide high strength under tensile loading conditions are redundant under the combined effects of cyclic loading and an aggressive chloride environment. This is thought to be due to the dependency of the corrosion fatigue process on surface defects, such as corrosion pits and the ability to initiate and

propagate a fatigue crack from the base of these corrosion pits. It must be noted that the reduction in fatigue strength due to the corrosive environment was not as significant as observed in some other materials, as shown in Figure 2.14 for a high strength steel.

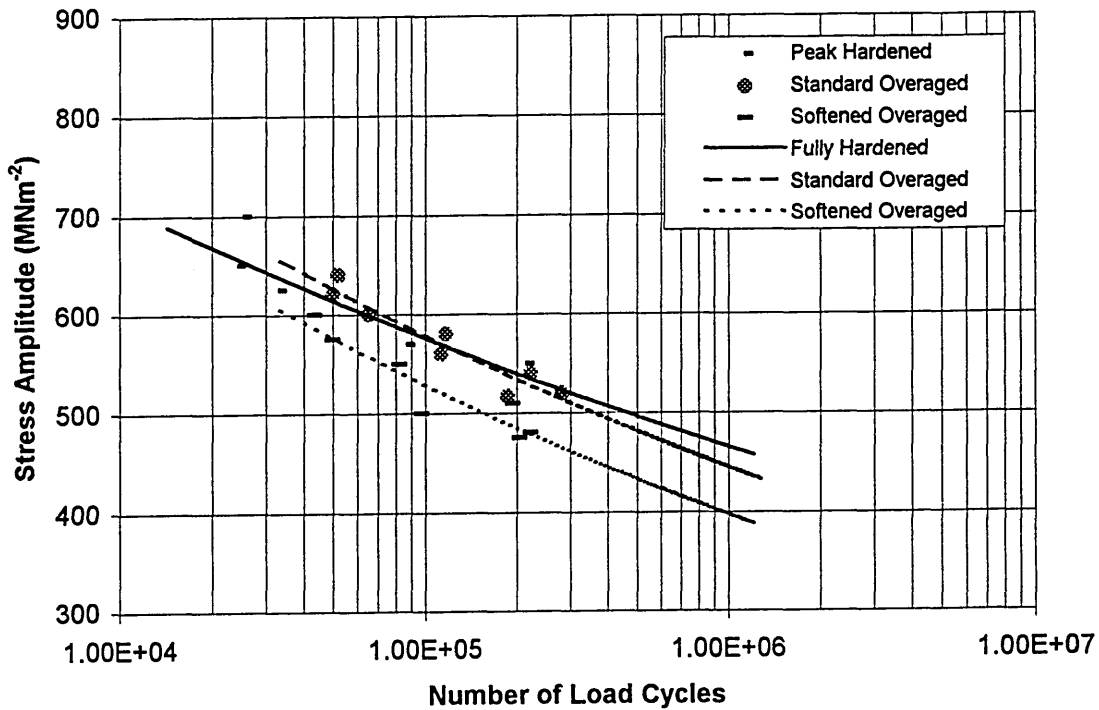


Figure 5.17 The Endurance Data for the Peak Hardened, Standard and Softened Overaged Conditions of FV520B in the Chloride Environment.

The corrosion fatigue strengths are compared with their respective tensile strengths in Table 5.6. A notable reduction in the strength level for the three microstructures is evident due to the combined effect of cyclic loading and aggressive environmental conditions. However, reasonably high strength levels were still maintained when compared with the tensile strength of a BS 970: Grade 080M15 carbon steel, in the normalised condition.

The endurance ratios, (based on $N_f=10^6$ cycles), in the chloride environment are also presented in Table 5.6. The values for the softened and standard overaged

conditions are 0.42 and 0.44 respectively. A lower value of 0.35 was obtained for the peak hardened condition.

Table 5.6 The Corrosion Fatigue and Tensile Strengths of FV520B and BS970: Grade 080M15.

Heat Treated Condition	Tensile Strength (MNm ⁻²)	Corrosion Fatigue Strength (MNm ⁻²)	Endurance Ratio in Chloride
Peak Hardened	1313-1325	465	0.35
Standard Overaged	1061-975	445	0.44
Softened Overaged	960-955	397	0.42
BS970: Grade 080M15	350 (min)	-	-

The absence of a corrosion fatigue limit at lower stress levels is also apparent. This is due to the increased time available for producing a critical corrosion pit. A table of the observed corrosion pit depths as a function of stress range and exposure time has been given in Tables 5.7a to 5.7c. These results suggest that in the present study pit growth is less dependent on the exposure time than previously found by others [83]. It seems apparent that pitting is independent of stress level and microstructure, in addition to this, there is little correlation between corrosion pit depth and the applied stress.

Table 5.7a Corrosion Pit Sizes for the Peak Hardened Condition.

Peak Hardened Condition		
Pit Depth (μm)	Stress Range (MNm ⁻²)	Exposure Time (hours)
30	1400	14
7.5	1300	14
3	1250	18
9	1200	23
6	1140	49
2.7	1100	120

Table 5.7b Corrosion Pit Sizes for the Standard Overaged Condition.

Standard Overaged Condition		
Pit Depth (μm)	Stress Range (MNm^{-2})	Exposure Time (hours)
3	1280	29
3.5	1240	28
17	1200	36
1.3	1160	65

Table 5.7c Corrosion Pit Sizes for the Softened Overaged Condition.

Softened Overaged Condition		
Pit Depth (μm)	Stress Range (MNm^{-2})	Exposure Time (hours)
7	1100	46
4	1000	54

5.4.3 Short Fatigue Cracks in FV520B

Several studies have shown that interactions between microstructural features and short fatigue cracks influence fatigue crack growth rates and affect fatigue lives [62] [36] [41]. These studies have clearly shown that microstructural features act as 'barriers', and therefore impede crack propagation. For the three microstructures of FV520B, the propagation of microstructurally short cracks has been affected by the material microstructure. The evidence to support this idea has been provided by the micrographs of the microstructure in Figures 5.18a and 5.18b, in addition to the scanning electron fractographs in Figures 5.19 and 5.20. Comparisons between these fractographs and the microstructures has led to an understanding of the nature of the crack path and relative crack growth rates in the different microstructural phases.

Figures 5.18a and 5.18b show the lath martensite structure of FV520B in the peak hardened and softened overaged conditions respectively. The reverted austenite phase appears white under the scanning electron microscope.

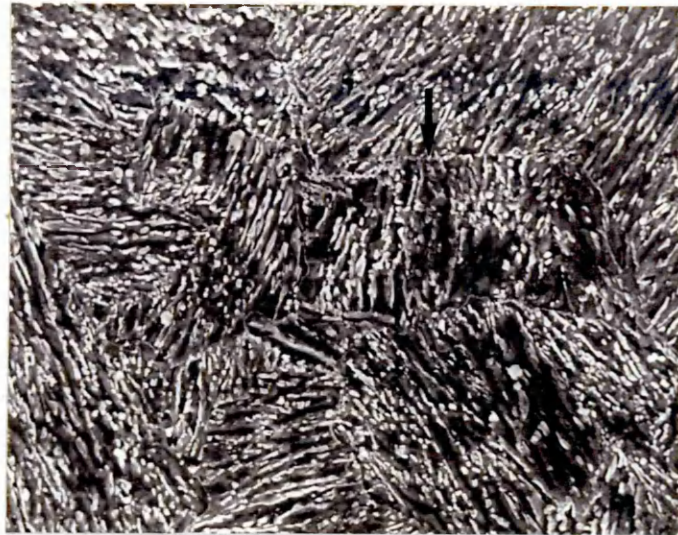


Figure 5.18a Scanning Electron Micrograph of the Peak Hardened Material.

The reverted austenite phase is indicated by the arrow.

Longitudinal section. Etched in Villela's reagent. Mag x2500.

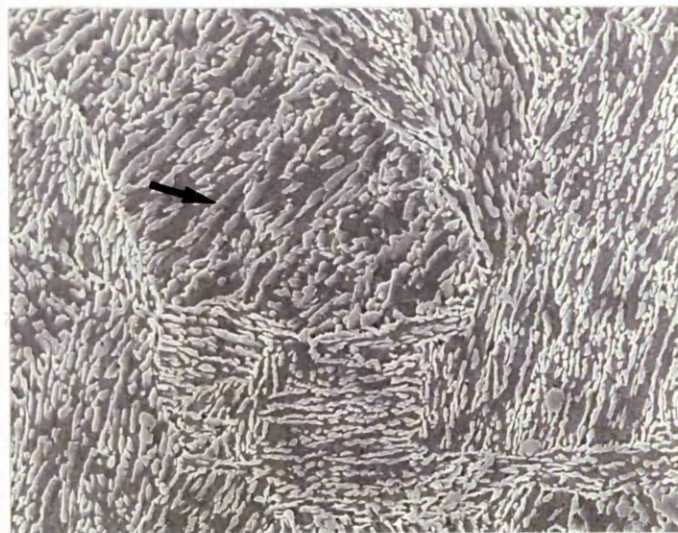


Figure 5.18b Scanning Electron Micrograph of the Softened Overaged Material.

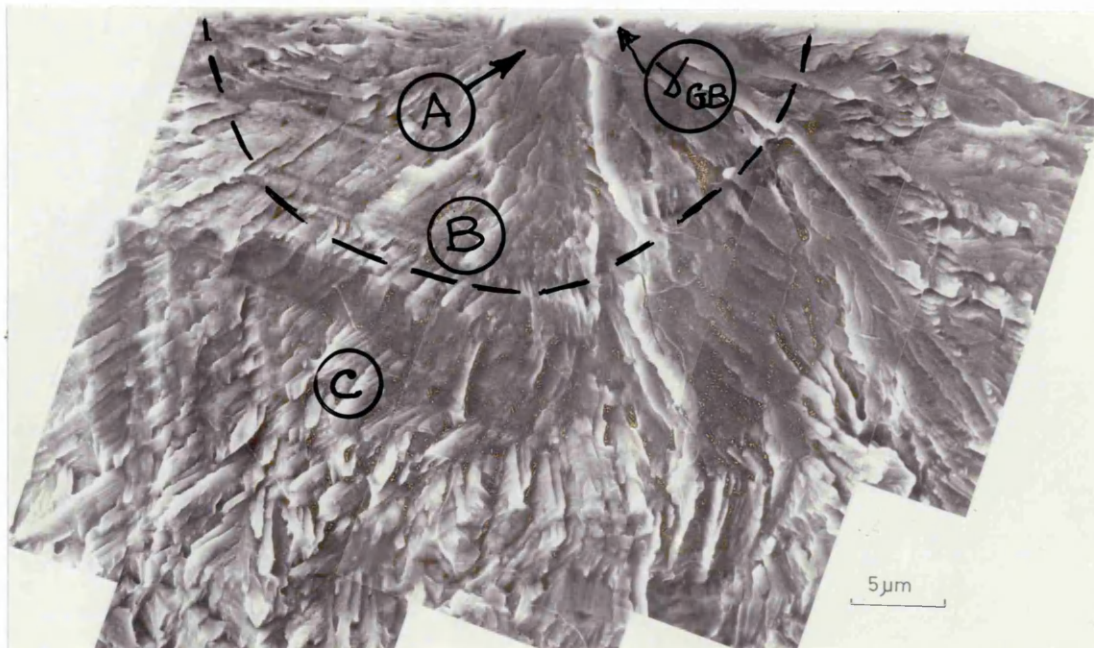
The reverted austenite phase is indicated by the arrow.

Longitudinal section. Etched in Villela's reagent. Mag x2500.

Within the complex microstructure of FV520B, it is thought that microstructural features which are likely to act as barriers to short crack propagation are the prior austenite grain boundaries, lath packet grain boundaries and possibly the martensite laths. Table 4.2 highlights the relative sizes of these microstructural features.

It is believed that the reverted austenite which is present in the three microstructures in varying quantities, will also affect the short crack propagation rate. The strength or the effectiveness of each of these microstructural barriers, especially the reverted austenite is also likely affect the short crack growth rate by varying degrees. It is also thought that particular features, namely the corrosion pits may assist in by-passing these microstructural barriers during the early stages of the fatigue crack propagation process.

Figure 5.19 is a scanning electron fractograph showing the fatigue surface of a specimen in the peak hardened condition. The crack initiation process at a prior austenite grain boundary and the base of a small corrosion pit has been highlighted. A tentative stage I and II fatigue crack has also been indicated.



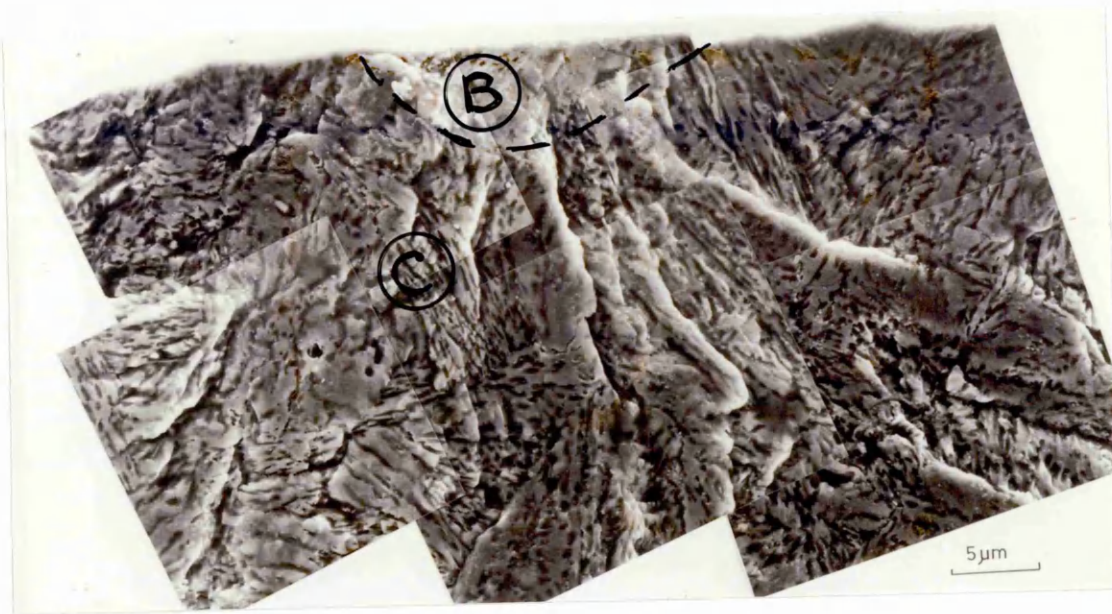
(A - nucleation site + γ_{GB} - grain boundary, B - Stage I crack, C - Stage II crack)

Figure 5.19 The Early Stages of Fatigue Crack Growth for the Peak Hardened Condition.

[$\sigma_a=587\text{MNm}^{-2}$, in chloride, pH2, R=-1, frequency=0.05Hz and $N_f=48,752$ cycles.]

The following discussion makes reference to the fracture surface of the peak hardened specimen presented in Figure 5.19. The texture of the fracture surface suggests that the crack has been 'weaving' through the specimen due to deflections by the certain microstructural features. The fine nature of these features would suggest that the crack tip has been deflected by the individual martensite laths acting as effective barriers which are known to be approximately 1 μ m in width. Indeed, it is evident that the crack propagated along and across the individual martensite laths.

The boundary between martensite laths and lath packets represent differences in crystallographic orientation between individual grains. It follows that, due to these differences in orientation, the slip characteristics ahead of the crack tip at these boundaries may render cyclic slip potentially difficult in adjacent grains [62]. It is thought that since the lath packets are high angle boundaries, cyclic slip between packets may be more difficult than between individual laths, which are known to be low angle grain boundaries. Therefore, lath packets may be more effective barriers to short fatigue crack propagation than the individual laths. It is also feasible to suggest that due to the relative size difference between prior austenite grains and the lath packet size, then the short cracks will be retarded by the lath packet boundaries more frequently than by the prior austenite grain boundaries. It follows that, lath packets will be more effective barriers than the prior austenite grains, in accordance with Figure 2.9. Other workers have indicated that a fine grain size can offer an enhanced resistance to crack initiation and growth of short fatigue cracks in carbon steels; thus offering longer corrosion fatigue lives [118].



(B - Stage I crack, C - Stage II crack)

Figure 5.20 Scanning Electron Fractograph Showing a Stage I Crack and the Early Stages of Stage II Fatigue Crack Propagation in a Specimen in the Softened Overaged Condition.

[$\sigma_a=600\text{MNm}^{-2}$, in chloride, pH=2, R=-1, frequency=0.5Hz and $N_f=43,470$ cycles.]

Figure 5.20 shows the early stages of fatigue crack growth in the softened overaged material which contains approximately 43% reverted austenite. It is likely that short cracks would propagate through any of the martensite laths, by mechanism previously outlined for the peak hardened condition. However, on propagating through the reverted austenite phase, the crack tip would be subjected to a considerable amount of blunting. This can be attributed to the greater ductility of the austenite phase (face-centred cubic) when compared to that of lath martensite (body-centred cubic). A blunted crack tip will behave like a notch with a less severe stress concentration, compared with the sharp crack tip weaving through the lath martensite microstructure. The significance of a having a greater quantity of reverted austenite within the microstructure would be that crack tip blunting will effectively increase the crack growth rate. It is suggested that a significant quantity of reverted austenite will act as a less effective barrier when compared to either the lath packet boundaries or even the individual laths themselves. It is also suggested that the short crack propagation rate may be greater in the softened overaged than the peak hardened material, hence leading to a shorter fatigue life.

5.4.4 The Stress Fatigue Life Relationship

The total fatigue life of FV520B for the range of stress amplitudes tested can be represented by using the well known Basquin relationship [38], as given in equation (2.9).

$$\sigma_a = \sigma'_f (2N_f)^b = \frac{\Delta \epsilon_E E}{2} \quad (2.9)$$

where σ_a is the stress amplitude and $2N_f$ is the number of reversals to failure (1 reversal is $\frac{1}{2}$ cycle). σ'_f is the fatigue strength coefficient whilst b represents the fatigue strength exponent (Basquin's exponent).

The Basquin relationship relates the applied stress amplitude to the number of load reversals to failure. It allows lifetimes to be predicted for a given stress value above the fatigue limit and for instances when the nominal stress is below the yield stress. The use of Basquin's relationship for the present study is acceptable, since the nominal applied strains in the high cycle regime will be predominantly elastic. Therefore, the plastic strain component in the expression for total life (see equation (2.10)) was ignored. Lifetimes in the high cycle fatigue regime are known to be dominated by the formation and growth of a stage I fatigue crack.

The fatigue strength coefficient (σ'_f) and fatigue strength exponent (b) for FV520B according to the Basquin expression are given in Table 5.8.

Table 5.8 The Values of σ'_f and b for the Three Microstructures in the Air and Chloride Environment.

Heat Treated Condition	Air Environment		Chloride Environment	
	σ'_f	b	σ'_f	b
Peak Hardened	1474.4	-0.053	2140.2	-0.107
Standard Overaged	1342.6	-0.050	2154.4	-0.109
Softened Overaged	1187.1	-0.056	1977.2	-0.098

The values of the fatigue strength exponent (b) for the three microstructures in air were similar, ranging between -0.050 to -0.056. These values almost lie within the range for most ductile materials which is known to be approximately -0.07 to -0.15 [39]. (As an example, the exponent for a low and high carbon steel was -0.11 and -0.081 respectively.) For the chloride environment, a decrease in the fatigue strength exponent was observed whilst the results which ranged from -0.098 to -0.109 appeared to be within that cited for ductile materials. The fatigue coefficient (σ'_f) for air, appeared to decrease in accordance with the tensile strength of the materials. In contrast, the value of the coefficient for the peak hardened and the softened overaged condition decreased in the chloride environment. The fatigue strength coefficient was found to increase for the standard overaged condition.

The fatigue strength exponent (b) and coefficient (σ'_f) are indicators of a materials resistance to cyclic loading and are therefore considered to be properties of the material. The fatigue strength exponents and coefficients for the tests performed in air, reflect the ease with which fatigue crack nucleation occurred. It is clear that the nucleation of a single fatigue crack is more difficult in the peak hardened material when compared to multiple crack nucleation in the softened overaged condition. This is simply due to the increased ductility within the reverted austenite which undergoes plastic deformation at relatively lower stresses when compared to slip within the martensite laths. The crack propagation mechanisms and the relative crack growth rates within the phases of austenite and martensite has previously been discussed in Section 5.4.3.

In the chloride environment, the values of the fatigue strength coefficient for the peak hardened and the standard overaged condition are very similar; even though multiple fatigue crack nucleation in air, was found to reduce the fatigue life. Increasing the volume percentage of reverted austenite to the levels evident in the softened overaged material, was found to cause a more notable decrease in the corrosion fatigue life. The slight increase in the fatigue strength exponent for the standard overaged condition may be due to the curve fitting method employed. Furthermore, it may be a reflection of the short crack growth perturbations due to the reverted austenite phase.

5.5 Fatigue Lifetime Prediction Model for FV520B

5.5.1 Fracture Processes in FV520B

An attempt has been made to describe the fracture process and produce a phenomenological model to represent the fracture behaviour of the microstructures. The account of the fracture process presented for FV520B was partly borne from observations of the fracture surface and information gathered from taking plastic replicas during the fatigue tests. The plastic replication technique has provided little information about the fracture process, ie the fatigue crack nucleation process and the formation of microstructurally short fatigue cracks. The possible reason for this can be related to the actual fracture behaviour. However, fractographic studies using a scanning electron microscope (SEM) has provided the supporting evidence which has provided a more detailed picture of the failure process.

The fracture process in FV520B is thought to occur by two methods. Figure 5.21 illustrates the fatigue behaviour which can be separated into a number of phasesⁱ as represented by (A) to (E). The size of each phase (A) to (E) has been approximated.

It was observed that crack initiation occurred by two distinct mechanisms. As shown in Figure 5.21a, the cracks initiated from either a corrosion pit or an inclusion and is represented by phase (A). The second mechanism depicts a slip band originating stage I crack and is shown in phase (B) of Figure 5.21b. In the first case, even though the cracks nucleated from either a pit or an inclusion, the slip band process may still be involved. However, in this instance, the stage I, phase (B) in most of the tests was unresolvable under the SEM and therefore was very small. In contrast, the length of the stage I crack (B) in the second case is of the order of one or two prior austenite grains, i.e. 25µm long.

ⁱ The term 'phase' represents a specific area on the fracture surface.

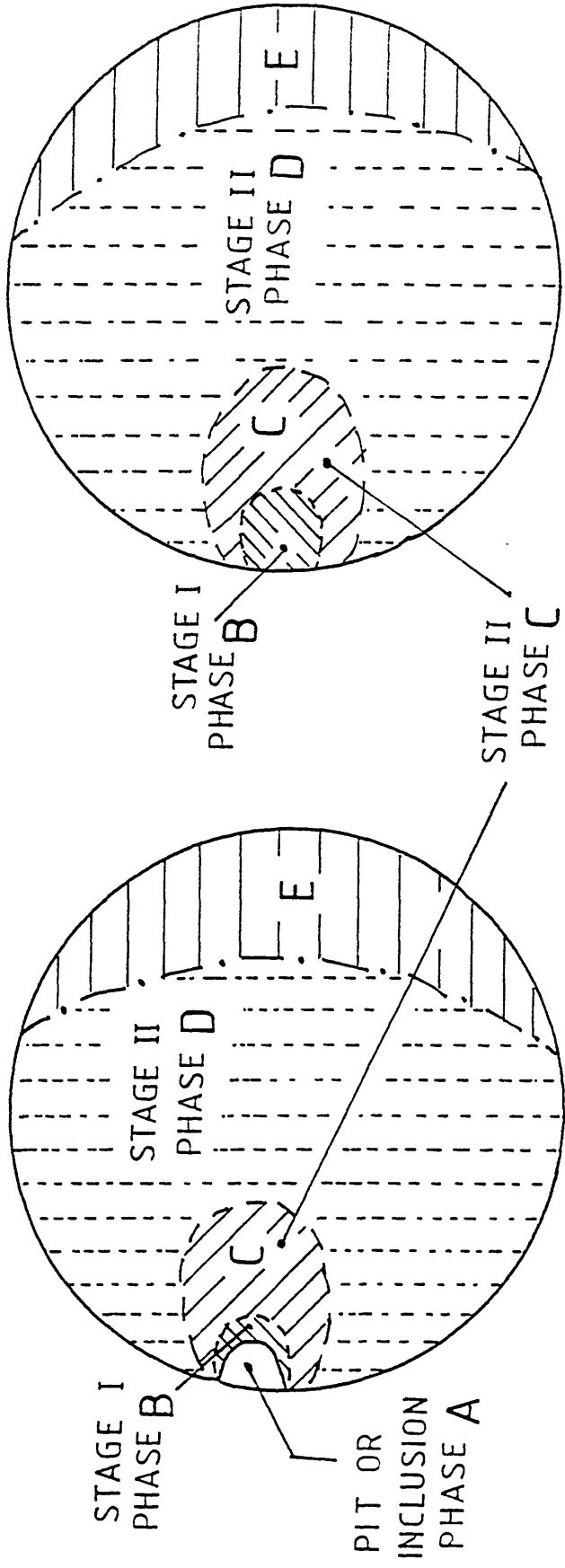


Figure 5.21a. Schematic Representation Depicting One Case of the Fatigue Process in FV520B.

Figure 5.21b. Schematic Representation Depicting the Second Case of the Fatigue Process in FV520B.

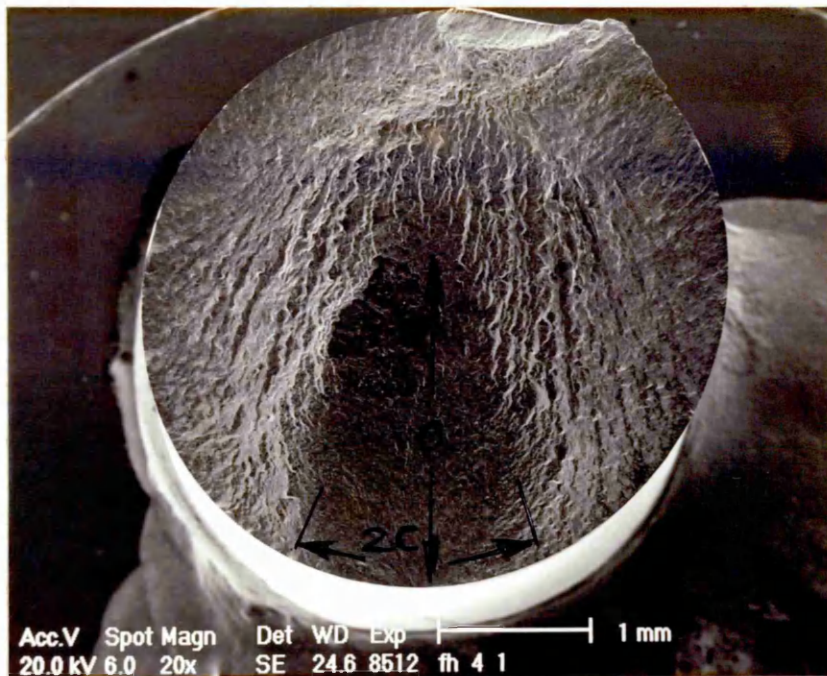


Figure 5.22 The Fracture Surface of a Peak Hardened Specimen Highlighting the Surface Crack Length (2c) and Crack Depth (a).

[$\sigma_a=807.7\text{MNm}^{-2}$, in air, $R=-1$, frequency=196Hz and $N_f=76,100$ cycles.]

In both cases, stage II crack propagation can be divided into two phases, namely, phases (C) and (D), although the demarcation between these phases is purely arbitrary. It has been observed that the major part of the fatigue life is spent in propagating a crack in phase (C) and the depth of the crack at the arbitrary boundary between (C) and (D) was approximately $150\mu\text{m}$. As shown in Figure 5.22, the aspect ratio of the crack in phase (C) was found to be greater than one, which suggested that the crack was shorter than its actual length. Indeed during one test, measuring a surface crack beyond the length of $12.5\mu\text{m}$, was difficult. Phase (D) of stage II occurred at a rapid rate. The growth rate during this phase of the fracture process is thought to be of the order of 10^{-8} m/cycle. This high rate of da/dN is typical for stainless steel for the stress values used and for a crack length of approximately $150\mu\text{m}$, as evident by other literature [39]. It was estimated that the lifetime spent in this phase was less than 50,000 cycles.

The final stage of the fracture process (E), i.e. fast fracture, occurred by ductile overload. The portion of the fracture surface for ductile overload was dependent on

the applied stress amplitude and can be related to the fracture toughness of the material, see Table 5.5.

In the chloride environment, due to combined dissolution and mechanical effects, phase (B) is small and so the lifetime is decided by phases (C), (D) and (E). It is thought that stage II crack propagation (phases (C) and (D)) is slightly affected by the environment. With reference to Figures 5.21a and 5.21b, the first case describes the fracture behaviour of the peak hardened condition, in addition to the standard and softened overaged conditions at low stress amplitudes. The second case depicts the fracture process for the standard and softened overaged conditions, particularly at high stress amplitudes.

5.5.2 Proposed Lifetime Prediction Model

Based on the fracture behaviour presented in Section 5.5.1, three important assumptions can be made.

1. The fatigue life in air can be divided into two parts, N_1 and N_2 . N_1 is the lifetime spent in generating a stage I crack up to a size of $25\mu\text{m}$, whilst N_2 represents the fatigue life of a $25\mu\text{m}$ long stage I crack propagating to stage II crack. Since the fatigue tests were conducted until the test specimens physically separated, then N_2 includes the process of final fracture.
2. Initiation occurs rapidly in the chloride environment. Therefore, the N_1 part is significantly lower and can be considered negligible in the chloride environment.
3. The fracture process in the N_2 stage is unaffected by the environment.

Based on the above assumptions for a given microstructure of FV520B, the chloride environment results gives the propagation life N_2 , while the air results represents the total life N_1+N_2 . (Note, both N_1 and N_2 are propagation lives.)

Thus total life N_f in air can be expressed by the following:

$$N_f = N_1 + N_2 \quad (5.6)$$

and in the chloride environment for the propagation life, $N_1 = 0$:

thus
$$N_f = N_2 \quad (5.7)$$

It is postulated that both N_1 and N_2 can be expressed as:

$$N_1 = B\sigma^n \quad N_2 = A\sigma^m \quad (5.8)$$

where n and m are considered to be material constants and σ is the applied stress amplitude. For FV520B, the value of n and m are independent of the material condition. The values of n and m were found to be:

$$n = -18.2 \quad m = -9.3 \quad (5.9)$$

The parameters A and B were found to be related to the percentage volume of the weaker reverted austenite phase (γ), as given below:

$$A = 18 \times 10^{30} [1 + e^{-10(\gamma-0.3)} - 933.3e^{-17(\gamma+0.22)}] \quad (5.10)$$

$$B = 10^{(57.73-4.25\gamma)} \quad (5.11)$$

The variation of parameters A and B with the percentage volume of reverted austenite (γ) in FV520B is shown in Figures 5.23a and 5.23b respectively.

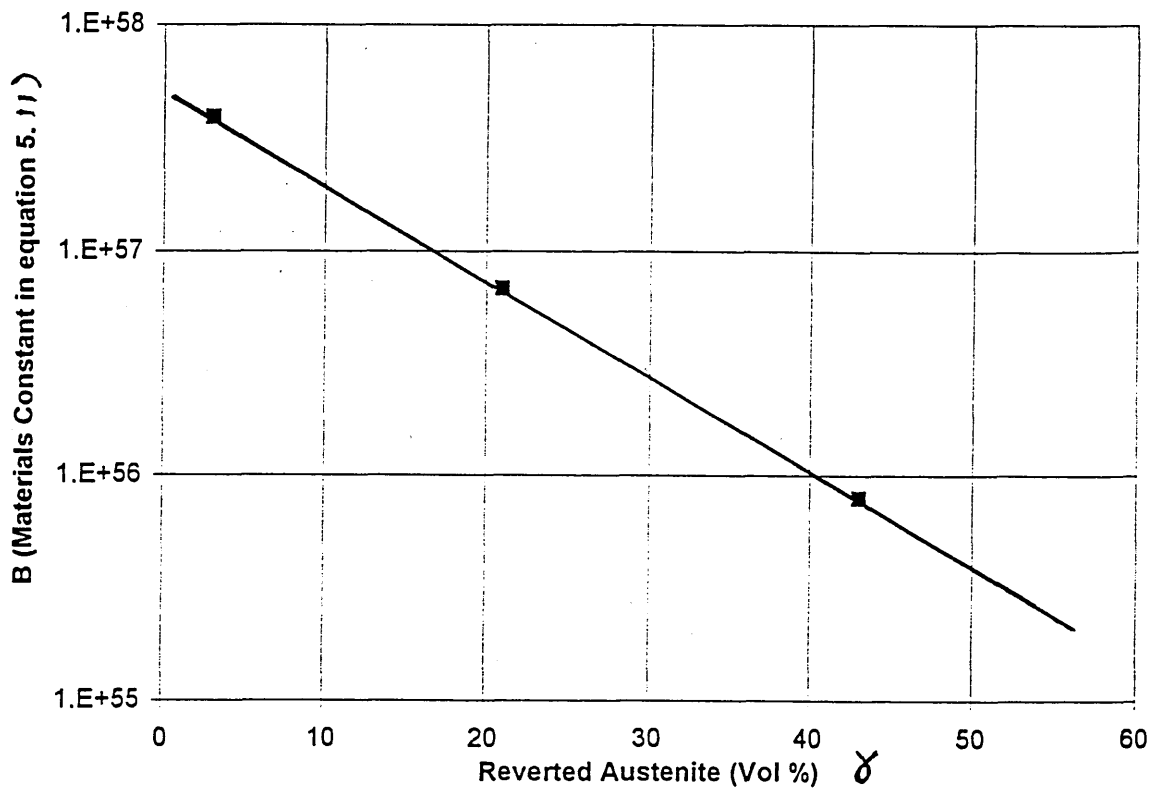
The materials parameter B defines the resistance to the early stages of the fatigue process occurs which includes crack nucleation and stage I crack propagation. The results presented in Figure 5.23a indicate that on increasing the quantity of reverted austenite (γ) in the microstructure, the resistance to crack nucleation will be reduced. This is due to the enhancement of slip which manifests itself as multiple crack nucleation. The trend in Figure 5.23a is similar to that found in Figure 5.3, which shows that under the application of a tensile load the stress at which FV520B begins to yield (or the 0.2% proof stress) decreases on increasing the amount of the weaker reverted austenite phase.

The materials parameter A defines the resistance to stage II crack propagation. The trend shown in Figure 5.23b suggests that the resistance of the microstructure to crack propagation was enhanced slightly on increasing the volume percentage of reverted austenite from 3 to 21%. Increasing the quantity of reverted austenite above 21% led to a reduction in the microstructure's resistance to crack growth.

The variation in resistance to crack propagation is thought not only to be due to the varying amounts of reverted austenite, but also its type, location and size of austenite "packets". One worker [31] has suggested that the reverted austenite within a martensite microstructure of a maraging steel influenced both the impact toughness and fatigue crack resistance.

Previous workers [27] [28] [29] have conducted detailed studies to characterise the reverted austenite found in maraging steels. The findings of these studies is presented in Table 2.2 which shows specific differences in the reverted austenite according to the precipitation hardening temperature employed. It is proposed that the reverted austenite within the three microstructures of FV520B will also exhibit similar characteristics to those steels presented in Table 2.2, as a function of the precipitation hardening temperature.

It is also proposed that during cyclic loading, the microstructural phases within the peak hardened, standard and softened overaged materials will offer differing degrees of resistance to crack propagation. An additional source of resistance is derived from the difficulty of the crack to propagate across the grain boundaries, i.e. at the lath; lath packet and prior austenite grain boundaries. This is due to differences in crystallographic orientation between adjacent grains and slip characteristics ahead of the crack tip.



Figures 5.23a The Variation in Parameter B with the Percentage Volume of Reverted Austenite (γ).

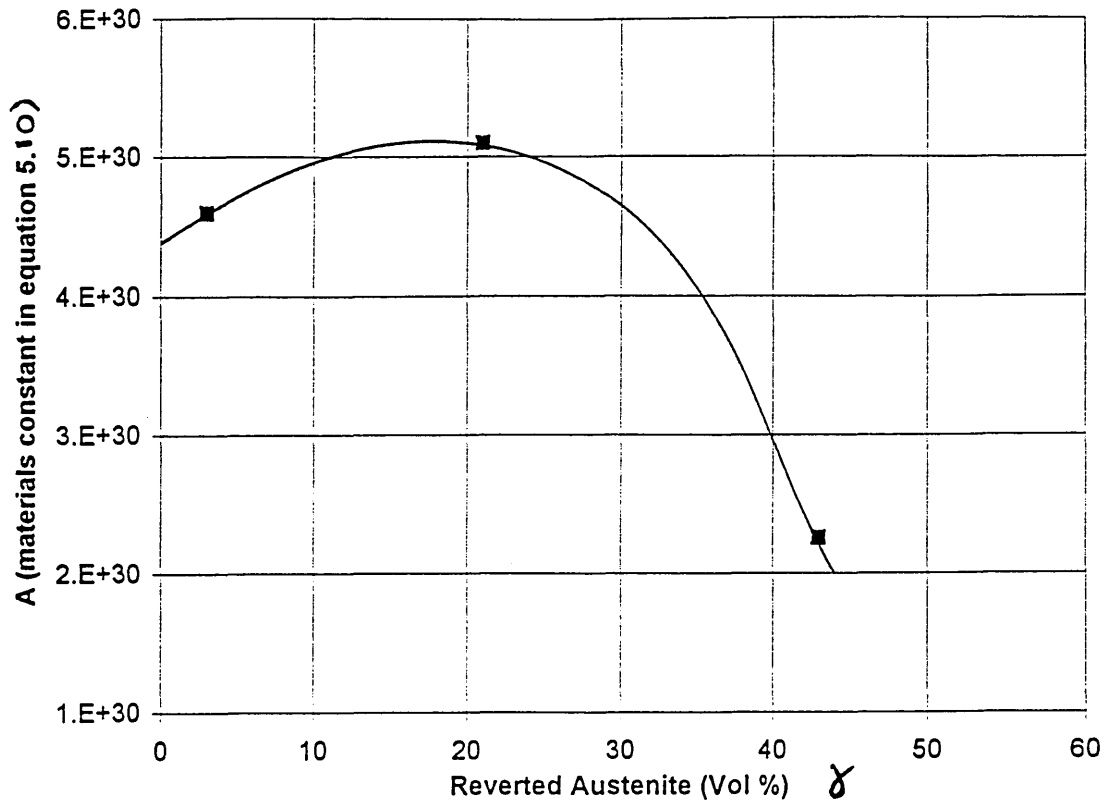


Figure 5.23b The Variation in Parameter A with the Percentage Volume of Reverted Austenite (γ).

Thus, for any heat treated condition, the fatigue life in air can be represented by the following expression:

$$N_f = B\sigma^{-18.2} + A\sigma^{-9.3} \quad (5.12)$$

In the chloride environment the expression becomes:

$$N_f = A\sigma^{-18.2} \quad (5.13)$$

The above model was used to predict the fatigue life for the three conditions of FV520B as shown in Figures 5.24a to 5.24c. The predictions have been compared with those using Basquin's model, equation (2.9) and are presented in Figures 5.24d to 5.24i for each microstructure in the either air or the chloride environment.

Figure 5.24a shows the comparison between predicted and experimental results for the total life in air and the propagation life in the chloride environment for the three microstructures. The results show that the most accurate predictions are given for lifetimes in the intermediate to high cycle fatigue regime for both air and chloride environments, i.e. from 10^4 to 10^6 load cycles. The prediction of lifetimes (in air) greater than 10^6 load cycles were found to deviate slightly from the predicted trend-line. These tests were performed at stresses below the fatigue limit and their relative position to the predicted trend-line suggested that for the majority of these results, conservative or 'safe' predictions would be given.

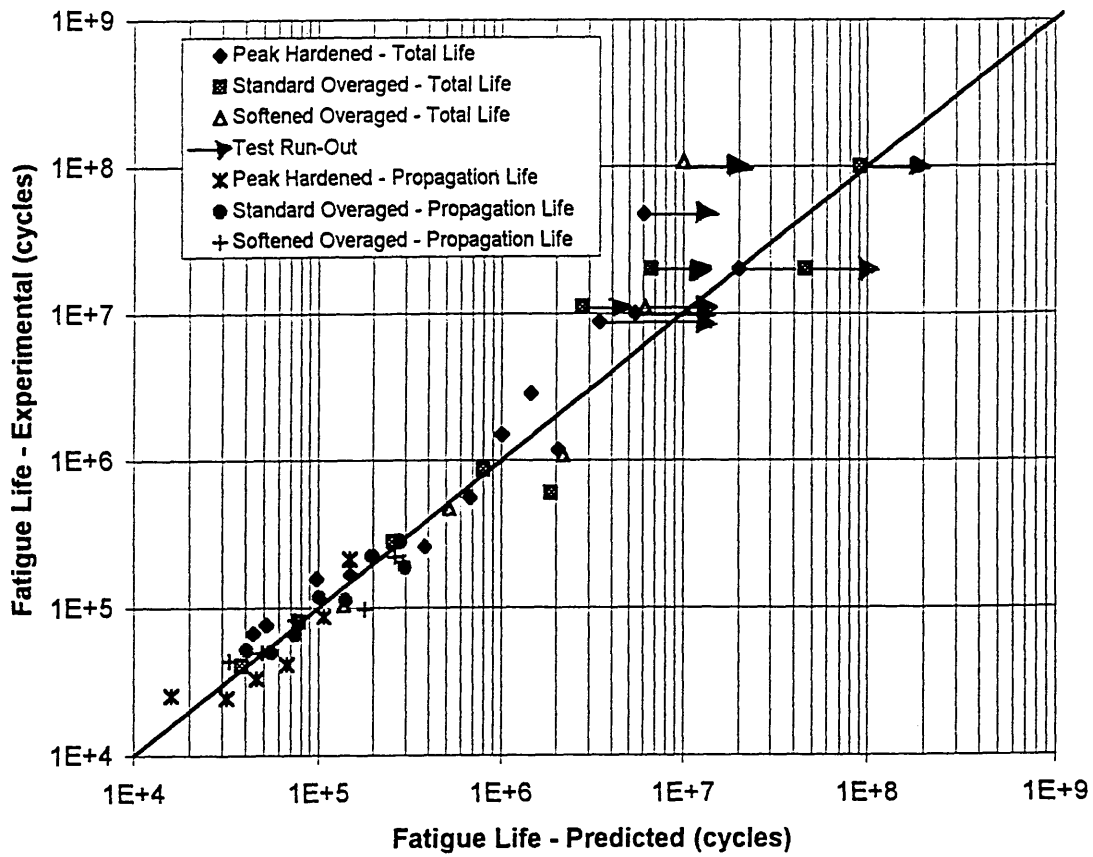


Figure 5.24a Predicted and Experimental Results for the both the Total Fatigue and the Propagation Lives of FV520B.

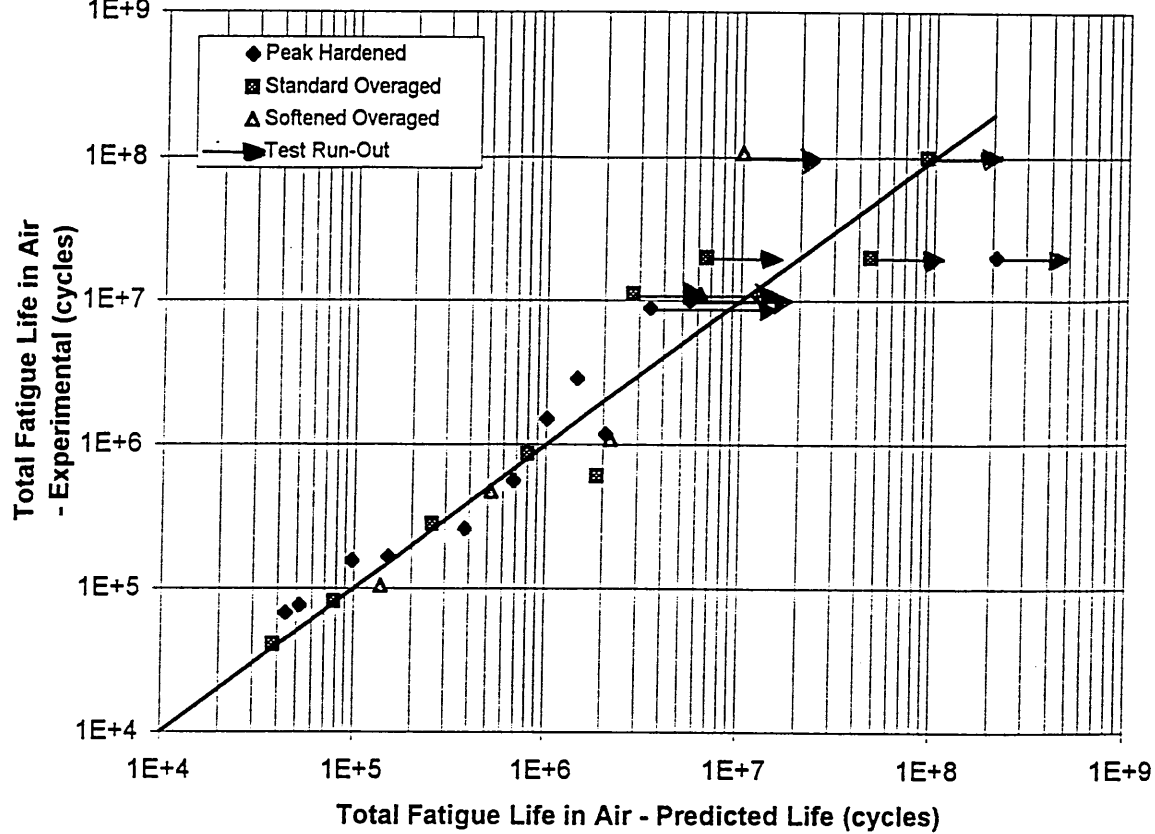


Figure 5.24b Predicted and Experimental Results of the Total Fatigue Life of FV520B in Air.

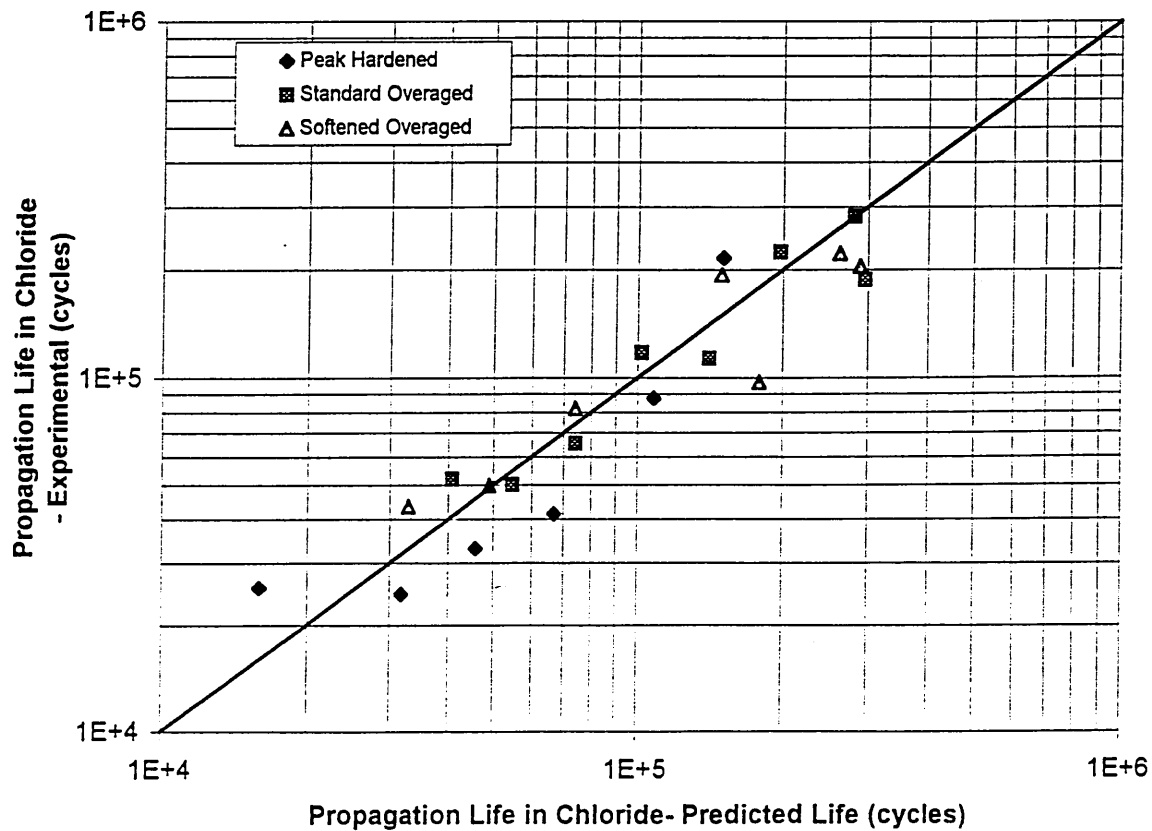


Figure 5.24c Predicted and Experimental Results of the Propagation Life of FV520B in the Chloride Environment.

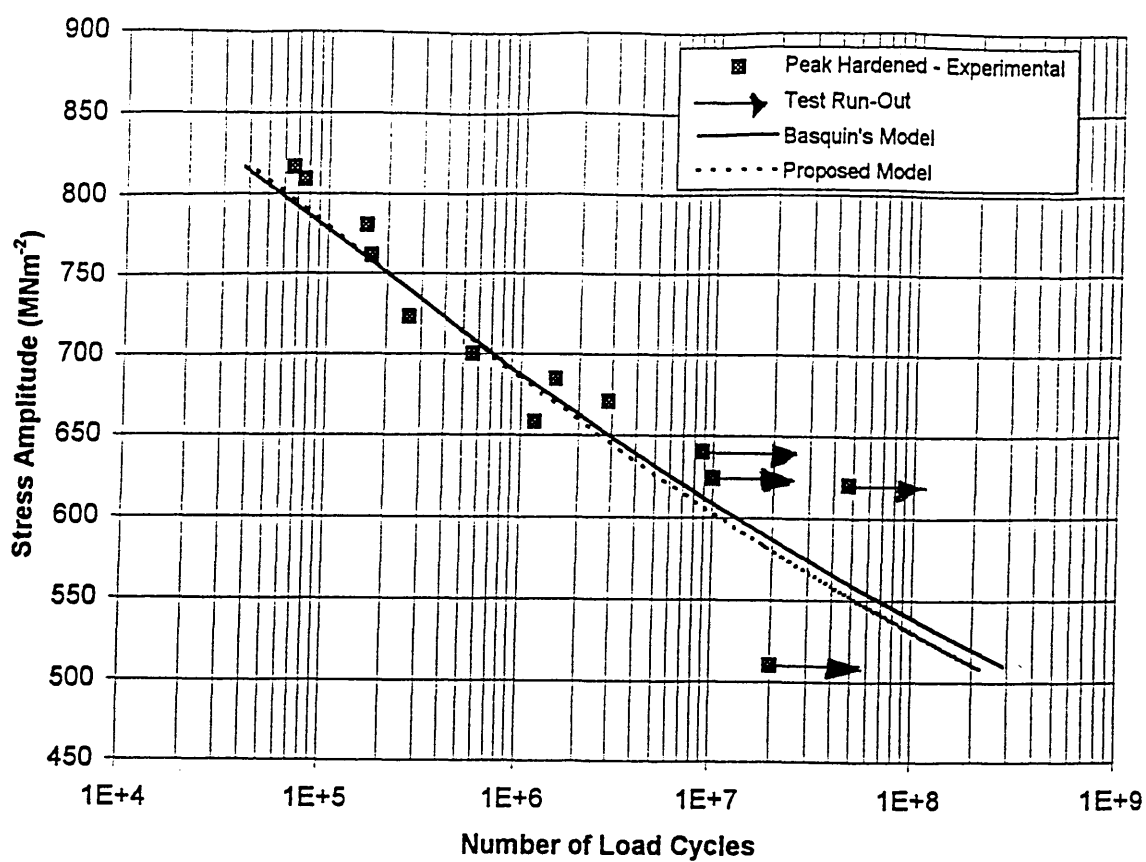


Figure 5.24d Comparison Between Predicted and Experimental Results for Total Fatigue Life of the Peak Hardened Condition in Air.

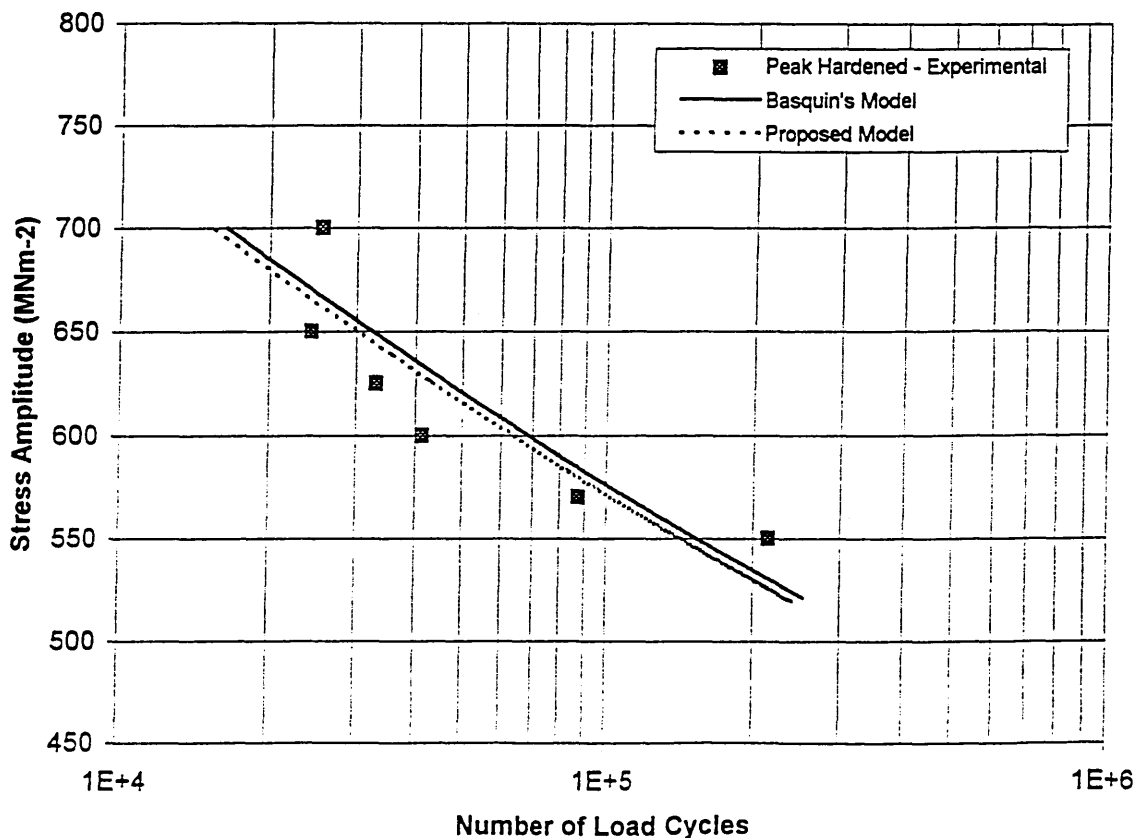


Figure 5.24e Comparison Between Predicted and Experimental Results for Propagation Life of the Peak Hardened Condition in the Chloride Environment.

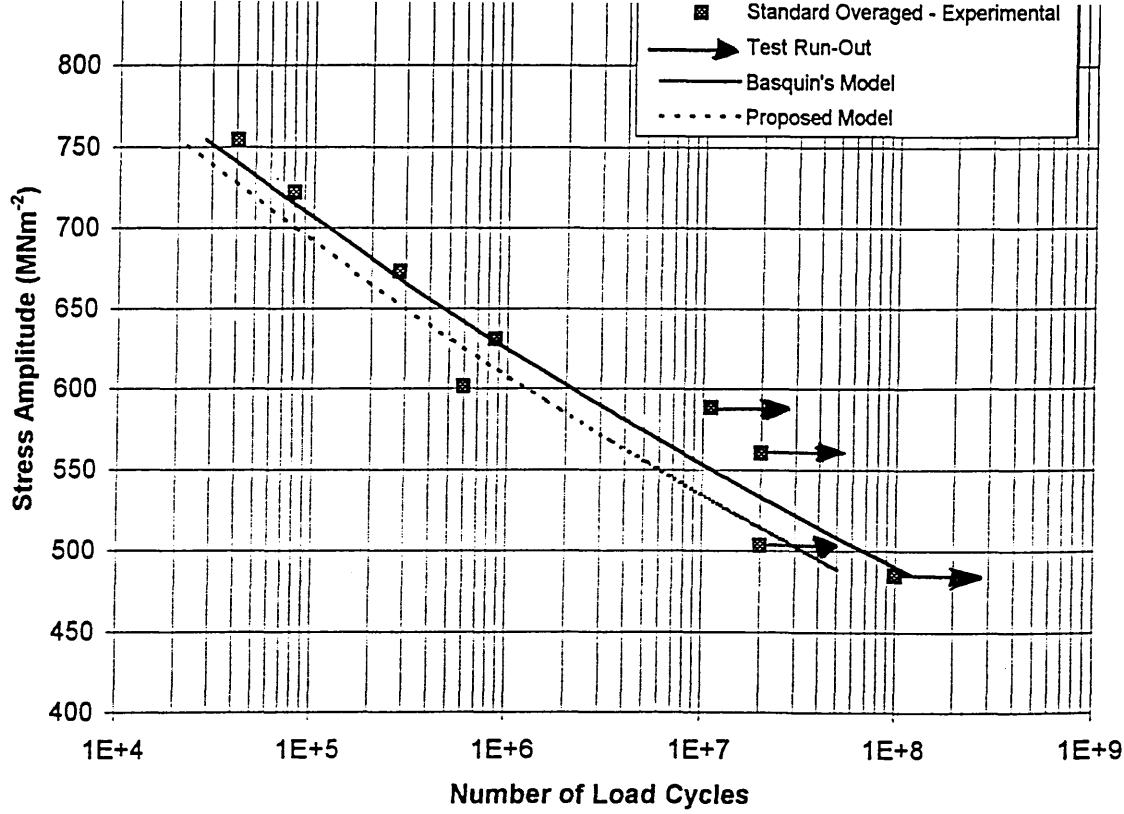


Figure 5.24f Comparison Between Predicted and Experimental Results for Total Fatigue Life of the Standard Overaged Condition in Air.

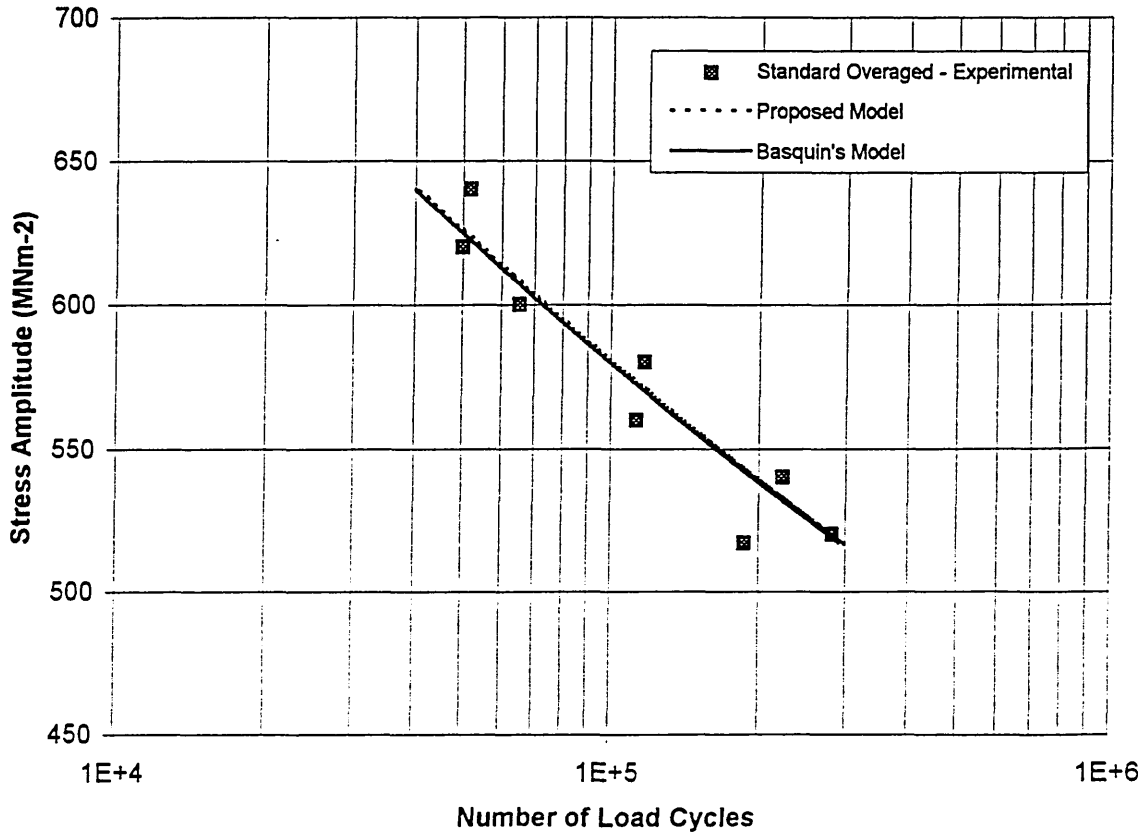


Figure 5.24g Comparison Between Predicted and Experimental Results for Propagation Life of the Standard Overaged Condition in the Chloride Environment.

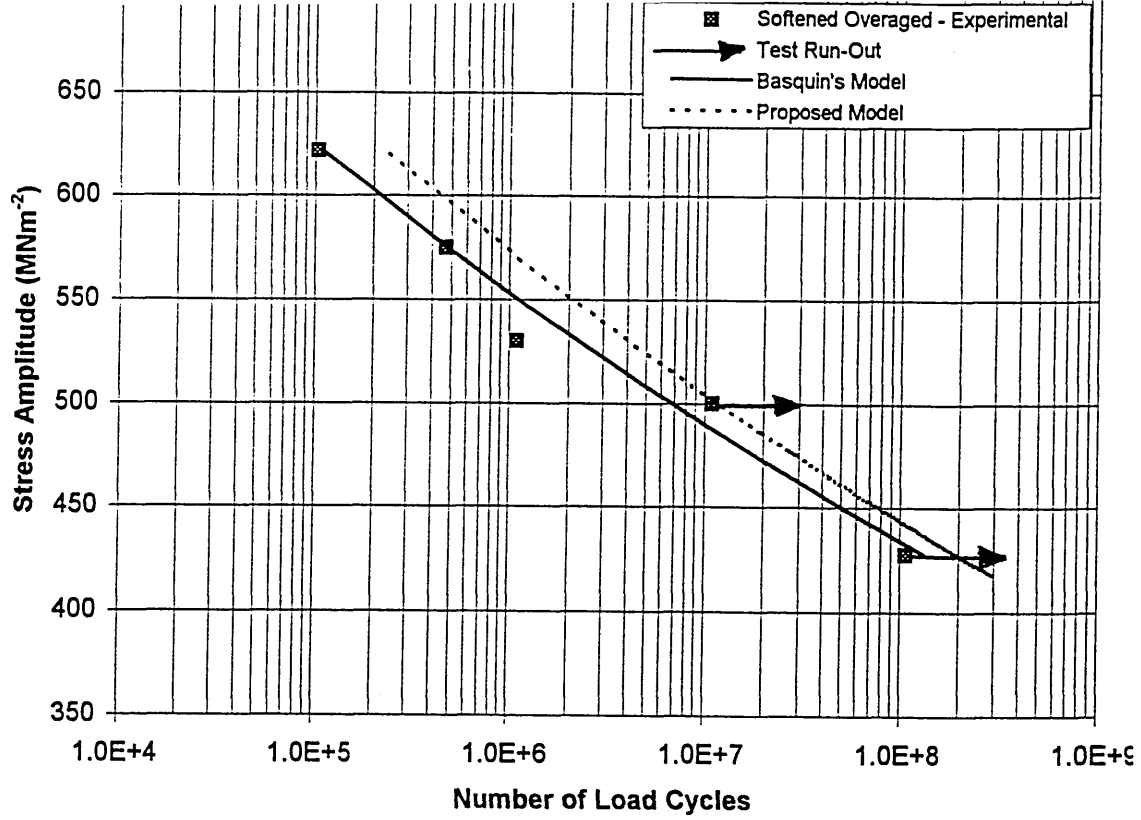


Figure 5.24h Comparison Between Predicted and Experimental Results for Total Fatigue Life of the Softened Overaged Condition in Air.

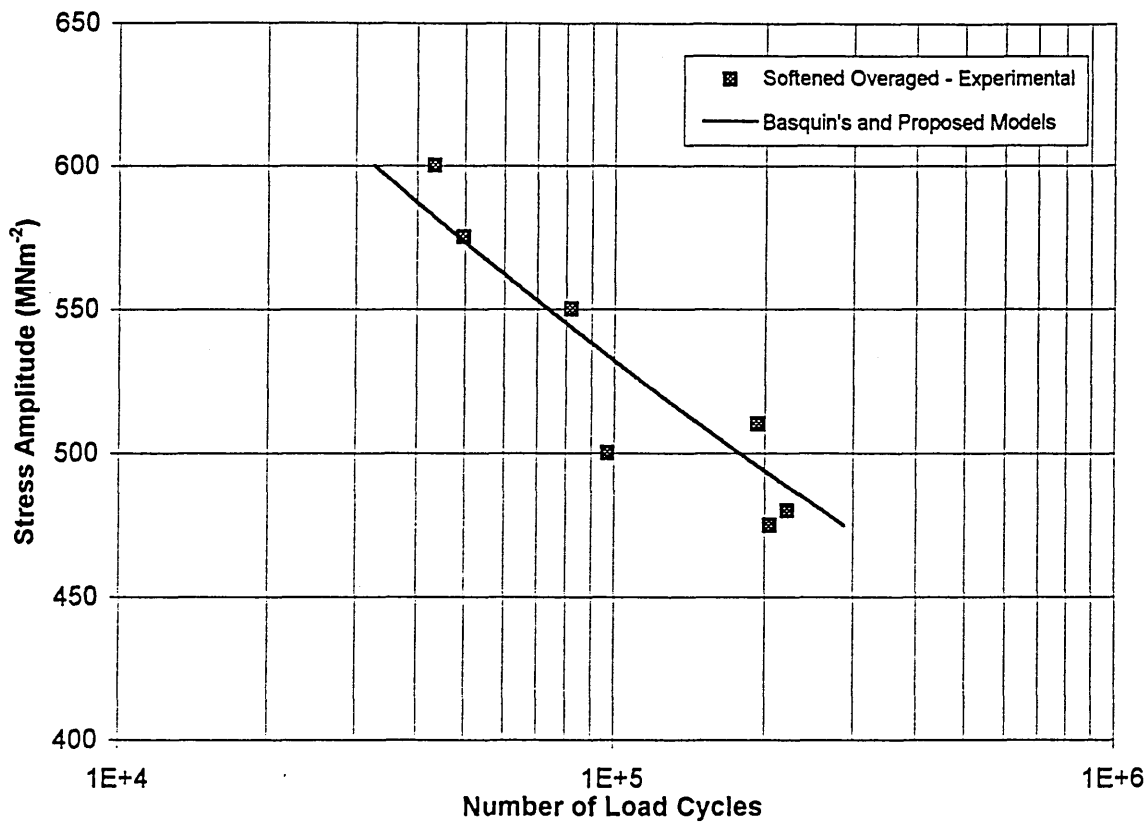


Figure 5.24i Comparison Between Predicted and Experimental Results for Propagation Life of the Softened Overaged Condition in the Chloride Environment.

5.6 Stress Corrosion Cracking in FV520B

Section 2.6 highlighted the propensity of high strength martensitic stainless steels to stress corrosion cracking in a chloride environment. Stress corrosion cracking in FV520B has previously been studied [83] and was characterised by distinctive intergranular fracture features which propagated along the prior austenite grain boundaries. During the course of this study, no intergranular fracture features were observed, i.e. the cracks propagated entirely in a transgranular manner which indicated that there was no incidence of stress corrosion cracking.

5.7 Concluding Remarks

The importance of the material microstructure under tensile and fatigue loading for a high strength stainless steel has been discussed. It has been clearly demonstrated that a weak microstructural phase, namely reverted austenite affected both the tensile and fatigue properties of the three microstructures, although this was not entirely clear from the endurance data alone. Under static loading, the tensile strength was impaired as the quantity of reverted austenite was increased. In contrast, under fatigue loading conditions, the presence of up to 21% was found to increase the resistance or the barrier effect imposed by the microstructure. The outcome was that the optimum resistance to crack propagation was observed when FV520B was heat treated to the standard overaged condition. Empirical formulas have been proposed to predict the 0.2% proof stress and the fatigue lives in air and the chloride environment, as a function of heat treatment and the percentage volume reverted austenite.

It has been shown that the fatigue crack nucleation mechanism is dependent on a number of factors which includes the amount of weaker reverted austenite phase, in addition to the applied stress amplitude. The size of the defects at the fatigue crack nucleation sites, i.e. the inclusions, corrosion pits or the "packets" of reverted austenite at which slip bands nucleated, were found to be small. Both types of defects were very small when compared to the corrosion pits which initiated fatigue cracks in a low alloy steel exposed to an aerated condensate in a published study [83]. Those pits were approximately 200-280 μm in depth [83].

The endurance data of the peak hardened condition of FV520B has been compared with the endurance data from two engineering steels; namely BS 251 grade A58 which is a high strength, low alloy steel [88] and BS 4360 grade 50B, a low carbon alloy steel [54]. The air and chloride endurance data which is presented in Figure 5.25 has been compared in terms of the equivalent shear stress amplitude.

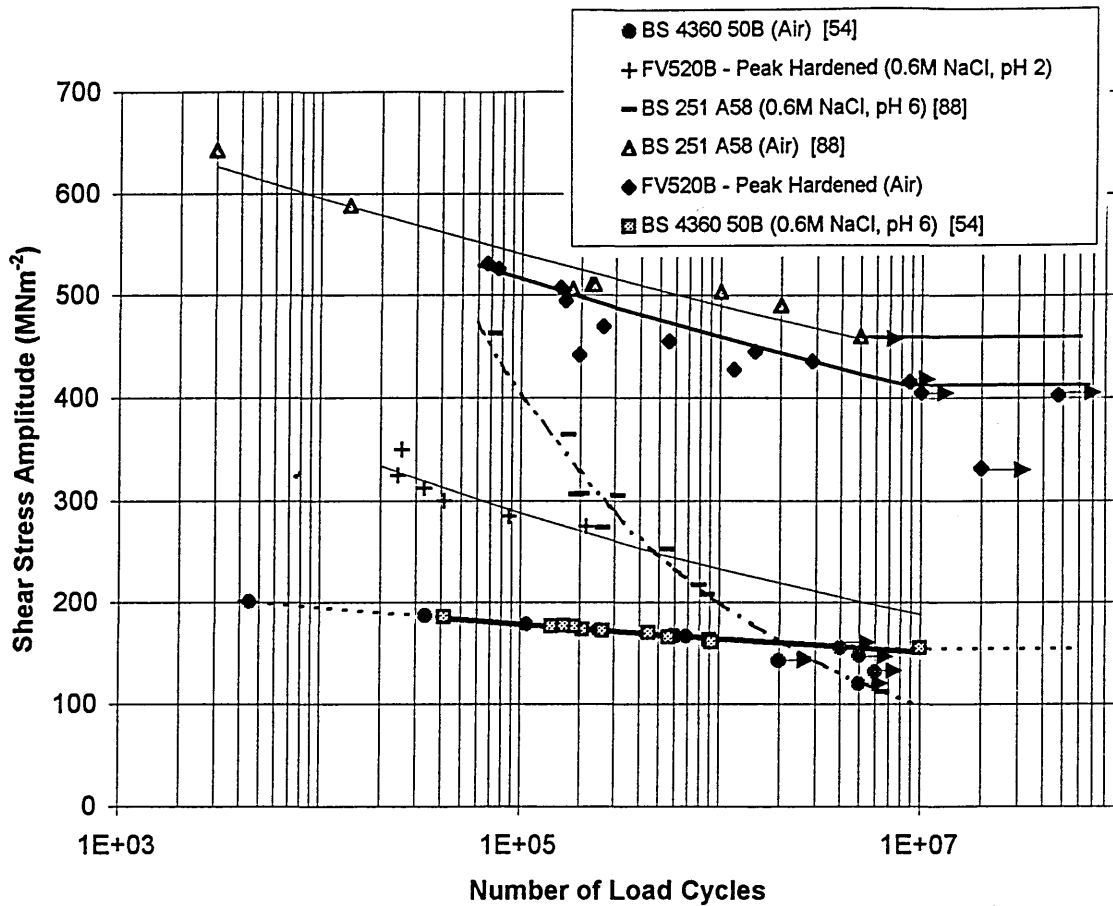


Figure 5.25 The Air and Chloride Endurance Data for the Three Engineering Steels.

The air fatigue endurance limit of FV520B in the peak hardened condition and BS 251 grade A58 are 407 MNm⁻² and 458 MNm⁻² respectively. These results suggest that the high strength for these essentially high tensile strength steels has been maintained under cyclic loading conditions. In contrast, a modest air fatigue endurance limit of 160 MNm⁻² is evident for the relatively lower strength, low alloy steel. Endurance data for the three steels subjected to a chloride environment is also presented in Figure 5.25.

The relative effect of a corrosive environment on the fatigue strength for each of the three steels is presented in Figure 5.26. In Figure 5.26, the ratio of fatigue strength in the chloride and the air environments is plotted against the fatigue endurance. A ratio equal to 1.0 indicates that the environment has no effect on the fatigue strength. Similarly, data points below 1.0 reflect the degree of environmental effect. It follows that, the greater the deviation from 1.0, the more damaging the effect of the environment on the fatigue strength.

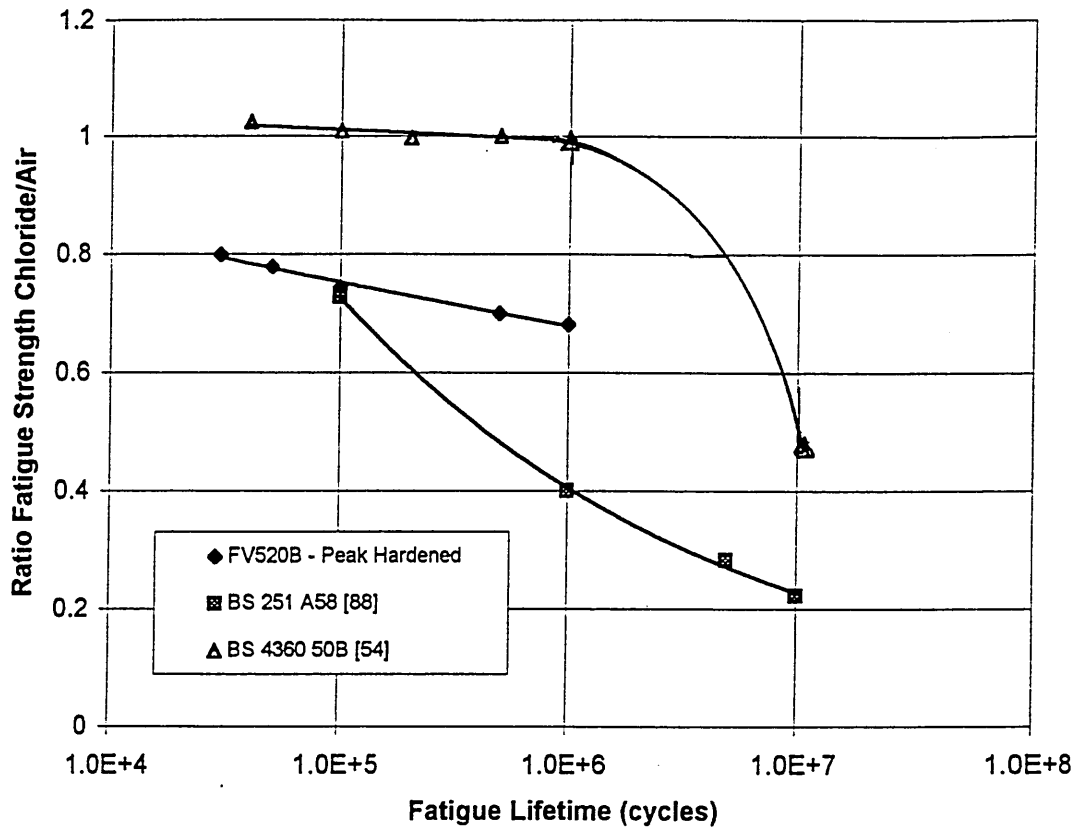


Figure 5.26 The Fatigue Performance of Three Engineering Materials in a Chloride Environment.

For lifetimes up to 1×10^6 cycles, the environment had little effect on the fatigue strength of the low carbon alloy steel [54], as evident by a ratio which was close to 1.0. At lifetimes greater than 1×10^6 cycles, the environment had a significant effect and reduced the ratio to a value of 0.5. In contrast, the ratio of the high strength, low alloy steel was 0.73 and 0.22 at lifetimes of 1×10^5 cycles and 1×10^7 cycles, respectively. This represents a loss of over 50% in the fatigue strength due to a longer exposure to the chloride environment. The results for FV520B falls between

the two alloys considered. Moreover, the high fatigue strength of the peak hardened condition of FV520B under more corrosive environmental conditions was sustained up to 1×10^6 cycles and is clearly shown. This is confirmation of FV520B's exceptional mechanical properties.

CHAPTER 6

CONCLUSIONS

1. The material microstructures of FV520B were found to be very complex as witnessed by Butterworth [14], Birch [15], Furniss et al [16] and Truman [21]. The expression developed to describe the flow stress of FV520B under tensile loading reflects the complex nature of the microstructure.
2. The high yield strength of the peak hardened condition can be attributed to a number of metallurgical factors, namely interstitial and substitutional solid solution hardening; precipitation hardening; grain boundary strengthening and dislocation strengthening.
3. During the precipitation hardening treatment, as the A_{C1} temperature is approached, the percentage of reverted austenite changes from 3% to 21%. A percentage of 43% of reverted austenite was detected on exceeding the A_{C1} temperature for a prolonged period of time.
4. The quantity of reverted austenite was found to have a profound effect on the fatigue properties, namely the fatigue crack nucleation phase and the materials resistance to fatigue crack propagation. If there was a continuous matrix of reverted austenite, i.e. when the percentage reverted austenite reached 43%, then a continuous crack path may have been available. However, when the quantity was 3%, the reverted austenite had little effect on the fatigue resistance since the crack path was at least discontinuous.
5. The fatigue strength of the peak hardened condition in the air and chloride environment was strongly dependent on the inclusion population over the range of applied stress amplitudes. In contrast, the standard and softened overaged conditions in the air and the chloride environment were more dependent on the quantity of the weak reverted austenite. The overaged conditions exhibited multiple crack nucleation probably due to slip band cracking originating from plastically deformed reverted austenite. The number of multiple nucleation sites was found to increase as the nominal stress amplitude increased.

6. This thesis discusses the differences between tensile deformation and fracture mechanisms and processes and those applicable to fatigue. In a corrosive environment, no correlation was found and in air only a tenuous relationship was indicated. However, there is no reason why the ratio fatigue limit/tensile strength, i.e. the endurance ratio, should have any physical reality.
7. The fatigue strength of the three microstructures in the corrosive chloride environment was found to be independent of their respective tensile strength. There was no corrosion fatigue limit at the lower nominal stress amplitudes studied here. For the case of the peak hardened material, reducing the test frequency had little effect on the corrosion fatigue strength.
8. The pitting corrosion kinetics of FV520B in the acidified chloride environment have been shown to be less dependent on time compared to previous studies [83] [124] [134]. An empirical formula defining the pit growth behaviour is therefore proposed as:

$$d = 7.8(1 - e^{-0.09t})$$

9. Compared against the peak hardened and softened overaged conditions the standard overaged condition exhibited a higher resistance to fatigue. The materials parameter (A), as outlined in equation (5.10), defines the materials resistance to crack propagation and is approximately 10% greater for the standard overaged condition than that in the peak hardened material. Similarly, the resistance of the softened overaged condition is reduced by approximately 55% when compared to the standard overaged condition.
10. An empirical relationship is proposed for the fatigue life prediction of FV520B for the air and the chloride environment.

The total fatigue life (N_f) in air is:

$$N_f = 10^{(57.73 - 4.25\gamma)} \sigma^{-18.2} + 18 \times 10^{30} [1 + e^{-10(\gamma - 0.3)} - 933.3 e^{-17(\gamma + 0.22)}] \sigma^{-9.3}$$

where N_f is the total fatigue life, σ represents the applied stress amplitude and γ the volume percentage reverted austenite.

Whilst in the 3.5% NaCl environment, when propagating a Stage I to a Stage II fatigue crack, the propagation life is defined by:

$$N_f = 18 \times 10^{30} [1 + e^{-10(\gamma - 0.3)} - 933.3 e^{-17(\gamma + 0.22)}] \sigma^{-9.3}$$

where N_f is the total fatigue life, σ represents the applied stress amplitude and γ the volume percentage reverted austenite.

CHAPTER 7

FURTHER WORK

Suggestions for further work in this area of research are as follows:

1. Characterise the reverted austenite within FV520B in terms of type and distribution using Transmission Electron Microscopy (TEM). This is because reverted austenite controls the fatigue resistance of the material in terms of crack path and crack propagation rate.
2. Investigate the stability of reverted austenite in FV520B after tensile and cyclic loading. This is important because a few interspersed high strain fatigue cycles may cause the reverted austenite to transform to martensite.
3. To evaluate the constants which account for strengthening due to alloy carbides in the proposed model describing the flow stress. These model constants can then be compared with the data available in the literature.
4. Determine the effect of microstructure on the polarisation characteristics of FV520B and evaluate the pitting potential (E_p). This is necessary since the effects of pitting may, under certain circumstances, be more damaging than in the present work.
5. To elucidate the effect of test frequency on the corrosion fatigue strength for the standard and softened overaged microstructures. This would complete our understanding gained from my investigation on the peak hardened material. Additionally, it should be noted that engineering plant operates over a wide range of frequencies.
6. Determine the effect of the chloride environment on the fatigue strength of FV520B at fatigue lifetimes in excess of 10^6 cycles. This is because the fatigue limit (in air) is approximately 10^6 to 10^7 cycles and the acidified 3.5% NaCl environment could essentially remove this limit.

REFERENCES

- [1] J. Denk (1994) *Materials for Advanced Power Engineering, Part 1*, Kluwer Academic Publishers, Netherlands, pp. 157-170.
- [2] R. Svoboda, H. Sandimann, S. Romanelli and M. Bodmer, Volatility of Anions in Steam-Water Systems of Power Plants. *Water Chemistry of Nuclear Reactor Systems 5*. BNES, London, 1989, pp. 229-234.
- [3] L.E. Willertz, T.M. Rust and V.P. Swaminathan (1982) High and Low Frequency Corrosion Fatigue of Some Turbine Blade Alloys. in *Ultrasonic Fatigue*, Vol. 1982, pp. 333-348. *Conf. Proc. 1st International Conference on Fatigue and Corrosion Fatigue up to Ultrasonic Frequencies*, held in Champion PA., 25-30 Oct 1981.
- [4] V.P. Swaminathan and J.W. Cunningham (1981) Correlations between LP Blade Failures and Steam Turbine Characteristics, *Conf. Proc. Corrosion Fatigue of Steam Turbine Blade Materials* (ed. R.I. Jaffree), Pergamon Press Limited, New York, USA, 1983, pp. 3-1 - 3-16.
- [5] L. Hagn (1981) Results of Corrosion Fatigue Tests with Blade Materials, *Conf. Proc. Corrosion Fatigue of Steam Turbine Blade Materials* (ed. R.I. Jaffree), Pergamon Press Limited, New York, USA, 1983, pp. 2-86 - 2-136.
- [6] W. Bertram, H. Buhl and K. Detert (1981) Screening Test Results for Evaluation of Corrosion Fatigue of Chromium-Stainless-Steels, *Conf. Proc. Corrosion Fatigue of Steam Turbine Blade Materials* (ed. R.I. Jaffree), Pergamon Press Limited, New York, USA, 1983, pp. 2.56-2.66.
- [7] P.-H. Effertz (1981) Tests in Order to Determine Pitting and Corrosion Susceptibility, *Conf. Proc. Corrosion Fatigue of Steam Turbine Blade Materials* (ed. R.I. Jaffree), Pergamon Press Limited, New York, USA, 1983, pp. 2-29 - 2-66.
- [8] Firth Vickers Data Handbook (1988) *Sheffield Forgemasters Limited Publ.*, Sheffield.
- [9] D.J. White (1970) Effect of Pins with Flats and Resin-Bonded Polytetrafluorethylene Coatings on the Fatigue Strength of Large Pinned Connections made from Alloy Steel FV520B. *Proc. Instn. Mech. Engrs.*, 1970-1, Vol. 185, No. 49, pp. 707-716.

- [10] D.J. White (1968) The Fatigue Strength of Large Single-Pinned and Double-Pinned Connections made from Alloy Steel FV520B. Proc. Instn. Mech. Engrs., 1968-9, Vol. 183, Pt. 1, No. 26, pp. 563-578.
- [11] D.J. White (1968) Fatigue Strength of Small Pinned Connections made from Alloy Steel FV520B. Proc. Instn. Mech. Engrs., 1967-8, Vol. 182, Pt 1, No.28, pp. 615-630.
- [12] J.E. Truman, R. Perry and G.N. Chapman (1964) Stress-Corrosion Cracking of Martensitic Stainless Steels. *J. Iron Steel Inst.*, Vol. 202, p. 745.
- [13] M. Henthorne, Private Communication with J.D. Atkinson.
- [14] D.P. Butterworth (1982) The Effect of Heat Treatment on the Structure and Mechanical Properties of FV 520(B), A Precipitation Hardening Martensitic Stainless Steel. BSc Project thesis, Sheffield City Polytechnic.
- [15] P. Birch (1984) The Effect of Heat Treatment on the Structure and Mechanical Properties of FV 520(B). A Precipitation Hardening Martensitic Stainless Steel. BSc Project thesis, Sheffield City Polytechnic.
- [16] I. Furniss and E.A. Wilson (1987) Studies on Stainless Maraging Steels Hardened with Copper. Project thesis, Sheffield City Polytechnic, pp. 1-26.
- [17] G.M. Sparkes (1981) Stress Corrosion Crack Propagation in FV520B Turbine Blade Steel, CEGB Internal Report, Ref. MID/SSD/81/0055/R, Contract Number ZC 320A, pp. 1-7.
- [18] H. Kitagawa, (1972) A Fracture Mechanics Approach to Ordinary Corrosion Fatigue of Unnotched Steel Specimens, National Association of Corrosion Engineers, pp. 521-528.
- [19] A. Atrens, H. Meyer, G. Faber and K. Schneider Steam Turbine Blades. Conf. Proc. *Corrosion In Power Generating Equipment*, held in Switzerland, 19-20 Sept, 1983, pp. 299-330.
- [20] B. Knosp, H. Saisse and A. Coulon (1984) Influence of Corrosive Environment on Fatigue Crack Initiation in Alloys for Steam Turbine Blades. Conf. Proc. *Advances in Fracture Research (Fracture 84)*, Vol. 4, held in India, 4-10 Dec 1984, pp. 2497-2504.
- [21] J.E. Truman (1994) Jessop Saville Limited, Private Communication.

- [22] P. Liu, A. Hultin Stigenberg and J.-O. Nilsson (1994) Isothermally Formed Quasicrystalline Precipitates used for Strengthening in a New Maraging Stainless Steel. *Scripta Metallurgica*, Vol. 31, No. 3, pp. 249-254.
- [23] S. Floreen (1968) The Physical Metallurgy of Maraging Steels. *Metallurgical Reviews*, Review No. 126, pp. 115-128.
- [24] A.R. Cox (1967) Metallography of a 0.3%C and a 0.3%C-1.5%Cu Steel in the Tempered Condition, *Journal of the Iron and Steel Institute*, Vol. 205, pp. 51-57.
- [25] S.R. Goodman, S.S. Brenner and J.R. Low (1973) An FIM-Atom Probe Study of the Precipitation of Copper from Iron-1.4 At. Pct Copper. *Metallurgical Transactions*, Vol. 4, pp. 2363-2369.
- [26] E. Hornbogen (1964) Aging and Plastic Deformation of an Fe-0.9%Cu Alloy. *Transactions of the AIME*, Vol. 57, pp. 120-132.
- [27] X. Li and Z. Yin (1995) Reverted Austenite during Aging in 18Ni(350) Maraging Steel, *Materials Letters*, Vol. 24, pp. 239-242.
- [28] N. Atsmon and A. Rosen (1981) Reverted Austenite in Maraging Steel, *Metallography*, Vol. 14, pp. 163-167.
- [29] A. Markfield and A. Rosen (1980) The Effect of Reverted Austenite on the Plastic Deformation of Maraging Steel, *Materials Science and Engineering*, Vol. 46, pp. 151-157.
- [30] R.W.K. Honeycombe (1981) *Steels: Microstructures and Properties*, Edward Arnold Publishers Limited, London.
- [31] V.M. Schastilivtsev, V.Y. Kaletina, I.L. Yakovleva, P.S. Lantsman, Y.N. Simonov, A.Y. Kaletin (1990) Stability of Reverted Austenite and its Influence on the Impact Toughness of Steel 03Kh11N8M2F, *Physics of Metals and Metallography*, Vol. 67. No. 2, pp. 148-155.
- [32] E.O. Hall (1951) The Deformation and Aging of Mild Steel: III Discussion of Results, *Proc. Royal Society* 64B, pp. 747-753.
- [33] N.J. Petch (1953) The Cleavage Strength of Polycrystals, *JISI*, Vol. 174, pp. 25-28.
- [34] D.W. Smith and R.F. Heheman (1971) Influence of Structural Parameters on the Yield Strength of Tempered Martensite and Lower Bainite. *JISI*, June, pp. 476-481.

- [35] A. Wöhler (1860) Versuche über die Festigkeit der Eisenbahnwagenachsen, *Zeitschrift für Bauwesen* Vol. 10. English Summary found in *Engineering*, (1867), Vol. 4, pp. 160-161.
- [36] R. Akid and K.J. Miller (1991) Short Fatigue Crack Growth Behaviour of a Low Carbon Steel under Corrosion Fatigue Conditions. *Fatigue Fract. Engng Mater. Struct.*, Vol. 14, No. 6, pp. 637-649.
- [37] F.B. Pickering (1978) *Physical Metallurgy and the Design of Steels*. Applied Science Publishers, London, UK, p. 3.
- [38] O.H. Basquin (1910) The Exponent Law of Endurance Tests. Conf. Proc. ASTM, Vol. 10, Part II, pp. 625-630.
- [39] R.W. Hertzberg (1989) *Deformation and Fracture Mechanics of Engineering Materials*, 3rd edition, John Wiley & Sons, Singapore, Hong Kong, p. 497.
- [40] T.V. Duggan and J. Byrne (1977) *Fatigue as a Design Criterion*, The Macmillan Press Limited, London, UK, p. 70.
- [41] K.J. Miller (1982) The Short Crack Problem. *Fatigue and Engineering Materials and Structures* Vol. 5, No. 3, pp. 223-232.
- [42] N. Thompson and N.J. Wadsworth (1958) Metal Fatigue. *Adv. Phys.*, Vol. 7, pp. 72-169.
- [43] P.J.E. Forsyth (1953) Exudation of Material from Slip Bands at the Surface of Fatigued Crystals of an Aluminium-Copper Alloy, *Nature* Vol. 171, p. 172.
- [44] P.J.E. Forsyth (1957) Slip Band Damage and Extrusion, *Proc. Roy. Soc.*, Vol. A242, pp. 198-202.
- [45] A.H. Cottrell and D. Hull (1957) Extrusion and Intrusion by Cyclic Slip in Copper, *Proc. Roy. Soc.*, Vol. A242, pp. 211-213.
- [46] W.A. Wood (1958) Formation of Fatigue Cracks. *Phil. Mag.*, Vol. 3, pp. 692-699.
- [47] P.J.E. Forsyth (1955) The Slip Band Extrusion Effect Observed in some Aluminium Alloys Subjected to Cyclic Stresses, *J. Inst. Met.*, Vol. 83, pp. 393-398.
- [48] C. Laird (1976) The Fatigue Limits of Metals. *Materials Science and Engineering*, Vol. 22, pp. 231-236.

- [49] J.D. Atkinson (1973) Fatigue and the Bauschinger Effect in Dispersion Hardened Copper Single Crystals. Ph.D. thesis, Univ. of Cambridge.
- [50] A.T. Winter (1974) A Model for the Fatigue of Metals at low Plastic Strain Amplitude. Ph.D. thesis, Univ. of Cambridge.
- [51] P. Mayr and E. Macherauch (1980) Influence of Stress Amplitude on Crack Initiation in a Normalised Plain Carbon Steel with 0.2wt% Carbon. *Scripta Metallurgica*, Vol. 14, pp. 1167-69.
- [52] T. Yokobori, M. Nanbu and N. Takeuchi (1968) On The Initiation and Propagation of Fatigue Crack. Conf. Proc. *3rd Conference on Dimensioning*, held in Budapest, Hungary, 1968, pp. 363-376.
- [53] J.K. Solberg (1988) Fatigue Crack Initiation in Quenched Low Carbon Steel Microstructures. *Materials Science and Engineering A*, Vol. 101, pp. 39-46.
- [54] R. Akid (1987) The Initiation and Growth of Short Fatigue Cracks in an Aqueous Saline Environment. Ph.D. thesis, Univ. of Sheffield.
- [55] J.G. Taylor (1976) Fatigue in Pearlitic Structures. Ph.D. thesis. Sheffield City Polytechnic.
- [56] P. Fox (1969) Fatigue Crack Initiation and Propagation in Plain Carbon-Manganese Steels. M. Phil thesis. Sheffield City Polytechnic.
- [57] P.J.E. Forsyth (1961) A Two Stage Process of Fatigue Crack Growth. *Symposium on Crack Propagation*, Cranfield, England, pp. 76-94.
- [58] E.R. de los Rios (1989) Experimental Techniques to Observe and Monitor Short Fatigue Cracks. in *Advances in Fatigue Science and Technology* (edited by C. Moura Branco and L. Guerra Rosa), Kluwer Academic Publishers, pp. 265-281.
- [59] P.D. Hobson, M.W. Brown and E. de los Rios (1986) Two Phases of Short Crack Growth in a Medium Carbon Steel in *The Behaviour of Short Cracks EGF1*, (Eds K.J. Miller and E.R. de los Rios), MEP Inst Mech Engrs, pp. 441-459.
- [60] A. Navarro and E.R. de los Rios (1988) A Microstructurally Short Crack Equation. *Fatigue Fract. Engng. Mater. Struct.*, Vol. 11, pp. 383-396.
- [61] M.A. Hicks and C.W. Brown (1984) A Comparison of Short Crack Growth Behaviour in Engineering Alloys. *Conf. Proc. Fatigue 84*, pp. 1337-1347.

- [62] J. Lankford (1982) The Growth of Small Fatigue Cracks in 7075-T6 Aluminium. *Fatigue of Engineering Materials and Structures*, Vol. 5, No. 3 pp. 233-248.
- [63] S. Suresh (1996) *Fatigue of Materials*, Cambridge University Press, London UK, p. 310 and pp. 363-367.
- [64] R.P. Gangloff (1981) The Criticality of Crack Size in Aqueous Corrosion Fatigue, *Res Mechanica Letters*, Vol. 1, pp. 299-306.
- [65] F.B. Pickering, Some Effects of Non-Metallic Inclusions on the Properties of Steels. Conf. Proc. *31st Mechanical Working and Steel Processing*, held in Illinois, USA, 22-25 Oct 1989, pp. 381-401.
- [66] K. Kovacs, M. Reger and Y.P. Tardy (1992) The Role of Inclusions in Different Fracture Types. Conf Proc. *Clean Steel 4*, pp. 44-60, 8-10 June 1992, Hungary.
- [67] N.M.A. Eid and P.F. Thomason (1979) The Nucleation of Fatigue Cracks in a Low-Alloy Steel under High-Cycle Fatigue Condition and Uniaxial Loading. *Scripta Metallurgica* Vol. 27, pp. 1239-1249.
- [68] J. Lankford and F.N. Kusenberger (1973) Initiation of Fatigue Cracks in 4340 Steel. *Metallurgical Transactions* Vol. 4, pp. 553-559.
- [69] A.I. Gustavsson and A. Melander The Influence of Inclusions on the Fatigue Limit of Hardened Steels, Conf Proc. *5th International. Conference Fatigue and Fatigue Thresholds*, held in Canada 3-7 May 1993, Vol. 1, pp. 297-302.
- [70] W.E. Duckworth and E. Ineson (1963) Title. Special Report No. 77, *Iron and Steel Inst.*, p. 87.
- [71] Y. Murakami and T. Endo (1994) Effects of Defects, Inclusions and Inhomogeneities on Fatigue Strength, *Int. J. Fatigue*, Vol. 6, pp. 163-182.
- [72] Y. Murakami and T. Endo (1992) The $\sqrt{\text{Area}}$ Parameter Model for Small Defects and Inclusions on Fatigue Strength: Experimental Evidence and Applications, in *Theoretical Concepts and Numerical Analysis of Fatigue* (eds A.F. Blom and Beevers), Chpt 28, pp. 51-71.
- [73] J. Congleton and T.P. Wilks (1988) The Air Fatigue and Corrosion Fatigue of a 13%Cr Turbine Blade Steel. *Fatigue Fract. Engng Mater. Struct.*, Vol. 11, No. 2, pp. 139-148.

- [74] N.E. Frost (1961) A Note on the Behaviour of Fatigue Cracks. *J. Mech. Phys. Solids*, Vol. 9, pp. 143-151.
- [75] H. Kobayashi and H. Nakazawa (1969) In Proceedings 1st International Conference Mechanical Behaviour of Materials, Japan, Vol. II, pp. 199-208.
- [76] Y. Murakami, S. Kodama and S. Konuma (1989) Quantitative Evaluation of Effects of Non-Metallic Inclusion of Fatigue Strength of High Strength Steels. I: Basic Fatigue Mechanism and Evaluation of Correlation Between the Fatigue Fracture Stress and the Size and Location of Inclusions. *Int J Fatigue*, Vol. 11, No. 5, pp. 291-298.
- [77] A. Clark (1997) Examination of Failed Actuator Springs, ex BP Bruce Well A09 (A4), Internal Report, Oilfield Inspection Services (OIS) plc. Aberdeen, UK
- [78] H.H. Uhlig (1971) *Corrosion and Corrosion Control*, 2nd edition, John Wiley & Sons, USA.
- [79] D.A. Vermilyea (1976) Physics of Corrosion, *Physics Today*, Sept pp. 23-31.
- [80] R. Kiessling (1989) *Inclusions in Steel. Part V*, The Institute of Metals, London, UK.
- [81] J.D. Redmond and K.H. Miska (1982) The Basics of Stainless Steels. *Chemical Engineer*, 18th Oct, pp. 79-93.
- [82] W.F. Smith (1990) *Principles of Materials Science and Engineering*, 2nd Edition, McGraw-Hill International Editions, Singapore.
- [83] G.M. Sparkes and P. Mulvihill (1987) The Implications of Corrosion Pitting for the Refurbishment of Low-Pressure Turbine Rotor Shafts. Internal Report No. C302/87, Published by I Mech E, pp. 315-322.
- [84] J.H. Gough (1932) Corrosion Fatigue of Metals. *J. Inst. Metals*, Vol. 49, pp. 17-92.
- [85] P. Mulvihill (1998) Powergen, Power Technology Centre, Nottingham, Private Communication.
- [86] M.K. Wedgbury (1990) Environmentally-Assisted Crack Growth in Deaerator Storage Vessel Steels. Ph.D thesis, CNAAs.
- [87] J.C. Scully (1975) *The Fundamentals of Corrosion*, 2nd Edition, Pergamon Press, Oxford, p. 202.

- [88] X-D Wu (1996) Experimental and Theoretical Studies of Corrosion Fatigue in a High Strength Steel. Ph.D thesis, Univ. of Sheffield.
- [89] B.P. Haigh (1917) Experiments of the Fatigue of Brasses. *J Inst. Metals*, Vol. 18, pp. 55-77.
- [90] D.J. McAdam (1926) Stress-Strain Cycle Relationship and Corrosion Fatigue of Metals, *Proc. Amer. Soc. Test. Mat.*, Vol. 26, (II) pp. 224-254.
- [91] H.J. Gough and D.G. Sopwith (1932) Atmospheric Action as a Factor in Fatigue of Metals. *J. Inst. Metals*, Vol. 49, pp. 92-122.
- [92] T. Magnin (1995) Recent Advances for Corrosion Fatigue Mechanisms. *Iron and Steel Journal International*, Vol. 35, No. 3, pp. 223-233.
- [93] Y. Kondo and R.P. Wei (1989) Approach on Quantitative Evaluation of Corrosion Fatigue Crack Initiation Condition. Conf. Proc. *Evaluation of Material Performance in Severe Environments*, Japan, Vol. 1, pp. 135-142, , 2
- [94] J.C. Scully (1979) The Role of Surface Films in Stress Corrosion Cracking and Corrosion Fatigue. Conf. Proc. *Environment Sensitive Fracture of Engineering Materials*, Oct 1979, Vol. 77, pp. 595-613.
- [95] R. Mathis (1987) Initiation and Early Growth Mechanisms of Corrosion Fatigue Cracks in Stainless Steels. *Journal of Materials Science*, Vol. 22, pp. 907-914.
- [96] R.E. Wilde (1971) Mechanism of Cracking of High Strength Martensitic Stainless Steels in Sodium Chloride Solutions. Corrosion - National Association Corrosion Engineers (NACE), Vol. 27, No. 8, pp. 326-333.
- [97] C.J. Thomas, R.G.J Edyvean, R. Brook and W.G. Ferguson (1986) Environmentally Assisted Crack Growth in a Martensitic Stainless Steel. *Materials Science and Engineering*, Vol. 78, pp. 55-63.
- [98] E.H. Phelps (1973) Stress Corrosion of Ferritic Martensitic Stainless Steel, *Metals Engng Q*, May p. 44-49.
- [99] P. Hewitt and B.S. Hockenhull (1976) The Effect of Microstructures on the Stress Corrosion Cracking Susceptibility of a 13%Cr Martensitic Stainless Steel. *Corrosion Science* , Vol. 16, pp. 47-51.
- [100] Homer Research Laboratories, Bethlehem Steel Corp. (1983) Metallographic Reagents for Iron and Steel. *Metal Progress*, pp. 91-96.

- [101] BS 7590:1992. British Standard Methods for Statistically Estimating the Volume Fraction of Phases and Constituents by Systematic Manual Point Counting with a Grid, British Standards Institution, BSI, UK.
- [102] BS 4490:1989 Section Three. British Standard Methods for Micrographic Determination of the Grain Size of Steel, British Standards Institution, BSI, UK.
- [103] F. B. Pickering (1976) *The Basis of Quantitative Metallography*, Monograph No. 1 Publ Metals and Metallurgy Trust for the Institute of Metallurgical Technicians, London, pp. 15-20.
- [104] J. Durnin and K. A. Ridal (1968) Determination of Retained Austenite in Steel By X-Ray Diffraction. *Journal of the Iron and Steel Institute*, Vol. 206, pp. 60-67.
- [105] B.D. Cullity (1978) *Elements of X-Ray Diffraction*, 2nd edition, (edited by M. Cohen), Addison-Wesley Publishing Company USA, pp. 407-412, p 506, pp. 514-517.
- [106] *International Tables for X-Ray Crystallography, Vol IV: Revised and Supplementary Tables* (1974), Kynoch Press Birmingham, pp. 71-97, pp. 148-151.
- [107] *International Tables for X-Ray Crystallography, Vol II: Mathematical Tables* (1959), Kynoch Press Birmingham, pp. 241-255.
- [108] *International Tables for X-Ray Crystallography, Vol III: Physical and Chemical Tables* (1962), Kynoch Press Birmingham, pp. 233-235.
- [109] C. Li (1996) Effect of Heat Treatment on the Microstructure of a 2CrMoNiWV Rotor Steel. Ph.D. Thesis, Sheffield Hallam University, pp. 60-61.
- [110] A. Sayles (1994) British Steel Swinden Technology Centre, Private Communication.
- [111] American Society for Metals (1985) *Metals Handbook*, 9th Edition, Vol 9, Chapter "Metallography and Microstructures", Ohio USA, pp. 89-102.
- [112] J.Z. Briggs and T.D. Parker (1965) *The Super 12% Cr Steels*, published by Climax Molybdenum Company, USA, pp. 6.
- [113] E.R. Petty (1970) *Martensite: Fundamentals and Technology*, Longman Group Limited, London, UK, p. 119.

- [114] J-B Vogt, G. Degallaix and J. Foct (1988) Cyclic Mechanical Behaviour and Microstructure of a 12Cr-1Mo-V Martensitic Stainless Steel, *Fatigue Fract. Engng Mater. Struct.*, Vol. 11, No. 6, pp. 435-446.
- [115] I.L.W. Wilson and B. W. Roberts, Conf. Proc. *Environment-Sensitive Fracture of Engineering Materials*, October 1977, AIME-ASM (1979) pp. 595-612.
- [116] Iron and Steel Specifications Handbook (1989) 7th Edition published by British Steel plc. UK.
- [117] S.S Manson (1953) Behaviour of Materials under Conditions of Thermal Stress, Heat Transfer Symposium, University of Michigan Engineering Research Institute, pp. 9-75.
- [118] M. Kawahara, T. Fujita, M. Kurihara, H. Inagaka, H. Kitagawa (1988) Corrosion Fatigue Crack Initiation of Carbon Steels in Seawater. ASTM STP 924, Some Basic Questions in Fatigue, Vol. 2, pp. 145-163.
- [119] H. Schneider (1960) Investment Casting of High-Hot-Strength 12-per-cent. Chrome Steel. *Foundry Trade Journal*, May, pp. 562-563.
- [120] P.J. Goodhew (1984) *Specimen Preparation for Transmission Electron Microscopy of Materials*, Royal Microscopical Society Microscopy Handbooks 03, Oxford University Press, pp. 29.
- [121] B. Lewis (1994) Sheffield Hallam University, Private Communication.
- [122] H. Conrad (1961) Yielding and Flow of Iron in *Iron and its Diluted Solid Solutions*, (Eds C.W. Spencer and F.E. Werner), AIME/Interscience-Wiley, Metallurgy Conference Volume, p. 315.
- [123] R.L. Fleischer (1962) Solution Hardening, *Acta Metallurgica*, Vol. 10, pp. 835-842.
- [124] Aluminium. (1983) Konstruktions-och Materiallära. Metallnormcentralen, Stockholm, MNC Handbook nr 12, p.85.
- [125] P.G. Winchell and M. Cohen in *Electron Microscopy and the Strength of Solids*, eds G. Thomas and J. Washburn, Interscience Publications, New York, USA, pp. 995-1006.
- [126] W.A. Wood (1958) Recent Observations on Fatigue Failure in Metals, Symposium on Basic Mechanisms in Fatigue, pp. 110-119.

- [127] J.A. Ewing and J.L.W. Humphrey (1903) The Fracture of Metals under Repeated Alternations of Stress, *Phil. Trans Roy Soc.*, A200 pp. 241-250.
- [128] R.A. Smith and K.J. Miller (1977) Fatigue Cracks at Notches, *Int. J. Mech. Sci.*, Vol 19, pp. 11-22.
- [129] S. Suresh (1996) *Fatigue of Materials*, Cambridge University Press, London UK, p. 294, 310 and pp. 363-367.
- [130] N.F. Mott (1958) A Theory of the Origin of Fatigue Cracks, *Acta Metallurgica*, Vol. 6, pp. 195-197.
- [131] C.M Maggi and K. Schneider (1981) Corrosion Resistant Alloy Approach for Steam Turbine Blades, Conf. Proc. *Corrosion Fatigue of Steam Turbine Blade Materials* (ed. R.I. Jaffree), Pergamon Press Limited, New York, USA, 1983, pp. 5-37 - 5.46.
- [132] P.M. Kelly and J. Nutting (1965) Strengthening Mechanisms in Martensite, *ISI Special Report 93*, pp. 166-170.
- [133] L.F. Coffin Jr. (1954) A Study of the Effects of Cyclic Thermal Stresses on a Ductile Metal, *Trans. ASME*, Vol. 76, pp. 931-950.
- [134] D. Knotkova et al (1982) *Atmospheric Corrosion of Metals*, ASTM STP 767, Philadelphia, p. 7.
- [135] G. Wranglén (1974) Pitting and Sulphide Inclusions in Steel, *Corrosion Science*, Vol. 14, pp. 331-349.
- [136] J.A. Bannantine, J.J. Comer and J.L. Handrock (1990) *Fundamentals of Metal Fatigue Analysis*, Prentice-Hall Inc., New Jersey, US, p.103.

APPENDICES

Appendix I - Data Tables

Appendix II - FV520B Manufacturer's Data Handbook

Appendix III - Chemical Analysis of Maraging Steels

Appendix IV - Published Work

APPENDIX I - Data Tables

Table D1	X-Ray Diffraction Data for the Peak Hardened Condition.
Table D2	X-Ray Diffraction Data for the Standard Overaged Condition.
Table D3	X-Ray Diffraction Data for the Softened Overaged Condition.
Table D4	Isothermal Precipitation Hardening Data at 450°C.
Table D5	Endurance Test Data for the Peak Hardened Condition.
Table D6	Endurance Test Data for the Standard Overaged Condition.
Table D7	Endurance Test Data for the Softened Overaged Condition.
Table D8	Corrosion Fatigue Endurance Data for the Peak Hardened Condition.
Table D9	Corrosion Fatigue Endurance Data for the Standard Overaged Condition.
Table D10	Corrosion Fatigue Endurance Data for the Softened Overaged Condition.
Table D11	Corrosion Fatigue Endurance Data for the Peak Hardened Condition.

Line	2θ	θ ($^\circ$)	θ (rads)	$\sin^2\theta\lambda^{-1}$	Lattice	d (Å)	N	(hkl)	Phase
1	50.80	25.40	0.4433	0.278	fcc	1.7955	4	200	γ
2	64.89	32.44	0.5663	0.348	bcc	1.4358	4	200	α'
3	74.84	37.42	0.6531	0.394	fcc	1.2677	8	220	γ
4	82.12	41.06	0.7166	0.426	bcc	1.1727	6	211	α'
5	90.73	45.36	0.7918	0.462	fcc	1.0834	11	311	γ
6	98.64	49.32	0.8608	0.492	bcc	1.0157	8	220	α'

Table D1 X-Ray Diffraction Data for the Peak Hardened Condition.

Line	2θ	θ ($^\circ$)	θ (rads)	$\sin^2\theta\lambda^{-1}$	Lattice	d (Å)	N	(hkl)	Phase
1	50.81	25.40	0.4434	0.278	fcc	1.7955	4	200	γ
2	64.90	32.45	0.5663	0.348	bcc	1.4356	4	200	α'
3	74.68	37.34	0.6517	0.394	fcc	1.2699	8	220	γ
4	82.14	41.07	0.7168	0.426	bcc	1.1725	6	211	α'
5	90.63	45.31	0.7909	0.461	fcc	1.0834	11	311	γ
6	98.66	49.33	0.8609	0.492	bcc	1.0156	8	220	α'

Table D2 X-Ray Diffraction Data for the Standard Overaged Condition.

Line	2θ	θ (°)	θ (rads)	$\sin^2\theta\lambda^{-1}$	Lattice	d (Å)	N	(hkl)	Phase
1	50.89	25.40	0.4434	0.278	fcc	1.7929	4	200	γ
2	64.94	32.45	0.5664	0.348	bcc	1.4348	4	200	α'
3	74.77	37.34	0.6517	0.394	fcc	1.2687	8	220	γ
4	82.17	41.07	0.7168	0.426	bcc	1.1721	6	211	α'
5	90.73	45.31	0.7909	0.461	fcc	1.0825	11	311	γ
6	98.68	49.33	0.8609	0.492	bcc	1.0154	8	220	α'

Table D3 X-Ray Diffraction Data for the Softened Overaged Condition.

Ageing Time (mins)	Cumulative Precipitation Hardening Time (mins)	Mean Vickers Hardness (Hv ₃₀)
0	0	350
2	3	385
4	7	386
8	15	398
16	31	400
32	43	421
64	107	426
128	235	436
256	491	430
480	971	414
1024	1995	422
1934	3929	432
4140	8069	434
7440	15509	445
16740	32249	446

Table D4 Isothermal Precipitation Hardening Data at 450°C.

The air fatigue tests were performed in laboratory air at ambient temperature.

Sample ID	σ_{minimum} (MNm ⁻²)	σ_{maximum} (MNm ⁻²)	σ_{mean} (MNm ⁻²)	$\sigma_{\text{amplitude}}$ (MNm ⁻²)	Test Freq (Hz)	N _r (cycles)
FH 4 (1)	-808.7	808.7	9.1	808.7	196	76100
FH 4 (2)	-713.8	732.1	4.2	722.9	192	261300
FH 4 (3)	-812.0	820.4	-8.5	816.2	195	67000
FH 4 (4)	-518.6	501.6	0	510.0	196	2.00E+07*
FH 4 (5)	-623.8	623.8	-2.56	623.8	194	1.00E+07*
FH 4 (6)	-675.1	666.5	-5.34	670.8	194	2864000
FH 4 (7)	-765.5	756.6	0.5	761.1	193	166900
FH 4 (8)	-700.0	696.6	-0.85	700.0	125	559700
FH 4 (9)	-680.3	688.9	5.13	684.6	125	1504000
FH 4 (10)	-645.6	670.1	12	657.9	125	1178600
FH 4 (11)	-763.0	793.0	15	780.0	124	157200
FH 4 (12)	-623.5	658.1	15	640.0	126	8776200*
FHH 4(5)	-599.2	629.4	0.17	620.0	126	47393700*

Table D5 Endurance Test Data for the Peak Hardened Condition.

* denotes specimen not broken

Sample ID	σ_{minimum} (MNm ⁻²)	σ_{maximum} (MNm ⁻²)	σ_{mean} (MNm ⁻²)	$\sigma_{\text{amplitude}}$ (MNm ⁻²)	Test Freq (Hz)	N _r (cycles)
ST 3	-548.4	618.2	16.5	601.3	125	600000
ST 4	-476.1	493.8	8.8	484.9	125	1.00E+08*
ST 5	-665.6	680.7	8.4	673.1	127	281000
ST 6	-747.9	760.5	5.9	754.0	127	40600
ST 7	-715.8	727.7	5.9	721.8	127	80500
ST 8	-630.3	631.1	0.4	630.7	101	864000
ST 9	-588.2	588.2	0	588.2	102	1.10E+07*
ST 10	-559.5	561.2	0.85	560.3	108	2.00E+07*
ST 11	-504.2	502.5	-0.85	503.4	108	2.00E+07*

Table D6 Endurance Test Data for the Standard Overaged Condition.

* denotes specimen not broken.

Sample ID	σ_{minimum} (MNm ⁻²)	σ_{maximum} (MNm ⁻²)	σ_{mean} (MNm ⁻²)	$\sigma_{\text{amplitude}}$ (MNm ⁻²)	Test Freq (Hz)	N _r (cycles)
CF S 2	-500.0	500.0	0	500.0	20	1.09E+07*
CF S 5	-649.9	649.9	0	649.9	5	79500
CF S 6	-621.6	621.6	0	621.6	5	1.04E+05
CF S 9	-530.0	530.0	0	530.0	4	1.09E+06
CF S 10	-575.0	575.0	0	575.0	5	472640
S 12	-427.4	427.4	0	427.4	196	1.07E+08*

Table D7 Endurance Test Data for the Softened Overaged Condition.

* denotes specimen not broken

Corrosion fatigue tests were performed in an aerated 0.6M NaCl solution, acidified to a pH = 2 using concentrated hydrochloric acid. The corrosion fatigue tests were performed at ambient temperature at a test frequency of 0.5Hz. The samples corroded at their free corrosion potential.

Sample ID	σ_{minimum} (MNm ⁻²)	σ_{maximum} (MNm ⁻²)	σ_{mean} (MNm ⁻²)	$\sigma_{\text{amplitude}}$ (MNm ⁻²)	Test Freq (Hz)	N _r (cycles)
CF FH 4	-650	650	0	650	0.5	24380
CF FH 5	-625	625	0	625	0.5	33040
CF FH 6	-600	600	0	600	0.5	41290
CF FH 8	-550	550	0	550	0.5	215110
CF FH 9	-570	570	0	570	0.5	87370
CF FH 10	-700	700	0	700	0.5	25450

Table D8 Corrosion Fatigue Endurance Data for the Peak Hardened Condition.

Sample ID	σ_{minimum} (MNm ⁻²)	σ_{maximum} (MNm ⁻²)	σ_{mean} (MNm ⁻²)	$\sigma_{\text{amplitude}}$ (MNm ⁻²)	Test Freq (Hz)	N _r (cycles)
CF STD 12	-580	580	0	580	0.5	117330
CF STD 13	-620	620	0	620	0.5	49980
CF STD 14	-640	640	0	640	0.5	51800
CF STD 15	-560	560	0	560	0.5	113010
CF STD 17	-600	600	0	600	0.5	65410
CF STD 18	-517	517	0	517	0.5	187470
CF STD 20	-540	540	0	540	0.5	223350
CF STD 21	-520	520	0	520	0.5	281770

Table D9 Corrosion Fatigue Endurance Data for the Standard Overaged Condition.

Sample ID	σ_{minimum} (MNm ⁻²)	σ_{maximum} (MNm ⁻²)	σ_{mean} (MNm ⁻²)	$\sigma_{\text{amplitude}}$ (MNm ⁻²)	Test Freq (Hz)	N _r (cycles)
CF S 11	-500	500	0	500	0.5	97040
CF S 12	-600	600	0	600	0.5	43470
CF S 13	-475	475	0	475	0.5	204230
CF S 14	-550	550	0	550	0.5	81950
CF S 15	-575	575	0	575	0.5	49770
CF S 18	-480	480	0	480	0.5	221720
CF S 19	-510	510	0	510	0.5	193340

Table D10 Corrosion Fatigue Endurance Data for the Softened Overaged Condition.

The following corrosion fatigue tests were performed at a test frequency of 0.05Hz.

Sample ID	σ_{minimum} (MNm ⁻²)	σ_{maximum} (MNm ⁻²)	σ_{mean} (MNm ⁻²)	$\sigma_{\text{amplitude}}$ (MNm ⁻²)	Test Freq (Hz)	N _r (cycles)
CF FH 11	-587	587	0	587	0.05	48752
CF FH 12	-612	612	0	612	0.05	29794

Table D11 Corrosion Fatigue Endurance Data for the Peak Hardened Condition.

FV.520B

A PRECIPITATION HARDENING
MARTENSITIC STAINLESS STEEL

A Subsidiary of Sheffield Forgemasters Ltd



Firth Vickers Special Steels

FV.520B

A PRECIPITATION HARDENING MARTENSITIC STAINLESS STEEL

FV520B is a weldable, low carbon precipitation hardening martensitic stainless steel, which may be heat treated to give a wide range of strengths, together with excellent toughness even at low temperatures.

Its resistance to corrosion is substantially better than the simpler 12-13% Chromium steels and is similar to that of 304 type austenitic steel for many environments.

FV520B combines the best features of both the austenitic and martensitic steels and has found very wide engineering applications particularly for shafts, blades, fans, pump parts, valves, fasteners and transducers. [FV520B can be supplied in accordance with **British Standards 4S100**, International Aerospace Specifications and M.O.D. Def Stan 95-14 (STA. 59.)]

COMPOSITION

C	Si	Mn	Cr	Ni	Mo	Cu	Nb
.07	.70	1.00	13.2/14.7	5.0/6.0	1.2/2.0	1.2/2.0	.20/.70
max.	max.	max.					

PRE-MANUFACTURE

FV520B is melted by the basic electric steel practice followed by vacuum degassing and cast into ingots. Hot working to billet takes place in the 1200°C to 900°C range followed by softening and dressing. Experience has shown that in order to attain maximum consistency of mechanical properties, the billets should be subjected to ultrasonic test, cleanness and macro examination and any unacceptable material discarded prior to release for re-rolling.

BAR ROLLING

Rolling from billet to bar takes place in the 1150°C-900°C range.

HEAT TREATMENT

After rolling to size a wide variety of heat treatments is available which give an attractive range of mechanical properties. For most of the standard conditions a triple heat treatment cycle has been developed consisting of the following:

- A homogenisation treatment between 1000°/1050°C to ensure that residual influences from the previous hot working operations are removed.
- A second treatment in the 750°/850°C range which results in the precipitation of alloy carbides and a raising of the martensitic finish temperature. This stage is known as 'solution treatment' or 'primary hardening treatment'.
- Three standard ageing treatments have been selected. Ageing at 450°C gives maximum strength and 620°C the softest condition. 550°C gives an intermediate strength condition. Fig. 1 shows the effect of ageing for 4 hour periods on hardness at various temperatures.

FIG. 1. SOLUTION TREATED 1050°C a/c + 2 HRS 750°C

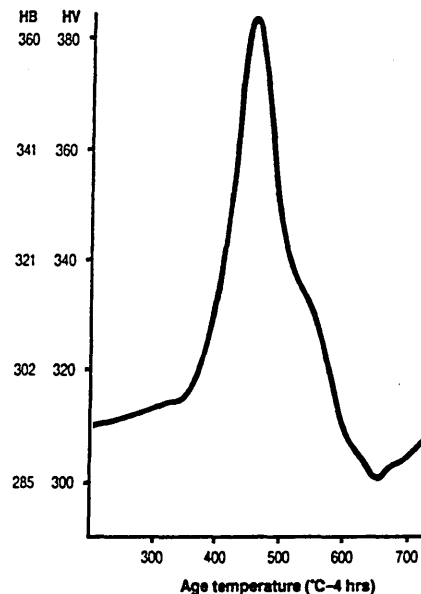


FIG. 2. SOLUTION TREATED 1050°C a/c + 850°C (2 HRS) a/c

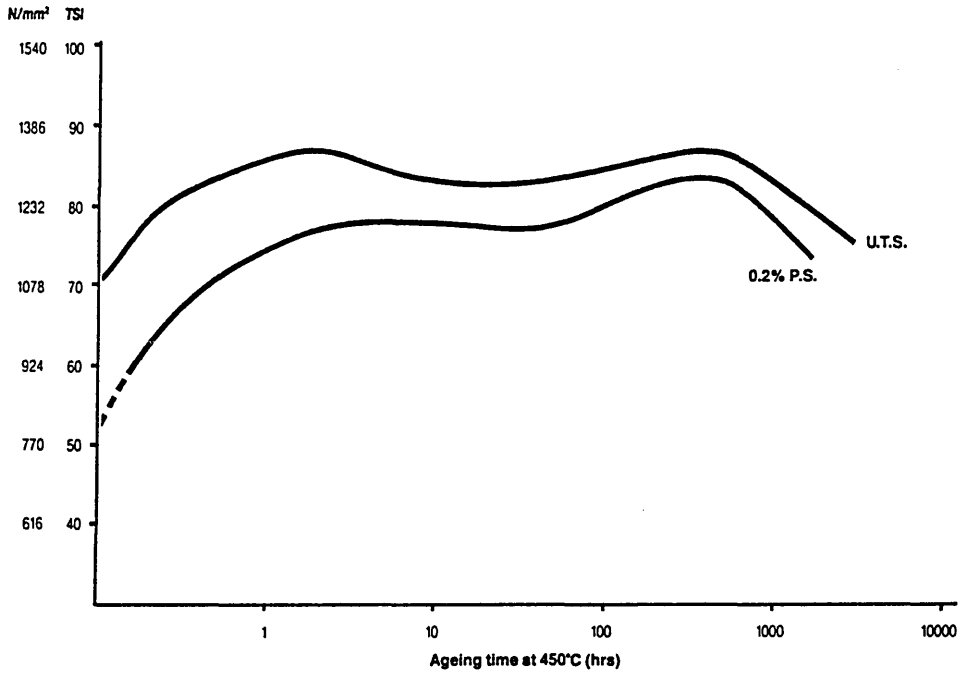
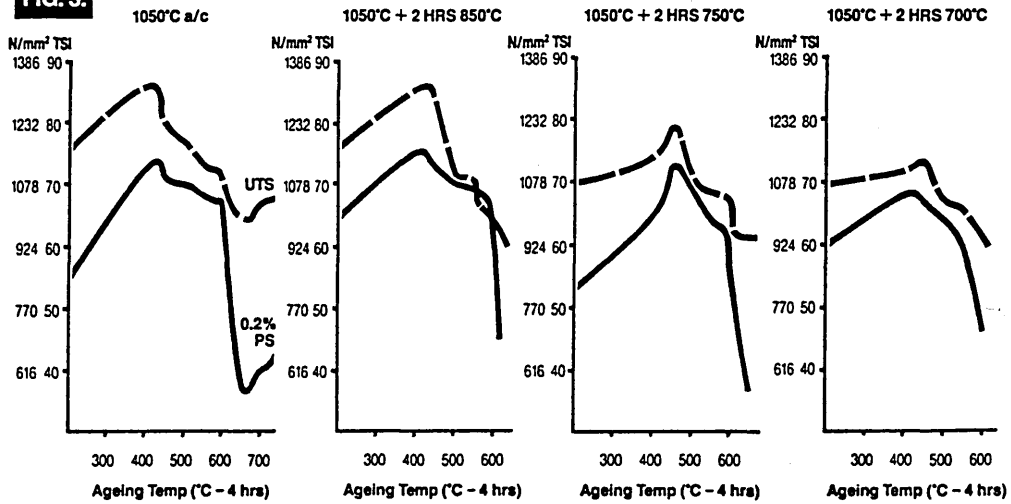


FIG. 3.



c. (Cont. from page 2) Fig. 2 shows the effect of ageing at 450°C, the peak hardening temperature on tensile strength. Fig. 3, 3A and 3B illustrate the interactions of solution treatment temperature and ageing temperature on mechanical properties. Fig. 4 shows the tensile strength

and proof stress plotted against testing temperatures for peak hardened, 550°C and 620°C overaged conditions.

FIG. 3A.

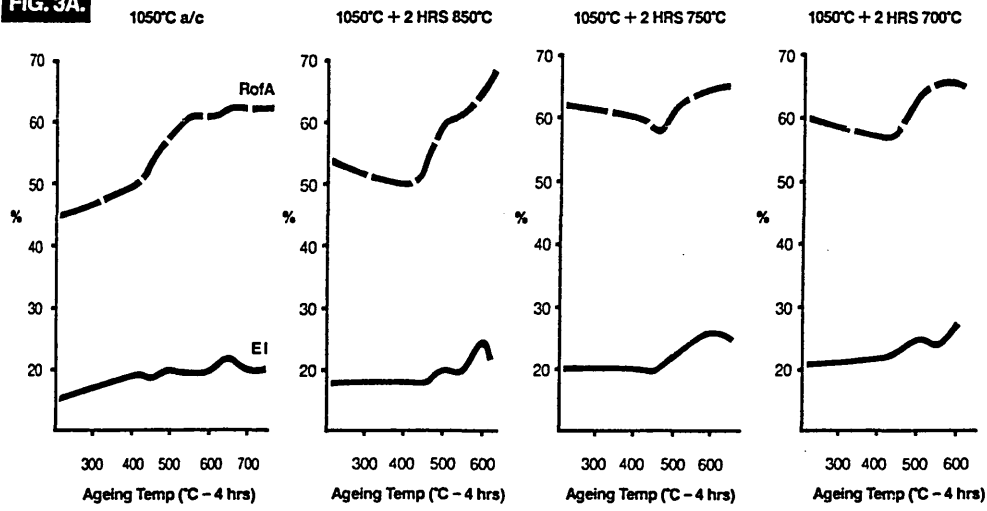


FIG. 3B.

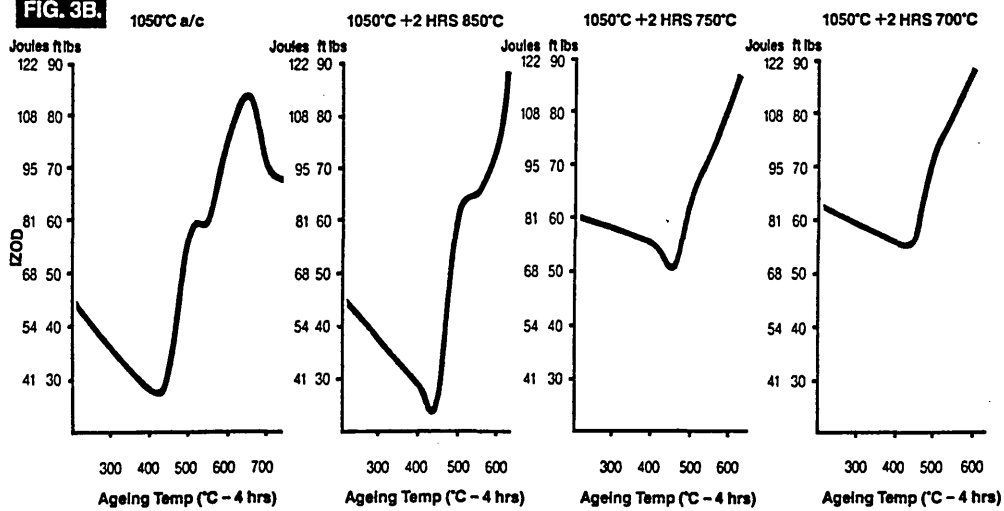
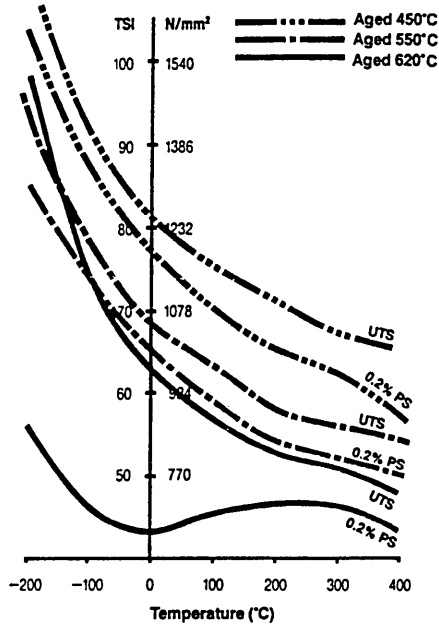


FIG. 4. TENSILE STRENGTHS AT VARIOUS TEMPERATURES



In order to attain the highest hardness condition available a two stage heat treatment is applied which is only recommended for bars of 2.5" equivalent diameter or less. It consists of a normalising treatment at 950°C which is a compromise temperature between the first two stages of the triple treatment followed by a 450°C ageing treatment.

Material may also be supplied in the softened condition by heat treating at 620°C following rolling.

The standard heat treatments are listed in Table 1 and selected mechanical properties in Table 2 and Table 3.

MATERIAL INTENDED FOR FURTHER WORKING

Laboratory treatments can be carried out to the specification required, and a test certificate issued accordingly, indicating the heat treatment required to achieve final mechanical properties.

TABLE 1. The standard conditions of heat treatment are as detailed below:

PEAK HARDENED

30 minutes 1050°C cool in air + 2 hours at 750/850°C cool in air + 4 hours at 450°C cool in air.

550°C OVERAGED

30 minutes 1050°C cool in air + 2 hours at 750°C cool in air + 2 hours at 550°C cool in air.

620°C OVERAGED

30 minutes 1050°C cool in air + 2 hours at 750°C cool in air + 2 hours at 620°C cool in air.

NORMALISED

Applied to bars of less than 2.5" dia. 30 minutes 950°C cool in air.

NORMALISED AND AGED

Applied to bars of less than 2.5" dia. 30 minutes 950°C cool in air + 2/4 hours at 450°C cool in air.

SOFTENED

As rolled + 2 hours at 620°C cool in air.

N.B.

It is advisable that after the intermediate treatment the material is allowed to stand at ambient temperature for 24 hours to allow adequate transformation prior to the final ageing.

For component parts required to be in the peak hardened or normalised 450°C condition, machining to size normally takes place prior to ageing. The subsequent 450°C ageing treatment gives only a superficial oxidation and a very small predictable dimensional change.

TABLE 2. MECHANICAL PROPERTIES OF ROLLED BAR – Standard Conditions

CONDITION	0.2% Proof Stress N/mm ² (min)	Tensile Strength N/mm ²	Elongation 5D % min	Hardness Brinell	Izod Joules (typical)	Fatigue (Wholer) 10 ⁶ revolutions N/m ² (typical)	* B.S. Aerospace Equivalent	* Def Stan 95-14 (STA 59)
1050*AC + 2 hrs 750/850* AC + 4 hrs 450* AC	1030	1170/1310	12	352/395	47	±508	2S144	C + H
Solution treatment at the lower end of the range gives improved ductility with a slight fall off in tensile properties.								
1050*AC + 2 hrs. 750*AC + 2 hrs. 550*AC	800	925/1080	15	276/321	102	±555	2S143	D + F
1050*AC + 2 hrs. 750*AC + 2 hrs. 620*AC	540	850/1000	20	255/302	115	±585	—	D + G
950*AC	—	—	—	320/380	—	—	—	B
950*AC + 2/4 hrs. 450*AC	1030	1265/1465	10	380/425	24	±460	2S/45	—
620*AC	—	—	—	266/321	—	—	—	A

NOTE: Information on SI units is given in BS3763 'The International System of Units (SI)' and BS350 'Conversion factors and table'.

*Orders placed to B.S.2S 143, 144, 145 or Def Stan 95-14 (STA 59) would meet the full specification requirements. Non standard conditions are available on request.

TABLE 3. TYPICAL PROPERTIES OVERAGED 550°C CONDITION

Testing Temp. °C	0.2% Proof N/mm ²	Tensile Strength N/mm ²	E1 5D %	Izod Joules	Fatigue (Wöhler) 10 ⁶ revolutions N/mm ²
-196	1257	1432	23	14	—
-78	1080	1173	23	96	—
20	955	1029	17	102	±585
100	892	975	18	108	—
200	810	892	17	88	—
300	781	861	14	77	±416
400	735	838	11	71	±416
450	688	804	10	65	±431
550	511	644	14	—	—

NOTES

1 IMPACT STRENGTH

The notched impact strength of FV520(B) is high in relation to its tensile strength. Actual values depend on several factors in addition to strength, i.e. grain size and test direction relative to grain flow. There is also some cast to cast scatter. The range of results obtained with Izod tests carried out at ambient temperature is given in Fig. 5.

Results for Izod tests carried out at various temperatures on specimens machined from small diameter bars in various conditions of heat treatment are shown in Fig. 6.

FIG. 5. IZOD VARIATION WITH TENSILE STRENGTH

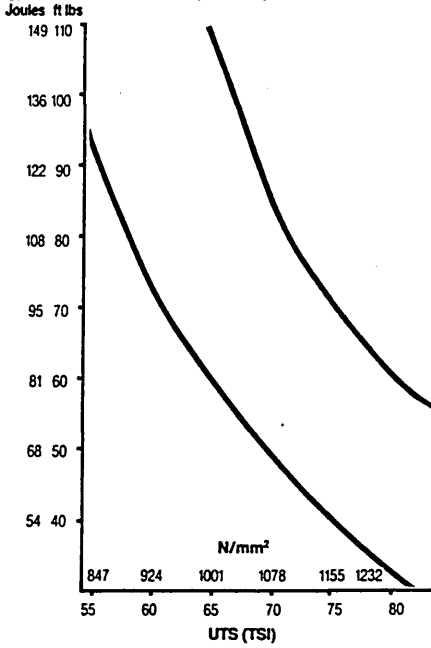
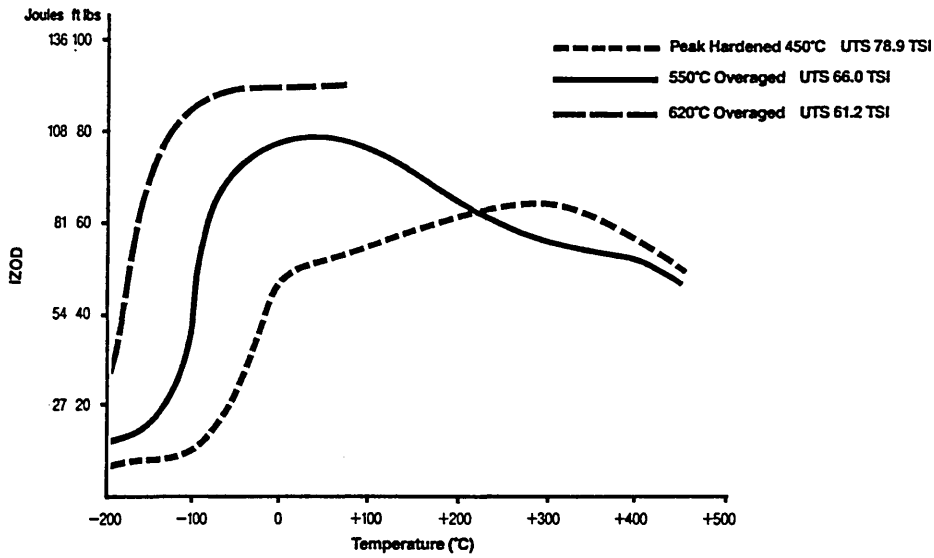


FIG. 6.

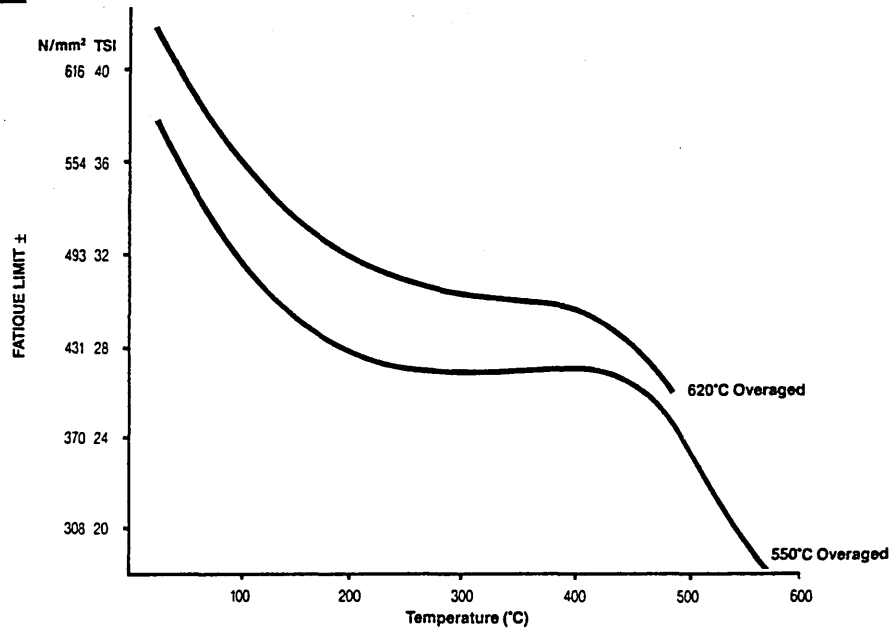


2 FATIGUE STRENGTH

FV520(B) exhibits its optimum fatigue behaviour in the 620°C overaged condition. Fatigue properties in the peak hardened condition vary significantly with melting route. Values of ± 525 N/mm² are usual for longitudinal tests on air melt material but can increase to ± 650 N/mm² for vacuum arc remelt.

The differences are less marked on the overaged 550°C and overaged 620°C condition. Vacuum arc remelting gives a marked improvement in transverse direction properties. The effect of test temperature on fatigue limit of air melt material is illustrated in Fig. 7.

FIG. 7.



3 STABILITY AT ELEVATED TEMPERATURES

In common with all precipitation hardening steels, exposure at elevated temperatures can cause a reduction of impact strength in FV520(B). This is an extension of the basic ageing system of the material and can be detected to a slight degree as low as 300°C after exposure.

At higher temperatures of exposure an overaging condition is more rapidly reached and properties recover. This peak condition is expected to be around 6 to 8 months at 450°C.

As most applications of FV520(B) are at temperatures below 350°C this effect will not normally be a cause for concern.

PHYSICAL PROPERTIES

A. COEFFICIENT OF LINEAR EXPANSION PER °C

Temperature °C	Peak Hardened 450°C	550°C Overaged	620°C Overaged
20/100	0.000011	0.0000115	0.0000126
20/200	0.0000115	0.000012	0.0000134
20/300	0.000012	0.000012	0.0000138
20/400	0.000012	0.0000125	0.0000142
20/500	0.0000125	0.000013	0.0000145

B. YOUNG'S MODULUS (DYNAMIC)

Temperature °C	Peak Hardened 450°C N/mm ²	550°C Overaged N/mm ²	620°C Overaged N/mm ²
20	210,210	214,368	195,580
100	203,896	210,441	—
200	200,354	203,434	—
300	191,884	193,732	—
400	182,875	186,032	—
500	169,554	172,634	—

C. THERMAL CONDUCTIVITY G.CAL/SEC/CM/°C

Temperature °C	Peak Hardened 450°C	550°C Overaged	620°C Overaged
20	0.041	0.041	0.046
200	0.052	0.052	—
450	0.061	0.060	—

D. ELECTRICAL RESISTIVITY MICRO OHMS/CM.

Temperature °C	Peak Hardened 450°C	550°C Overaged	620°C Overaged
20	77.2	77.1	77.9
200	86.4	86.6	—
450	99.4	98.6	—

E. SPECIFIC GRAVITY

	Peak Hardened 450°C	550°C Overaged	620°C Overaged
	7.82	7.83	7.87

F. POISSONS RATIO

	Peak Hardened 450°C	550°C Overaged	620°C Overaged
	0.292	0.292	0.290

G. MAGNETIC PERMEABILITY Data will be supplied on request.

CORROSION RESISTANCE

Resistance to corrosion is much superior to that of the simpler 12% chromium types and is similar to that of the austenitic 304S15 type for many environments. There is useful resistance to some acid conditions and rusting rate in marine and industrial atmospheres is low. The steel is more resistant to saline solutions than are the simpler 13% chromium types and can give good service in sea water in splash zones and for intermittent immersion. It is subject to pitting corrosion under marine organism growths and crevice corrosion on prolonged immersion however.

General and localised corrosion resistance without stress is not influenced by heat treatment but there is some effect on corrosion fatigue resistance. It should also be noted that there can be stress corrosion cracking in some environments with steel in the peak hardened state if subject to sustained high tensile loading. If in doubt, advice should be sought regarding this aspect.

	Peak Hardened	550°C Overaged	620°C Overaged
Pitting corrosion initiation potential, mV (S.C.E.)*	-80	-80	-80
Corrosion fatigue endurance limit (10^8 cycles), N/mm ² †	+200	+230	+300

* Determined using a solution containing 0.6M NaCl and 0.1M NaHCO₃ at 25°C.

† Determined using a 3% NaCl solution at room temperature.

WELDING

A notable feature of FV520B is its good weldability. It can readily be welded by normal techniques, although oxy-acetylene welding is undesirable in view of possible pick up of carbon. Submerged arc welding techniques can be used provided that conditions can be maintained which will avoid pick up of alloying elements from the flux.

For gas shielded and metal arc processes, matching wire and electrodes are available.

When welding structures which are required in medium to high tensile strengths, it is usual to part machine, prepare surfaces for welding and weld, in the two stage treatment condition, either 1050°C + 750°C or 1050°C + 850°C. Pre-heat to 100/150°C is recommended.

Post weld heat treatment should comprise the normal second and third treatment operations, i.e. 850°C + 450°C for the peak hardened condition and 750°C + 550°C for the overaged 550°C condition. The same recommendations as given under 'Heat Treatment' i.e. ensuring full transformation after the 750°C or the 850°C stage should be observed.

MACHINING

Detailed machining information for FV520B is available, some of which is summarised here.

SPEEDS FOR ROUGH TURNING

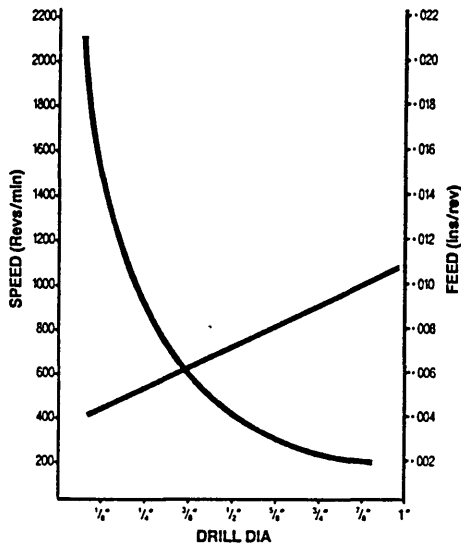
Dia of Work Ins	Surface speed ft/min	
	High Speed Steel	Carbide
1	60/80	150/200
3	40/60	150
10	30/40	80/100

SPEEDS FOR FINISH TURNING

Dia of Work Ins	Surface speed ft/min	
	High Speed Steel	Carbide
1	90/120	225/300
3	60/90	225
10	45/60	120/150

SPEEDS FOR PLAIN AND FACE MILLING – High speed steel cutters:- 60-80ft/min.

DRILLING CHART



The straight line indicates the best feeds for the different drill sizes.

More detailed information can be forwarded on request.

GALLING CHARACTERISTICS

Numerous successful applications have shown that FV520B has excellent antigalling characteristics.

The table lists the results of laboratory galling tests for Polished samples rotated against each other under load.

COMBINATION OF CONDITIONS TESTED

BHN		BHN		Load to cause galling N/mm ²	
N and aged	420	Vs	N and aged	420	42
Peak Hardened	400	Vs	620° Overaged	280	162
550° Overaged	331	Vs	N and aged	420	137

STRESS CONVERSION TABLE

tonf/in ²	kgf/mm ²	N/mm ²	p.s.i.	tonf/in ²	kgf/mm ²	N/mm ²	p.s.i.
20	31.5	308.9	44800	61	96.1	942.1	136640
21	33.1	324.3	47040	62	97.6	957.5	138880
22	34.6	339.8	49280	63	99.2	973.0	141120
23	36.2	355.2	51520	64	100.8	988.4	143360
24	37.8	370.7	53760	65	102.4	1004.0	145600
25	39.4	386.1	56000	66	103.9	1019.0	147840
26	40.9	401.6	58240	67	105.5	1034.0	150080
27	42.5	417.0	60480	68	107.1	1050.0	152320
28	44.1	432.4	62720	69	108.7	1066.0	154560
29	45.7	447.9	64960	70	110.2	1081.0	156800
30	47.2	463.3	67200	71	111.8	1097.0	159040
31	48.8	478.8	69440	72	113.4	1112.0	161280
32	50.4	494.2	71680	73	115.0	1127.0	163520
33	52.0	509.7	73920	74	116.5	1143.0	165760
34	53.5	525.1	76160	75	118.1	1158.0	168000
35	55.1	540.5	78400	76	119.7	1174.0	170240
36	56.7	556.0	80640	77	121.3	1189.0	172480
37	58.3	571.4	82880	78	122.8	1205.0	174720
38	59.8	586.9	85120	79	124.4	1220.0	176960
39	61.4	602.3	87360	80	126.0	1236.0	179200
40	63.0	617.8	89600	81	127.6	1251.0	181440
41	64.6	633.2	91840	82	129.1	1266.0	183680
42	66.1	648.7	94080	83	130.7	1282.0	185920
43	67.7	664.1	96320	84	132.3	1297.0	188160
44	69.3	679.5	98560	85	133.9	1313.0	190400
45	70.9	695.0	100800	86	135.4	1328.0	192640
46	72.4	710.4	103040	87	137.0	1344.0	194880
47	74.0	725.9	105280	88	138.6	1359.0	197120
48	75.6	741.3	107520	89	140.2	1375.0	199360
49	77.2	756.8	109760	90	141.7	1390.0	201600
50	78.7	772.2	112000	91	143.3	1405.0	203840
51	80.3	787.7	114240	92	144.9	1421.0	206080
52	81.9	803.1	116480	93	146.5	1436.0	208320
53	83.5	818.5	118720	94	148.0	1452.0	210560
54	85.0	834.0	120960	95	149.6	1467.0	212800
55	86.6	849.4	123200	96	151.1	1483.0	215040
56	88.2	864.9	125440	97	152.8	1498.0	217280
57	89.8	880.3	127680	98	154.3	1514.0	219520
58	91.3	895.7	129920	99	155.9	1529.0	221760
59	92.9	911.2	132160	100	157.5	1544.0	224000
60	94.5	926.7	134400				

PRODUCTION CAPABILITIES

Round Bars



Black/Descaled 9 to 112 mm Up to 6.096 m
Intermediate Tolerance 9 to 100 mm Up to 6.096 m
Close Tolerance 9 to 100 mm Up to 6.096 m
Peeled 20 to 100 mm Up to 6.706 m

Square Bars



Black/Descaled 14.5 to 100 mm Up to 6.096 m

Hexagon Bars



Black/Descaled 15 to 70 mm A/F Up to 6.096 m
Intermediate Tolerance 14 to 60 mm A/F Up to 6.096 m
Close Tolerance 14 to 60 mm A/F Up to 6.096 m

Flat Bars



Black/Descaled 19 x 5 to 230 x 70 mm Up to 6.096 m

The above table shows the capabilities of the Firth Vickers Mills.

Round bars in the range 12mm to 190mm diameter can be supplied ex-stock.

APPENDIX III - Chemical Analysis

Table E1 Chemical Analysis of Maraging Steels.

Material Specification	Element										
	Ni	Co	Mo	Ti	C	Si	Mn	Al	Cr	Fe	
18Ni(350) Maraging Steel [27]	18.09	12.16	4.54	1.27	0.04	0.05	0.03	-	-	bal	
Maraging Steel [28]	18	11.5	5.1	0.87	-	-	-	-	-	bal	
18Ni(300) Maraging Steel [29]	18.4	8.9	4.9	0.74	-	-	-	0.7	0.2	bal	

Table E1 Chemical Analysis of Maraging Steels, after Various Workers.

A Technical Note

FURTHER OBSERVATIONS OF EARLY FATIGUE CRACK DEVELOPMENT

Y.-Z. WANG¹, R. AKID², A. CLARK¹, J. D. ATKINSON¹

¹School of Engineering, Sheffield Hallam University, Sheffield S1 1WB, U.K.

²SIRIUS, Department of Mechanical & Process Engineering, University of Sheffield, S1 3JD, U.K.

Received in final form 12 October 1995

Abstract—A scanning electron microscope (SEM) has been used to examine plastic replicas taken from the surface of fatigue specimens in order to understand the role of microstructure on the early stages of fatigue crack development under various environmental conditions. This involved shadowing and coating replicas and pre-marking appropriate areas of interest prior to SEM examination.

Keywords—Environment–microstructure interactions; SEM studies; Non-metallic inclusions; Fatigue crack initiation sites

INTRODUCTION

The advent of fracture mechanics based tests using pre-cracked specimens has greatly improved the understanding of cracking processes. However, this test methodology can have limited applicability to service situations, where failures resulting from fatigue or corrosion fatigue usually occur after a prolonged time of operation, and often consists primarily of the so-called “crack initiation regime”. Direct observation of the behaviour of a crack from the very early stages of lifetime until final failure can be extremely laborious, since the site for crack nucleation is of a random characteristic and often cannot be easily identified at the embryonic stage. The technique which involves the plastic replication of a specimen’s surface has been particularly successful in overcoming some of these difficulties. In this method a section of acetate film is applied to the area of interest at selected intervals, from the start of loading to the ultimate fracture of the specimen. The replicas provide a permanent record of the changes in surface topography of the specimen during the fatigue life and therefore enables a method of tracking the morphological features related to crack development after the test is terminated.

Previous work [1,2] using this technique has revealed that the early stages of fatigue crack development involve strong crack/microstructural interactions, i.e. for the high strength steel studied, non-metallic inclusions played a very important role in providing sites for crack nucleation. However, the limited resolution associated with optical microscopy can significantly restrict observations of the details of fatigue crack development and reduce the amount of information available from the replicas.

In an effort to gain a clearer understanding of the role of non-metallic inclusions in fatigue crack development, replicas taken during a previous study [1], have been re-examined using a scanning electron microscope (SEM). It has been shown that, through careful preparation of the replicas and by optimising the scanning electron microscope operating conditions (see the following section), electron microscopy can markedly improve the detail of the image and thereby reveal substantially more information of microstructural features associated with the early stages of cracking.

EXPERIMENTAL DETAILS

The material used and details of the fatigue experiments during which plastic replicas were taken have been reported previously [1]. A further examination of these replicas has now been carried out using a Philips XL40 scanning electron microscope. Before examination the SEM replicas were marked, with the aid of an optical microscope, to locate crack sites. This was achieved using a non-xylene-containing, ultra-fine point conducting pen. Replicas were then shadowed by evaporating a Pt–Au alloy at a direction of 45° onto the surface of the replica, to achieve a thickness of about 15 Å. Finally the replicas were coated with carbon. It should be noted that in some cases re-marking of crack sites was necessary after the shadowing and coating procedure.

The SEM settings used to examine the replicas were carefully selected and it was found that a low electron beam acceleration voltage of less than 5 kV was essential to avoid damage to the replicas. The most difficult part of the SEM examination was the identification of areas of interest, i.e. the locations of cracks, especially on replicas taken during the very early stages of the test. Pre-marking around the areas of interest was found to be essential for any measure of success. Once the desired area is found, the normal procedure for examining samples under the SEM can be employed.

RESULTS AND DISCUSSION

The microstructural features associated with the initial growth of cracks, formed under identical stress amplitude levels ($\sigma_a = 750$ MPa) but within different environments, are shown in Figs 1–3. The optical micro-graphs of these cracks were presented previously in Figs 2–4 of Ref. [1]. Since the observation was carried out on direct replications of the cracks, the topographic features shown in Figs 1–3 appear to be somewhat different from those directly observed from the specimens. When compared with optical micrographs, the SEM images offer improved resolution and reveal finer details of the features of crack/microstructural interactions.

Figure 1 shows an example of crack initiation under air fatigue conditions illustrating the association between crack initiation and non-metallic inclusions. Figure 1A–C shows debonding of an inclusion from the matrix, having occurred at a very early stage in life, i.e. around 6% of life. After debonding an elongated “oval-shaped” surface cavity was created, orientated at about 45° to the loading axis, i.e., coincident with the maximum shear plane. In the first photograph, Fig. 1A, a very small crack can be seen at the top left-hand end of the cavity. This crack ceases to grow after reaching the boundary of an adjacent grain. Two new cracks then develop at the top and bottom of this cavity (Fig. 1B). The crack at the bottom right-hand side of the defect initially grew along the shear plane, but later changed direction to propagate perpendicular to the loading axis (Fig. 1C). Whilst it has been observed in numerous cases that crack development involved the debonding of an inclusion from the matrix, pre-existing defects can also be the source of cracking. Figure 1D shows an example of what appears to be a crack emanating from the edge of an inclusion. The replica illustrating this feature was taken prior to loading, i.e., at $N=0$ cycles. As seen in Fig. 1E there is no evidence of surface crack growth after 5000 cycles, suggesting that in-depth cracking occurs at the expense of surface cracking. This is an important consideration, from the point of lifetime evaluation, and raises serious doubt on the application of “initiation-based” procedures for predicting lifetime. Finally, crack propagation from the original defect site can be seen in Fig. 1F.

Figure 2 presents fatigue cracking in a specimen exposed to an 0.6 M NaCl solution at its open circuit potential (OCP). From this figure it can be seen that cracks develop from a site at which localised corrosion takes place. The local corrosion cell being formed at the interface of the matrix

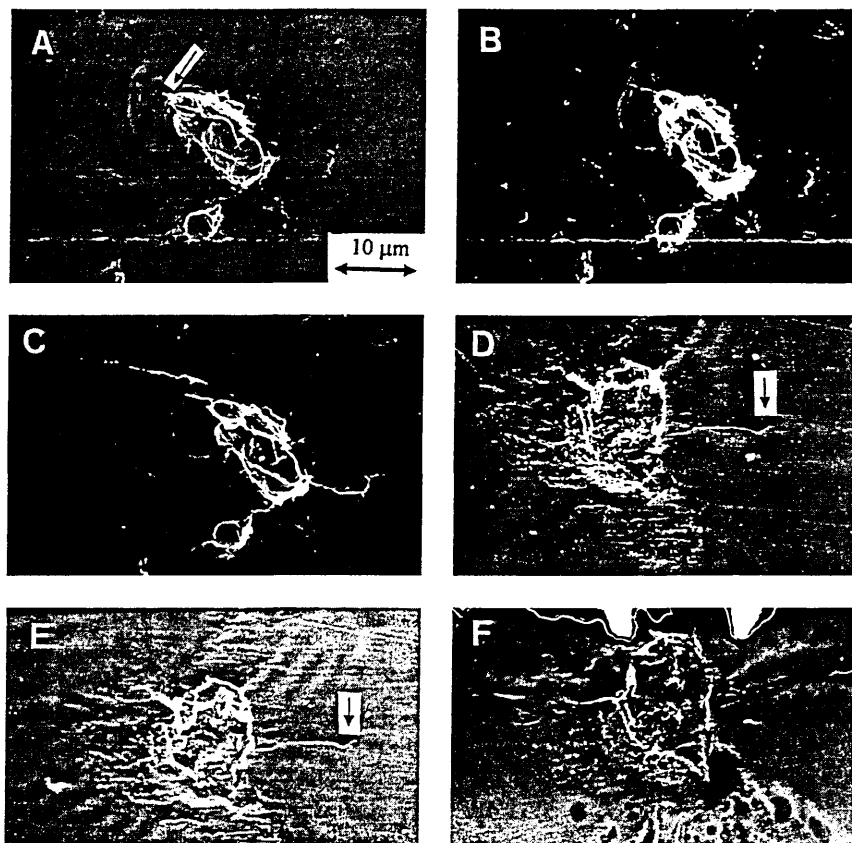


Fig. 1. SEM observations at the same magnification of coated replicas showing early stages of air fatigue cracks, $\sigma_a=750$ MPa, $f=10$ Hz, $R=-1$, $N_f=79,400$ (loading direction—parallel to vertical edge of photographs). Crack one: (A) 5000 cycles, (B) 15,000 cycles, (C) 40,000 cycles. Crack two: (D) 0 cycles, (E) 5000 cycles, (F) 30,000 cycles.

and a non-metallic inclusion. Figures 2B and 2E show that localisation of corrosion is restricted to an area of approximately $50 \mu\text{m}$ in diameter. This is an interesting feature and illustrates the inequality of anode and cathode areas, a feature which can contribute to high local anodic current densities. Finally, Figs 2C and 2F show that corrosion fatigue cracks are unlike air fatigue cracks in that they do not exhibit a fine “hair-line”-type appearance, but show signs of localised dissolution at the crack flanks. Such details highlight the important role of micro-environmental climates and localised corrosion in corrosion fatigue cracking.

Crack development, under the same conditions as shown in Fig. 2, but with a cathodic polarization of -1250 mV (SCE), is shown in Fig. 3. Here cracking exhibits a behaviour somewhat different to that in air and in solution at the OCP, although it should be noted that damage is again related to the presence of a non-metallic inclusion. Unlike open circuit potential tests, localised corrosion was not observed and although crack development involved the debonding of an inclusion from the matrix (Fig. 3A), substantial surface cracking only occurred at the edge of the cavity after a considerable number of load cycles ($N/N_f=0.75$). However before the crack can be detected at the edge of the cavity produced by the large inclusion, at $N=24,000$, a number of tiny cracks can be observed ahead of the large cavity, associated with some form of micro-defects

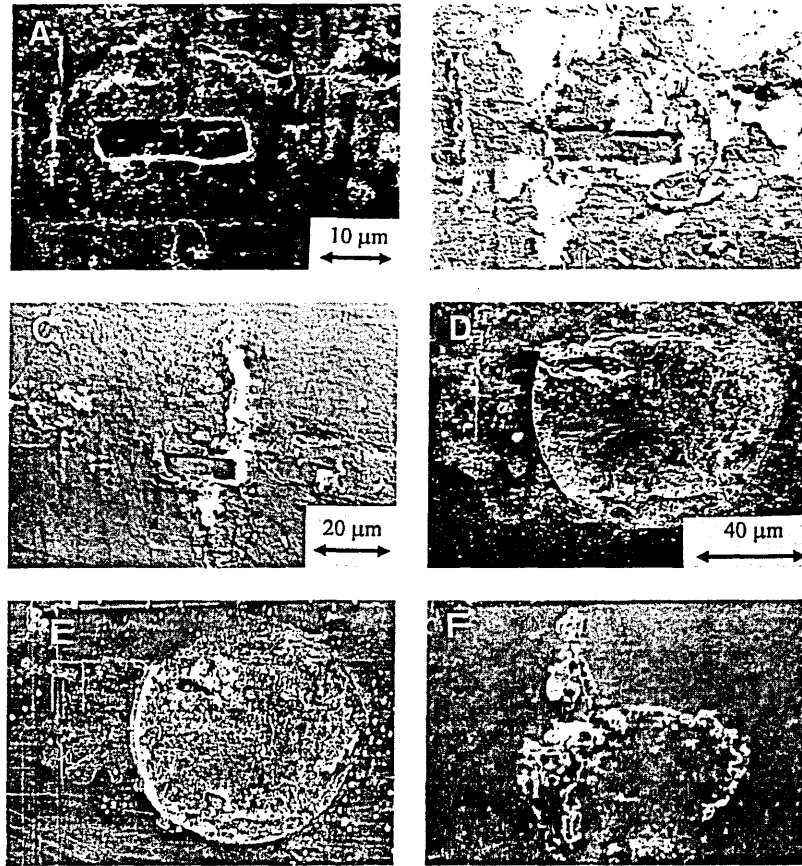


Fig. 2. SEM observations of coated replicas showing early stages of corrosion fatigue cracking in 0.6 M NaCl at OCP. $\sigma_a = 750$ MPa, $f = 1$ Hz, $R = -1$, $N_f = 15.710f$ (loading direction—parallel to horizontal edge of photographs). Crack one: (A) 600 cycles, (B) 3000 cycles: same magnification as (A), (C) 5200 cycles. Crack two: (D) 600 cycles, (E) 4200 cycles: same magnification as (D), (F) 9947 cycles, same magnification as (D).

(Fig. 3B). These small cracks later merge with each other and with the major crack to form the main failure crack, as shown in Fig. 3C.

These observations confirm the results of previous studies which highlight the very important role non-metallic inclusions play in fatigue crack development. They also show that both microstructural features and experimental conditions can significantly affect cracking behaviour. Fig. 1A shows that cracks can form during the very early stages of lifetime, but grain boundaries may act to retard subsequent growth. Cracks can become inactive on reaching a grain boundary with further cracking possible through the development of a new cracks, perhaps aligned along more favourable metallographic orientations. Although crack development involved the debonding of a non-metallic inclusion, surface crack propagation did not appear to result from the cavity until a considerable number of cycles had elapsed. Furthermore, crack development involved the coalescence of several minor cracks. These minor cracks being associated with micro-defects, of unknown origin, on the surface. Despite the presence of pre-existing micro-defects or the formation of surface cavities it is noted that surface crack development does not always appear to result immediately

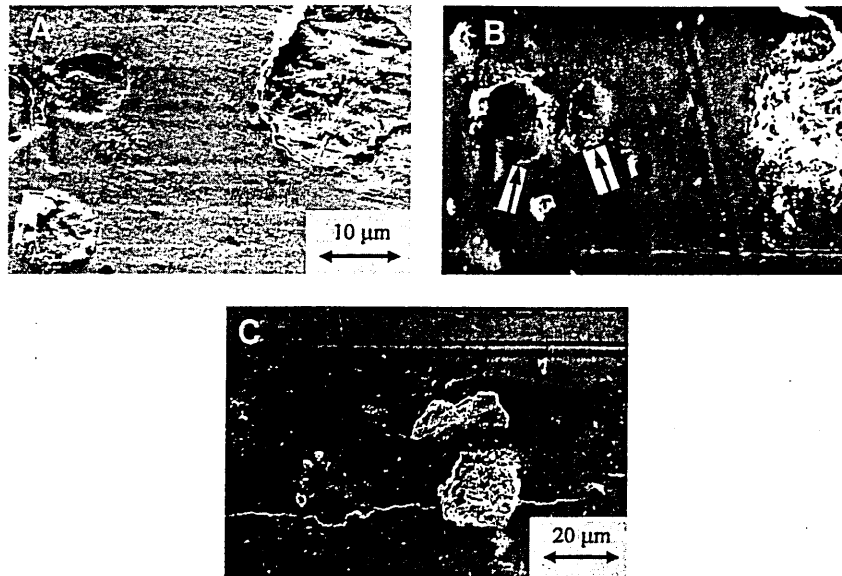


Fig. 3. SEM observations of coated replicas showing early stages of corrosion fatigue cracking in 0.6 M NaCl at an applied potential -1250 mV (vs. SCE) $\sigma_a = 750$ MPa, $f = 1$ Hz, $R = -1$, $N_f = 41,838$ (loading direction—parallel to vertical edge of photographs). (A) 15,000 cycles, (B) 24,000 cycles; same magnification as (A), (C) 36,000 cycles.

and this would suggest that a plasticity localisation phase is involved in the early development of fatigue cracks. Those micro-cracks that are seen to develop within a certain distance from the large cavity, as illustrated in Fig. 3, may be attributed to the presence of initial micro-defects, although hydrogen discharged by cathodic polarisation may contribute to micro-damage and cannot be ignored, as during loading hydrogen can be re-distributed in the material with a tendency to concentrate at positions where the hydrostatic stress is at a maximum.

SUMMARY

1. Through careful preparation and optimisation of operating conditions the SEM can be used to examine acetate replicas thereby revealing significantly more detail of initial crack development involving microstructural interactions.
2. Non-metallic inclusions appear to play a very important role in fatigue crack initiation and development under a number of different environmental conditions. The nature of the environment also significantly affects the mechanism through which crack development occurs.

Acknowledgements—The authors thank British Steel plc, the Royal Academy of Engineering for sponsoring one author (RA) as a Senior Research Fellow and the Universities of the respective authors for providing the necessary facilities for the investigations.

REFERENCES

1. Y.-Z. Wang, R. Akid and K. J. Miller (1995) The effect of cathodic polarization on corrosion fatigue of a high strength steel in salt water. *Fatigue Fract. Engng Mater. Struct.* **18**, 293–303.
2. Y. Z. Wang and R. Akid (1995) The role of non-metallic inclusions in fatigue, pitting and corrosion fatigue. Accepted for publication in *Corrosion (J. Sci. Engng)*.